INVESTIGATIONS OF LITHOSPHERIC SHORTENING ON MERCURY: INSIGHTS INTO STRUCTURE AND ORIENTATION OF THRUST FAULTS AND APPLICATION TO GLOBAL CONTRACTION

by

STEPHAN RAY LOVELESS

(Under the Direction of Christian Klimczak)

ABSTRACT

Mercury, the smallest planet in the Solar System and closest planet to the Sun, has undergone global contraction, which is a process causing the planet to shrink due to its long, sustained cooling. This has led to the formation of thousands of shortening landforms distributed across Mercury's surface. These positive-relief, surface-breaking landforms are caused by the folding over thrust faults. Traditionally, Mercury's shortening landforms have been classified into one of three categories: "lobate scarps", "wrinkle ridges", and "high-relief ridges". In this dissertation, these categories are assessed through multiple statistical analyses. The subsurface fault geometry is then modeled for a large sample size of Mercury's shortening landforms. These statistical and modeling efforts both inform a new assessment of Mercury's global contractional strain. Finally, Mercury's current orbit and rotation is assessed for its influence on the observed systemic thrust fault orientations. Through this work, Mercury's shortening landforms are found to exist along a morphological spectrum between "lobate scarp" and "wrinkle ridge" designations, suggesting that the morphology of Mercury's shortening landforms does not support these

categories. Mercury's shortening landforms are also shown to host a wide range of thrust

system geometries that include single-listric faults, imbricate stacks, and push-up

structures. This data set is then used to establish globally observed ranges of geometric

fault parameters which are then used to inform strain calculations. Using multiple thrust

fault data sets, Mercury's radial contraction is estimated to be multiple kilometers over a

wide range of plausible physical parameters. The systematic orientations of Mercury's

thrust faults also seem to be influenced by the stresses caused by the planet's current orbital

configuration overlain onto global contraction. The collection of research presented in this

dissertation provides valuable insight into Mercury's tectonic character.

INDEX WORDS:

Mercury, thrust faults, planetary tectonics, structural geology,

global contraction, geologic modeling

INVESTIGATIONS OF LITHOSPHERIC SHORTENING ON MERCURY: INSIGHTS INTO STRUCTURE AND ORIENTATION OF THRUST FAULTS AND APPLICATION TO GLOBAL CONTRACTION

by

STEPHAN RAY LOVELESS

B.Sc., University of California Santa Cruz, 2017M.Sc., Tel Aviv University, 2020

A Dissertation Submitted to the Graduate Faculty of The University of Georgia in Partial

Fulfillment of the Requirements for the Degree

DOCTOR OF PHILOSOPHY

ATHENS, GEORGIA

2025

© 2025

Stephan Ray Loveless

All Rights Reserved

INVESTIGATIONS OF LITHOSPHERIC SHORTENING ON MERCURY: INSIGHTS INTO STRUCTURE AND ORIENTATION OF THRUST FAULTS AND APPLICATION TO GLOBAL CONTRACTION

by

STEPHAN RAY LOVELESS

Major Professor: Committee: Christian Klimczak Steven M. Holland Robert B. Hawman Isamu Matsuyama

Electronic Version Approved:

Ron Walcott Vice Provost for Graduate Education and Dean of the Graduate School The University of Georgia May 2025

DEDICATION

For Elinoy, who always believes in me.

ACKNOWLEDGEMENTS

First and foremost, I am tremendously grateful to have been advised by Dr. Christian Klimczak. None of this research would be possible without his profound guidance. Dr. Klimczak is an expert in planetary tectonics who is very passionate about the mentorship of his graduate students. He took the time to guarantee that I was meeting my academic goals while challenging me to think more creatively about my research and how to communicate my scientific findings to the world. Throughout my academic career, I have learned the most under Dr. Klimczak's guidance. His feedback has been fundamental in making me not only a better scientist but someone who can confidently call himself a scientist. I enjoyed our talks about plants, guitars, and life over a coffee when we needed to take a step back from research. I am grateful for Dr. Klimczak's mentorship as well as his friendship.

I would also like to thank my Ph.D. committee for their insightful contributions to my research. Dr. Steven Holland provided crucial feedback on my academic writings and advised me on the statistical analyses needed for my work. Dr. Holland is also a great mentor who talked with me about the hardships of graduate school and made the time to talk to me about guitars and music when I needed an academic break. Dr. Robert Hawman also provided very useful feedback on my academic writings and always checked in on me from his lab across the hallway. I greatly enjoyed our talks during my Ph.D. Lastly, I want to thank Dr. Isamu Matsuyama for his valuable input towards the tidal deformation research that I had worked on during my Ph.D. in addition to the insights he shared during

our committee meetings. I am fortunate to have a committee of such knowledgeable experts in their respective fields. The work I present here is a direct result of their input and expertise.

Furthermore, I would like to thank the undergraduate student researchers Madelyn Hurd and James Muilenburg whom I mentored during my Ph.D. I am grateful to both of them for allowing me to mentor them through some very interesting research. I hope they enjoyed working on Mercury's tectonics as much as I did.

Next, I would like to express my sincere gratitude to those who funded my research and travel to various conferences throughout my Ph.D. The Miriam Watts Wheeler Travel Grant from the UGA Department of Geology, travel stipends from NASA to attend the last Insight Science Meeting, and the UGA Domestic Graduate Student Travel Grant all provided the necessary funds for me to attend conferences where I communicated my research findings. I would also like to thank the NASA SSW program that funded part of my Ph.D. at UGA. Additionally, I thank the Center for Teaching and Learning for accepting me as a Future Faculty Fellow. This program positively impacted my ability to be an effective teacher.

I also want to extend my sincere thanks to my friends who have supported me throughout my Ph.D. I specifically want to mention my lab mates, Jupiter and Sydney, who always made the planetary tectonics lab a joy to be in, even during the most stressful times of being a graduate student. I also want to mention Lea, who carpooled with me from Atlanta to UGA. I really enjoyed our talks about life and research, and driving together made the commute a lot more bearable. Additionally, I am grateful for all of the close friends I have made in Atlanta, who all, at some point, have been forced to sit through an

explanation of part of my research. Finally, I want to extend thanks to all of the other graduate and undergraduate students in the UGA Geology Department, who all worked towards creating and maintaining an amazing community.

I also want to express my gratitude to my family, specifically my mother Holly Loveless, and brothers, Conner and Danny Loveless, for listening to me complain about research shortcomings or watching me go through practice talks. Even though they may not understand everything I am doing, they always showed their support. This list also includes my late father, James Loveless, who unfortunately passed a year before I was accepted to UGA. If it was not for him convincing me with guitar lessons to get straight A's in middle and high school, I am not sure where I would be now. I hope being the first "Dr. Loveless" in our family is making him proud.

Lastly, I would like to express my immense gratitude to Elinoy, my wife, who has supported me from the last year of my undergraduate degree to now. Through every moment of success, failure, happiness, and doubt, Elinoy has provided unwavering love, support, and compassion. I genuinely believe I would not be where I am without her, and I am forever grateful to be married to such an amazing woman. I am so excited to see where our lives take us next.

TABLE OF CONTENTS

Page
ACKNOWLEDGEMENTSv
LIST OF TABLESxii
LIST OF FIGURESxiii
CHAPTER
1 INTRODUCTION AND LITERATURE REVIEW1
Diversity of shortening landforms on Mercury4
Thrust fault geometries underlying shortening landforms on Mercury6
Mercury's global contractional strain
Fault orientations on a contracting planet9
Overview and Significance of Dissertation Chapters11
2 A STATISTICAL EVALUATION OF THE MORPHOLOGICAL
VARIABILITY OF SHORTENING LANDFORMS ON MERCURY13
Abstract14
2.1 Introduction
2.2 Methods
2.3 Results
2.4 Discussion
2.5 Conclusions
2.6 Acknowledgements

	2.7 Data Availability37	7
	2.8 Figures	3
	2.9 Tables44	1
3	GEOMETRIC FORWARD MODELING OF THRUST FAULTS	
	UNDERLYING SHORTENING LANDFORMS ON MERCURY45	5
	Abstract40	5
	3.1 Introduction	3
	3.2 Methods	2
	3.3 Sensitivity Study60)
	3.4 Results	2
	3.5 Discussion69)
	3.6 Conclusions 79)
	3.7 Acknowledgements80)
	3.8 Data Availability80)
	3.9 Figures8	1
	3.10 Tables90)
4	SEVERAL KILOMETERS OF GLOBAL CONTRACTION ON	
	MERCURY: A SAMPLE-SIZE INDEPENDENT ASSESSMENT OF	
	FAULT STRAIN92	2
	Abstract93	3
	4.1 Introduction94	4
	4.2 Methods90	5
	4.3 Results	2

A	CHAPTER 2181
В	CHAPTER 3
C	CHAPTER 4246

LIST OF TABLES

	Page
Table 2.1: Loadings for PCA and LDAs	44
Table 3.1: Parameters of sensitivity study	90
Table 3.2: Compiled average modeled parameters	91
Table 4.1: Parameters used to solve for fault strain	110
Table 4.2: Radius change results	113
Table 5.1: Parameters used to solve for tidal influence on fault orientations	135
Table 5.2: Predicted fault orientations compared with observations	137
Table A2.1: Transformations to normalize morphological parameters	181
Table A2.2: Extracted morphology values for 100 shortening landforms	183
Table B3.1: Extracted model values for 55 shortening landforms	221
Table C4.1: Complete ΔR and strain results table	246

LIST OF FIGURES

Page
Figure 2.1: Examples of traditional categories of shortening landforms38
Figure 2.2: Global map of Mercury showing 100 shortening landforms analyzed39
Figure 2.3: Examples of five map patterns observed in <i>Chapter 2</i>
Figure 2.4: Block diagram with morphological parameters annotated41
Figure 2.5: PCA sample scores
Figure 2.6: Classification of landforms by LDA
Figure 3.1: Examples of lobate scarp and wrinkle ridges on Mercury
Figure 3.2: Global distribution of 55 shortening landforms modeled in <i>Chapter 3</i> 82
Figure 3.3: Block diagram of modeled parameters
Figure 3.4: Box and whisker plot of observed strain compared with modeled strain84
Figure 3.5: Three thrust fault models that replicate same topography85
Figure 3.6: Three different thrust fault systems from Mercury from models86
Figure 3.7: Box and whisker plots for eight parameters from modeled solutions88
Figure 3.8: Transect and subsurface model of Enterprise Rupes
Figure 4.1: Comparison of mapped thrust fault populations considered in <i>Chapter 4</i> 107
Figure 4.2: Block diagram of fault geometric parameters
Figure 4.3: Thrust fault population statistics for three datasets on Mercury109
Figure 5.1: Map of time-averaged radial displacement from tides and rotation130
Figure 5.2: Principal stresses produced by Mercury's orbit and rotation alone131

Figure 5.3: Principal stresses of orbit and rotation overlapping global contraction	132
Figure 5.4: Optimal thrust fault orientations from stresses shown in Figure 5.3	133
Figure 5.5: Predicted thrust fault patterns compared with observations	134
Figure A2.1: Scree plot of percent variance described by 12 principal components	182
Figure A2.2: 100 Shortening landforms analyzed in <i>Chapter 2</i>	208
Figure B3.1: Subsurface models of 55 shortening landforms in <i>Chapter 3</i>	227

CHAPTER 1

INTRODUCTION AND LITERATURE REVIEW

The surface of Mercury is host to a global network of positive relief, surfacebreaking shortening landforms, indicating a complex tectonic history (e.g., Byrne et al., 2014). Early interpretations attributed these tectonic features to crater forming events (Strom et al., 1975). However, modeling informed by early observations from the Mariner 10 mission had predicted that Mercury has undergone global contraction: the process in which a planet shrinks due to long, sustained cooling (e.g., Solomon, 1977). A planet undergoing global contraction experiences a horizontally isotropic, fully compressional stress state throughout its lithosphere (Melosh and McKinnon, 1988). This build-up of stresses would eventually reach the brittle strength of the lithosphere and so initiate the growth of thrust faults to accommodate the contraction (Solomon, 1978). The shortening landforms are now widely accepted to be the surface manifestation of thrust faulting and folding caused primarily by global contraction (Byrne et al., 2018, 2014; Solomon et al., 2008; Strom et al., 1975). For the work presented here, I use the term "shortening landforms" as an identifier of all positive-relief landforms that are interpreted as having been formed by thrust faulting. Other works refer to such landforms as "lobate scarps", "wrinkle ridges", "shortening structures" or "thrust fault-related landforms" but shortening landforms is the preferred term here for consistency.

Shortening landforms on Mercury, and more generally on all planetary bodies with a solid surface, are identified as positive-relief cliffs, frequently demarcated by a surface break alongside the bottom of the cliff (e.g., Schultz and Watters, 2001; Watters, 2003). After the exploration of Mercury via three fly-bys by the Mariner 10 mission in 1974 to 1975 where only 45% of the innermost planet were imaged, the MErcury Surface, Space Environment, GEochemistry, and Ranging (MESSENGER) mission fully mapped Mercury from orbit from 2011 to 2015. It revealed the contractional tectonic character on Mercury in much greater detail (e.g., Byrne et al., 2018, 2014). On Mercury, these shortening landforms can have reliefs of up to 3 km and surface breaks that reach up to 1,000 km (e.g., Byrne et al., 2018; Ferrari et al., 2015; Watters et al., 2016). Hundreds to thousands of landforms that accommodate horizontal shortening have been identified, indicating extensive contraction of the planet's lithosphere (e.g., Byrne et al., 2014; Man et al., 2023a; Watters, 2021).

The geology of Mercury has been classified and mapped as three main morphological units: the impact crater facies, intercrater plains, and the smooth plains (e.g., Denevi et al., 2013, 2009; Trask and Guest, 1975). Impact crater facies are portions of Mercury's surface that have formed due to the direct, or long-term, consequences of medium-, or large-sized meteorite impacts. Intercrater plains are expanses of Mercury's surface that have been heavily cratered, representing the oldest surfaces of the planet. It is thought to consist of ancient volcanic crust. The smooth plains unit is geologically younger, hosting fewer craters and is thought to have formed by the emplacement of flood-volcanic lavas (Denevi et al., 2013; Head et al., 2011). Shortening landforms have formed within all of Mercury's geologic units (e.g., Byrne et al., 2014).

Recent efforts have been made to map the geology of Mercury's surface in greater detail for individual quadrangles (e.g., Buoninfante et al., 2025; Galluzzi et al., 2018, 2016;

Guzzetta et al., 2017). There are 15 near-equal area quadrangles of Mercury's surface divided by the International Astronomical Union, with 10 having been completely mapped at the 1:3 million scale (Buoninfante et al., 2025; Galluzzi et al., 2016; Giacomini et al., 2024, 2022; Guzzetta et al., 2017; Malliband et al., 2023; Man et al., 2023b; Mancinelli et al., 2016; Pegg et al., 2021; Wright et al., 2019). The ongoing mapping has revealed interesting structural characteristics across Mercury. For example, the recent work of Buoninfante et al. (2025) showed tectonic structures in the H12 quadrangle outside of the impact basins trend with primarily northwest-southeast strikes. Such trends have been observed previously as shortening landforms have systematic orientations on Mercury's surface, with strong north–south trends near the equator that become more variable towards the poles (e.g., Byrne et al., 2018; Klimczak et al., 2015). The, structural analysis of the H02 Victoria quadrangle on Mercury has revealed similar fault traces which highlighted a predominate stress field acting in the ENE-WSW direction (Galluzzi et al., 2019). Systematic fault orientations have been noted in global-scale structural maps and analyses (e.g., Byrne et al., 2018; Klimczak et al., 2025, 2015).

Other structural trends highlight that mantle convection may have played a role in deforming Mercury's surface producing long wavelength topographic undulations (Klimczak et al., 2013, 2012; Zuber et al., 2012). Additional recent mapping efforts have revealed small-scaled graben forming at the hinge lines of the anticlinal folding atop shortening landforms on Mercury, indicating that Mercury's global contraction may still be ongoing (Man et al., 2023a). The notion that tectonics are still active throughout Mercury's lithosphere has been additionally supported by the presence of relatively smaller fault segments and thrusts (Banks et al., 2015; Watters et al., 2016). With the BepiColombo

mission arriving at Mercury in November 2026, it is important to address open questions that pertain to Mercury's tectonics to help guide the scientific objectives of this mission (Benkhoff et al., 2021). This dissertation aims to shed light on the current questions regarding lithospheric shortening on Mercury.

Diversity of shortening landforms on Mercury

Shortening landforms on Mercury have typically been categorized into three morphological groups: lobate scarps, wrinkle ridges, and high-relief ridges (e.g., Melosh and McKinnon, 1988; Watters et al., 2004, 2001; Watters and Robinson, 1999). Lobate scarps are linear to arcuate surface-break structures in map-view. In cross-section, lobate scarps are asymmetric, with a steeply sloping forelimb that immediately trails the surface break, followed by a more gently sloping backlimb (e.g., Strom, 1979; Strom et al., 1975; Watters, 1993). The direction of tectonic transport, or vergence, is evident by the direction the forelimb faces, as the hanging wall folds over the footwall at the surface break (e.g., Byrne et al., 2014). Wrinkle ridges on Mercury tend to have lower structural reliefs than lobate scarps, while hosting more complex, often sinuous map patterns. In cross-section, wrinkle ridges display a superimposed ridge (the "wrinkle") above a primary, more-broad, ridge (e.g., Watters, 1988). Although surface breaks are common for wrinkle ridges (e.g., Golombek et al., 2001, 1991; Schleicher et al., 2019; Strom et al., 1975; Watters, 1988), these shortening landforms have often been interpreted as anticlinal structures that form above blind thrusts (e.g., Schultz, 2000) or back thrusts (Okubo and Schultz, 2004). More recently, wrinkle ridges have been interpreted as two oppositely facing monoclines that have formed over two oppositely verging thrusts (Byrne et al., 2018). High-relief ridges are described as being morphologically similar to lobate scarps but are more symmetric due to a steeper backlimb in cross-section (e.g., Watters et al., 2021). These shortening landforms have then been interpreted as anticlines forming above steeply dipping reverse faults (e.g., Watters et al., 2001).

The traditional landform categorical names "lobate scarps", "wrinkle ridges", and "high-relief ridges" have only been given qualitative descriptors. It is often difficult for planetary geologists to categorize landforms as they exhibit characteristics of two, or sometimes even all three of the traditional categories (i.e., Strom et al., 1975). Other works of contractional tectonics on Mercury have questioned the use of these traditional categories and have noted that although endmember shortening landforms of each type exist, many contractional landforms are difficult to distinguish as lobate scarps, wrinkle ridges, or high-relief ridges (e.g., Byrne et al., 2018, 2014; Crane and Klimczak, 2019a; Klimczak et al., 2018). Although terrestrial analogues have been suggested to describe non-Earth shortening landforms, such terminology has never been used to describe thrust systems observed on Earth and can often lead to false assumptions of the subsurface fault architecture and formation of such structures.

A quantitative definition of lobate scarps, wrinkle ridges, and high-relief ridges does not yet exist. Furthermore, a statistical analysis of the morphology of shortening landforms on Mercury's surface has never been performed to test the legitimacy of these traditional categories. The implementation of such work in this dissertation intends to better define the structural characteristics of lobate scarps, wrinkle ridges, and high-relief ridges, or alternatively, may dissuade the scientific community from using such terminology as to avoid the generalization and misinterpretation of complex contractional tectonics on Mercury.

Thrust fault geometries underlying shortening landforms on Mercury

Wrinkle ridges and lobate scarps have been used to describe almost all shortening landforms on Mercury's surface (e.g., Melosh and McKinnon, 1988; Watters et al., 2004). The large variation of thrust systems formed on Earth brings into question this generalization of Mercury's shortening landforms into these two groups. Positive relief, contractional tectonic landforms on Earth are created due to the stresses from plate tectonics and manifest as mountain ranges produced by complex systems of thrusts and folds (e.g., Boyer and Elliot, 1982; Chapple, 1978; Crane and Klimczak, 2019b; Matthews and Work, 1978; McClay, 1978; Morley, 1988). The Earth hosts fold and thrust belts attributed to large-scale crustal shortening accommodated by multi-fault thrust complexes (e.g., McClay and Price, 1981). Duplex thrust structures comprised of stacked panels of rock bounded by thrusts, imbricate thrusts branching of a single décollement, and other thrust complexes comprised of faults with identical to oppositely senses of vergence are all examples in the large variety of observed contractional tectonic geometries found on Earth (Boyer and Elliot, 1982).

Without plate tectonics, global contraction serves as the main driver for lithospheric deformation on Mercury. Often shortening landforms on non-Earth bodies are modeled with a single homoclinal-to-listric fault using elastic, dislocation modeling tectonics, or geologic forward modeling techniques (e.g., Byrne et al., 2016; Egea-Gonzalez et al., 2017; Egea-González et al., 2012; Peterson et al., 2020; Schultz and Watters, 2001; Williams et al., 2013). To date, only few works have proposed similar thrust geometries for Mercury's shortening landforms to that of the Earth. For example, Rothery and Massironi (2010) have suggested that Beagle Rupes, a large shortening landform on Mercury with apparent strike-

slip motion at its tips, is the manifestation of an extensive décollement. Crane and Klimczak (2019a) have proposed that the upper portions of Mercury's lithosphere may be mechanically weaker than the lower portions due to fracturing caused by many impacts over geologically long periods of time. This may influence the propagation of thrusts in the lithosphere from faulting in the basement rock. Such a mechanism has been linked to basement-reactivated thin-skinned tectonics, a fault propagation mechanism occurring on Earth (Pfiffner, 2017).

Currently most studies on the subsurface architecture of non-Earth shortening landforms have focused on only one landform, or up to just a few landforms, and have mostly constrained models by matching the overlying observed topography (Egea-Gonzalez et al., 2017, 2012; Herrero-Gil et al., 2020, 2019; Mueller et al., 2014; Peterson et al., 2020; Schultz and Watters, 2001; Williams et al., 2013). A comprehensive modeling effort for a large number of landforms to investigate the variability of fault geometries underneath Mercury's shortening landforms has not been carried out prior to this dissertation.

Mercury's global contractional strain

Mercury's global contraction has produced a horizontal compressive stress stat that has caused thrust faulting throughout the planet's lithosphere (e.g., Solomon, 1978). The amount Mercury has contracted has been estimated using two methods: thermal evolution modeling (e.g., Breuer et al., 2007; Hauck et al., 2004; Michel et al., 2013; Solomon, 1977; Tosi et al., 2013) or tectonic mapping and structural analysis (Byrne et al., 2014; Di Achille et al., 2012; Watters, 2021; Watters et al., 2015a, 2009, 1998; Watters and Nimmo, 2010). Thermal evolution models solve a series of physical equations to replicate how Mercury's

shape and interior structure has changed over time. Alternatively, structural mapping efforts rely on the sum of the shortening strain accommodated by thrust faults underneath shortening landforms. These have developed from works that estimate the strain of a volume using the lengths of a population of faults (Cowie et al., 1993; Scholz and Cowie, 1990). For Mercury, the relief of the shortening landforms is assumed to equal the throw of the underlying thrust fault (e.g., Byrne et al., 2014; Watters, 2021, Watters et al., 1998). Lengths of the faults are extracted from global structural maps and the reliefs of a subset of shortening landforms are extracted. Using trigonometry, and assuming the entire fault population hosts a common thrust fault dip, the displacement is calculated for this smaller set thrust faults. Displacement and length of thrust faults are observed to have a power-log relationship (Clark and Cox, 1996; Cowie and Scholz, 1992), which is used to estimate the displacement for the entire, mapped population of thrust faults. This method is prone to disagreement because the derived strain for Mercury's lithosphere is dependent on the number of faults studied (e.g., Byrne et al., 2014; Watters, 2021).

The mapping structural analysis technique has been used extensively producing a wide range of results, with estimates for Mercury's radial contraction, ΔR , to be as little as 0.8 km (Watters et al., 2015a) to as large as 7.1 km (Byrne et al., 2014). The disadvantage caused by the dependence on the number of shortening structures considered is reflected in the history of using this method to estimate Mercury's contraction. Watters et al. (1998) produced an initial estimate of Mercury's radial contraction of 1.5–2.9 km which has been revisited in the works Watters et al. (2009), Watters and Nimmo (2010), Watters et al. (2015a), and Watters (2021) that each produce a slightly different result by incrementally

changing the geologic interpretation of the shortening landforms considered for each respective analysis.

In order to resolve this discrepancy, alternative methods to estimate Mercury's global contraction that circumnavigate the dependency of thrust fault sample size are needed. In particular, the methodology proposed and utilized in Twiss and Marrett (2010a, b) provides a way to calculate the strain attributed by a population of faults in a faulted volume using fault-population statistics, which constitutes an independent assessment of fault strain for the study of global contraction. This method is based on the fact that a population of faults is never really completely measured when calculating the total strain of a volume. Prior to this dissertation, this methodology has never been used to estimate the strain of global contraction.

Fault orientations on a contracting planet

Mercury's global contraction has produced a widespread population of thrust faults (e.g., Byrne et al., 2014). The horizontal stresses caused by global contraction are isotropic (Melosh and McKinnon, 1988), and therefore, the tectonics produced by global contraction alone would show random orientations. However, the thrust fault orientations across Mercury's surface have systematic orientations, showing roughly north—south trends at the equatorial regions and generally east—west oriented towards the poles (e.g., Byrne et al., 2018; Klimczak et al., 2015). This systematic fracture pattern indicates that other tectonic processes have acting in conjunction with global contraction.

Multiple works have invoked different processes to try to explain the systematic fault orientations throughout Mercury's surface. Mercury's rotation is thought to have slowed over time (e.g., Burns, 1975 Kaula, 1968; Melosh, 1977; Melosh and McKinnon,

1988) which has been modeled to cause north—south oriented thrust faults near the equator and thrust faults without preferred orientations at the poles (e.g., Klimczak et al., 2015; Pechmann and Melosh, 1979) or normal faults orientated east—west at the poles (Beuthe, 2010). The Caloris impact driven reorientation, despinning, and global contraction combined had predicted thrust fault orientations that resembled the tectonic patterns observed with Mariner 10 data but did not resemble the more complete tectonic maps produced by MESSENGER data (Matsuyama and Nimmo, 2009).

No process or combination of processes has satisfactorily described the observed tectonic patterns on Mercury. However, these patterns may also reflect lighting bias as MESSENGER took imagery observing in the eastern or western directions that would highlight north—south trending structures. Despite this, previous studies have suggested that Mercury's current orbit may affect the fracture patterns on the planet's surface since thrust faulting shows concentric patterns around Mercury's hot poles (e.g., Byrne et al., 2018; Klimczak et al., 2025, 2015). Mercury is currently in an eccentric 3:2 spin—orbit resonance with the Sun. It's current orbital configuration causes pronounced solar tides within the planet's lithosphere (Hoolst and Jacobs, 2003). Mercury's current orbit superposed onto global contraction warrants further investigation, and a comprehensive study on how this combination of stresses influences the orientations of Mercury's tectonics has not been explored in detail prior to the work presented here. By conducting such an analysis, Mercury's current 3:2 spin-orbit resonance can be critically evaluated in its role in systematic fault patterns.

Overview and significance of dissertation chapters

Mercury is an ideal planet to directly explore the effects global contraction has on a brittle lithosphere. Although there has been extensive mapping and modeling efforts of Mercury's contractional tectonics, these tectonics have yet to be interpreted at the same level of detail as contractional tectonic systems on Earth. Furthermore, discrepancies in the literature regarding Mercury's amount of global contraction, and the analysis of the stress state and predicted fault orientations due to different superposed tectonic events leaves many questions regarding Mercury's tectonics inadequately answered. The goal of this dissertation is then to investigate, in great detail, the morphology and subsurface structure of Mercury's shortening landforms, as well as to provide an alternative assessment of estimating Mercury's contractional strain. In addition, the influence of Mercury's current orbital characteristics on the planet's fault orientations are studied.

Chapter 2 focuses on a statistical analysis of the morphology of the shortening landforms on Mercury's surface to test whether traditionally-used landform designations are indeed morphologically distinct from one another. Two multivariate statistical analyses assess a sample of 100 shortening landforms on Mercury made up of wrinkle ridges and lobate scarps. Chapter 3 investigates the variety of thrust systems within Mercury's lithosphere by modeling 55 morphologically variable shortening landforms based on the endmember lobate scarp and wrinkle ridge structures from Chapter 2. Kinematic forward models are constructed in 2-dimensions with fault-bend fold geometries using the MOVE geologic modeling software MOVE. The models are used to structurally interpret the subsurface of shortening landforms across Mercury's entire surface and to better constrain subsurface modeling with observations. Chapter 4 adapts the methodology created and

utilized by Twiss and Marrett (2010a, b) to estimating Mercury's radial contractional strain using three different fault data sets available in the literature. *Chapter* 5 compares Mercury's observed fault pattern to one that is predicted for overlapping stresses produced by solar tides and Mercury's rotation onto those produced by global contraction.

CHAPTER 2

A STATISTICAL EVALUATION OF THE MORPHOLOGICAL VARIABILITY OF SHORTENING LANDFORMS ON MERCURY¹

¹ Loveless, S.R., Klimczak, C., McCullough, L.R., Crane, K.T., Holland, S.M., Byrne, P.K., 2024. Icarus 416, 116106. Reprinted here with permission of the publisher.

Abstract

Observations of Mercury from both the Mariner 10 and MESSENGER missions showed that Mercury has a global population of shortening landforms, with several thousands of individual structures identified to date. The accommodation of widespread tectonic shortening is widely regarded to be the result of global contraction—the long, sustained cooling of the interior that has caused the planet to shrink. Shortening landforms on Mercury have been traditionally categorized into three distinct categories: lobate scarps, wrinkle ridges, and high-relief ridges. Although the clearest examples of shortening landforms at the time were used to describe and define these categories qualitatively, later studies showed that shortening landforms on Mercury display morphological characteristics that do not make for a ready classification into one of these "traditional" groups. More recently, other studies have classified shortening landforms based on the terrain that those landforms reside in to avoid generalizing morphology. In this study, we quantitatively assess the shape of shortening landforms by measuring and compiling a suite of 12 morphological parameters for 100 such structures across the planet. These parameters were evaluated for their importance in defining categories using two multivariate statistical analyses, a Principal Component Analysis (PCA) and Linear Discriminant Analysis (LDA). These methods allow us to assess any correlation that the traditional categories, terrain types, or alternative classification schemes have with the variation observed across our set of measurements. Our results show that the morphologic characteristics of shortening landforms on Mercury are not accurately captured by traditionally recognized groups. Instead, shortening landforms fall along a morphological spectrum, where only a few ideal examples of lobate scarps or wrinkle ridges provide clear endmembers.

Therefore, despite the frequent use of the terms "lobate scarps" and "wrinkle ridges" in works regarding planetary tectonics, we find that such terminology does not appropriately define the morphology of shortening landforms found on Mercury and may lead to the generalization, or misinterpretation of landforms described as accommodating shortening on Mercury's surface. Future studies should test if a distinction between the landforms is found in the underlying thrust fault systems.

2.1 Introduction

Categories of shortening landforms

Modeling motivated by early observations from the Mariner 10 mission of crustal shortening had predicted that Mercury had undergone global contraction, a phenomenon resulting from the long, sustained cooling of a terrestrial body that leads to a planetary volumetric decrease (e.g., Solomon, 1977). Global contraction was predicted to be principally accommodated via widespread thrust faulting throughout the brittle portion of Mercury's lithosphere (Solomon, 1978) that manifests at the surface as linear, positive-relief landforms. Observations from the MErcury Surface, Space Environment, Geochemistry, and Ranging (MESSENGER) mission provided greater detail of the crustal shortening that accommodated global contraction (e.g., Byrne et al., 2014). In this study, we focus on these tectonic landforms related to global contraction. We use the strain term "shortening landforms" as an identifier of all positive-relief landforms we interpret as having been formed by thrust faulting; such landforms have been described as "shortening structures" or "thrust fault-related landforms" in earlier works but we prefer this term for consistency.

Mercury's surface has been mapped into three main morphologic unit types: intercrater plains, smooth plains, and impact crater facies (e.g., Denevi et al., 2013, 2009; Trask and Guest, 1975). Inter-crater plains are heavily cratered and represent the oldest surfaces on the innermost planet. Smooth plains are interpreted to be more recently emplaced expanses of flood-volcanic deposits bearing fewer craters (Denevi et al., 2013; Head et al., 2011). Impact crater facies are collectively units that formed as direct or long-term consequences of large impacts, with most being contained within and around their host

impact basins. Shortening landforms occur in all surface morphologic units (e.g., Byrne et al., 2014) and are interpreted to have acquired most of their strain near the end of when the smooth plains were emplaced and somewhat thereafter (Byrne et al., 2018, 2016; Crane and Klimczak, 2017).

Shortening landforms are not only found on Mercury but on all major terrestrial bodies. Generally, they are manifest as surface-breaking scarps showing positive relief (Schultz and Watters, 2001; Watters, 2003). Early photogeologic data sets of Mercury, Venus, the Moon, and Mars revealed shortening landforms with several typical characteristics (e.g., Strom et al., 1975). Strom et al. (1975) attributed the morphology of shortening landforms on Mercury to tectonic processes and crater-forming events. Dzurisin (1978) initially categorized shortening landforms on Mercury into six morphological groups: arcuate scarps, lobate scarps, irregular intracrater scarps, irregular Caloris scarps, linear ridges, and irregular Caloris ridges. Of those, lobate scarps and wrinkle ridges were used to describe tectonics observed from the Mariner 10 mission (e.g., Strom, 1979) and were subsequently used widely to categorize shortening landforms throughout the Solar System, including Mercury (e.g., Melosh and McKinnon, 1988; Watters and Robinson, 1999; Watters et al., 2004), Venus (e.g., Solomon et al., 1992; Squyres et al., 1992), and Mars (e.g., Watters and Robinson, 1999; Mueller and Golombek, 2004). A few high reliefridges have been described in detail on Mercury (Watters et al., 2001). In this paper, we refer to lobate scarps, wrinkle ridges, and high relief-ridges as the "traditional categories" by which extraterrestrial crustal shortening structures have been identified and mapped.

Lobate scarps (Figure 2.1a) are linear to bow-like structures in map-view that have a surface break. In cross-section, they have asymmetric positive relief with a relatively

steep sloping forelimb that immediately trails the surface break followed by a more gently sloping backlimb (e.g., Strom et al., 1975; Strom, 1979; Watters, 1993). The shapes of lobate scarps provide evidence that the vergence, or direction of tectonic transport, of the thrust system is in the direction of the forelimb with anticlinal folding of the hanging wall (e.g., Byrne et al., 2014). Named examples of lobate scarps on Mercury have the International Astronomical Union (IAU) descriptor term rupes (pl. "rupēs") (e.g., Beagle Rupes, Enterprise Rupes, Carnegie Rupes, etc.).

Wrinkle ridges on Mercury (Figure 2.1b) generally have lower relief than lobate scarps and differ from other shortening landforms by their complex, sinuous map pattern and their superimposed ridge (the "wrinkle") above a primary broad ridge (e.g., Watters, 1988). Wrinkle ridges are common on the volcanic plains of many terrestrial bodies in the Solar System (e.g., Nahm et al., 2023; Plescia and Golombek, 1986). They are interpreted as anticlinal structures formed above blind thrust faults (e.g., Schultz, 2000) and potentially backthrusts (Okubo and Schultz, 2004); however, surface breaks are common (Golombek et al., 2001, 1991; Schleicher et al., 2019, Strom et al., 1975; Watters 1988).

High-relief ridges (Figure 2.1c) have been reported by a single author on both Mercury and Mars (Watters, 1993), with only a few examples on the former. In cross-section, high-relief ridges are morphologically similar to lobate scarps but are more symmetric due to the landforms hosting a steeper backlimb (e.g., Watters et al., 2021). High-relief ridges have been interpreted to be anticlines formed above steeply dipping reverse faults (e.g., Watters et al., 2001).

Byrne et al. (2014) avoided using these traditional morphological categories and instead classified shortening landforms by the terrain type in which they are found. These

authors' classification includes smooth-plains structures, cratered-plains structures, crater-related structures, and high-terrain bounding structures. Crater-related structures are defined as landforms bound to and/or found within an impact basin, and high-terrain bounding structures are described as landforms separating high-standing from low-lying terrain. However, both of these structure types still occur in either smooth- or cratered-plains, and so the four categories in Byrne et al. (2014) can be further simplified to smooth-plains structures or cratered-plains structures.

Motivation and goal of this study

The traditional landform categories of lobate scarps, wrinkle ridges, and high reliefridges are qualitative; no quantified definitions by which these landforms can be systematically classified or distinguished have been proposed. As Strom et al. (1975) stated regarding shortening landforms mapped around the Caloris basin using images from the Mariner 10 mission: "Many of the scarps in the plains surrounding the Caloris Basin grade into or are transitional with ridges, so that the two structures are difficult to distinguish". Other studies of Mercury's shortening landforms have questioned the traditional categories: although endmembers of the traditional categories are present, most structures are not so easily classified (e.g., Byrne et al., 2018, 2014; Crane and Klimczak, 2019a; Klimczak et al., 2018). We therefore carry out a statistical investigation of the morphology of the traditional categories of lobate scarps and wrinkle ridges on Mercury to establish whether there is a quantitative basis by which to use these traditional terms in studying the planet's inventory of crustal shortening structures. To do so, we based our study on multivariate statistical analysis of morphologic measurements of select shortening landforms of each assessed type. This approach allowed us to not only evaluate whether the traditional categories can be distinguished, but also to assess other categorizations, such as those based on terrain types (e.g., those advocated by Byrne et al., 2014). We do not consider high-relief ridges in our assessment due to the low sample size of landforms in this category and the statistical inaccuracies that may arise from it.

2.2 Methods

Data collection

The entire catalogue of global image mosaics at a resolution of 166 m/pixel and digital elevation models (DEMs) from the MESSENGER mission available on the Planetary Data System (PDS) was loaded into a Geographic Information System (GIS) using ArcMap® 10.8. This includes the 250 m/pixel northern hemisphere MLA DTM (Zuber et al., 2012). We also used the DEMs from MESSENGER flybys (Preusker et al., 2011) and the more recently resolved DEM of the south pole by Bertone et al. (2023) at a resolution 250 m/pixel. The lowest-resolution elevation dataset used in this study is the global USGS DEM, which is based on the Mercury Dual Imaging System narrow-angle camera and multispectral wide-angle camera and has a resolution of ~665 m/pixel (Becker et al., 2016). For coverage of topography see supplementary material (Loveless et al., 2024a).

In ArcMap, Mercury was divided into a 20°×20° grid, producing 162 grid boxes, of which 100 were randomly selected with uniform probability via a random number generator. Each grid box was thoroughly surveyed for shortening landforms, and one such landform was then chosen based on what would be the best candidate with respect to the rest of the data collection. Selections were made to account for good representations of global distribution (see Figure 2.2), size, traditional categories, and also DEM availability

and resolution. If shortening landforms fell into an area with only the lower-resolution, global DEM topography, only large shortening landforms (>100 km long) were selected to minimize the effect of DEM spatial resolution on the topographic measurements.

Each selected landform was assigned to a lobate scarp, wrinkle ridge, or transitional (i.e., a structure that transitions from a lobate scarp to a wrinkle ridge along its length) classification. High-relief ridges were not considered because only a small number have been described for Mercury (e.g., Watters, 2021; Watters et al., 2001). Several of the authors assigned each landform a lobate scarp or wrinkle ridge designation by visual inspection and then compared their assignments. Transitional structures could also be categorized as either wrinkle ridges or lobate scarps at the location of the profile showing the highest structural relief that was also used to collect our measurements. Following Byrne et al. (2014), we also categorized the shortening landforms as cratered-plains structures or smooth-plains structures.

All landforms were assigned to one of five map patterns: concave, sinuous, straight, convex, or switching vergence. Convexity and concavity were defined with respect to the hanging wall block. In a concave map pattern (Figure 2.3a), the hanging wall creates a concave scarp shape over the footwall; the concave pattern opens towards the footwall. Sinuous map patterns (Figure 2.3b) demonstrate a large amount of variation along strike as the surface break pattern switches between concave and convex patterns along the length of the structure. Straight map patterns (Figure 2.3c) show little curvature or variability along the length of the surface break. Convex map patterns (Figure 2.3d) depict the hanging wall extending in an arching manner over the footwall, such that the concave pattern opens towards the hanging wall (often described as an arcuate or bow pattern (e.g., Byrne et al.,

2018; Watters et al., 2015a). Shortening landforms that have a switching vergence map pattern (Figure 2.3e) demonstrate tectonic movement in opposite directions along the length of the structures; that is, the hanging wall and footwall switch sides along the structure's length (Figure 2.3e).

In ArcMap, each landform was analyzed using a stereographic projection centered on the landform. We mapped their surface breaks at a 1:250,000 scale as polylines using the streaming function with vertex placements every 500 meters. Marker points were placed every 10 km along the polylines/surface breaks, and topographic profiles were generated perpendicular to the landform at these marker points. Points that comprise the profile were evenly spaced every 245 m along the length as this is approximately the same as the highest resolution DEMs used in this work. All topographic profiles along a landform were compared to determine which displayed the maximum structural relief. Morphological measurements were made along the profile with maximum structural relief.

We measured and calculated twelve parameters on each shortening landform (Figure 2.4). The structural *relief* (in meters) is the elevation difference measured between the onset of the forelimb/surface break and the peak of the topographic profile. The *breadth* (meters) of the structure is the horizontal distance across the topographic profile measured from the surface break to the end of the backlimb (Figure 2.4), with the end of the backlimb being the point on the backlimb where the structure is no longer topographically distinguishable from the surrounding terrain. The breadth thus represents the final length of the transect after shortening occurred. *Total cross-sectional length* (meters) is the distance along the transect (Figure 2.4) and represents the initial length of the transect before shortening. *Shortening strain* (unitless) along the transect is the change in length

(breadth minus total cross-sectional length) divided by the total cross-sectional length, under the assumption that the total cross-sectional length is the initial length that was shortened entirely by the underlying thrust fault to the presently observed breadth. Forelimb length (meters) is the component of the total cross-sectional length measured from the surface break to the peak of the shortening landform, and backlimb length (meters) is the component of the total cross-sectional length measured from the peak of the topographic profile to the end of the backlimb.

Forelimb slope (measured in degrees, Figure 2.4) is the average slope between each pair of adjacent points along the transect from the surface break to the peak of the shortening landform. The same method was applied to find the backlimb slope (degrees). The forelimb generally slopes upwards, and thus has positive slope values, whereas the backlimb generally slopes down and thus has negative slope values. Symmetry (degrees) is the difference of the forelimb slope and absolute value of the backlimb slope. A symmetrical shortening landform will have a symmetry of 0°, whereas deviations from 0° represent asymmetrical landforms. Percent backlimb downslope is the ratio of downsloping (negative) backlimb slope segments to the total number of backlimb slope segments in the profile. A backlimb that slopes downward everywhere will have a percent downslope of 100%. This metric captures the complexity of topography on the backlimb, such as the wrinkle on wrinkle ridges.

The *length* (meters) of the shortening landform was identified using the mapped traces of the scarps and ridges (Figure 2.2). To avoid distortions from the projection of global data, we used the Tools for Graphics and Shapes Plugin for ArcMap 10.8 to calculate

geodesic lengths. The block diagram in Figure 2.4 shows half of the length of the shortening landform.

To test if our measurements are biased by dependencies of landform size on terrain ruggedness or DEM resolution, we also calculated the *Topographic Roughness Index* (TRI), given by Riley (1999) as:

TRI =
$$\sqrt{\frac{1}{N} \sum_{i=1}^{N} (x_i - x_{i+1})^2},$$

where N is the number of transect segments measured along the topographic profile, and x_i is the elevation at segment i on the profile.

Statistical analysis

We performed two types of statistical analyses to assess the existence of distinct categories of morphologic shortening landforms: a principal component analysis (PCA) and a linear discriminant analysis (LDA), a type of discriminant function analysis. As for all statistical techniques, these analyses assume random sampling. PCA and LDA also assume multivariate normality, which is achieved through data transformations of some variables (see Table A2.1). After the data were transformed, they were scaled by the *z*-score of each measurement: $z = (x - \mu)/\sigma$, where *x* is the measurement, μ is the average of the measurements, and σ is the standard deviation. This transformation places each measurement on the same scale with a mean of zero and a standard deviation of one, causing the LDA to be influenced purely by the variance of the data and not by the relative size of different measurements.

PCA is an eigenanalysis-based multivariate statistical method for rotating the data along orthogonal axes that explain a progressively decreasing proportion of the variance (i.e., principal components, PCs; Pearson, 1901). By selecting the PCs that explain the greatest proportion of the total variance, PCA can be used to reduce dimensionality and simplify analysis of multivariate data. For this study, these PCs can be used to detect whether the landforms cluster into distinct categories or lie along a continuum. Each PC is described by a set of linear coefficients called loadings that describe how much each variable contributes to each PC. Through these loadings, we can determine which morphologic characteristics account for the greatest variance in Mercury's shortening landforms.

Linear discriminant analysis constructs a linear mathematical model that maximizes the separation between predefined groups using eigenanalysis methods (Davis, 2002; Maindonald and Braun, 2003). LDA generates k-1 linear discriminants (LDs), where k is the number of predefined groups (landform categories or terrain types). Each sample has scores (positions) along these linear discriminants, and the positions of samples in this linear discriminant space is used to classify the samples into groups. If the model can successfully classify the samples into groups based on the morphological variables, the landform categories assigned by LDA will match those that we assigned during data collection.

We conducted two LDAs with two groups, one distinguishing lobate scarps and wrinkle ridges, the other distinguishing smooth-plains and cratered-plains structures. Once an LDA model was completed, it was evaluated using a "jackknife" validation technique with the original data to reduce the self-constructed biasing accuracy of the model. The jackknife technique is a resampling method in which a statistic—in our case the results of running our sample through our LDAs—is calculated repeatedly with one of the

observations excluded in turn. By calculating the statistic multiple times, an estimate of the parameter, or average of how accurate the LDA is, can be found.

2.3 Results

A catalog of 100 shortening landforms was compiled that contains the geographic position of each shortening landform, the highest-resolution DEM available at the time of this writing that covers the shortening landform, the 12 collected parameters, the visual assessment of the traditional category to which the shortening landform ought to be assigned, the map patterns of the scarp (Figure 2.3), and the terrain type in which the structure is found. The catalog comprises 75 lobate scarps and 25 wrinkle ridges, and is included in the supplementary material.

Principal component analysis

For our PCA, Figure A2.1 shows the scree plot that presents the percentage of variance that is explained by each of the 12 PCs. PCs 1 and 2 together describe 65% of the variance of the data, and therefore we use them to present and discuss the results for grouping of shortening landforms. Variable loadings (Table 2.1, columns PC1 and PC2) describe the contribution of each variable to each principal component. A positive loading has a positive correlation with its respective PC and likewise a negative loading is negatively correlated. Loadings for each PC were deemed important contributors if their absolute value exceeded the value of a loading if each loading contributed equally to the variance of a PC, i.e., given by $\sqrt{1/\#}$ of measurements (see the bold values in Table 2.1). The strongest influencing parameters on PC1 are those that pertain to the size of the shortening landforms, i.e., relief, breadth, total cross-sectional length, fore- and backlimb length, and mapped length (Table 2.1). PC2 is most influenced by the shortening strain and

both fore- and backlimb slopes; however, as shown below, TRI value, breadth, and cross-sectional length are also influential (Table 2.1).

PCA sample scores form a single cloud of points (Figure 2.5). These scores are coded in three ways to aid in the interpretation of the PCs (Figure 2.5), including the traditional categories for a clustering of lobate scarps and wrinkle ridges (Figure 2.5a), concave, convex, straight, sinuous, and switching vergence map patterns (Figure 2.5b), and smooth-plains structures and cratered-plains structures (i.e., those shortening landforms classified solely by terrain type) (Figure 2.5c). For each categorization, there is substantial overlap in categories with no distinct separation of groups. This indicates that the morphology of shortening landforms on Mercury provides no evidence of any distinct groups based on traditional categories, map pattern, or terrain type.

<u>Discriminant function analysis</u>

LDA produces a linear equation that maximizes the separation of pre-defined groups. LDA loadings are the coefficients (slopes) in this linear equation. Their signs indicate the directions in which they influence a discriminant function, and their magnitudes indicates their relative contributions. Therefore, the sign of large loadings is important in assigning the relative extent of where the shortening landform would be placed in LD space. We performed LDAs to classify landforms by traditional types and terrain types (Table 2.1). For both the traditional categories and structures categorized by their host terrain, the breadth of the landform holds a strong negative influence on the LDA, whereas the total cross-sectional length holds an almost equally strong, positive influence on the LDA. In both cases, breadth and cross-sectional length are substantially more

influential than any of the other measurements, and so they provide the greatest influence on the LDA predictions.

A jackknife resampling of the LDA indicates that it is 79% accurate in predicting the traditional categories of the shortening landforms. The LDA was 76% accurate in classifying landforms based on terrain type. Both LDAs were only moderately successful in predicting traditional categories and terrain types, and the 21–24% cases of inaccurate classification question the support of these classifications.

When a sample is assessed with an LDA, that sample is assigned an LD value that the LDA uses to distinguish the predefined group to which that sample belongs (Figure 2.6). In an LDA that attempts to distinguish between two groups, samples that cannot be differentiated would have LD values in and around zero. Our traditional category LDA (Figure 2.6a) assigns negative LD values to landforms where it predicts are lobate scarps, and positive LD values where it predicts wrinkle ridges. The negative and positive values produced by the terrain-type LDA correspond to predictions of cratered- and smooth-plains structures, respectively (Figure 2.6b).

Both LDAs show a substantial overlap of categories between LD values, with many structures clustering near zero. The traditional category LDA assigns the landforms of this work with LDs that fall in the range of -2.33 to +4.60. Of this, a total of 67 structures are assigned LDs that fall in the range between -0.82 and +1.54. In this range, lobate scarp designations greatly extend over wrinkle ridge designations, indicating that the quantitative morphological measurements that define wrinkle ridges and lobate scarps are not distinctly different when assessed with this method. This result is emphasized by the misclassification of structures relative to our visual inspection (e.g., wrinkle ridges

assigned negative-lobate scarp values Figure 2.6b). The overlap of LDs implies that most shortening landforms exist on a spectrum between lobate scarps and wrinkle ridges, whereas the small remainder can be identified as distinguishable endmembers. In this work, 33 of the 100 structures are clear endmembers: just 25 lobate scarps and 8 wrinkle ridges lie outside of this central cluster (Figure 2.6).

The LDA pertaining to the terrain type in which the structures reside (Figure 2.6b) also depicts a substantial amount of overlap between cratered-plains structures and smooth-plains structures, albeit with even fewer endmembers. This finding implies that the morphology of shortening landforms is not distinctly different across the terrains observed on Mercury's surface. All the structures in this study exist as either smooth-plains structures or cratered-plains structures (cf. Byrne et al., 2014), and so we interpret this result as indicating that a certain morphological variability of shortening landforms on Mercury is found in both terrain types. Unlike the traditional categories, however, categorization by terrain type does not assume specific morphological characteristics of shortening landforms, and so does not require (nor did we expect) the statistical detection of distinct groups based on morphology that were classified by Byrne et al. (2014) according to terrain type.

2.4 Discussion

We applied multivariate statistical analyses—principal component analysis and linear discriminant analyses —to assess if a systematic categorization of shortening landforms is possible based on morphological measurements alone. Prior to this study, shortening landforms on Mercury were assumed to fall into distinct categories based purely and subjectively on visual assessment of their map patterns and topography (Dzurisin,

1978; Melosh and McKinnon, 1988; Strom et al., 1975; Watters et al., 2004). Other studies have since challenged the use of these categories and have grouped Mercury's shortening landforms based on the terrain type in which they are located (e.g., Byrne et al., 2014). Although this latter approach is agnostic to landform morphology (and allows for the possibility that a continuum of landform shape exists), it sidesteps the issue of actually assessing quantitatively the morphology of shortening landforms on Mercury.

As with any statistical testing, it is important to note possible sources of bias and efforts for bias mitigation. One bias in our data collection may arise from the lack of equal and global coverage of high-resolution DEMs at present. This variability in data availability may bias our results toward larger landforms in more rugged terrain, such as cratered-plains landforms. We tested for dependency of landform size with terrain ruggedness by calculating the Topographic Roughness Index (TRI) along our profiles and observed its effect on our statistical results. The loadings of the TRI for both LDAs are negligible, whereas the loadings of the TRI for the PCA are small compared to the largest contributors (Table 2.1). A PCA performed without the TRI measurements (not included) produced nearly indistinguishable results. We take these results as support that our morphologic measurements are representative for a wide range of landform sizes on Mercury, irrespective of resolution and coverage of elevation data.

Moreover, our data include shortening landforms spanning a wide range of sizes (~30–1,000 km in length), thus accounting for a wide range of structure size. We also tested for size bias by scaling relief to shortening landform length, and then plotting the scaled relief against the LDs generated by the LDAs. No correlation between relief-to-length ratio and the LDs was found. Additionally, we performed the LDAs without the breadth and

topographic profile-length measurements, the most influential parameters in the original LDAs, to evaluate size bias. Excluding these data produced a similar spectrum rather than distinct groups: there was a substantial overlap in LD space for both the traditional categories and terrain type, and the success of the LDA correctly assigning the categories to our samples was approximately the same (80% and 73% for the traditional categories and terrain types respectively). These results indicate that additional evaluation of the LDA does not alter its outcome: the morphology of shortening landforms on Mercury does not separate such landforms into distinctly different groups.

"Lobate scarps" and "wrinkle ridges"

Our principal component analysis and linear discriminant analyses demonstrate that morphological measurements do not support the grouping of shortening landforms on Mercury into distinctly different categories. Only one cluster of data points is displayed based on the sample scores created in our PCA, showing no distinct patterns within the data scatter. For shortening landforms classified into the traditional categories (Figure 2.5a), our findings indicate that they are not distinctly different from one another for the morphologic parameters we assessed. PC1 is strongly anticorrelated with relief, breadth, total cross-sectional length, fore- and backlimb lengths, and mapped lengths (Table 2.1), implying that landform size may help in differentiating landform types. Although wrinkle ridge endmembers have generally lower relief than lobate scarps, there is substantial overlap of the two groups, with only few distinct lobate scarp and wrinkle ridge endmembers (note the lobate scarp and wrinkle ridge endmembers on the left and right of Figure 2.5a, respectively). This finding indicates that the size of the landforms, as a function of their relief, breadth, and total cross-sectional length, does not unequivocally

distinguish these categories. PC2 has a strong positive correlation with shortening strain and the slopes of the fore- and backlimb. Influential parameters on PC2 such as the slopes and shortening strain are measurements of a landform's relative shape along its topographic profile, suggesting that the gradients of shortening landforms are also important in distinguishing landform type. However, lobate scarps and wrinkle ridges fully overlap along the PC2 axis, strongly implying that the parameters governing PC2 alone do not unequivocally distinguish between the traditional categories.

Principal component analysis is based only on the morphological measurements; it is agnostic to any group classification. In contrast, LDA constructs a linear model that maximizes the separation of pre-defined groups. In the LDA assessing the difference between lobate scarps and wrinkle ridges, higher (positive) LD values predicted a structure to be a wrinkle ridge, whereas lower (negative) LD values predict lobate scarps. Substantial overlap along the LD axis (Figure 2.6a) highlights a broad region where lobate scarps and wrinkle ridges cannot be distinguished by this basis. Moreover, ~20% of structures are misclassified by a jackknife of the LDA. If lobate scarps and wrinkle ridges truly fell into distinct categories, there would be two clusters on opposite ends of the LD axis with little to no overlap and a minimum of false predictions. The LDA therefore supports the results of the PCA, indicating that although clear endmembers of what have been traditionally identified as "lobate scarps" and "wrinkle ridges" do exist, shortening landforms on Mercury form a spectrum between these morphologically idealized endmembers. This result is supported by observations of transitional structures (e.g., Clark et al., 2017; Watters, 2021; Watters and Nimmo, 2010) and by structures for which traditional classification is not obvious.

In the LDA, the total cross-sectional length and breadth are much more influential than any other measurements (Table 2.1). This is an interesting outcome as both measurements give first-order estimates of the shortening caused by the faulting and folding of the structure. Breadth is particularly notable because it is governed by the geometry of the underlying thrust fault and associated folding (e.g., Brandes and Tanner, 2014). Specifically, shortening-landform breadth is influenced by a combination of fault and depth of penetration, and it may thus reflect a difference in the type of thrust system underlying the landforms (e.g., some examples in Boyer and Elliot, 1982; Crane, 2020a; Martinez-Torrest et al., 1994). Therefore, the distinction between lobate scarps and wrinkle ridges on Mercury may lie in the underlying thrust system structure rather than their morphology. Future studies should perform detailed analysis of the underlying fault geometries of lobate scarps and wrinkle ridges and compare the thrust systems of the two categories.

To visually assess the traditional categories, we first independently (i.e., individually) classified the thrust-fault related landforms and compared our heuristic assessments for each structure. In several instances, we debated our assessments of structures between our authorship group because our interpretations did not agree or because it was too difficult to decide between assigning only the terms lobate scarps and wrinkle ridges to landforms. The quantitative results of the PCA and LDA reflect this heuristic, qualitative ambiguity. Crane and Klimczak (2019a) reached the same conclusion, confirming the finding stated in Byrne et al. (2018): "a classification scheme for shortening structures based on morphology, such as that used historically for Mercury, works only in a general way but cannot capture the broad variation in geometry of these landforms".

One defining criterion of wrinkle ridges is the presence of a wrinkle that typically sits atop and frequently parallels the strike of the ridge (e.g., Dzurisin, 1978; Nahm et al., 2023; Strom et al., 1975). Of our 25 wrinkle ridges, 14 do not show this superimposed wrinkle and their categorization was based purely on the complex map pattern. Most shortening landforms on Mercury's smooth plains have a wrinkle-ridge-like map pattern (Crane and Klimczak, 2019a) but lack a clearly defined, superposed wrinkle that parallels the main ridge. Although small, wrinkle-like structures are widespread in the planet's smooth plains, these structures are frequently not situated atop a broader ridge. That many ridges lack wrinkles may indicate that wrinkles did not form or that they are too degraded to be preserved—but speaks subjectively to the conclusion that not all wrinkle ridges are actually, in fact, wrinkle ridges.

While several thousands of shortening landforms have been mapped across Mercury's surface (n \approx 6000; e.g., Byrne et al., 2014), only a few structures (n \approx 60) have been regarded as high-relief ridges (Watters, 2021). Due to this small sample size, high-relief ridges were not analyzed with the statistical methods presented in this study. High-relief ridges are noted to be more symmetrical in cross-section, as their general morphological characteristics resemble that of a lobate scarp aside from a steeper backlimb. Provided that symmetry and backlimb slope are not the most influential parameters in our statistical analyses (Table 2.1), and that high-relief ridges previously described in the literature are on the order of tens to hundreds of km in length (Watters, 2021)—which scales similarly to many shortening landforms in this work—we anticipate that high-relief ridges would lie in the shortening landform spectrum produced from our results, indistinguishable from the other traditional categories.

The traditional categories of shortening landforms have also been used for Mars (e.g., Watters and Robinson, 1999), the Moon (Watters, 1988), and Venus (e.g., Bilotti and Suppe, 1999). Our finding that morphology does not support the classification of landforms on Mercury into binary categories raises questions about the suitability of these classifications on other planetary bodies. In a recent study, McCullough et al. (2023) focused on highlighting the differences between lobate scarps and wrinkle ridges on Mars by also conducting several LDAs based on morphology of shortening landforms there. Their LDA focused on surface observations also achieved only 79% accuracy, with broad overlap between lobate scarp and wrinkle ridge morphology. These results largely match those in this study and suggest that shortening landforms on Mars also form a morphological spectrum defined by the "traditional" endmembers, further supporting that the retention of the existing, binary classification scheme obfuscates the complexity and natural variability that defines the real-world continuum of shortening landform morphologies.

Other categories

We also assessed if a distinct grouping of shortening landforms by terrain type can be statistically detected, as such groupings have been applied to Mercury (Byrne et al., 2014). Both the PCA and LDA showed that our landforms are not distinctly different from one another in different geological units across Mercury (Figure 2.4c, 2.6b). There are 8 endmembers for cratered-plains structures, which are the largest shortening landforms of our analysis. This finding supports the finding by Byrne et al. (2014) that the largest shortening landforms generally occur in Mercury's cratered plains. However, our PCA shows that structure size or strain alone are not unequivocal criteria to distinguish smooth-

and cratered-plains structures, especially when comparing landforms of intermediate and smaller sizes (≤ 600 km in length).

The substantial overlap of landforms in the LDA (Figure 2.6b) with many structures having small absolute LD values shows that the morphology of shortening landforms do not differ distinctly by terrain type on Mercury. In particular, the loading of the TRI is very small (Table 2.1), indicating that terrain type does not influence the morphological variability on Mercury, particularly for attributes related to landform size and shape. However, as we note above, categorization by terrain type does not rely on morphologic characteristics of shortening landforms, and we therefore suggest that this classification scheme is appropriate so long as no assumptions are made regarding the morphology of the individual landforms themselves.

Finally, we also assessed if shortening landforms can be discretely categorized based on the map patterns they display (Figures 2.3, 2.4b). Given the varying sample sizes between the five map patterns, a PCA was the only suitable method for assessing categories from map patterns. The PCA sample scores depict no distinct groupings based on map patterns, and all five patterns collectively form a single cloud of points. These results indicate that any shortening landform can exhibit any map pattern, regardless of various morphologic parameters such as those associated in PCs 1 and 2 with landform size and shape, or accumulated strain amount.

2.5 Conclusions

Shortening landforms on Mercury have been traditionally classified into three categories: lobate scarps, wrinkle ridges, and high-relief ridges. This distinction has primarily been based on subjective, visual assessment of structures in photogeologic

datasets. The goal of this study was to assess if the traditional classification scheme for shortening landforms on Mercury can be applied based on the morphologic variability using multivariate statistical tests. We find that the morphology of most shortening landforms on Mercury is consistent with elements of both wrinkle ridges and lobate scarps, with few distinct endmembers of either category. We also find that any morphology of shortening landforms can be observed in any terrain type and that the different observed map patterns can belong to any shortening landform regardless of its morphology.

In conclusion, the terms "lobate scarp," "wrinkle ridge," and "high-relief ridge," although having found widespread use in planetary tectonics literature (e.g., Melosh and McKinnon, 1988; Watters and Robinson, 1999; Watters et al., 2004), do not adequately capture the variability of shortening landform shape, and can erroneously undermine the true complexity of such landforms. The continued use of these terms will oppose the facilitation of new insights into the geometry of crustal shortening on rocky planetary bodies and may reduce the accessibility of planetary tectonics to those who study shortening systems on Earth—where such terms have never been routinely used.

2.6 Acknowledgements

We thank Seiji Sugita for their editorial assistance as well as Lisa Schleicher and an anonymous reviewer for their helpful suggestions. This research was supported by NASA's Solar System Workings program under grant 20-SSW20-0153.

2.7 Data availability

The supplementary material for this research is available in Loveless et al. (2024a).

2.8 Figures

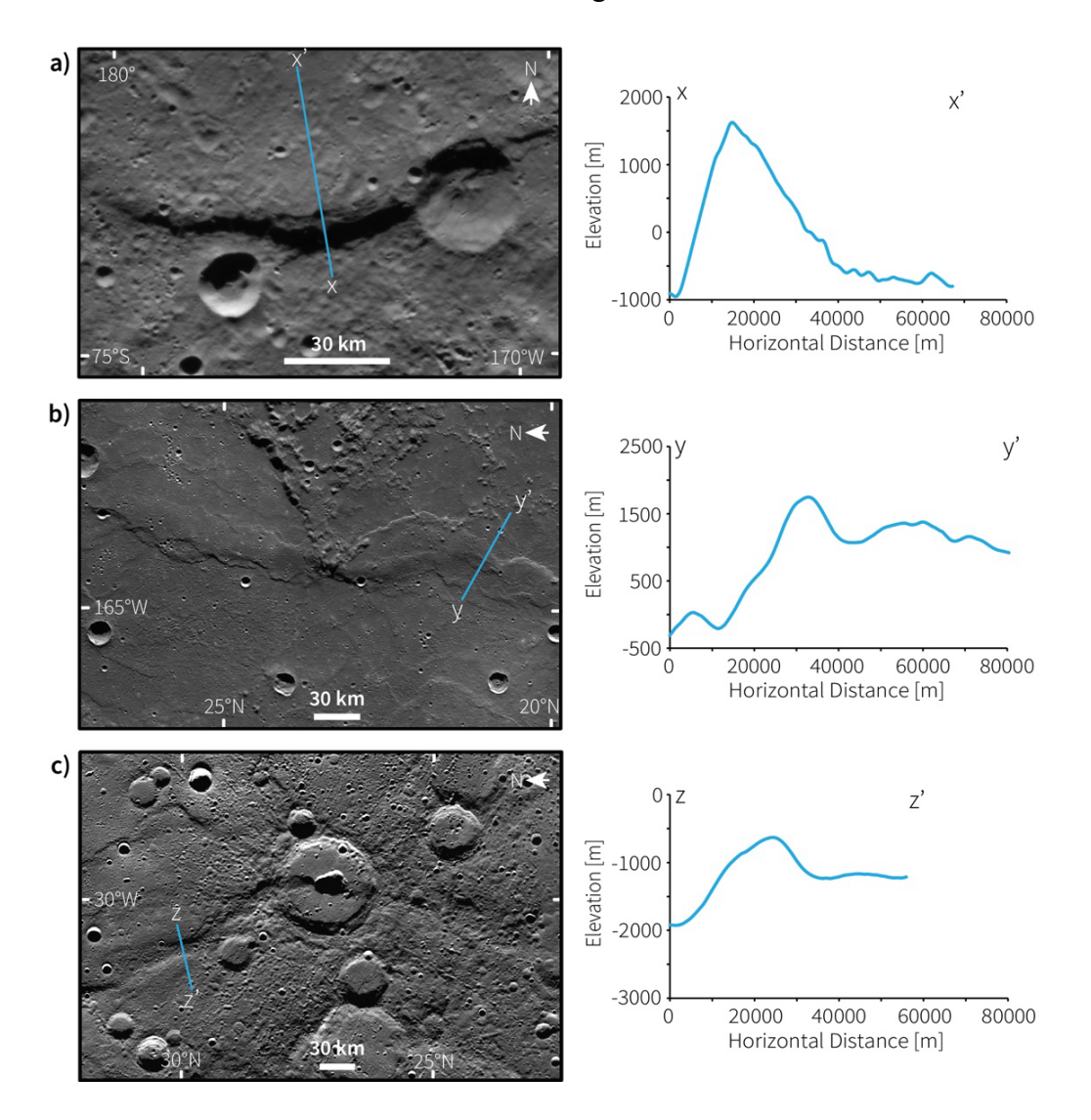


Figure 2.1: Examples of the three "traditional" categories of shortening landforms found on Mercury. a) Map view of an unnamed lobate scarp near the south pole (left) along with the corresponding topographic profile from x to x'. b) The wrinkle ridge Schiaparelli Dorsum in map view (left) along with the corresponding topographic profile from y to y'. c) The high relief-ridge Antoniadi Dorsum in map view (left) and its corresponding topographic profile from z to z'. All images are shown in a stereographic projection

centered on the shortening landform and all profiles are shown at $\sim 16 \times$ vertical exaggeration.

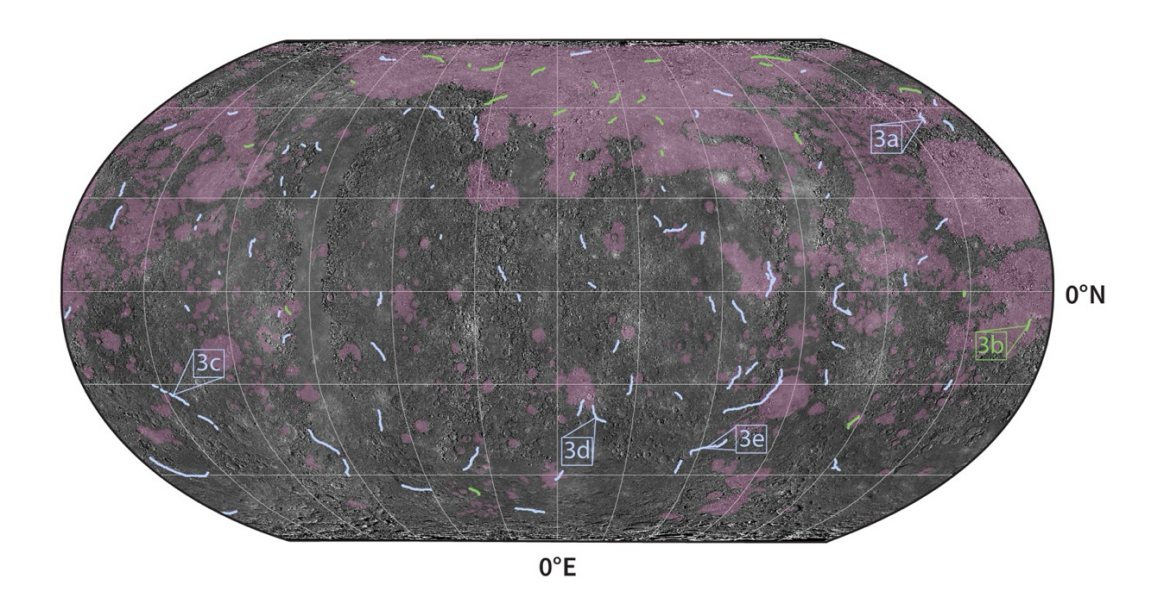


Figure 2.2: Global map of Mercury in Robinson projection, showing the 100 shortening landforms analyzed in this study. Those that were traditionally identified as lobate scarps are shown in light blue, while those identified as wrinkle ridges are shown in green. Smooth-plains units (Denevi et al., 2013) are highlighted in pink. The map indicates the locations of five examples of shortening landforms, shown in Figure 2.3 (a–e).

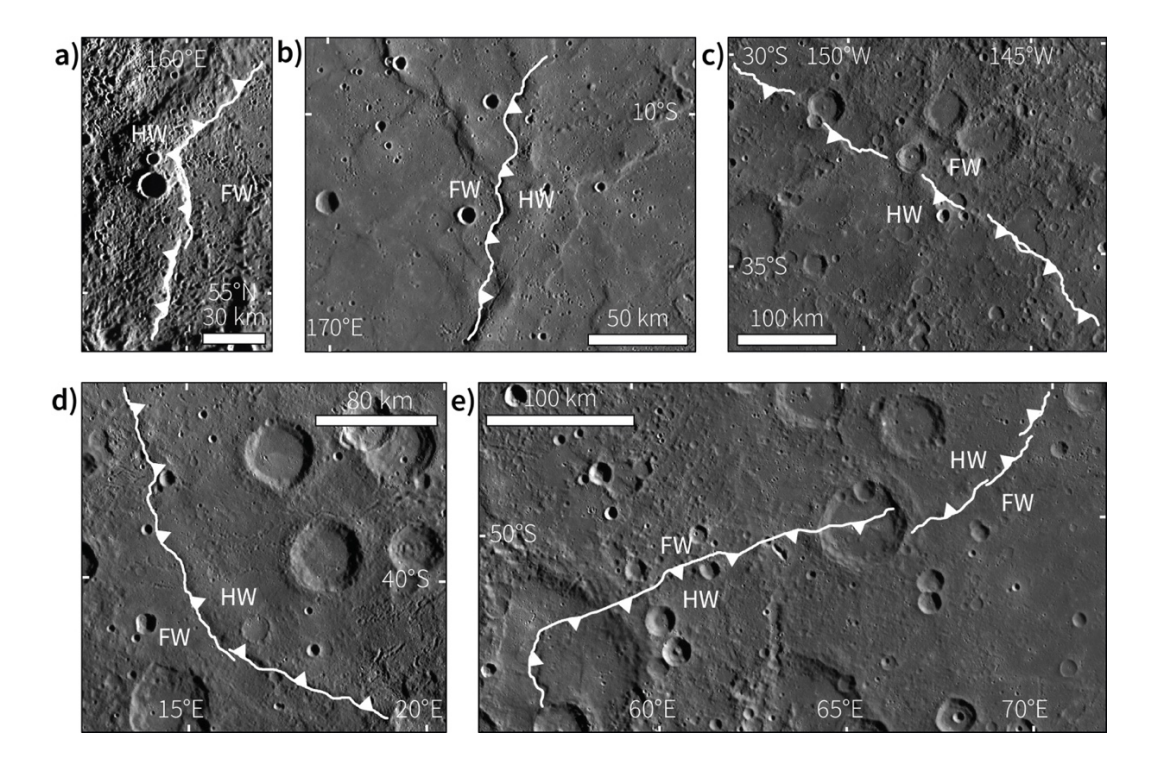


Figure 2.3: Examples of the five scarp map patterns observed in this study. Here, the hanging walls are denoted with 'HW' and the footwalls are labeled with 'FW'. a) A scarp with a concave map trace. b) A scarp with a sinuous map trace. c) A scarp with a straight map trace. d) A scarp with a convex map pattern. e) A scarp for which vergence switching is evident. All images are shown in a stereographic projection centered on the shortening landform.

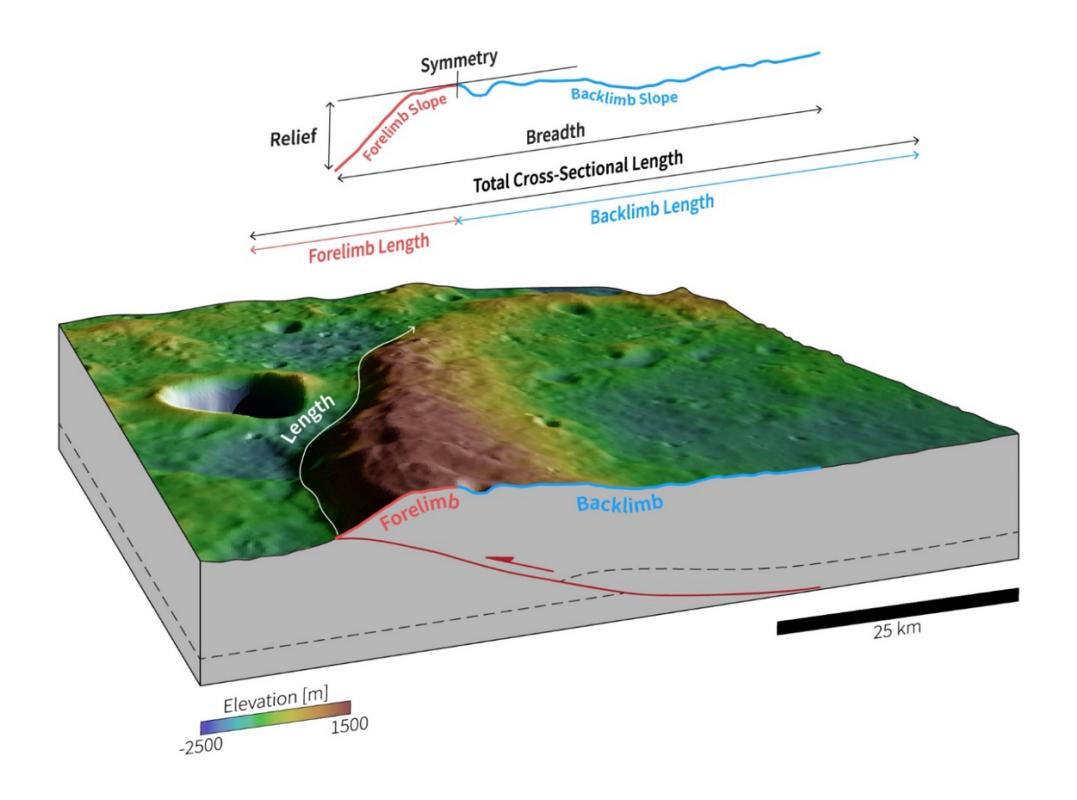


Figure 2.4: Block diagram of a shortening landform annotated with parameters measured for each landform in Figure 2.2. The landform shows the shape of the forelimb (in red) and backlimb (in blue) and part of the map trace (in white) along which the fault length was measured. The extracted profile with the maximum relief shows the breadth and locations where symmetry and slopes of the forelimb and backlimb were derived. The horizontal lines labeled Forelimb Length, Backlimb Length, and total Cross-Sectional Length are representations of the unfolded topographic profile. Thrust fault geometry in the subsurface is interpreted based on the morphology of the structure. The assumed fault geometry is based off simple cross-sectional balancing, and similar fault structures generated in previous modeling studies (e.g., Herrero-Gil et al., 2020). The dashed line in the subsurface represents an arbitrary marker horizon to depict deformation along the fault. The image in this figure is taken from the low-incident angle global mosaic. Elevation (Bertone et al., 2023) is shown as blue for low-lying areas and brown for high-standing terrain.

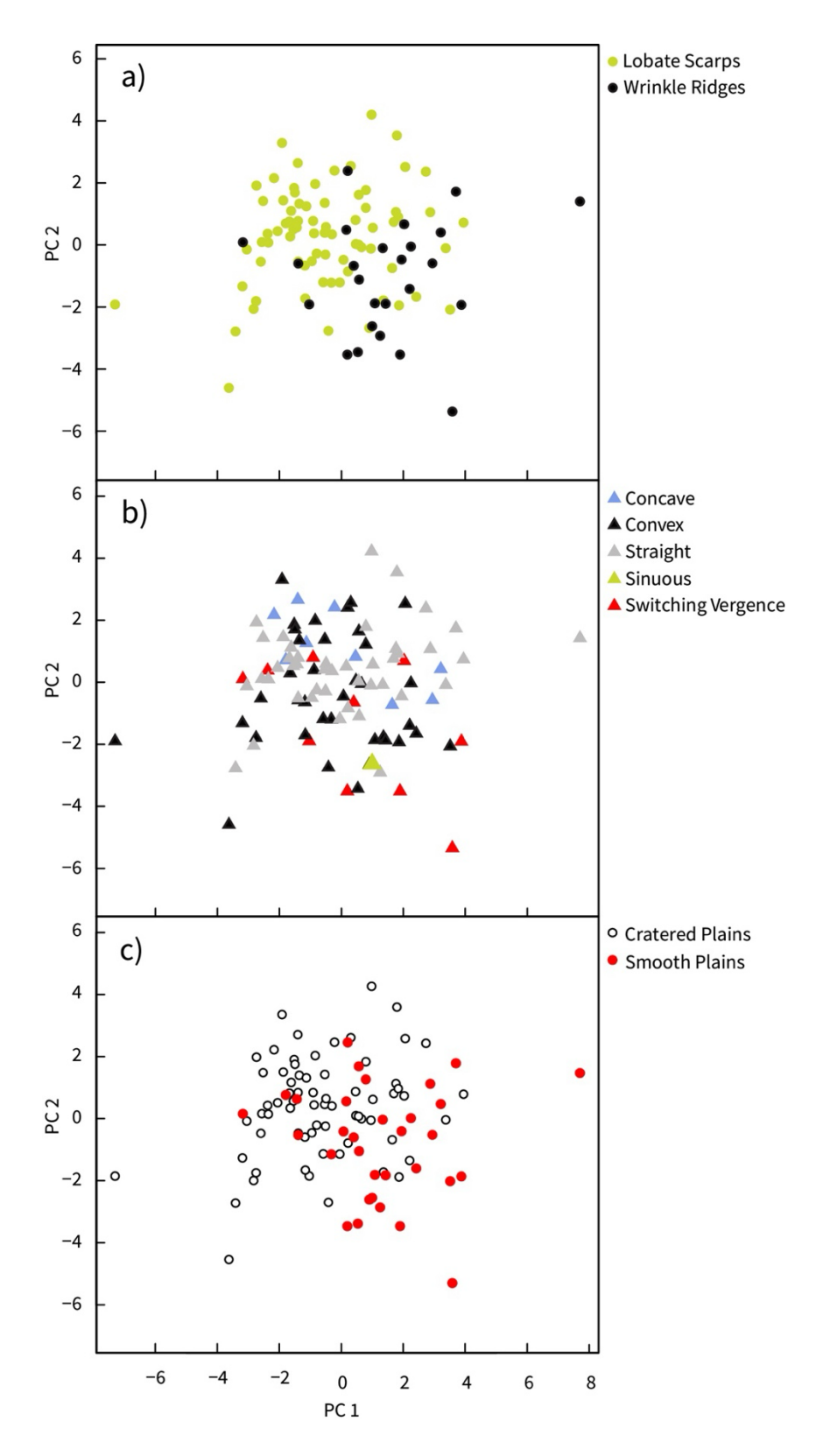


Figure 2.5: PCA sample scores coded by traditional categories (a), map trace (b), and (c) terrain type.

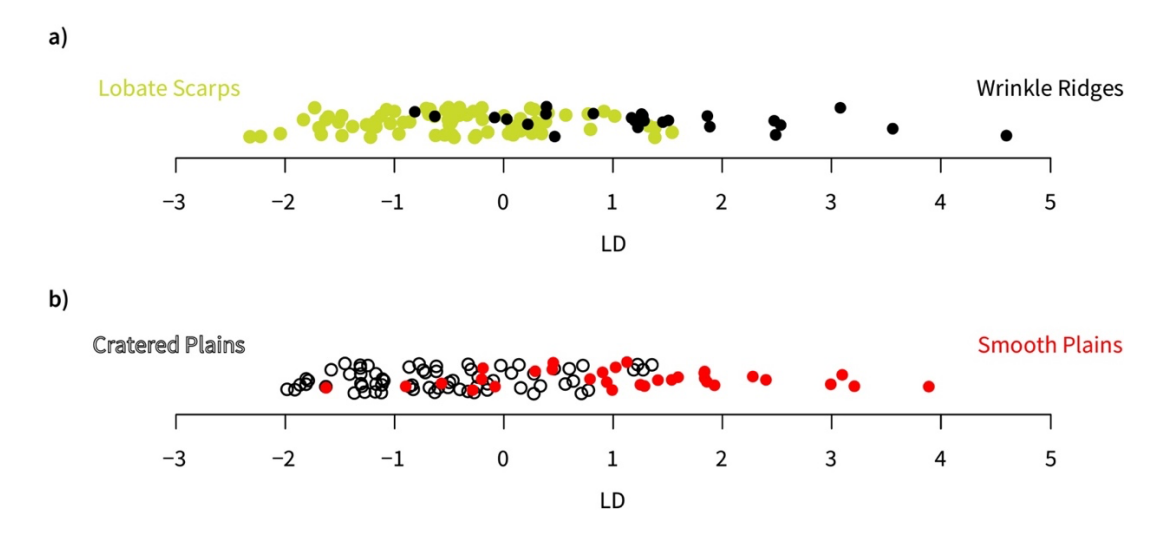


Figure 2.6: Classification of landforms by linear discriminant analysis based on traditional categories (a) and terrain types (b). Note the poor discretization of landforms in both cases, suggesting that landform morphology does not support the existence of distinct categories per this technique.

2.9 Tables

Table 2.1: Loadings of variables on PCs 1 and 2 and linear discriminant loadings for the traditional category LDA (LD TC) and terrain type LDA (LD TT). Bolded values indicate the most important loadings for each axis.

Parameter	<u>PC1</u>	<u>PC2</u>	LD TC	LD TT
Relief	-0.38	0.26	-3.70	-2.87
Breadth	-0.43	-0.18	-28.97	-39.81
Total Cross-Sectional Length	-0.43	-0.18	26.79	42.68
Shortening Strain	-0.12	0.50	-0.15	0.72
Forelimb Slope	-0.16	0.48	1.70	0.41
Backlimb Slope	-0.05	0.43	0.17	-0.25
Symmetry	-0.20	0.29	0.13	0.49
Forelimb Length	-0.30	-0.17	2.81	0.63
Backlimb Length	-0.41	-0.14	1.41	-2.64
% Backlimb Downslope	0.13	0.09	-0.41	-0.10
Mapped Length	-0.32	-0.10	0.51	0.18
TRI	-0.17	0.21	0.27	0.04

CHAPTER 3

GEOMETRIC FORWARD MODELING OF THRUST SYSTEMS UNDERLYING SHORTENING LANDFORMS ON MERCURY 2

² Loveless, S.R., Klimczak, C., Crane, K.T., and Byrne, P.K., Submitted to Journal of Structural Geology, 2025

Abstract

Mercury hosts thousands of shortening landforms that are widespread across the entire planet. The shortening is widely accepted to be caused by a combination of thrust faulting and folding, resulting from the global contraction of Mercury caused by long, sustained cooling. Most shortening landforms on Mercury's surface have been classified into one of two groups: lobate scarps or wrinkle ridges. There is no distinct statistical difference in the surface morphology of these shortening landform classifications. Only a small subset of shortening landforms are clear-endmember wrinkle ridges and lobate scarps. The difference between geomorphic manifestations of shortening landforms may be governed entirely by the thrust systems and associated folding that form them. We therefore model thrust systems associated with 55 lobate scarp and wrinkle ridge endmember shortening landforms found across the surface of Mercury. Structures were modeled in 2D sections below the topographic profiles of landforms with the greatest structural reliefs. Models utilized the fault-bend fold algorithm in the MOVE geologic modeling software. Once models matched the observed topography and shortening strain, fault geometric parameters, such as number of structures, dip, depth extent of faulting, height, etc., were extracted and compiled for all structures. Our modeling shows that Mercury hosts a wide range of complex thrust systems, including single, listric faults, imbricate thrusts, and pop-up structures. In particular, the morphologies of lobate scarps end-member structures are best explained by models of a single, listric fault, whereas most wrinkle ridge end-member structures require more than one fault. We identify a large overlap in the variation of fault geometric parameters for both wrinkle ridge and lobate scarp archetypes, confirming the results of our previous geomorphic analysis that shortening landforms do not comprise two distinct categories. The overlap in geometric parameters also suggests that global contraction generated most of these structures.

3.1 Introduction

Mercury hosts a global population of positive-relief, tectonic shortening landforms as revealed by both the Mariner 10 (e.g., Strom et al., 1975) and MEcury Surface, Space Environment, GEochemistry, and Ranging (MESSENGER) missions (e.g., Byrne et al., 2018). Such landforms are thought to be produced by global contraction (e.g., Solomon, 1978) and are widely accepted to be formed by thrust faulting and folding (e.g., Byrne et al., 2018, 2014; Strom et al., 1975). Many terms have previously been used to describe tectonic landforms formed by thrust faults, e.g., "shortening structures" or "thrust fault-related landforms", but for simplicity we will refer to all such structures as "shortening landforms" throughout this study.

Shortening landforms are common on all major rocky bodies in the Solar System. Such structures depict positive-relief cliffs, often paralleled by breaks along the surface (e.g., Schultz and Watters, 2001; Watters, 2003). Since the earliest observations of tectonic features on terrestrial bodies, shortening landforms have been categorized into groups based on surface morphology alone (e.g., Dzurisin, 1978; Strom, 1979). Of the different classifications used to describe shortening landforms, lobate scarps and wrinkle ridges have been used as designations for almost all shortening landforms found on Mercury's surface (e.g., Melosh and McKinnon, 1988; Watters et al., 2004). Lobate scarps are described to show clear linear-to-arcuate surface breaks in plan view, with topographic characteristics of steeply sloping forelimbs at the surface break trailed by gradual sloping backlimbs (Figure 3.1a; e.g., Strom et al., 1979, 1975; Watters, 1993). Such surface expression is linked to asymmetric anticlinal folding of the hanging wall (Byrne et al., 2014) with the

asymmetry, or vergence, providing clear indication of tectonic transport to be in the direction in which the forelimb slopes (i.e., the vergence). This geometry is akin to the folding geometry of fault-displacement gradient folds described by Wickham (1995).

Wrinkle ridges have been described as having complex, sometimes sinuous map patterns in plan view that are accompanied by cross-sectional topographic profiles demonstrating a superimposed ridge (the "wrinkle") on top of a primary ridge (e.g., Watters, 1988). Shortening landforms of this class are common within volcanic plains of terrestrial planetary bodies throughout the Solar System (e.g., Nahm et al., 2023; Plescia and Golombek, 1986). On Mercury, wrinkle ridges frequently host faults that break at the surface (Golombek et al., 2001; Schleicher et al., 2019; Strom et al., 1975; Watters, 1988), but many have also been interpreted to be anticlinal folds above blind thrust faults (e.g., Schultz, 2000) containing backthrusts (Okubo and Schultz, 2004). Byrne et al. (2018) argued that wrinkle ridges host two oppositely facing monoclines which may indicate vergence of two opposing thrusts.

The oversimplification that categorizing shortening landforms into these two groups is challenged by the large variation of thrust systems found on Earth. Mountain ranges that formed by shortening display a wide range of complex systems of thrust faults and folds (e.g., Boyer and Elliot, 1982; Crane and Klimczak 2019b; Chapple, 1978; Matthews and Work, 1978; McClay, 1978; McClay and Price, 1981; Morley, 1988). There is no evidence that suggests that thrust systems on Earth operate differently and therefore thrust systems on other planets should not be treated otherwise than those observed on Earth. Fold and thrust belts are common large-scale crustal shortening systems that are accommodated by multi-fault thrust complexes (e.g., McClay and Price, 1981). Common

Earth thrust systems like duplex structures are described with listric or curved fault geometries with either stacked panels bounded by thrust faults or as imbricate thrusts with multitude of thrusts branching off a single décollement (Boyer and Elliot, 1982). Many of these thrust systems are created by displacement along multiple faults to build positive relief. In contrast, thrust systems on other planets are commonly interpreted as single, homoclinal (non-curved) fault planes (e.g., Schultz and Watters, 2001).

Few studies have suggested fault geometries on Mercury like to those on Earth. Some examples include for an extensive décollement underlying Beagle Rupes (Rothery and Massironi, 2010) and pop-up thrust system structure for shortening landforms and complex compound landforms on Borealis Planitia (Crane and Klimczak, 2019a). Other analogies between Earth and Mercury tectonics have been drawn from the conceptualization of thin- and thick-skinned deformation (Crane and Klimczak, 2019a). Thin-skinned deformation is strain accommodated by faults in weak upper horizons of the lithosphere (originally, for Earth, the sedimentary cover atop crystalline basement rock), whereas thick-skinned deformation is strain accommodated by faults that have penetrated deep into the basement (Chapple, 1978; Pfiffner, 2017). Analogies of thrust fault-related landforms to shortening structures on Earth have been made for thin-skinned tectonics features like the Yakima fold and thrust belt in Washington State (e.g., Watters et al., 2004), and the Lesser Himilayan Duplex (Crane and Klimczak, 2019a). Thick-skinned deformation has been used to describe Mercury's shortening landforms with comparisons to the Wind River thrust fault (Mueller et al., 2014; Watters and Robinson, 1999). Although impact-weakened stratigraphic horizons or volcanic layering are frequently invoked as layers permitting thin-skinned tectonics in volcanic plains, basement-reactivated thinskinned tectonics has been invoked as a hybrid mechanism on Borealis Planitia (Crane and Klimczak, 2019a). By this mechanism, faulting and folding within the smooth plains are influenced by fault activity in the basement rock (Pfiffner, 2017).

Many previous subsurface modeling efforts for shortening landforms on rocky bodies have used the elastic halfspace mechanical dislocation COULOMB code (e.g., Byrne et al., 2016; Egea-González et al., 2017, 2012; Peterson et al., 2020; Schultz and Watters, 2001; Williams et al., 2013) or geometric cross-balancing techniques including trishear modeling (e.g., Herrero-Gil et al., 2020, 2019) or fault-propagation folding (Mueller et al., 2014). Using COULOMB, a set of physical parameters for a predefined fault plane are invoked as the surrounding lithosphere is elastically deformed to match the observed topography (Toda et al., 2005). Early studies modeled simple homoclinal faults with uniform displacements (e.g., Schultz and Watters, 2001) that can produce artifacts in the predicted topography if the superposed displacement is not tapered toward the fault tips. However, listric fault geometries have also been applied to COULOMB modeling to produce acceptable model topographies (e.g., Byrne et al., 2016; Peterson et al., 2020; Watters and Schultz, 2002), but other studies have found listric faults to inaccurately represent the uplifted topography (e.g., Egea-Gonźalez et al., 2012; Herrero-Gil et al., 2019). Alternatively, the trishear forward modeling technique recreates fault propagation folding, which uses cross-balancing techniques that relates folding deformation at the upper fault tip to a specialized limb angle and hinge ratios. These cross-balancing methods have been used in conjunction with faulted offset craters to model the underlying fault geometry (e.g., Herrero-Gil et al., 2020; Mueller et al., 2014). These methods come with a set of drawbacks. First, not every surface-breaking thrust fault has a superposed offset crater. Second, the trishear approach requires introducing additional geometric complexities and a wide, largely unknown parameter space associated with planetary shortening landforms.

The goal of this study is to investigate the variety of thrust systems in Mercury's subsurface. This is done by modeling 55 morphologically variable shortening landforms by selecting the endmember lobate scarp and wrinkle ridge structures from the data set published in Loveless et al. (2024a). To be concise, we refer to these endmember structures as lobate scarp archetypes and wrinkle ridge archetypes, however, we note that some wrinkle ridge endmember structures were classified as lobate scarps in the LDA of *Chapter 2*. Our modeling utilizes the fault-bend fold algorithm in the MOVE geologic modeling software from PE Limited (Petex). Fault-bend folding is a proven geometric forward-modeling technique that can be applied to fault displacement-gradient folds (e.g., Brandes and Tanner, 2014; Connors et al., 2021; Hughes et al., 2014; Medwedeff and Suppe, 1997; Suppe, 1983). We collect and synthesize fault geometric parameters for our 55 models to identify the structural characteristics of shortening landforms on Mercury.

3.2 Methods

Landform selection

We previously assessed the morphological variability of 100 randomly selected shortening landforms on Mercury to distinguish lobate scarps and wrinkle ridges (*Chapter* 2). In particular, we conducted a Linear Discriminant Analysis (LDA) that maximizes the difference between two predefined groups by creating a linear equation that classifies cases based on their correlated parameters. An LDA used to distinguish two groups assigns to each case a positive or negative value, or linear discriminant (LD) for its classification. For

example, an LDA of lobate scarps and wrinkle ridges shows a large degree of overlap in the LD (Figure 2.6; *Chapter 2*), indicating that the morphology of these shortening landforms on Mercury does not support distinct groups. To further investigate if a structural difference between these categories exists, we use the end members of the lobate scarps (n=30) and all of the wrinkle ridges (n=25; Figure 3.2) to model their underlying thrust systems. We use the terms lobate scarp archetypes and wrinkle ridge archetypes when referencing these lobate scarp and wrinkle ridge shortening landforms that we model in this work.

Modeling

We construct models using the 2D Move-On-Fault module in the MOVE modeling software by PE Limited (Petex). Our models make use of the Fault-Bend Fold algorithm, which is a geologic restoration technique that directly relates folding in the hanging wall of the fault to the shape and displacement along the fault plane. Describing deformation as a fault-bend fold uses structural balancing, which is the integration of satisfying a set of conditions between the interpreted initial state and observed deformed state of the area or volume of interest (Dalhstrom, 1969). Such conditions include the maintenance of length of the interpreted geologic horizons pre- and post-deformation.

A fault-bend fold is a fault-related geometry, where folding of the hanging wall is caused by distortions along the fault plane (Suppe, 1983). The relationship between the slip along the fault plane and the folding of the above horizons is modeled through a series of trigonometric relationships dependent on changes of the fault dip. The specific shape of the fault and the amount of along-slip displacement govern the distorted shape of the overlying layers of rock. Whereas a homoclinal fault experiencing simple shear

accommodates all of the shortening through the displacement along the fault, a fault-bend fold will drive different amounts of shortening accommodated along the fault plane through a combination of slip and folding arising from changes in the dip of the fault plane. Homoclinal portions of a fault in a fault-bend fold will accommodate shortening with more slip, and as the fault changes dip, or ruptures the surface, folding becomes more prevalent. The faults modeled in this study break the surface, so the fault-bend fold geometry simulates how the uplifted hanging wall folds over the footwall.

Such geometric configurations have been used for many years to characterize contractional tectonic architecture on Earth (e.g., Connors et al., 2021; Suppe, 1983; Suppe and Namson, 1979). Fault-bend folds are present in seismic reflection profiles of contractional tectonics on Earth (e.g., Shaw et al., 2005). Fault-bend fold architectures have also been used to describe or model the structural geology of shortening landforms on Mercury (Byrne et al., 2018; Crane, 2020a; Crane and Klimczak, 2019a). This type of fault geometry is a good representation of surface-breaking thrust faults for which displacements are large enough to permit the hanging wall to fold over the footwall.

We model the fault structure under each of our selected shortening landforms along the inferred direction of tectonic transport and at the point of highest structural relief along the topographic profile. The direction of tectonic transport is assumed to be perpendicular to the long axis of a landform, except where an impact crater is crosscut and shortened by the fault, indicating the direction of displacement (Galluzzi et al., 2015). The selected topographic profile is then imported into the MOVE software and 50 arbitrary, evenly spaced horizontal geologic horizons are constructed underneath the topographic profile to track the modeled deformation. The uppermost of these horizons is taken as the planetary

surface. The elevation of this surface horizon is set equal to the measured elevation at the start of the forelimb. We vary the specific spacing of the horizons based on the length of the landform.

After the horizons are constructed, we draw a fault plane within the model setup. We conduct the modeling while simultaneously assessing the photogeology of the shortening landform to accurately inform the model with all of the available observations. Initially the fault is assumed to be a homoclinal fault plane with a reverse sense of slip and a dip angle of 30°. Iterative model previews are generated as the fault plane geometry, depth, and displacement are changed until the modeled surface horizon matches the observed topography. Fault parameters were adjusted based on the results from the previous models by raising or lowering areas the fault in the respective areas of the surface that needed alterations. The amount by which a fault was changed is relative to the discrepancy between the modeled surface and the observed surface in the previous model. Once the observed topography is matched, we calculate the shortening strain from folding for our model to test against the observed shortening strain as an additional control point. More details on this control point are provided in section titled *Controls of the Models*. A model is deemed to be a successful match once the modeled topography matches the observed topography within 10% of the maximum relief of the structure and the shortening strain from folding of the model matches within 0.2% of the observed shortening strain across the structure (Loveless et al., 2024a).

If two or more surface breaks are present on image data, then we include more than one fault in the model. In this case, we model the primary fault first, which we determine using photogeological observations. The geometries and displacements of any other faults are subsequently added to replicate the desired deformation.

Once a model was complete, 13 modeled fault parameters were extracted (Figure 3.3), including near-surface fault dip, average dip, maximum dip, input shortening, average heave, average throw, average slip, maximum slip, depth of faulting, fault height, and modeled strain from folding. Near-Surface Fault Dip is defined as the dip of the fault in the uppermost 10% of the fault. Average Dip (α in Figure 3.3) is the average downward angle the fault makes with a horizontal plane, and Maximum Dip is the maximum downward angle relative to a horizontal plane. All dips are measured in degrees. Input Shortening, measured in kilometers, is the horizontal shortening implemented in the Fault-Bend Fold algorithm to which the model displaces the deformed horizons.

The slip accommodated along a fault in a fault-bend fold structure varies along the height of the fault (Suppe, 1983); therefore, we include additional measurements from our models. Average Heave and Average Throw, both measured in kilometers, are the average horizontal and vertical components of the displacement laterally along the fault. Average Slip is the average displacement laterally along the fault. Maximum Slip is the maximum amount of displacement that occurs along the fault. Other measurements include Depth of Faulting, measured in kilometers, as the depth extent measured vertically from the surface to the lowermost portion of the fault and Fault Height, measured in kilometers, which is the down-dip length of the modeled fault plane (red line in Figure 3.3). From fault height, we calculate Aspect Ratio, which is the fault height divided by the mapped length of the fault taken from Loveless et al. (2024a). If more than one fault was needed for a model, the fault height of the largest of the faults is reported. Number of Faults is the number that was

needed to model the observed deformation for each landform. Finally, the modeled strain from folding of the uppermost hanging-wall horizon produced by the model is calculated as:

$$\varepsilon_{\text{Fold}} = \frac{L_{\text{H}} - L_{\text{T}}}{L_{\text{T}}},$$

where L_H is the horizontal hanging wall horizon length and L_T is the total hanging wall horizon length.

Thrust System Type and Fault Shape are two qualitative metrics that describe the subsurface structure of the shortening landforms. Thrust System Type refers to the number of faults (one, two, or three) and their respective directions of tectonic movement, or direction of tectonic transport from one another. Fault Shape describes whether the fault plane is listric (curved) or planar.

Controls of the models

As for cross-section restoration and balancing, a model can be deemed successful once it satisfies all control parameters. For geologic restoration of studies on Earth, such controlling parameters include interpretations of seismic sections and lithologic changes and repeated or missing sequences in borehole data (e.g., Egan et al., 1997; Pierdominici et al., 2011). Fault geometry, depth, and dip can be directly correlated to the seismic response of faults in the subsurface, and surface dips from *in situ* field measurements can all serve as controls.

For other terrestrial planets, subsurface data and *in situ* analyses are more difficult or impossible to obtain. The current standard of fault modeling efforts in the past has been to match the topography by forward modeling of an initially undeformed surface. This technique has been applied to many bodies that host faulting such as Mercury (e.g., Crane,

2020b; Watters et al., 2016), the Moon (e.g., Byrne et al., 2015; Collins et al., 2023; Williams et al., 2013), and Mars (e.g., Herrero-Gil et al., 2019; Schultz and Watters, 2001). Topography is a reasonable control for these bodies because they lack substantial surface erosion. However, forward modeling can produce more than one solution for the same topography (Egea-González et al., 2017), and that there is an element of non-uniqueness to such modeling. Therefore, for our modeling efforts we use the matching the topography within $\pm 10\%$ of the structure's vertical relief as the minimum criterion to be met for a model to be deemed acceptable. This is done by creating copies of the topographic profile at elevations $\pm 10\%$ of the vertical relief and forward modeling the surface until it lies between those boundaries.

To maximize the likelihood of producing a unique solution for our models, we must use additional control points aside from the observed topography. To better constrain our models, the modeled strain from folding must be as close as possible to the observed shortening strain. The observed shortening strain values are taken from Loveless et al. (2024a). These values were calculated as the change in length (landform breadth minus the total cross-sectional length) divided by the total cross-section length. In a fault-bend fold, shortening along the fault is accommodated by both the heave (the horizontal component of displacement) and by folding of the hanging wall. The amount of strain accommodated by folding is a function of the shape of the fault.

At the surface, the amount of shortening accommodated by folding is governed by the depth of faulting, input shortening, and variations of the fault dip (See Section 3.3). A deeper modeled fault requires less input shortening to match the actual topography as more material displaced from depth to the surface, but more folding will be accommodated at

the surface. An increase in modeled depth of faulting increases the strain from folding. Alternatively, more shallowly penetrating faults require greater shortening, but the modeled strain from folding will decrease. Therefore, a unique solution for fault depth, input shortening, and fault dip is achieved by matching the modeled strain from folding to the observed shortening strain values in addition to matching the modeled topography with the observed topography.

We try to match the modeled strain from folding to the observed shortening strain values exactly but find negligible changes in the overall fault geometry in a $\pm 0.2\%$ range of the modeled strain from folding. We summarize our strain-matching efforts with box-and-whisker plots, a non-parametric way to portray variance (Figure 3.4). The distribution of the sample size for our modeled strain from folding and the distribution of the observed shortening strain from the same landforms compiled from Loveless et al. (2024a) aligns well (Figure 3.4). We interpret this as an indication that our models provide a good representation of the folding at the surface and the subsurface fault architecture of the shortening landforms.

On Mercury, some shortening landforms crosscut craters. If a crater is assumed to be initially circular, the overall shortening deformation of the cut crater can be used to constrain geometric properties of the fault, such as fault dip and displacement vector (Galluzzi et al., 2015), which can be another control point for a structural model. Most of the shortening landforms selected in our study do not crosscut craters, and if they do, the craters are either not adequately deformed enough to extract any meaningful structural information or are located far from our cross-section line and so do not contain the exact information needed for our model. Only in a couple instances does this method work in our

sample of shortening landforms as this method works only on well-preserved craters. For 11 of the 55 landforms, deformed craters were present near the cross-section. However, most of the faults assessed in this work that show cross-cutting relationships with craters do not unequivocally show the direction of tectonic transport. Therefore, this is a valid control point that is considered but is only used for a small subset of our sample size.

3.3 Sensitivity study

We conducted a sensitivity study to test the efficacy of our workflow, the impact of control points, and the resulting fault geometries. For that, we construct three models for the same shortening landform (Figure 3.5). All models satisfy the topographic control point and match the direction of tectonic transport from a nearby shortened crater but vary with fault geometric parameters (Table 3.1). Out of the three, only one satisfies the second control point by matching the modeled to the observed strain from folding. In Model 1, we construct a fault that matches the observed topography and that penetrates to 11.4 km and dips an average of 9°, leading to a slip on the fault of ~5700 m from an input shortening of 5500 m. In Model 2, we construct a fault that matches the same topography but penetrates to a depth of 24.2 km and dips at an average 21°. Model 2 requires an input shortening of 2400 m producing a slip along the fault of 2800 m. The fault for Model 3 also was constructed to match the input topography, but penetrates to 48.1 km, dips at an average of 40°, and requires 850 m of shortening to produce 1673 m of slip on the fault.

The shortening strain observed along the landform for all three models is -0.806%. The modeled strain from folding is -0.622%, -0.801%, and -1.255% for Models 1 to 3, respectively (Table 3.1). The modeled strain from folding of Model 1 matches the observed folding strain with a percent match of 77.2%. The modeled strain from folding of Model 2

most closely resembled the observed folding strain matching at 99.4% of the observed value. Model 3 has a percent match of 31.9% to the observed folding strain. Model 2 represents a successful model that both matches the observed topography and accords with the observed folding strain. The result of this sensitivity study highlights the dependence of the modeled strain from folding on the depth of faulting, dip of the fault, and input shortening. Therefore, by using both topography and the strain produced from folding as control points, we produce well constrained solutions of our shortening landform models.

In a fault-bend fold, the strain accommodated by folding varies fault geometry (Figure 3.5, Table 3.1). Therefore, matching the observed and modeled folding strain plus the observed topography yields unique, doubly constrained solutions for the underlying fault geometry. Folding at the surface is directly related to the dip and depth of faulting. For the same landform, a fault penetrating to greater depths will have a greater dip than those penetrating to shallower depths. Slip in fault-bend folds decreases with steeper dips while greater amounts of deformation are accommodated by antiformal folding (Suppe, 1983). Therefore, our models produce less folding if the modeled fault penetrates to shallower depths, and the average slip along the fault increases (Table 3.1).

Larger amounts of input shortening and thus slip along the fault are needed to uplift the hanging wall block to match the topography (Model 1, Figure 3.5). This increases the total shortening strain of the surface, with consequently less strain accommodated by only the folding (Model 1, Table 3.1). We interpret such fault geometry as overestimating the accommodated shortening but producing faults that are too shallow with too gentle dips. Faults penetrating deeper need lower amounts of input shortening and so accommodate more folding at the surface (Model 2, Figure 3.5). Model 2 is the best-fit solution in which

the model matches the observed topography and strain from folding, and so we take the modeled fault geometry as the best representation of reality. The smallest amount of input shortening, largest fault dip and deepest extent of fault produce equally good topographic matches, but the modeled strain from folding exceeds the observed strain (Model 3, Table 3.1). This model likely underestimates the accommodated shortening while producing very deep faults that dip too steeply.

3.4 Results

We applied our workflow and matched the two or, where possible, three controls to model the thrust systems of 55 shortening landforms on Mercury. From these models, 13 values were compiled to study the variability of these thrust systems. Additionally, thrust system type and overall fault shape (i.e., listric or homoclinal) was specified for each landform. We summarize our observation in a catalogue containing 30 lobate scarp and 25 wrinkle ridge archetypes. The summary of observations and individual MOVE models are published in the online repository accompanying this paper (Loveless et al., 2024b).

Thrust system types

Among the 55 landforms, we modeled thrust systems that can be described as having one of three general geometries. The most prominent thrust system type we model are *single*, *listric faults* (Figure 3.6a), with 38 shortening landforms showing this geometry. In these thrust systems, the depth and curvature of the fault dictate how the hanging wall is folded. The large variety of modeled listric fault shapes span the entire range of modeled fault parameters, accommodating small and large strains and lithospheric penetration depths from <10 km to as deep as ~50 km.

The remaining 17 modeled thrust systems have multiple faults. Of those, we modeled seven *imbricate thrusts* (Figure 3.6b). These are a series of sub-parallel thrusts for which tectonic transport is occurring in the same direction and that may be rooted by a floor-thrust or décollement (Boyer and Elliot, 1982). Such structures are known on Earth to consist of overlapping, stacked series of blocks of rock separated by subparallel thrust-faults (Hopgood, 1987). Imbricate thrusts were modeled to occur underneath shortening landforms that displayed vergence in the same or nearly the same direction and to be tectonically related by their geographic proximity to one another or by their map patterns. In some instances, the vergence may change along the length of the shortening landform resulting in possible changing thrust system geometries underneath the shortening landform. This phenomenon occurs at the shortening landform shown on the right panel of Figure 3.6b. Along the surface break towards the southwest, one of the shortening landforms changes vergence and thus may transition from an imbricate thrust to a pop-up structure.

Indeed, *pop-up structures* comprise the third thrust system type we identified, of which we modeled 10 of them. Pop-up structures were interpreted to occur under those shortening landforms that have two or more sets of tectonic vergence in opposite directions (Figure 3.6c). These pop-up structures host a central crustal block that has been uplifted due to two oppositely dipping thrust faults that border its sides, where the bigger structure is the primary thrust and the smaller structure the secondary or back thrust (Butler, 1987). Generally, pop-up structures on terrestrial planets are found to vary in terms of the size relation of the primary thrust and secondary thrust. Most pop-up structures we model on

Mercury, however, show a primary thrust that greatly exceeded the size of the back thrust in terms of fault depth and height, similar to the example in Figure 3.6c.

Comparison between shortening landform archetypes

We average all of the parameters generated by the modeled shortening landforms in this work (Table 3.2). Across all structures, the average near surface fault dip, average dip, and maximum dip are 21°, 22°, and 40°, respectively. The average input shortening for all shortening landforms is ~1.5 km. The mean values for average heave, average slip, maximum slip, and average throw are 1.2 km, 1.4 km, 1.6 km, and 0.6 km, respectively. The average depth of faulting across all shortening landforms is 21.9 km and the average fault height is 65.4 km. The sample of shortening landforms in this work produced a modeled strain from folding of –0.28%.

We compiled the parameters of our models to analyze their averages and variability for the wrinkle ridge (n = 25) and lobate scarp archetypes (n = 30) for their comparison. First, we averaged each parameter for each archetype landform to identify what defines a typical lobate scarp and wrinkle ridge on Mercury; the results are presented in Table 3.2. The representative thrust fault architecture underlying a lobate scarp archetype is a single, listric thrust fault that shallows with depth (e.g., Figure 3.5 Model 2; Figure 3.6a). These shortening landforms have an average dip of $\sim 26^{\circ}$ and fault to depths of ~ 27 km. The faults accommodate an average of ~ 2 km of slip and produce an average of $\sim 0.4\%$ of modeled shortening strain from folding in the hanging wall.

The typical trust system underlying a wrinkle ridge archetype requires more than one fault, either as imbricate thrusts (Figure 3.6b) or pop-structures (Figure 3.6c). The most representative wrinkle ridge archetype model is shown in Figure 3.6c. Such shortening landforms are underlain by faults with an average dip of ~19° that penetrate to depths of

 \sim 13 km. These structures accommodate an average slip of \sim 0.7 km and produce an average of \sim 0.16% of modeled shortening strain from folding in the hanging wall.

Second, we compute box-and-whisker plots for the aspect ratio, depth of faulting, the maximum and average dip angles, the maximum and average slip, the input shortening, and the shortening strain from folding (Figure 3.7) to document and compare the variability of the fault geometries associated with wrinkle ridge and lobate scarp archetypes on Mercury. We find that these parameters capture all aspects of modeled fault geometries. As with Figure 3.4, the bold lines within the boxes indicate the median value for each distribution, whereas the upper and lower bounds of the boxes are the first and third quartile values of each distribution. Minima and maxima data are indicated by the bounds of the line segment. Statistical outliers are shown as hollow dots along the axis.

The majority of aspect ratios for both wrinkle ridge and lobate scarp archetypes fall between 0.1 and 0.6 (Figure 3.7a). The average aspect ratio among all shortening landforms is 0.4. The range of aspect ratios for lobate scarp archetypes is from 0.1 to 1.3. Wrinkle ridge archetypes have an aspect ratio range of 0.1 to 1.4. Both archetypes show large overlap, but generally lobate scarp archetypes have higher aspect ratios as a result of their greater relief with respect to their lengths than wrinkle ridge archetypes do. We also find that lobate scarp archetypes penetrate to greater depths than their wrinkle ridge archetype counterparts (Figure 3.7b). Lobate scarp archetypes host faults that penetrate to depths of 8.4 km to 48 km, whereas the range of wrinkle ridge archetypes depth of faulting spans from 1.9 km to 38 km. These ranges of depths are nearly identical as only 6 lobate scarp archetypes are modeled to fault at depths greater than 38 km and only 7 wrinkle ridge archetypes are modeled to fault at depths less than 8.4 km.

Lobate scarp archetypes host faults with a median maximum and a median average dip of 43° and 24° respectively (Figure 3.7c and d). Wrinkle ridge archetypes dip more shallowly than lobate scarp archetypes with a median maximum dip of 36° and a median average dip of 17°. The range for both maximum and average dip values overlap for both wrinkle ridge and lobate scarp archetypes. The maximum dip angle for lobate scarp archetypes ranges from 21° to 66° and wrinkle ridge archetype maximum dip angles ranges from 16° to 60° (Figure 3.7c), almost covering the same range of dip angles.

For both maximum and average slip values, wrinkle ridge archetypes overlap with the lower extent of lobate scarp archetype values (Figure 3.7g and h). A similar trend is shown in the ranges of input shortening values for wrinkle ridge and lobate scarp archetypes, where wrinkle ridge archetypes overlap with the lower extent of lobate scarp archetype values. The modeled strain from folding for wrinkle ridge and lobate scarp archetypes also demonstrates considerable overlap (Figure 3.7h). More negative values of modeled strain from folding indicate a greater amount of folding. Wrinkle ridge archetypes show less modeled shortening strain from folding than lobate scarp archetypes, but almost the entire range of wrinkle ridge archetype values falls within the lower range of modeled strain from folding values for lobate scarp archetypes.

The largest shortening landform on Mercury: Enterprise Rupes

Enterprise Rupes is widely regarded as one of the largest shortening landforms on Mercury's surface (e.g., Byrne et al., 2018; Ferrari et al., 2015; Watters et al., 2016) so we include it in our analysis (Figure 3.8a). Its highest vertical relief exceeds 3 km, and it has a mapped fault length of ~1000 km (Loveless et al., 2024a). Owing to its size, Enterprise Rupes was statistically classified with the highest lobate scarp designation in *Chapter 2*.

Enterprise Rupes is located in the southern hemisphere and crosscuts multiple impact craters including Rembrandt Basin: a large, 715 km diameter impact basin. Its highest structural relief towards the southeastern portion of its surface break. In this region, Enterprise Rupes is unaffected by large impacts or the geology of the Rembrandt basin, which is host to other smaller impacts, extensional and contractional tectonic features, thus providing an ideal cross-section to model the subsurface structure solely as it relates to the underlying fault architecture.

Northwestward along the surface break, there are notable topographic highs that are likely unrelated to the deformation produced by the primary fault that formed Enterprise Rupes. To better constrain the shortening strain of Enterprise Rupes, we subtract these topographic variations from the observed topography (light blue line, Figure 3.8b). The displacement and strains generated by our model can therefore be assumed to be a lower bound for the possible displacements and strains. In this region, the morphology of Enterprise Rupes indicates two fault surface breaks and forelimbs with opposing vergence. The primary direction of tectonic transport along Enterprise Rupes is towards the southeast, as indicated by the pronounced forelimb along much of the structure and the multiple impact craters that Enterprise Rupes crosscuts.

The vertical relief at this area has been measured to be 3.3 km (Loveless et al., 2024a). The backlimb beyond the pop-up created by the oppositely verging thrust is also uplifted. To achieve such relief, a model input of 9 km of shortening was applied to the main thrust. The role of the secondary thrust only affects the peak at the tip of the shortening landform. The input shortening for this thrust was 2.7 km. These input shortenings for the primary and secondary thrusts translated to a maximum slip value of

9.3 km and 2.7 km, respectively. The primary fault has an average dip of 9° and a maximum dip of 17°. The secondary fault has an average dip of 11° and a maximum dip of 21°. The lower average dip angles are because of the extensive listric architecture of the fault geometry. We model Enterprise Rupes to fault to a depth of 34 km. The modeled strain from folding for Enterprise Rupes is –0.13, which is less than the median value of –0.34 found among lobate scarp archetypes (Figure 3.7h). However, the maximum slip, average slip, and slip components (average heave and throw) for Enterprise Rupes are, unsurprisingly, the largest values modeled in our data set.

3.5 Discussion

Lobate scarp and wrinkle ridge archetype thrust systems

We modeled the subsurface structure of 55 shortening landforms on Mercury to learn about the thrust systems that generated them. The results of our study show a large variation of fault geometric parameters (Figure 3.7). This finding demonstrates that thrust systems on Mercury are complex and host a large variation of thrust geometries, similar to what is observed in thrust systems on Earth. Based on a linear discriminant analysis of the shapes of these landforms (*Chapter 2*), we selected those shortening landforms for our modeling that showed the biggest differences to one another with the intention of analyzing the broadest variation of thrust system morphologies that occur on Mercury's surface. We interpret the large variation of dip angles, depth of faulting, and slip as indicative of highlighting the innate complexities of Mercury's thrust systems.

The morphology of shortening landforms on Mercury supports wrinkle ridges and lobate scarps as endmember categories on a spectrum of shortening landforms (*Chapter 2*). The results in this study provide additional support for these as archetypes as the average

values for all shortening landforms consistently lie between average parameter values for the archetypes (Table 3.2). In addition, the distributions of fault parameters of wrinkle ridge and lobate scarp archetypes either overlap or form a continuum, as seen in the first and third quartile values of wrinkle ridge archetypes beginning or ending where those of lobate scarp archetypes end or begin (see position of boxes in Figure 3.7).

The most notable difference between archetype types is the *number* of faults, and the least amount of overlap occurs in the *depth* of faulting. A typical lobate scarp archetype was modeled using one listric thrust fault that penetrated to depths of ~ 27 km (e.g., Figure 3.6a) whereas a typical wrinkle ridge archetype was modeled with 2 faults (Table 3.2) and penetrates only to depths of ~13 km (e.g., Figure 3.6c). The differences between wrinkle ridge and lobate scarp archetypes are likely to arise differences in host lithology. Most of the wrinkle ridge archetypes in this study are situated in the smooth plains units, whereas most of the lobate scarp archetypes are located in the intercrater plains units (Figure 3.2). Regardless, with an average depth of faulting of 13 km, wrinkle ridge archetypes penetrate deeper than estimates of up to 2 km for the depth of the volcanic emplacements that make up the smooth plains units (Du et al., 2020; Head et al., 2011; Ostrach et al., 2015). This geometry suggests that the mechanisms that produce lobate scarp and wrinkle ridge archetypes are the same. However, geographically, the lithosphere underlying the smooth plains units may have hosted very deeply penetrating thrust faults, the surface expression of which would have been muted by the subsequent emplacement of relatively well-layered smooth plains. These newer mechanical layers were not present in the intercrater plains, and such faulting underneath the smooth plains lava emplacements may have been reactivated upward, creating the shortening landforms observed in these units without slip

occurring at deeper depths. When a geologically younger, thin unit of rock is placed on top of a faulted rock volume and is then mechanically faulted through, more complex deformation in the upper layer is caused by the basement-reactivated fault.

Both endmember types vary widely in subsurface geometry, with some wrinkle ridge archetypes being modeled with single faults and some lobate scarp members hosting multi-fault thrust systems. These results illustrate further that the "typical" archetype lobate scarp and wrinkle ridge structures show some differences, but that the spectrum of thrust architecture underlying both of these landform types shows substantial overlap. These findings echo those of *Chapter 2*, further corroborating that shortening landforms on Mercury's surface exist on a spectrum between the traditional nomenclature of lobate scarps and wrinkle ridges.

Tectonic architecture of thrust systems on Mercury

All shortening landforms in this study are underlain by listric faults (e.g., Figure 3.6). The typical lobate scarp archetype structure contains only a single, listric fault. Shortening landforms that are modeled with more than one fault may either be constructed with multiple listric faults, or the secondary (and possibly tertiary) faults may have a more homoclinal geometry (e.g., the secondary faults in Figure 3.6c and Figure 3.8). The listric geometry of the fault is what dictates the shape of the overlying topography in a fault-bend fold. When comparing lobate scarps on Mercury with tectonic deformational features on Earth, Byrne et al. (2018) had described lobate scarps "as upthrust volumes of rock that are likely the folded portions of hanging walls atop of thrust faults." This analogy describes lobate scarps that have formed from surface breaking thrusts on Mercury as fault-bend folds.

Previous studies using the COULOMB dislocation modeling found listric faults to be a viable architecture underlying contractional tectonics on terrestrial planets (e.g., Peterson et al., 2020; Watters and Schultz, 2002). However, these studies also show that listric faults and homoclinal faults generate similar topography, suggesting non-unique solutions. Other studies using the same modeling technique have argued that listric faults fail to accurately generate observed topography (e.g., Egea-González et al., 2012; Herrero-Gil et al., 2019). This modeling technique does not consider folding. If the hanging wall is faulted over the footwall at the surface, it will likely fold over the fault. By using a fault-bend-fold geometry, our models replicate this folding. In a fault-bend-fold model, the listric shape of the underlying fault greatly affects the way the surface folds after the input shortening is applied. The change in dip along a listric geometry affects the displacement along the fault as governed by the same trigonometric relationships described by a rampup structure in Suppe (1983).

A typical archetype wrinkle ridge structure requires two or more faults to accurately replicate topographic observations (Figure 3.7c). Pop-up structures are more common than imbricate thrusts for multi-fault thrust systems used to model wrinkle ridge archetypes. For wrinkle ridge archetypes, we see that the folding of the hanging wall produced by the pop-up structure creates a plateau flanked on either side by monoclines that are folded over their fault plains. This agrees with previously proposed structural interpretations of wrinkle ridges (Byrne et al., 2018). Slope-asymmetry analysis of wrinkle ridges on Mars supports similar geometries (Okubo and Schultz, 2004). These Martian wrinkle ridges are the accumulation of a primary thrust and secondary back and fore thrusts that branch off the primary thrust. We find some similar subsurface geometries for shortening landforms with

opposing thrust-fault vergence. However, the wrinkle ridge archetypes on Mercury described here have greater relief than the Martian landforms analyzed in Okubo and Schultz (2004). We also find simpler fault architectures to be able to replicate many of our wrinkle ridge archetypes than some of the geometries suggested by Okubo and Schultz (2004). Additionally, contractional tectonics on Earth that result in a hanging-wall folding over the thrust and footwall (e.g., Last et al., 2012; Petterson et al., 1997) are frequently used as analogous structures for contractional tectonics on other terrestrial planets (e.g., Crane, 2020b; Crane and Klimczak, 2019a; Plescia and Golombek, 1986; Watters, 1988). The results presented here then suggest that fault-bend fold architectures should be further utilized when structurally assessing contractional tectonics in Mercury's smooth plains.

Imbricate thrust structures are the least common fault geometry we model in our sample of shortening landforms. Only two lobate scarp archetypes and five wrinkle ridge archetypes were modeled as imbricate thrusts. The small sample size of multi-fault lobate scarp archetypes is likely a result of the sample selection process, as the LDA in *Chapter 2* classified the most endmember lobate scarps by their larger sizes. The size of these structures may be indication that the faults matured to the point that previous imbricate thrusts linked into a large singular fault plane, indicative of how Cowie and Scholz (1992) suggest faults grow within the Earth's lithosphere. Alternatively, more shortening landforms occupy the geologically younger smooth plains than the geologically older intercrater plains units (Byrne et al., 2014). The concentration of shortening landforms in the smooth plains attests to the greater number of shortening landforms we modeled in the smooth plains to host more than one fault in the underlying structure. However, many shortening landforms on Mercury display multiple sub-parallel to parallel surface breaks

similar in photogeology to the imbricate thrusts modeled here (e.g., Crane and Klimczak, 2019a). Expanding the sample size of this work may then increase the shortening landforms in the intercrater plains units.

Implications for Mercury tectonics

Many studies use the vertical relief of a structure as equal to the throw of the underlying fault to infer the displacement along the fault plane (e.g., Byrne et al., 2014; Klimczak et al., 2018; Watters, 2021; Watters et al., 2001). Friction theory predicts optimal dip angles for thrust faults in a basaltic rock volume to be ~31° and thus displacements are typically inferred for angles of 30°±5°. Results of our analysis show that the average and maximum dip angles of thrust faults on Mercury are $\sim 22^{\circ}$ to $\sim 40^{\circ}$, respectively (Table 3.2). This is a larger range of dip angles of thrust faults than used previously, including thrust faults with much shallower and steeper dips. Our results thus warrant considerations of a wider range of dip angles for any analysis inferring thrust fault displacements from measurements of structural relief. Using the traditional method of deriving shortening strain for planetary thrust faults (e.g., Byrne et al., 2014; Watters, 2021), an average dip value of ~22° would increase previous estimates of Mercury's global strain whereas an angle of 40° would reduce strain estimates (e.g., Byrne et al., 2014; Watters 2021). The larger range of dip angles found in this study suggests that previous assumptions of the range of dip angles for Mercury's population of thrust faults yielded a too narrow range of strain estimates.

Enterprise Rupes is a shortening landform that Galluzzi et al. (2015) assessed with crosscut craters. They found a large range of dip angles for the faults underlying Enterprise Rupes, ranging from $15^{\circ}\pm5^{\circ}$ to $57^{\circ}\pm16^{\circ}$, which agrees well with our range of modeled dips.

Our results indicate that Enterprise Rupes has an average dip angle of $\sim 10^{\circ}$ and a maximum dip of 21° close to the surface, agreeing well with the lower estimates of two of the three crosscut craters near our transect. However, the crater evaluated by Galluzzi et al. (2015) that is closest to our transect has the steepest dip angles. This mismatch may be due to the degradational state of this crater or to the natural complexity of the fault system in this area. Galluzzi et al. (2015) consider a single fault when assessing the deformation of this crater, while multiple faults are required to match the map pattern and topography of Enterprise Rupes. If this crater was deformed by two opposing faults, this may explain the mismatch between the two analyses.

A second shortening landform in our study also crosscuts a crater assessed by Galluzzi et al. (2015) (their Crater 05-C). We find a near-surface dip angle and average dip angle of 29° and 30° , respectively, which is relatively close to the dip angle range of $20^{\circ} \pm 3^{\circ}$ reported in Galluzzi et al. (2015). The discrepancies of our results may be due to the fact that a crosscut crater only captures the local, near-surface dip of the fault. Our modeling efforts capture the broader structure and take into account the topography beyond the extent of the crater.

The mean of the average dips for our modeled lobate scarp archetypes averages at \sim 27° for all models. This value agrees with previous modeling results of individual or small sets of shortening landforms (e.g., Egea-González et al., 2017, 2012; Schultz and Watters, 2001). The mean of the maximum dips for lobate scarp archetypes is \sim 43°, with a few individual structures even showing maximum dips of \sim 60° (Figure 3.7c), which is rather atypical for thrust faults. However, our wrinkle ridge archetypes have an average dip of \sim 19°. This value is considerably less than the range of dip angles found in COULOMB

dislocation modeling efforts by Peterson et al. (2020). Multiple models constructed in Peterson et al. (2020) were shown to produce similar topographies for the same shortening landform and listric fault geometries were created by using a step curvature function from one fault tip to the other. In our study we find that folding at the surface plays a substantial role in dictating the depth and dip angle of our faults. The COULOMB modeling software cannot take into account distortion from folding and instead assumes fully elastic deformation around the fault from a single faulting event, scaled up to the shape of the landforms after many slip events, which becomes unrealistic for the large displacements associated with these shortening landforms. This limitation in COULOMB is likely the reason for the discrepancy in dip angles for wrinkle ridge archetypes in the two approaches.

Our models indicate a wide range of depths of faulting for all shortening landforms. The average depth of faulting for all modeled shortening landforms is ~22 km and shortening landforms inside the intercrater plains fault to an average depth of ~27 km. Intercrater plains likely are composed of a brittle volume of basaltic crust that may act as a single mechanical unit. The greatest penetration depths we find extend to ~48 km (Figure 3.7b), suggested that the faulted volume of Mercury's lithosphere reaches depths perhaps as much as 50 km. Previous studies that have investigated the depth extent of faulting for shortening landforms on Mercury provide similar values, such as 25–40 km for faults in the intercrater plains (e.g., Egea-González et al., 2012; Ritzer et al., 2010; Watters and Schultz 2002).

Alternatively, the basaltic lava emplacements of the smooth plains units are only estimated to be only a few hundred meters to up to ~2 km thick and they sit on top of basement rock (Du et al., 2020; Head et al., 2011; Ostrach et al., 2015). The modeled

average depth of faulting of 13 km for the wrinkle ridge archetypes in this study greatly exceeds these thickness estimates. This model depth indicates that many of the modeled wrinkle ridge archetypes are not by any measure constrained to within the smooth plains units. Previous work has also suggested that smooth plains structures can fault to comparable depths to intercrater plains structures (e.g., Peterson et al., 2020). In these geographic regions, Mercury's lithosphere is composed of volcanic deposits overlaying mechanically weak layers of rock due to impacts. Therefore, there are likely multiple mechanical interfaces of different deformed basaltic layers, and so the terms thin and thickskinned tectonics as described for Earth's tectonics by Pfiffner (2017) are likely an inaccurate way to structurally describe Mercurian tectonics. However, we find that these faulting depths for wrinkle ridge archetypes agree with the term "basement involved thinskinned tectonics" attributed to Mercury's tectonics by Crane and Klimczak (2019a). In this case, the deformation in the smooth plains units are influenced by the faulting in the underlying basement rock such that deformation in the basement produces a series of structural geometries and patterns in the smooth plains that are characteristic of thinskinned deformation. Many of our wrinkle ridge archetype models are consistent with basement involved thin-skinned tectonics, where, for example, pop-up structures that reside in the smooth plains units typically contain a primary fault that penetrates 10 km below the surface but the secondary fault only penetrating no deeper than ~ 3 km (Figure 3.6c). In a 2–3 km thick smooth plains units, then, these secondary faults may be the result of more complex deformation occurring solely within these unit but that connect to, and were initiated by faulting at depth, in the underlying basement rock. The mechanically distinct plains units may then partition strain off of the primary, deeply rooted thrust,

resulting in additional faults and folds that are only confined to the smooth plains units. This is similar to the process described by Crane and Klimczak (2019a) for contractional tectonics in Mercury's smooth plains units where thrusts rooted in the underlying lithosphere causes deformation in the overlying, mechanically-weak layer.

Wrinkle ridges in the smooth plains units on Mercury have been compared with shortening structures in the lunar maria, with those landforms on the Moon being ascribed to loading-induced subsidence with contributions from global contraction (Schleicher et al., 2019). However, loading-induced subsidence is inconsistent with basement-involved thin-skinned thrust tectonics and a formation of such structures on Mercury by global contraction alone is more plausible. In fact, thrust faults underlying shortening landforms described as wrinkle ridges found in several mare units in lunar mascon basins are found to be deep-seated (Byrne et al., 2016; Collins et al., 2023). Their origin is ascribed to mascon tectonics (Byrne et al., 2015), and their continued growth and surface expression in the surficial mare units did not require loading stresses from the mare units whereas contributions of stresses from the lunar global contraction are plausible (Byrne et al., 2015).

We do not detect a systematic pattern of the distribution of shortening strains across Mercury, albeit wrinkle ridge archetypes tend to produce somewhat less strain than lobate scarp archetypes. However, the variance of shortening strain from wrinkle ridge archetypes and lobate scarp archetypes overlaps substantially (Figure 3.7f). These findings agree with previous studies that observed geologic trends in morphology and timing (e.g., Banks et al., 2015; Crane and Klimczak, 2019a; Peterson et al., 2019). If global contraction were the source of stresses driving faulting, there would be no systematic pattern of strain distribution expected, even if it overlapped with other processes. Other processes that have

been invoked for Mercury to produce global fracture patterns like despinning (e.g., Matsuyama and Nimmo, 2009; Melosh, 1977) or reorientation (Matsuyama and Nimmo, 2009) would only influence the orientation of fracture patterns (Klimczak et al., 2025) when working in conjunction with global contraction. However, the shortening strain of the landforms likely would not have a global systematic pattern if global contraction is the primary source of stresses to cause faulting.

3.6 Conclusions

We investigated the thrust fault geometries beneath 55 shortening landforms on Mercury. We specifically selected wrinkle ridge and lobate scarp archetypes to highlight the differences in thrust system geometries that are present within Mercury's lithosphere. We find that while Mercury hosts diverse thrust systems, including single, listric faults, imbricate thrusts, and pop-up structures, the thrust fault geometries of wrinkle ridge and lobate scarp archetypes overlap or form a continuum (Figure 3.7). This overlap and continuation in range of fault geometric parameters confirm our previous results (*Chapter 2*), where shortening landforms on Mercury form a spectrum of landform shapes rather than discrete categories. The results of the work presented here further illustrates the impracticality of traditional "lobate scarp" and "wrinkle ridge" nomenclature to describe landforms that are much more similar than they are different.

We find a large range of fault geometric parameters for the thrust systems that underly Mercury's shortening landforms. The average fault dip of all the structures ranges from \sim 22° and to \sim 40°. We also find that the deepest fault penetrates Mercury's lithosphere to 48 km, whereas the average depth of faulting for all studied structures is 22 km. These

parameters may serve to better constrain future studies estimating fault strain or analyzing lithospheric structure on Mercury.

Our modeling results inform an understanding of Mercury's tectonic character. The shortening landforms that reside in Mercury's smooth plains units are likely caused by the basement involved thin-skin tectonics mechanism suggested by Crane and Klimczak (2019a), with thrusts penetrating well below the lavas that makeup the smooth plains units. As the faults penetrate deep into the underlying basement rock and show no noticeable difference in strain compared with faults in intercrater plains, the formation of these thrusts by loading-induced subsidence can be ruled out and instead are likely to have been primarily driven by global contraction.

3.7 Acknowledgements

The research presented here was funded by NASA's SSW program under grant 20-SSW20-0153. We make use of 14 MESSENGER products available on the PDS Geoscience Node in the MDIS archive specifically in node PDS3 and in the MLA archive in node PDS4. We thank PE Limited (Petex) for their donation of academic licenses of the MOVE modeling software to the University of Georgia. We thank Dr. Steven Holland and Dr. Robert Hawman for their valuable revisional contributions.

3.8 Data availability

The supplementary material for this research is available on Mendeley Data at Loveless et al. (2024b): https://data.mendeley.com/datasets/k4yrmr5j6k/1.

3.9 Figures

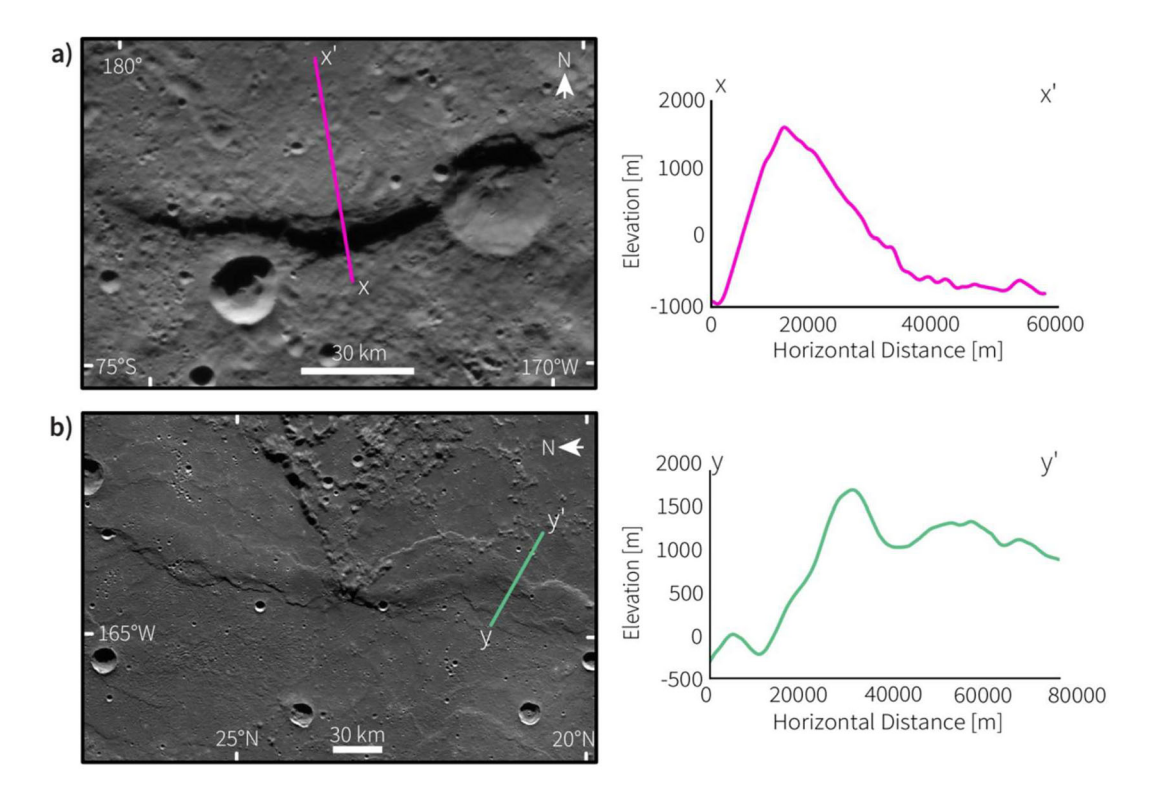


Figure 3.1: Examples of what have been classified as "!abate scarps" (a) and "wrinkle ridges" (b) on Mercury (modified from Chapter I). a) Map view of an unnamed !abate scarp near the south pole (left) with the corresponding topographic profile from x to x' (right). b) Map view of Schiaparelli Dorsum, a prominent wrinkle ridge (left) with the corresponding topographic profile from y' (right). Maps use a stereographic projection centered on the shortening landform. Both profiles are shown at ~J 6x vertical exaggeration.

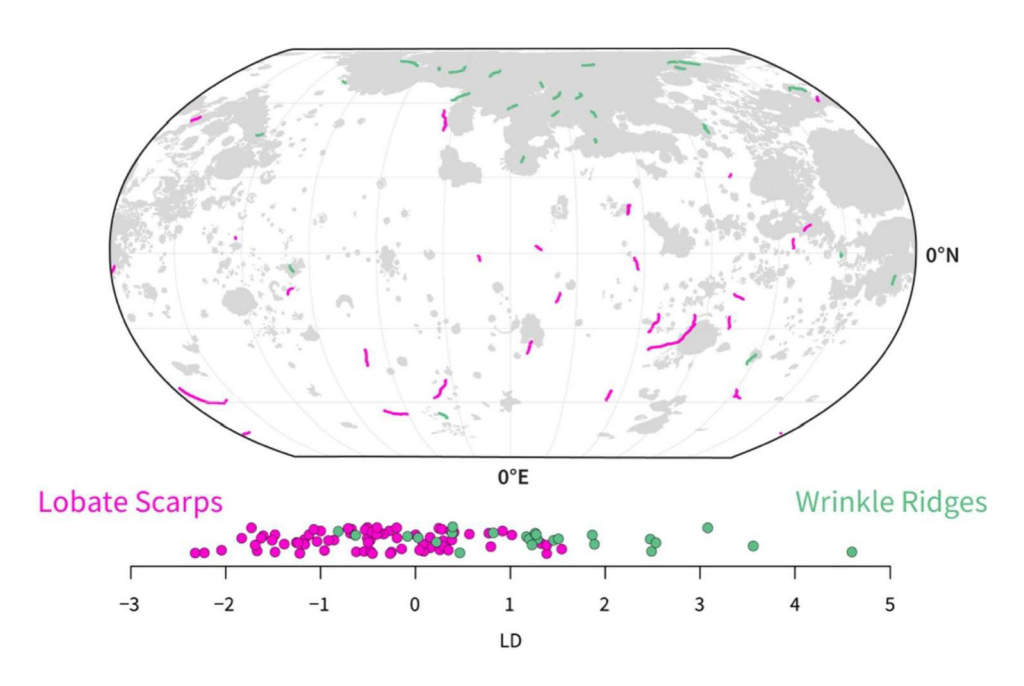


Figure 3.2: Global distribution of 55 shortening landforms modeled in this study shown in Robinson projection. Landforms traditionally identified as !abate scarps are shown in magenta, while those previously identified as wrinkle ridges are shown in green. For reference, the smooth-plains units (Denevi et al., 2013) are shaded in gray. The LDA analysis of the 100 shortening landforms assessed in Chapter 2 is shown on the LD axis below.

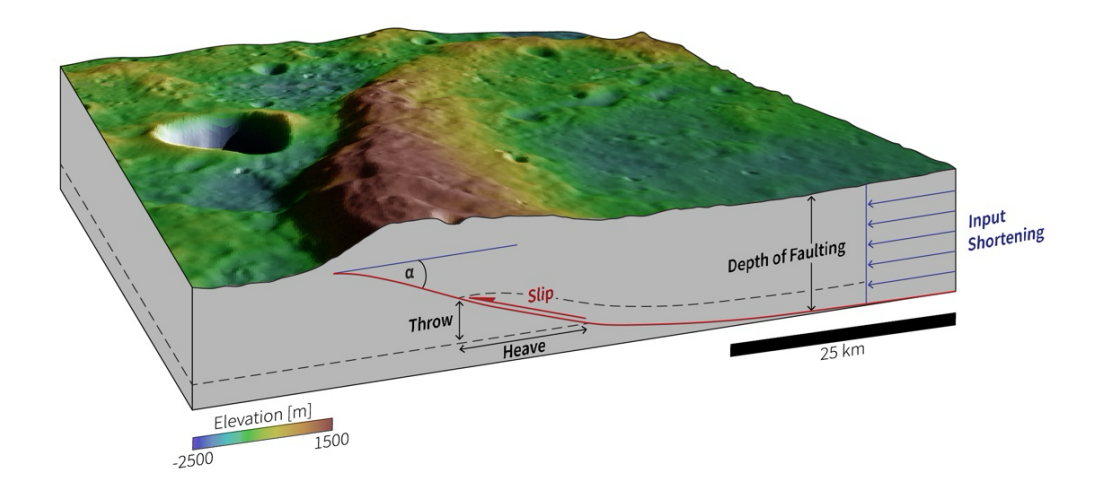


Figure 3.3: Block diagram of a shortening landform with stylized fault plane to highlight the fault geometric parameters extracted from each model. The dashed line in the subsurface represents an arbitrary marker horizon to depict deformation along the fault. The image in this figure is taken from the MESSENGER low-incident angle global mosaic (Denevi et al., 2017). Elevation data are from Bertone et al. (2023).

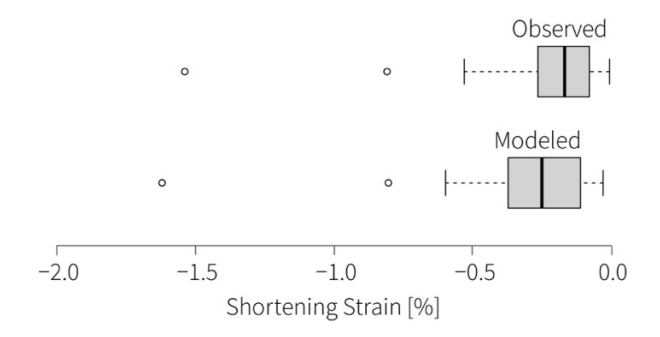


Figure 3.4: Box and whisker plot of the observed strain from folding compared with the modeled strain from folding. Bold lines indicate the median, the left and right edges of the gray box are the first and third quartiles, and maxima and minima are indicated by the vertical segments. Outliers are shown as dots.

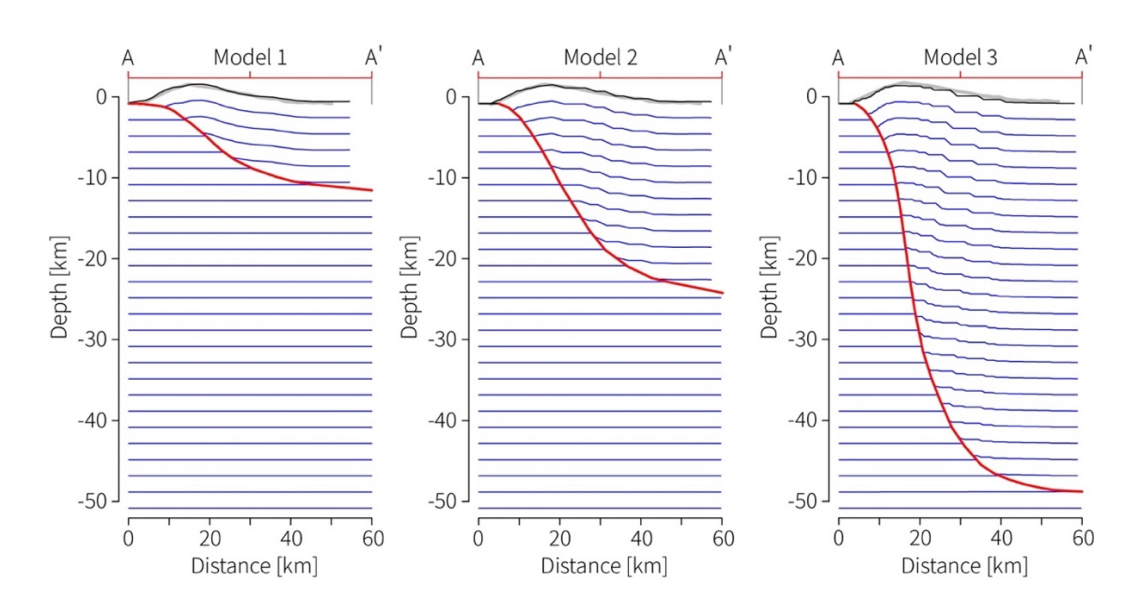


Figure 3.5: Three thrust fault models replicating the topography of the shortening landform depicted in Figure 3.3. All models are shown with 2× vertical exaggeration. Red line is the modeled fault. Blue lines are arbitrary horizons used to visualize subsurface deformation. Gray lines are observed topography; black, the modeled topography.

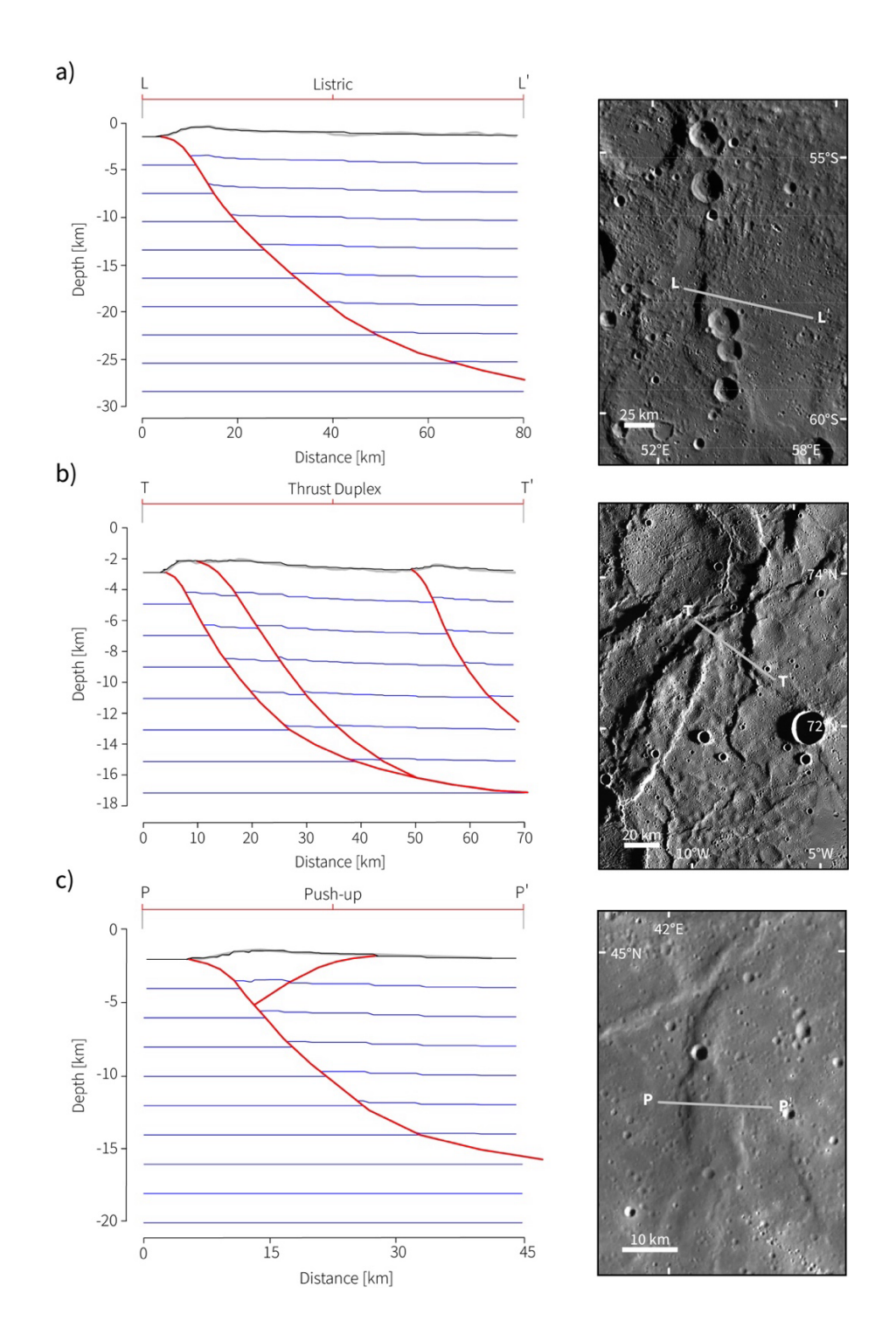


Figure 3.6: Three different thrust fault systems from Mercury with subsurface models shown on the left and map view on the right panel. a) An example of a single, listric fault $(1.8 \times \text{vertical exaggeration})$. b) An imbricate thrust $(3.0 \times \text{vertical exaggeration})$. c) A

pop-up structure (1.8 \times vertical exaggeration). Model line colors are the same as in Figure 3.5.

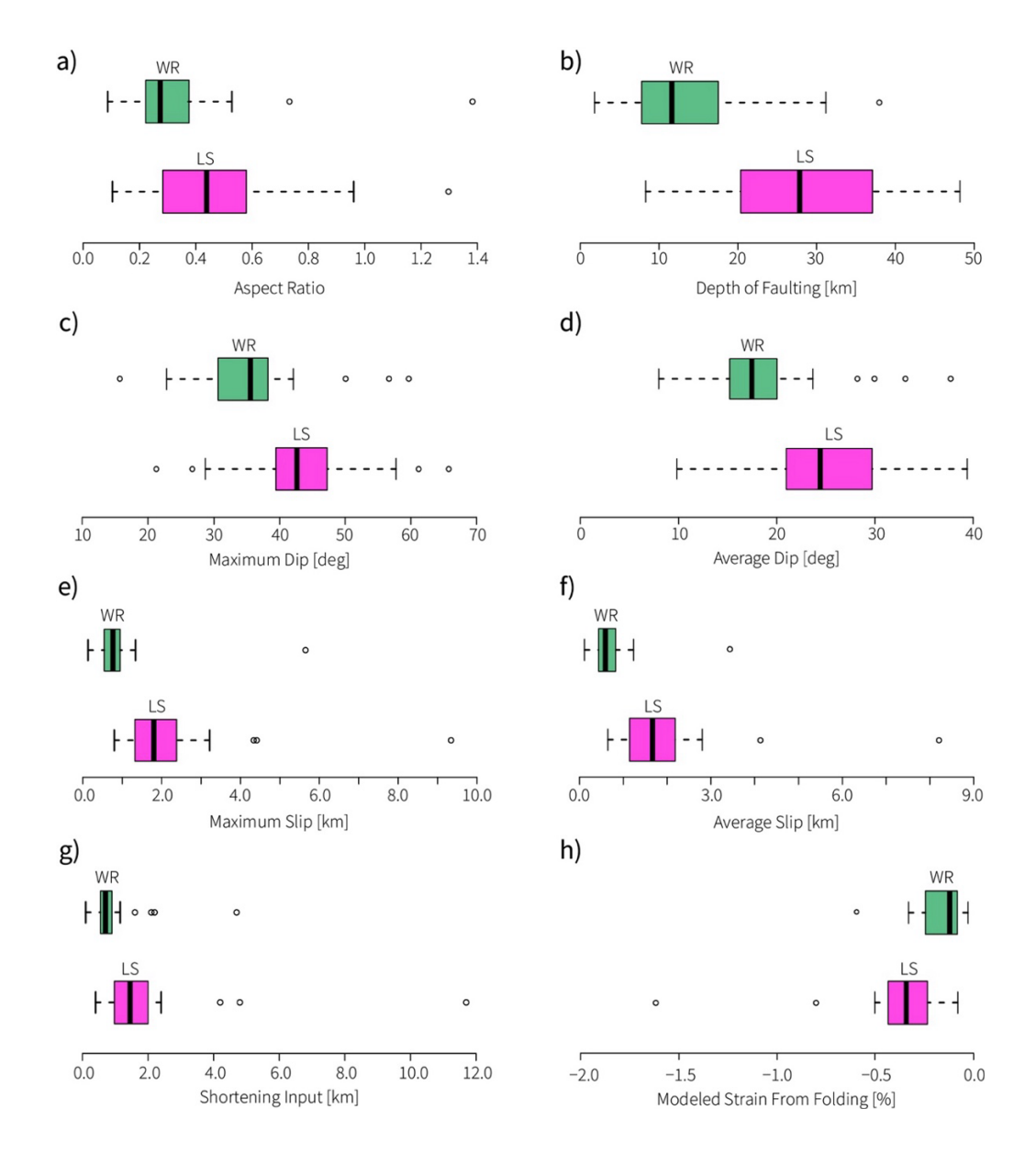


Figure 3.7: Box-and-whisker plots for eight parameters of our model solutions, showing the distributions of fault geometries of wrinkle ridge and lobate scarp archetypes on Mercury. These plots show comparisons of: (a) aspect ratios; (b) depth of faulting; (c) maximum dip; (d) average dip; (e) maximum slip; (f) average slip; (g) input shortening; (h) modeled strain from folding.

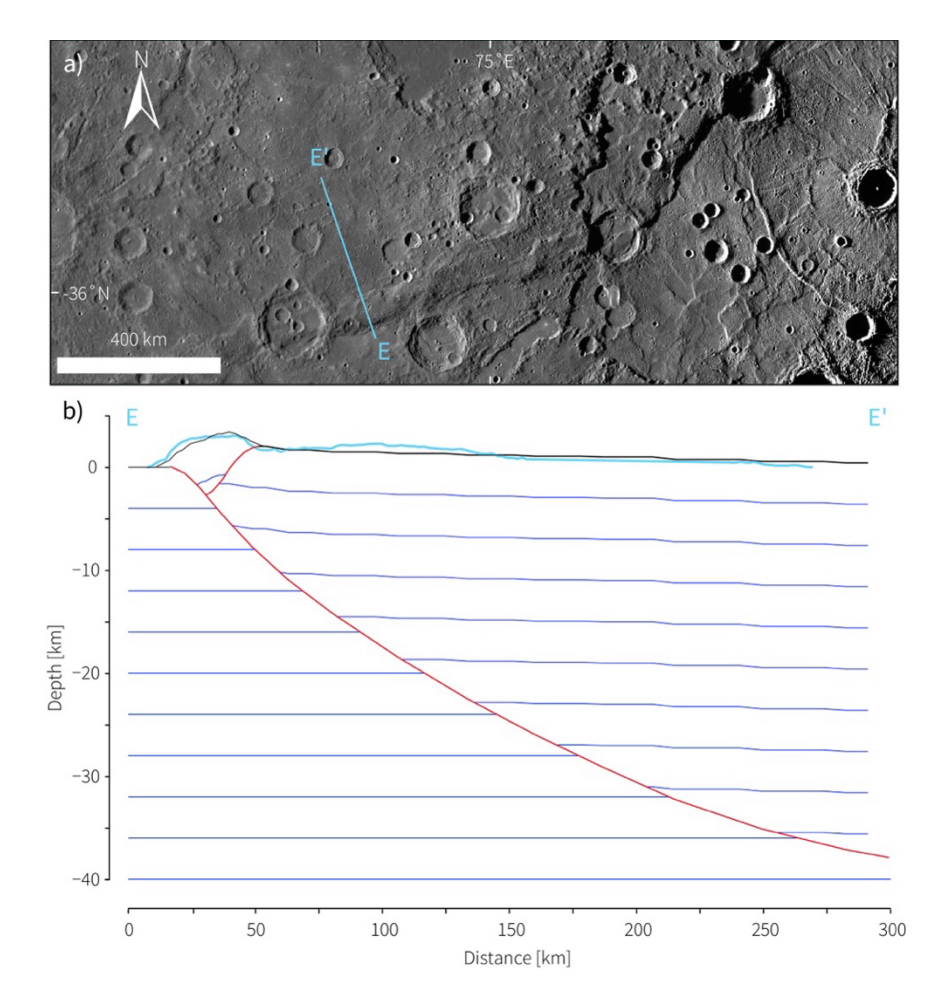


Figure 3.8: Top panel depicts the photogeology of Enterprise Rupes. Bottom panel depicts the model constructed underneath the transect E to E' in the image. Color coding is the same as in Figure 3.5 but observed topography corrected for anomalous topographic variations is shown in light blue. Model and topography in $4 \times VE$.

3.10 Tables

Table 3.1: Comparison of parameters for the three subsurface models of the same shortening landform in Figure 3.4. Input shortening is a constraint of the model.

Parameters	Model 1	Model 2	Model 3
Observed Folding Strain [%]	-0.81	-0.81	-0.81
Modeled Strain from Folding [%]	-0.62	-0.80	-1.36
% of Match Modeled to Observed Folding Strain	77.2	99.4	31.9
Input shortening [km]	5.5	2.4	0.9
Depth of Faulting [km]	11.4	24.2	48.1
Average dip [°]	9	21	40
Maximum slip [km]	5.9	3.2	2.3

Table 3.2: Averaged values of modeled parameters for lobate scarp and wrinkle ridge archetypes. Medians and ranges of these modeled parameters are shown in Figure 3.7.

Modeled Parameter	All Shortening	Lobate Scarp	Wrinkle Ridge	
	Landforms	Archetypes	Archetypes	
Near Surface Fault Dip (°)	21	25	17	
Average Dip (°)	22	26	19	
Maximum Dip (°)	40	43	36	
Input shortening (km)	1.5	2.0	1.0	
Average Heave (km)	1.2	1.7	0.7	
Average Slip (km)	1.4	2.0	0.7	
Maximum Slip (km)	1.6	2.2	0.9	
Average Throw (km)	0.6	0.8	0.3	
Depth of Faulting (km)	21.9	27.4	13.3	
Fault Height (km)	65.4	90.0	64.5	
Modeled Strain from	0.200/	0.200/	0.16	
Folding (%)	-0.28% -0.39%		-0.16	
Number of Faults	1.36	1.12	1.7	
Aspect Ratio	0.41	0.44	0.28	

CHAPTER 4

SEVERAL KILOMETERS OF GLOBAL CONTRACTION ON MERCURY: A SAMPLE-SIZE INDEPENDENT ASSESSMENT OF FAULT STRAIN.³

³ Loveless, S.R. and Klimczak, C. Submitted to AGU Advances, 2025.

Abstract

Mercury underwent global contraction due to the sustained cooling of the planet. Positive-relief landforms, found widespread across Mercury, are thought to be the surface expressions of thrust faults accommodating the contraction. Disagreement exists in the literature on the amount of contraction, with estimates of radius change ranging from ~1 to 7 km. These differences solely arise from the method used to estimate the fault population strain, which relies on the number of structures. Here, we adapt previous framework by which the continuum approximation to shortening strains can be determined from fault length and displacement statistics for an incompletely sampled fault population. We apply this method to three datasets that sample different numbers of faults. Our results show that even for conservative fault parameters, two to three kilometers of radial contraction are returned, irrespective of the dataset used, and thus resolving the debate on the amount of global contraction on Mercury.

4.1 Introduction

Disagreement on Mercury's radial contraction.

Thermal evolution models and observations of Mercury's surface indicate that the planet has undergone global contraction, a process caused by long, sustained planetary cooling (e.g., Solomon, 1978). Shortening strain from global contraction is widely accepted to be accommodated in the lithosphere via thrust faulting, which manifest at the surface as positive-relief landforms (Byrne et al., 2018, 2014; Solomon et al., 2008; Strom et al., 1975). Previous studies measured the length and relief of these shortening landforms to estimate the total contractional strain of Mercury (Di Achille et al., 2012; Byrne et al., 2014; Watters and Nimmo, 2010; Watters et al., 1998). These previous studies rely on the same method, by which a map of thrust fault related landforms is produced, lengths of the landforms are extracted, relief of a subset of structures is measured and assumed to be related to fault displacement via the fault dip such that a displacement-to-length relationship is established, which then is extrapolated to all mapped structures. Strain is then calculated for the area of the faulted domain by summing the strain of each of the mapped structures. This method is thus dependent on the number of structures considered.

The dependency on the number of faults produced a discrepancy in radius change estimates in the literature. Watters (2021), who used n=653 faults, calculated Mercury's radius to have decreased by 0.9–1.3 km, whereas (Byrne et al., 2014), who considered a population of faults containing n=5934 structures, determined a range of 3.1–7.1 km of radius change. Watters (2021) assumed that shortening landforms in Mercury's smooth plains units are attributed to lithospheric loading and associated subsidence from the emplacement of the volcanic units rather than global contraction and thus excluded the

structures and area covered by plains units from the calculation. Byrne et al. (2014) considered a wider range of possibilities, including *and* excluding the smooth plains units. In their work, radial shortening was calculated using shortening landforms across eight great circles and by using the displacement length scaling. In all cases, with or without the shortening landforms in the smooth plains units, Byrne et al. (2014) mapped more faults in the same area that was considered by Watters (2021). Therefore, the method used in these studies is a disadvantage, as different geological interpretations result in a different number of considered structures, and in turn, cause the discrepancy in estimates of the amount of global contraction despite sampling the same population of faults.

An additional component of radius change occurs prior to the onset of faulting because the lithosphere resists faulting until its strength is reached (Klimczak, 2015). For a wide range of strength considerations, Klimczak (2015) estimates an additional 0.4 to 2.1 km of radius decrease to be added to the estimates calculated from fault strain. This results in radius changes from as little as 1.3 km, when adding the lowest possible amounts from Watters (2021) and Klimczak (2015), to as much as 9.2 km, when considering the upper estimates from Byrne et al. (2014) and Klimczak (2015). This range of values is a critical constraint for thermal evolution models, whereby the most plausible solutions require a radial shortening of ~5–10 km (Breuer et al., 2007; Hauck et al., 2004; Michel et al., 2013; Solomon, 1977; Tosi et al., 2013). Driven by the constraint of low values of radial contraction by Watters et al. (1998), Tosi et al. (2013) identified a very small fraction of model solutions that required less than 3.5 km of radial shortening when assuming very large reference viscosities.

The large range of estimated amounts of radial shortening on Mercury is only a very loose constraint for thermal evolution models, highlighting the need for improvement in the method on which the estimations are based on. Thus, we provide an alternative assessment of Mercury's global contractional strain, for which we apply fault strain theory introduced and tested by Twiss and Marrett (2010a, b) to three published Mercury thrust fault datasets to reevaluate to amount of radial contraction.

4.2 Methods

The fault strain theory laid out by Twiss and Marrett (2010a) is based on the fact that an entire population of faults is never really fully considered when estimating the strain of a faulted volume. Instead, this approach utilizes the displacement of the largest fault in the population, which is easiest to detect, and scales it using both displacement-to-length and fault-length-frequency statistics to estimate the total strain of the faulted volume. This method assumes infinitesimal strain, where the faulted volume must be large relative to the dimensions of the largest fault. This assumption is valid for our purposes, as we are considering the entire brittle volume of Mercury's lithosphere. This method also assumes that all structures in the population have the same fault geometric parameters, such as dip and fault shape, which was also assumed in previous works (Byrne et al., 2014; Di Achille et al., 2012; Watters et al., 1998; Watters and Nimmo, 2010).

The method by Twiss and Marrett (2010a) allows us to calculate the strain in Mercury's faulted portion of the lithosphere independent of the number of considered faults. We test this approach for three different datasets in the literature that sample substantially different numbers of thrust faults from the same population of structures (Figure 4.1). We use the previously mentioned data from Byrne et al. (2014) who sample

n=5934 structures, from Watters (2021), who samples n=653 structures, and from *Chapter* 2, 3 and Loveless et al. (2024b), in which n=100 structures were considered.

Twiss and Marrett (2010a) derived the equation for the total strain of faults sampled in three dimensions of a volume in the horizontal direction t:

$$e_{3,t}^{\text{tot}} = e_{3,t}^{(1)} \left(\frac{1 + \frac{2}{p}}{1 - s_3 + \frac{2}{p}} \right),$$
 1

where $e_{3,t}^{(1)}$ is the shortening strain of the fault with the highest displacement in the volume. The parameters p and s are derived from statistics based on the total population of fault parameters (Table 4.1). The strain of fault i in direction t is given by:

$$e^{(i)} = \mathfrak{P}_{3,t}^{(i)} \left[\frac{\delta^{(i)} \cos(\phi)}{T} \right], \qquad 2$$

where $\delta^{(i)}$ is the displacement of the *i*th fault and ϕ is the angle between the horizontal direction t and the slip direction on the fault (Figure 4.2), corresponding to subtracting the fault dip, α , from 180°. Here, $\mathfrak{P}^{(i)}$ is the probability of the fault being intersected by a random line parallel to t. The parameter T is the dimensional length of the faulted volume in direction t (Figure 4.2). The probability for an individual fault written as a continuous function of fault-displacement δ is:

$$\mathfrak{P}_{3,t}^{(i)} = \frac{A_f^i \cos \theta^i}{A_t} = \frac{\lambda B^{\frac{2}{p}} \cos(\theta)}{A_t} \delta^{(i)\frac{2}{p}}.$$

Here, A_f is the area of the fault plane. The angle θ is measured between the normal vector to the fault plane and t, or by subtracting α from 90° (Figure 4.2). The denominator, A_t , is the total cross-sectional area of the faulted volume, which is normal to t. The parameter λ is a geometrical shape factor that accounts for the fault height, as defined by down-dip

minor axis length, l, and the length, L, specifying either rectangular or elliptical shapes of the fault tip line. For rectangular fault shapes, λ is simply the ratio of l and L (as shown in Figure 4.2), whereas for elliptical shapes this ratio is multiplied by $\pi/4$. The factor B is a scaling parameter derived from the displacement-to-length statistic of the faults (see below). The probability in Eq. 3 then is the ratio of the area of the fault plane that is projected onto the total cross-sectional area of the faulted volume to the total cross-sectional area (Figure 4.2). This probability can be estimated for any fault in a population, as the areas of the fault planes are obtained from the displacement-length and cumulative number-length relationships. Note the absence of the superscript i for the geometric parameters λ and θ on the right-hand side of Eq. 3, as these are assumed to be the same for all faults in the population.

The faulted volume, V, is then calculated as the product of A_t and T. We define the faulted volume to be equal to the outer shell of Mercury that has a thickness defined by the depth-extent of the deepest faults, D, and planetary radius, R_M , as:

$$V = A_t T = \frac{4}{3} \pi R_M^3 - \frac{4}{3} \pi (R_M^3 - D^3).$$

Following the approach by Twiss and Marrett (2010a) we combine Eqs. 1 to 4, yielding:

$$e_{3,t}^{\text{tot}} = \frac{\lambda B^{\frac{2}{p}} \cos \theta \cos \phi}{V} \left(\delta^{(1)}\right)^{1+\frac{2}{p}} \left(\frac{1+2p}{1-s_3+\frac{2}{p}}\right).$$
 5

Here, the displacement, δ , has the superscript of (1), indicating that it is only the value from the largest fault.

Finally, the amount to radial contraction can be derived by calculating the initial radius of Mercury, R_i , from the fault population strain in Eq. 5 via the relation presented by (Watters and Nimmo, 2010):

$$R_i = \left(\frac{R_f^2}{e_{3,t}^{\text{tot}} + 1}\right)^{0.5},$$

where R_f is the final radius, which we take to be Mercury's current mean radius of 2440 km. The change in radius, corresponding to the radius decrease from global contraction, is then calculated as $\Delta R = R_f - R_i$.

Parameterization

We use the data from Byrne et al. (2014), Watters (2021), and the data from Chapters 2, 3, and Loveless et al. (2024b), hereon referred to as the Loveless et al. dataset, to parameterize Eq. 5 with all required fault-geometric values (Table 4.1). Geometric forward modeling of 55 shortening landforms on Mercury (Chapter 3) yielded thrust fault parameters that provide detailed observational constraints, including ranges of values for fault dips and fault aspect ratios needed here to calculate the geometric shape factor. In particular, Chapter 3 establishes that the average ranges of fault dip on Mercury are between 22° and 40°, a wider range than those considered in the previous global contractional strain analyses of Mercury. We therefore calculate the fault strain for dip values bounded by 22° and 40°, as well as the case for rock-mechanically calculated optimal dips of 30°. The depth extent of the faulting was determined to be 22 km on average with the largest structures to be no deeper than ~50 km (Chapter 3), and thus we use values of 30 km, 40 km, and 50 km in our calculations to constrain the thickness of the faulted volume, which agree well with lithospheric thickness and crustal depth estimates (Padovan

et al., 2015). We find that a value of 40 km best represents the thickness of the faulted volume because the vast majority of fault models return faults with shallower depths and only a few faults exceed depths of 40 km (*Chapter 3*). This thickness is not likely to be constant throughout Mercury, and a thickness of 40 km likely averages variations in the faulted volume.

We parameterize the shape factor λ by taking the average aspect ratio derived in *Chapter 3* as the ratio of the modeled down dip length of the fault plane to the map-view length of the fault (Table 4.1). This value was found to be 0.41 and is thus equal to λ if all faults are assumed to be rectangular. If faults are assumed to have an elliptical planar geometry, then we multiply this aspect ratio by $\pi/4$, providing a value of $\lambda = 0.32$. The aspect ratio was derived from listric fault geometries modeled in *Chapter 3*. It is defined only by the horizontal and downward dipping dimensions of the fault plane and not by variations in dip along the fault plane (i.e., listric or homoclinal). We note that the block diagram in Figure 4.2 shows a rectangular shape of a homoclinal plane for simplicity.

Enterprise Rupes is the largest shortening landform on Mercury both in mapped length and vertical relief (Byrne et al., 2018; Ferrari et al., 2015; Watters et al., 2016) and thus is likely underlain by the thrust fault accommodating the largest displacement on Mercury. In order to detect the maximum displacement of the fault, *Chapter 3* constructed a 2D balanced cross-section of the fault system along the location of maximum relief, matching observed topography, shortening strain from folding, and the slip vector that was indicated by offset impact craters. It was found that Enterprise Rupes consists of two oppositely dipping thrust faults with the primary thrust showing a displacement of value of $\delta^{(1)} = 9300$ m.

Values B and p in Eq. 5 are identified from the power-law displacement-to-length relationship of the population of faults (Cowie and Scholz, 1992):

$$\delta = \frac{1}{B}L^p. 7$$

Previous studies used model 1 regressions to derive a scaling relationship (e.g., Byrne et al., 2014; Watters, 2021). To provide statistically unbiased results for the regression parameters, we apply a model 2 linear regression to all datasets, as the independent variables (x values) of the regression, i.e., the fault length values, are not taken at controlled intervals, which is an assumption of a model 1 least squares regression (Sokal and Rohlf, 1995).

The fault displacements in Byrne et al. (2014) and Watters (2021) were found by relating the observed structural relief via the fault dip, where dips were assumed to be 25° , 30° , and 35° . We carry out three model 2 regressions for these two datasets to account for the updated range of dip angles (*Chapter 3*). We show those regression results in Figure 4.3a along with displacement-to-length data derived from 55 balanced cross-sections of thrust fault systems in *Chapter 3*. From these regressions, we extracted the values p and p and listed their values in Table 4.1. Because no fault dip values are known in the structural relief measurements by Byrne et al. (2014) and Watters (2021) the three different assumptions of dips produce three different values for parameter p remain unchanged for different assumptions of fault dip values.

The value for s used in Eq. 5 is derived from the slope, -m, of the power-law length-frequency distribution, NUM(L), of the mapped fault population (Cladouhos and Marrett, 1996; Watterson et al., 1996) as follows:

$$NUM(L) = G L^{-m}; s = \frac{m}{p}.$$

Here, G is the scaling factor relating the cumulative number of faults to the fault length. It is equal to the cumulative number of faults that have a unit length (Twiss and Marrett, 2010a). Because extrapolation over the total spread of the cumulative length frequency distribution produces overestimates of the strain, we follow practices laid out in Twiss and Marrett (2010a) and apply a regression to only its linear portion (Figure 4.3b). For each dataset, we extract the values for m, calculate s (Eq. 8) and list the results in Table 4.1. We note that the displacement-to-length data for all three datasets (Figure 4.3a) is a subset of the fault sample size (Figure 4.3b), producing a different number of data points between the two graphs.

4.3 Results

Radial contraction estimates

We present our results of radial contraction for the combination of possible geometric properties in Table 4.2. Overall, our analysis reveals that the amount of radial contraction on Mercury is anywhere between 1.5 and 4.4 km for the Loveless et al. dataset, 0.9 and 7.6 km for the Watters (2021) dataset, or 1.3 and 8.4 km for the Byrne et al. (2014) dataset. These total ranges depend on the combination of the thickness of the faulted volume, fault dips, and shapes of the fault plane. Thinner faulted volumes, higher fault dips, and rectangular fault shapes produce higher amounts of strain when compared to thicker faulted volumes, shallower fault dips, and elliptical fault shapes, respectively.

In particular, the volumetric strain decreases the deeper we assume the faulted volume to extend. With decreasing dip, the one-dimensional strain of the largest fault increases (i.e., the term in brackets in Eq. 2), but the proportion of the projected area of the

fault plane onto the cross-sectional area of the faulted volume goes down, and thus the probability, \mathfrak{P} , goes down (Eq. 3). Therefore, the strain calculated in one dimension follows the trend in Byrne et al. (2014) and Watters (2021) where strain estimates increase with lower fault dips. However, the probability governs the total outcome of Eq. 5, and therefore, explains why lower amounts of strain are produced for lower dip angles. Rectangular shapes of the fault tip line create a larger area of fault planes to be projected onto the cross-sectional area of the faulted volume than elliptical shapes. Therefore, the calculated amount of strain is larger for rectangularly shaped fault tip lines.

We find a combination of parameters that produce a minimal amount of global contraction (ΔR_{\min}), a combination of optimal parameters that produces the most probable amount of global contraction ($\Delta R_{\rm opt}$), and a combination of parameters that produces a maximum amount of global contraction ($\Delta R_{\rm max}$) from the investigated fault population datasets. The combination of parameters that produces $\Delta R_{\rm min}$ includes an average thickness of the faulted volume of 50 km, with all faults in the population dipping 22° (Table 4.2). This set of parameters produced a $\Delta R_{\rm min}$ of 1.5–1.9, 0.9–1.1, and 1.3–1.5 km for the Loveless et al., Watters (2021), and Byrne et al. (2014) datasets respectively. The lower and upper bounds for these ranges of ΔR represent elliptical and rectangular shapes of the fault tip line, respectively

While dip values of 30° and a thickness of the faulted volume of 40 km imply that they are assumed to be constant for the fault population and throughout Mercury, they also represent conservative estimates of averages, as there are established ranges of variations of these parameters around these values. Therefore, we consider the resulting ΔR values

(Table 4.2) as being optimal, producing $\Delta R_{\rm opt}$ of 2.3–2.9, 2.4–3.0, and 2.8–3.5 km for the Loveless et al., Watters (2021), and Byrne et al. (2014) datasets respectively.

A maximum amount of radial contraction is calculated by assuming a thickness of the faulted volume of 30 km depth and that all faults in the fault population dip 40°. With this combination of fault population parameters, the Loveless et al. dataset returns a $\Delta R_{\rm max}$ of 3.5–4.4 km. The Watters (2021) and Byrne et al. (2014) datasets produced $\Delta R_{\rm max}$ of 6.0–7.6 and 6.6–8.4 km, respectively (Table 4.2).

4.4 Discussion and conclusions

Our results establish that each dataset, irrespective of the number of considered faults, produces similar amounts of contractional strain, which, in turn, yields radius change estimates that are comparable to one another. For the Watters (2021) dataset, we find radial contraction estimates of 0.9 to 7.6 km, with the optimal range of $\Delta R_{\rm opt}$ being 2.4–3.0 km. Watters (2021) calculated substantially smaller values of ΔR , amounting to 0.9, 1.1, and 1.3 km for $\alpha = 35^{\circ}$, 30°, and 25°, respectively. These values appear to agree with our $\Delta R_{\rm min}$ values across all three datasets (Table 4.2). However, the $\Delta R_{\rm min}$ values in this work represent the extreme lower bounds of physical parameters, whereas the range of radius change values produced in Watters (2021) spans the entire considered parameter space in that publication. Therefore, the $\Delta R_{\rm min}$ results presented here cannot be considered to confirm the range of estimates presented in Watters (2021). The low values for Mercury's contraction presented in Watters (2021) arise from the low number of shortening landforms considered to have contributed to global contraction.

Using the same method as Watters (2021) but for a larger number of faults, Byrne et al. (2014) estimated Mercury's radial contraction to be ~3.1–7.1 km, which falls in the

range of $\Delta R_{\rm opt}$ to $\Delta R_{\rm max}$ calculated in this study (Table 4.2). The larger sample size is likely closer to the true number of faults in Mercury's population of thrust faults, which likely explains their results showing a better overlap with ours. The large sample size of this dataset and the sampling of structural reliefs over a wide range of fault lengths—as seen in the spread of the displacement-to-length data when compared to the length frequency distribution (Figure 4.3, right column)—makes this dataset statistically more probable. In contrast, the dataset by Watters (2021) sampled the structural relief of only the largest of shortening landforms, which is seen in the spread of the data being skewed toward the longest faults (Figure 4.3, center column).

We find Mercury's radius change that can be attributed to thrust faulting to show optimal values between 2.3 and 3.5 km consistently across all three datasets. In order to overcome the frictional resistance to sliding, Mercury would have to contract to build up stresses beyond the brittle strength of its lithosphere (Klimczak, 2015). For a variety of rock-mechanical properties, this study found that Mercury would have had to experience 0.4–2.1 km of radial contraction before thrust faults could form and that this range would need to be added to any estimates from faulting. Adding the findings by Klimczak (2015) to the range of values calculated in this study yields a range radial contraction of 2.7 to 5.6 km that is likely to have occurred on Mercury. This result is in reasonable agreement with many thermal evolution modeling efforts (e.g., Breuer et al., 2007; Hauck et al., 2004; Michel et al., 2013; Solomon, 1977) and, in combination with timing and strain rate estimates of global contraction (Crane and Klimczak, 2017), may be used to tightly constrain future thermal evolution modeling.

In this work, we adapted the methodology presented and tested by Twiss and Marrett (2010a, b) to estimate the amount of thrust fault strain Mercury experienced from global contraction. Using three datasets sampling vastly different numbers of faults of the same population (Figure 4.1), we demonstrated that any bias that incompletely sampled fault populations introduced using the previous method is avoided using the method presented here. Thus, future calculations of Mercury's radial contraction will produce more robust estimates using the framework of Twiss and Marrett (2010a). We also suggest that this methodology can be used to calculate fault population strain for other planetary processes and bodies.

4.5 Acknowledgments

We thank Dr. Steven Holland and Dr. Robert Twiss valuable discussions on the topic.

4.6 Figures 30°N 30°N 30°S Byrne et al. (2014) Watters (2021) Loveless et al. (2024) 180° 120°W 60°W 0° 60°E 120°E 180°

Figure 4.1: Comparison of mapped thrust fault populations considered in this study across Mercury in Winkel Tripel projection, color-coded based by source. The dataset by Byrne et al. (2014) is displayed in blue atop the dataset by Watters (2021), which is displayed in orange. The faults from Chapter 1 are displayed in thick black lines. For reference, smooth plains units (Denevi et al., 2013) are colored in light green.

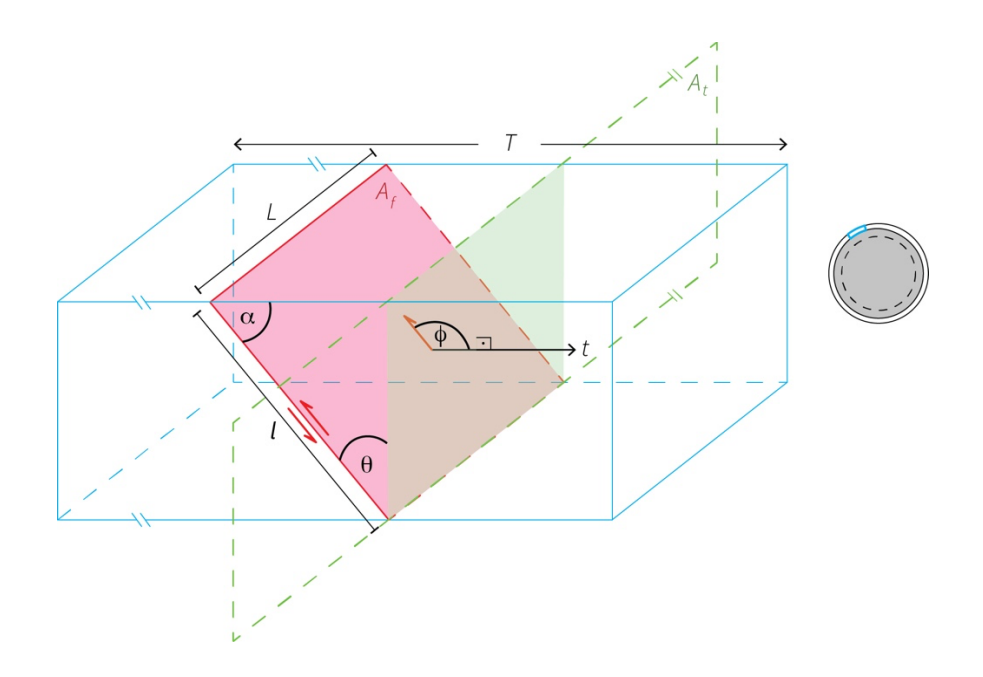


Figure 4.2: Block diagram of fault geometric parameters modified after Twiss and Marrett (2010a, b). The block (blue outline) is a representative portion of the faulted volume of Mercury's lithosphere. In this diagram the fault plane (A_f) is the area marked as red shaded region and it is here shown as rectangular shape. The plane outlined with green dashes is the total cross-sectional area (A_t) of the faulted volume. The green shaded region represents A_f projected onto A_t .

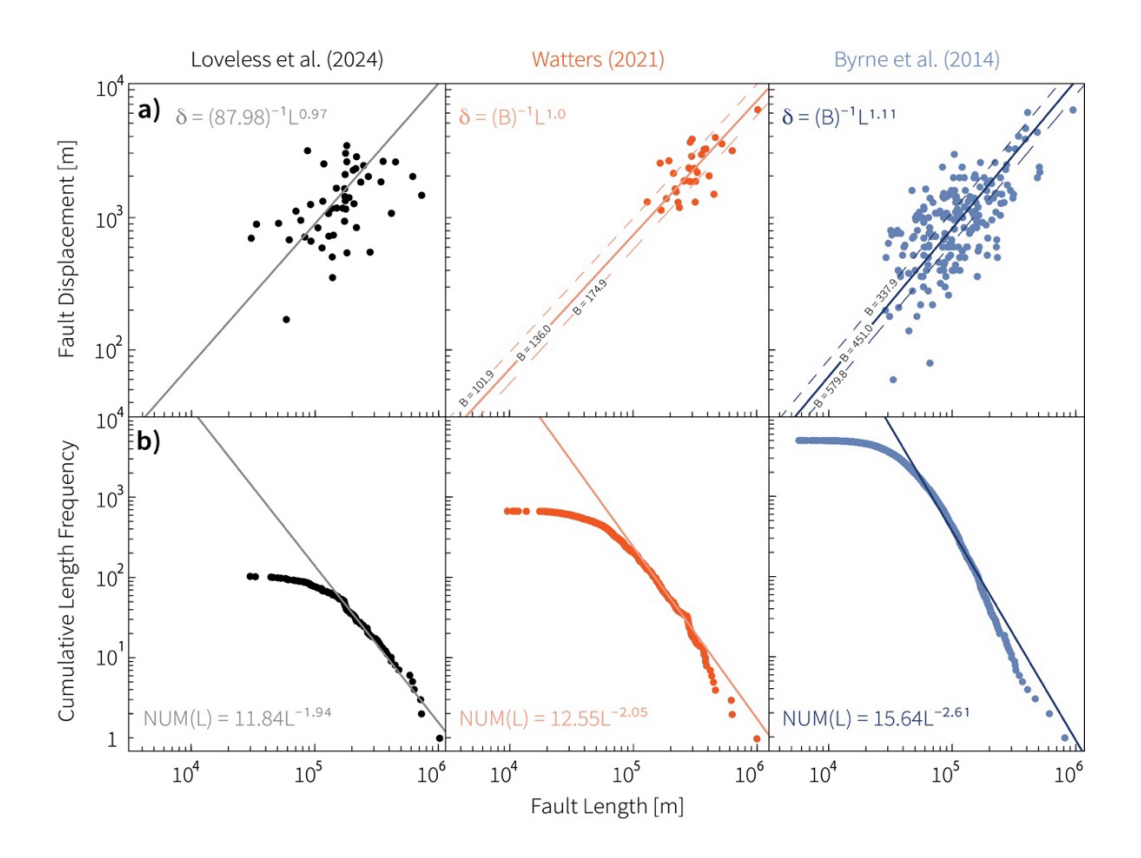


Figure 4.3: Thrust fault population statistics for three datasets on Mercury, where the data by Loveless et al., Watters (2021), and Byrne et al., (2014) are shown in black, orange, and blue in the left, center, and right columns, respectively. (a) Fault displacement-to-length data and the corresponding regressions shown for all datasets in the top row. Data (points) and regression (solid line) for Chapter 3 (Loveless et al., 2024 panel) was derived from model results. Data from Byrne et al. (2014) and Watters (2021) is shown for the assumption that all measurements are from faults with dips of for $\alpha = 30^{\circ}$. Regressions for those data are shown for $\alpha = 30^{\circ}$ with a solid line and for $\alpha = 22^{\circ}$ and 40° with dashed lines, respectively. (b) Cumulative fault length frequency distributions shown for all datasets in the bottom row. Cumulative length-frequency regressions are shown as solid lines for the linear portion of the data distribution. Color-coding of the datasets corresponds to that in Figure 4.1.

4.7 Tables

Table 4.1: Parameters used to solve for fault strain. Statistical parameters B, p, s, and m were derived from regressions performed in this work using measurements published in the original datasets.

Symbol	Definition	Value
α	Fault dip angle.	$\alpha = 22^{\circ}, 30^{\circ}, \text{ or } 40^{\circ a}$
θ	Angle between the normal vector to the	$\alpha = 22^{\circ}; \ \theta = 68^{\circ}$
	fault plane and the horizontal vector t.	$\alpha = 30^{\circ}; \theta = 60^{\circ}$
		$\alpha = 40^{\circ}; \theta = 50^{\circ}$
ϕ	Angle between the horizontal vector t and	$\alpha = 22^\circ$; $\phi = 158^\circ$
	the slip direction of the fault.	$\alpha = 30^\circ$; $\phi = 150^\circ$
		$\alpha = 40^\circ$; $\phi = 140^\circ$
$\delta^{(1)}$	Maximum displacement of the largest	$\delta^{(1)}=9300~m^a$
	fault in the faulted volume.	
λ	Geometric shape factor defining shape of	Rectangular faults; $\lambda = 0.41^{a}$
	the fault plane as either rectangular or	Elliptical faults; $\lambda = 0.32$
	elliptical.	
D	Thickness of the faulted volume.	$D = 30 \text{ km}, 40 \text{ km}, \text{ or } 50 \text{ km}^{\text{a}}$

B Inverse of the scaling factor of the
$$B=87.98^{\rm a}$$
 displacement-to-length relationship.

$$\alpha = 22^{\circ}$$
; $B = 337.9^{\circ}$

$$\alpha = 30^{\circ}$$
; $B = 451.0^{\circ}$

$$\alpha = 40^{\circ}$$
; $B = 579.8^{\text{b}}$

$$\alpha = 22^{\circ}$$
; $B = 101.9^{\circ}$

$$\alpha = 30^{\circ}$$
; $B = 136.0^{\circ}$

$$\alpha = 40^{\circ}$$
; $B = 174.9^{\circ}$

p Exponent of the power law displacement-
$$p = 0.97^{a}$$

to-length relationship.
$$p = 1.11^{b}$$

$$p = 1.00^{\circ}$$

m Additive inverse of the exponent of the
$$m = 1.94^a$$

cumulative length-frequency
$$m = 2.61$$

relationship.
$$m = 2.05^{\circ}$$

s Ratio of m to p.
$$s = 2.00^a$$

$$s = 2.35$$

$$s = 2.05^{c}$$

^a Value taken or derived from data from *Chapters 2, 3* and Loveless et al. (2024b)

^b Value derived from data published in Byrne et al. (2014)

^c Value derived from data published in Watters (2021)

Table 4.2: Radius change values listed for those parameters that have the largest impact on calculations. The lower and upper bounds of each of the ranges listed for ΔR represent elliptical and rectangular shapes of the fault tip line, respectively.

			Δ <i>R</i> [km]	Δ <i>R</i> [km]	Δ <i>R</i> [km]
	D [km]	α [°]	Chapters 2 and 3	Watters	Byrne et al.
				(2021)	(2014)
			(n = 100)	(n = 653)	(n = 5934)
Minimum	50	22	1.5–1.9	0.9–1.1	1.3–1.5
Optimal	40	30	2.3–2.9	2.4–3.0	2.8–3.5
Maximum	30	40	3.5–4.4	6.0-7.6	6.6–8.4

CHAPTER 5

EFFECTS OF SOLAR TIDES ON MERCURY'S GLOBAL FAULT PATTERN. 4

⁴ Loveless, S.R. To be submitted to Icarus.

Abstract

The long, sustained cooling of Mercury caused the planet to undergo global contraction, which is accommodated in the lithosphere by a population of surface-breaking thrust faults. Horizontal stresses from global contraction alone are isotropic, and thus they predict that thrust fault orientations across the planet are random. However, Mercury's thrust fault orientations are observed to be systematic, showing general north-south alignment in the equatorial regions and more variation in preferred orientations near the poles. This observation is widely considered to indicate other tectonic processes overlapped with global contraction. Planetary reorientation, tidal despinning, solar tides, and mantle convection all having been invoked individually or in combination to have produced the global pattern of faults. The specific scenario by which only solar tides and Mercury's rotation overlap with global contraction has yet to be fully explored. Here, we calculate the time-averaged stresses produced by tides to assess their effects over geologically long timescales and then superpose these stresses over an isotropic horizontal stress field caused by global contraction that would produce thrust faulting throughout Mercury's lithosphere. We find that stresses produced from Mercury's current orbit alone are on the order of 1 KPa and are therefore insufficient to cause faulting as a stand-alone process. However, as these stresses are superposed onto the stresses of a few MPa caused by global contraction, we find that the slight differences in the horizontal principal stresses are enough to influence thrust fault orientations. The predicted optimal thrust fault orientations show a widespread match to the observed pattern. The superposition of stresses caused by solar tides and Mercury's rotation onto global contraction may thus explain much of the observed tectonic pattern on Mercury. Future work will include the modeling

of cyclical stresses over Mercury's orbital cycle and compare the recurring loading of those stresses with empirical mechanical fatiguing of basalts to assess the influence the fatiguing of Mercury's lithosphere has on Mercury's thrust fault pattern.

5.1 Introduction

Mercury has undergone global contraction due to its long, sustained cooling (Solomon, 1978). This contraction is the major source of tectonic stress and has driven the formation of a globally distributed population of thrust faults and folds manifest at the surface as positive relief landforms (e.g., Byrne et al., 2014, Chapter 1). Horizontal compressive stresses from global contraction when acting as the sole tectonic process are isotropic (Melosh and McKinnon, 1988), which would result in random thrust fault orientations and thus showing no systematic pattern across the planet. However, Mercury's thrust fault orientations are observed to be systematic, displaying north-south trending fracture patterns at the equatorial regions that become less pronounced, or east-west oriented, towards the poles (e.g., Byrne et al., 2018; Klimczak et al., 2015). Therefore, it is widely thought that other tectonic processes must have overlapped with global contraction to have influenced the observed fault orientations. Different studies have assessed various combinations of processes to explain the observed fault pattern, including Mercury's True Polar Wander (TPW) (e.g., Benz et al., 1988), impact damage from the Caloris basin (Klimczak et al., 2025) or TPW from the Caloris impact (Matsuyama and Nimmo, 2009), and rotational spin-down (Klimczak et al., 2015; Melosh and McKinnon, 1988) to predict different fault patterns.

Mercury is in a 3:2 spin orbit resonance with the sun, where Mercury spins about its axis three times for every two orbits around the Sun. This resonance caused it to have slowed in rotation, a process widely referred to as tidal despinning (e.g., Kaula, 1968; Burns, 1975; Melosh 1977; Melosh and McKinnon, 1988). Rotational spin-down overlapping global contraction is predicted to cause north—south oriented thrust faulting at

the equatorial regions with no preferred polar thrust fault orientations (e.g., Klimczak et al., 2015; Pechmann and Melosh, 1979) or east—west oriented normal faults at the poles (Beuthe, 2010). The predictions for the equatorial orientations agree well with observations; however, thrusts near the poles have preferential orientations (Klimczak et al., 2025) that poorly match the predictions. Reorientation of Mercury's spin axis caused by the Caloris impact in combination with tidal despinning (Matsuyama and Nimmo, 2009) agrees with the patterns revealed by the Mariner 10 mission but showed disagreement with tectonic patterns revealed from mapping efforts from the MESSENGER mission (Byrne et al., 2018). Prior to Klimczak et al. (2015) studies that predicted fault orientations provided a set of orbital events did not use rock-mechanics to predict their resulting fault orientations.

The 3:2 spin orbit resonance on Mercury also causes systematic, repetitive time-dependent tidal displacements as well as temperature variations as two points on Mercury's surface tend to face the sun for extended periods of time. These points are called Mercury's hot poles and located along the equator of the planet at longitudes 0° and 180°. The solar tides driven gravitational potential Mercury experiences through its orbit is among the largest of the planetary bodies in the solar system (Hoolst and Jacobs, 2003). These tides may influence global fault patterns within Mercury's lithosphere (Byrne et al., 2018; Klimczak et al., 2025; Williams et al., 2011), and fault orientations show concentric patterns around the hot poles. Additionally, Mercury's surface is systematically heated due to its orbital configuration leading to variations in both the thickness and strength of the lithosphere geographically around the hot poles (Williams et al., 2011). With an eccentricity of 0.2056, Mercury's orbit is also the most eccentric in the solar system, thus

creating a complex suite of orbital characteristics producing stresses throughout the planet's surface that warrants further investigation.

Various other planetary bodies throughout the solar system display fracture patterns or seismicity that is linked to tides. Most of these planetary bodies are satellites with eccentric orbits or have undergone some orbital change, such as despinning, precession, or a change in orbital resonance that would have induced systematic stress patterns in their lithospheres. On the Moon, systematic fracture orientations have been linked to some combination of global contraction overlapping with diurnal tidal stresses and orbital recession (Watters et al., 2019, 2015b) or with despinning, and various true polar wander parameters (Matsuyama et al., 2021). Furthermore, seismic activity on the Moon is time dependent on tides induced by Earth (e.g., Latham et al., 1971; Toksöz et al., 1977; Turner et al., 2022; Watters et al., 2019).

Tidal deorbiting of Phobos into Mars has also been linked to systematic orientations of extensional landforms about the sub-planet point of the satellite (Hurford et al., 2016). Tidal effects from both the Sun and Phobos have also been predicted to induce seismicity on Mars (Manga et al., 2019). Models of stresses from diurnal tides on Europa are large enough to initiate cracking and match Europa's large-scale linear and cycloidal fractures (Greenberg et al., 1998; Marshall and Kattenhorn, 2005). Further evidence of tidally induced fracturing on Europa has been linked to left-lateral strike slip deformation patterns (Collins et al., 2022). Tidal displacements of the subsurface ocean of Enceladus have been modeled to predict seismicity within its icy lithosphere (Olsen et al., 2021), and tides influence the tectonic and cryovolcanic activity of the large-scale tiger-stripe fractures on the moon's surface (Hedman et al., 2013; Nimmo et al., 2014). Cycloid fracture patterns

present on both Europa and Enceladus are hypothesized to be caused by cyclical tidal stresses (Greenberg et al., 1998; Rhoden et al., 2021, 2010). Stellar induced tidal stresses acting upon exoplanets may even be responsible for the initiation of exoplanetary tectonics (Zanazzi and Triaud, 2019) and have been modeled to induce seismic activity for various exoplanets with nonzero eccentric orbits (Hurford et al., 2020).

Because the major effects that tides have on tectonic patterns and seismicity on planetary bodies, we investigate how much solar tides overlapping with global contraction influence Mercury's tectonics, as that combination of processes has not yet been specifically studied. We explore the effects that Mercury's current orbit and spin-orbit resonance have on the orientations of its population of thrust faults by investigating the impact of tidally-induced stresses on fault orientations and the weakening effect they have on the lithosphere due to their cyclical variations.

5.2 Methods

To explore the effect of Mercury's eccentric 3:2 spin—orbit resonance with the Sun, we calculate the tidal displacement across the planet and derive the resultant stresses of the surface of Mercury. We follow the methods laid out by Matsuyama and Nimmo (2009, 2008). A complete list of the parameters and values we use is located in Table 5.1. The stress sign convention for the physical framework in those works is such that tensile stresses are positive and compressive stresses are negative. While tidal displacements and corresponding stresses change throughout the 3:2 spin—orbit resonance cycle stresses, radial displacement and stresses arising from tides oscillate as the relative positions of Mercury's subplanet point changes throughout the planet's orbit. The displacements can be averaged over geologically long time periods to study their long-term effects as the

geographic location of the subplanet point averaged over time is a fixed location on Mercury's surface. For that, the radial displacement, $r_{\text{rot,tidal}}(\theta, \phi)$, at colatitude θ and longitude ϕ , of a body distorted by rotation and solar tides can be found using:

$$r_{\text{rot,tidal}}(\theta, \phi) = R \left[1 - f_r \left(\cos^2 \gamma_{\text{rot}} - \frac{1}{3} \right) + 3f_t \left(\cos^2 \gamma_{\text{tidal}} - \frac{1}{3} \right) \right],$$
 1

where R is the mean radius of the planet, f_r is the flattening caused by rotation, and f_t is the flattening caused by tidal bulging (Matsuyama and Nimmo, 2008). Here, rotational deformation is geographically dependent on the rotation pole, with averaged coordinates, $(\theta_{rot}, \phi_{rot})$:

$$\cos^2 \gamma_{\text{rot}} = \cos \theta \cos \theta_{\text{rot}} + \sin \theta \sin \theta_{\text{rot}} \cos(\phi - \phi_{\text{rot}}).$$
 2

Tidal deformation is geographically dependent on the sub-planet point with averaged coordinates (θ_{tidal} , ϕ_{tidal}):

$$\cos^2 \gamma_{\text{tidal}} = \cos \theta \cos \theta_{\text{tidal}} + \sin \theta \sin \theta_{\text{tidal}} \cos(\phi - \phi_{\text{tidal}}).$$
 3

We adopt the flattening terms used by Matsuyama and Nimmo (2009), which take into account Mercury's 3:2 spin-orbit resonance by including the Hansen coefficients:

$$f_r = \frac{1}{4} h_2^T \frac{n^2 R^3}{GM} \left[2p^2 + 3(1 - e^2)^{-\frac{3}{2}} - 3H(p, e) \right]$$
and
$$f_t = \frac{1}{4} h_2^T \frac{n^2 R^3}{GM} H(p, e).$$
4

Here, h_2^T is the degree 2 spherical harmonic Love number, n is the mean motion, G is the gravitational constant, and M is the mass of Mercury. The values p and e are the spin/orbit rate (3/2) and the eccentricity respectively. The Hansen coefficients, H(p,e), are a series of coefficients that are commonly used in mathematical expansions of elliptical motion related to the ratio (p) of angular velocity and mean motion tabulated by (Goldreich and

Peale, 1966). For a 3:2 spin orbit resonance, we follow the work of Matsuyama and Nimmo (2009) by using the Hansen coefficients to the order e^3 :

$$H(3/2,e) = \frac{7e}{2} - \frac{123e^3}{16} + \dots$$

The normal stresses acting in the horizontal plane tangential to the surface along the north–south direction $(\sigma_{\theta\theta})$ are:

$$\sigma_{\theta\theta} = \frac{2}{3} \left(\frac{1+\nu}{5+\nu} \right) \mu \, f_n(6\sin^2 \gamma_n \cos^2 \psi_n + 9\cos^2 \gamma_n - 5), \tag{6}$$

and the normal stresses in the horizontal plane acting in east–west $(\sigma_{\phi\phi})$ directions are:

$$\sigma_{\phi\phi} = \frac{2}{3} \left(\frac{1+\nu}{5+\nu} \right) \mu f_n (-6\sin^2 \gamma_n \cos^2 \psi_n + 3\cos^2 \gamma_n + 1).$$
 7

Finally, shear stresses $(\sigma_{\theta\phi})$ acting in the horizontal direction tangential to Mercury's surface due to tides are:

$$\sigma_{\theta\phi} = -2\frac{1+\nu}{5+\nu}\mu f_n \sin^2 \gamma_n \sin(2\psi_n).$$
 8

Equations 6, 7, and 8 use the following relationships:

$$\sin \gamma_n (\theta_n, \phi_n, \theta, \phi) \cos \psi_n (\theta_n, \phi_n, \theta, \phi) = \cos \theta_n \sin \theta - \sin \theta_n \cos(\theta) \cos(\phi - \phi_n),$$

$$\sin \gamma_n (\theta_n, \phi_n, \theta, \phi) \sin \psi_n (\theta_n, \phi_n, \theta, \phi) = \sin \theta_n \sin(\phi - \phi_n),$$
9

where the coordinates (θ_n, ϕ_n) are either coordinates for the sub-planet point for n = tidal or the coordinates for the rotational axis for n = rot. In equations 6, 7, and 8, ν is the Poisson's ratio and μ is the rigidity of the lithosphere. We calculate rigidity as $\mu = \frac{E}{2(1+\nu)}$, where E is Young's Modulus. We use a value of E = 29 GPa to represent the deformation modulus integrated over the thickness of Mercury's fractured lithosphere (Klimczak and McCarthy, 2025). The subscript n indicates that these stresses are calculated for both tidal (n = tidal) and rotational (n = rot) distortions. The total normal stresses acting in the north—

south and east—west directions and the total shear stresses caused by tides and rotation are then the sums of the tidal and rotational components:

$$\sigma_{\theta\theta} = \sigma_{\theta\theta_{\rm rot}} + \sigma_{\theta\theta_{\rm tidal}}; \sigma_{\phi\phi} = \sigma_{\phi\phi_{\rm rot}} + \sigma_{\phi\phi_{\rm tidal}}; \sigma_{\theta\phi} = \sigma_{\theta\phi_{\rm rot}} + \sigma_{\theta\phi_{\rm tidal}}.$$
 10

We solve for this stress field in 30° by 30° latitudinal and longitudinal regions across Mercury.

The principal horizontal stresses, σ_+ and σ_- arising from tides are calculated from the combination of $\sigma_{\theta\theta}$, $\sigma_{\phi\phi}$, and $\sigma_{\theta\phi}$ using the following relationships (Turcotte and Schubert, 2014):

$$\sigma_{+} = \frac{\sigma_{\theta\theta} + \sigma_{\phi\phi}}{2} + \left[\left(\frac{\sigma_{\theta\theta} - \sigma_{\phi\phi}}{2} \right)^{2} + \left(\sigma_{\theta\phi}^{2} \right) \right]^{0.5};$$

$$\sigma_{-} = \frac{\sigma_{\theta\theta} + \sigma_{\phi\phi}}{2} - \left[\left(\frac{\sigma_{\theta\theta} - \sigma_{\phi\phi}}{2} \right)^{2} + \left(\sigma_{\theta\phi}^{2} \right) \right]^{0.5}.$$
11

The angle, ω , to which σ_+ acts with respect to the east–west direction can be found using the relation (Turcotte and Schubert, 2014):

$$2\omega = \operatorname{atan}\left(\frac{2\sigma_{\theta\phi}}{\sigma_{\theta\theta} - \sigma_{\phi\phi}}\right),\tag{12}$$

while the direction σ_{-} makes with σ_{+} is 90° by definition.

5.3 Results

We find that the time average radial displacement of Mercury's surface due to tides and rotation is on the order of ± 1 m (Figure 5.1). A positive radial displacement occurs at the equator, with maximum peaks at the hot pole locations (warm colors in Figure 5.1). The polar regions experience a negative radial experience due to flattening caused by rotation and solar tides (cool colors Figure 5.1). A radial displacement of ± 1 m agrees with other works that have calculated radial displacement due to tides (e.g., Hoolst and Jacobs, 2003; Thor et al., 2020).

We first calculate the average stresses produced by the tides and rotation of Mercury's current 3:2 spin-orbit resonance alone (Figure 5.2). These stresses are calculated in 30° by 30° bins. We represent the horizontal principal stresses as line segments oriented in the direction they are acting on, with blue lines showing horizontal compression and orange lines showing horizontal tension. Throughout Mercury's surface, the principal stresses generated from solar tides and Mercury's rotation alone are compressive and tensile only on the order of a few kPa (Figure 5.2). These stresses are not strong enough to overcome the unconfined compressive strength of rock, and therefore, solar tides and Mercury's rotation are insufficient to induce faulting of the lithosphere. Stresses in the equator show tensile principal stress components acting in north-south direction and compressive principal stress components acting in the east-west direction. The magnitudes of the tensile north–south trending stresses substantially increase away from the equator in mid-latitude regions, and at the poles the orientations of the tensile stresses show more deviation from the north–south trend produced at the equator. The orientations of the stress field show systematic variations around the hot poles.

Global contraction imposes a global compressive stress state (Melosh and McKinnon, 1988) which has created a global population of thrust faults on Mercury (Byrne et al., 2014). We note that solar tides and Mercury's rotation do not generate stresses that are large enough to fracture Mercury's lithosphere. Therefore, we superpose enough compressive stress to predict thrust faulting at all locations across the tidally stressed surface of Mercury. For this, we assume an unconfined compressive strength of a fractured basaltic rock mass at ~10 MPa (Schultz, 1993), which equals the stresses needed at the surface to produce thrust faulting. We superpose compressive stresses onto our solutions

for tidal stresses in a manner such that a minimum of 10 MPa are reached for all principal stress components. The larger of the two principal stresses, σ_+ , is more tensile than σ_- . Therefore, as compression is added, the stresses acting in the direction of σ_+ become less compressive than those acting in the direction of σ_- , and so the direction of σ_+ becomes the direction of the intermediate, compressive principal stress acting in the horizontal direction, σ_h . Conversely, the stresses acting in the σ_- direction become more compressive, resulting in the maximum compressive principal stress, σ_H to be acting in the direction of σ_- .

Superposing global contraction onto the stresses caused by solar tides and Mercury's rotation shifts all stress components to be compressive. Therefore, we now show a map of the principal stresses caused by solar tides, Mercury's rotation, and global contraction acting together (Figure 5.3). The maximum horizontal principal stress, σ_H , are represented with thick, blue lines, and the minimum horizontal principal stress, σ_h , are represented with thin, blue lines. The addition of ~10 MPa to the stresses shown in Figure 5.2 causes the stresses σ_H and σ_h to be near isotropic as the differential stresses from tides and rotation are on the order of only a few KPa. We find that the maximum horizontal principal stress component—is oriented in east—west direction in a wide region of the equatorial and mid-latitudes (σ_H , Figure 5.3). Its orientation varies in northwest—southeast and northeast—southwest orientations towards the poles. In turn, the minimum horizontal principal stress components are oriented north—south a wide region of along the equator and mid-latitudes and show more variation in the polar region (σ_h , Figure 5.3). This principal stress shows subtle systematic variations around the hot poles.

Next, we calculate the optimal orientations of thrust faults predicted by the stress field where stresses from global contraction and tides and rotation are superposed. Since we previously selected the superposed compressive stresses from global contraction to exceed the unconfined compressive strength across all locations, thrust faulting will occur in this stress state. Because of the anisotropy the tidal and rotational forcing introduces to the horizontal principal stress components, it is possible to determine optimal thrust fault orientations. For our stress field (Figure 5.3), the minimum principal stress component acts vertically and is equal to the overburden, while the intermediate and maximum principal stresses are horizontal. Per definition, the strike of an optimally oriented dip-slip fault forms in the direction of the intermediate compressive principal stress component. On our stress map (Figure 5.3), the orientations of σ_h are then equal to the optimal thrust fault orientations, which we have highlighted in Figure 5.4. This map shows the optimal orientations for the same 30° by 30° latitudinal and longitudinal regions across Mercury with the black lines aligning with the predicted strikes of the thrust fault planes. We predict predominantly north-south trending thrust fault orientations in a broad region around the equator and mid-latitudes. Optimal thrust fault orientations are predicted to show greater variations near the poles, showing northwest–southeast and northeast–southwest strikes.

We compare our predictions for Mercury's global thrust fault pattern caused by tides and rotation overlapping with global contraction with the observed fault orientations on Mercury. Rose diagrams of fault orientations of 30° by 30° regions were generated by Klimczak et al. (2025) and are represented in grey in Figure 5.5. These show lengthweighted modes of the azimuths of Mercury's faults. We overlay these rose diagrams with the predicted fracture patterns we calculated shown in Figure 5.4 (blue lines, Figure 5.5).

The predicted thrust fault orientations produced in this work reasonably agree in almost all of the 30° by 30° regions with the orientations analyzed by Klimczak et al. (2025) as the line segments from the predictions align well with the rose diagrams of faults produced by observations (Figure 5.5).

We compare our thrust fault predictions to both the length-weighted averages, standard deviations, and modes of the observed thrust faults produced by Klimczak et al. (2025) (Table 5.2). All the predicted thrust orientations fall within one standard deviation of the observed fault orientations for each region, predicted thrust fault orientations fall within ½ of the respective bins observed standard deviations for 58 of the 72 bins, and as much as 40 of the 72 bins have predicted thrust fault patterns that fall within ¼ of the observed standard deviation (Table 5.2). The average angular difference across all of the predicted thrust fault orientations with observed thrust fault orientations is 12.7°, however we note a latitudinal variation. In near equatorial latitudes, the average difference between predicted orientations and observed orientations is 6.6°, at mid latitudes the average difference is 9.1°, and at near polar latitudes, the average difference is 22.6°. We consider these alignments as good indication that our modeled thrust fault network successfully matches observations.

We also show the observed modes of the thrust faults produced by Klimczak et al. (2025) which is the fault orientation that is observed to occur the most per 30° by 30° region in Table 5.2. This data shows that many regions are multimodal, meaning that Mercury's faults tend to show multiple reoccurring strikes per region. We bold the values in Table 5.2 where our predictions fall within 10° of either the weighted mean or one of the observed modes per region. Predictions in all but 19 of the regions fall within 10° of

either the weighted mean or any of the modes in its respective region. The rose diagrams in Figure 5.5 are constructed of bins of $\sim 10^{\circ}$ which was found to be the bin size that best visualizes structure orientations (Klimczak et al., 2025) and so we consider these alignments as good indication that our modeled thrust fault network successfully matches observations.

5.4 Discussion

In this work we predict thrust fault orientations from the time-averaged stress field caused by the deformation that Mercury experiences from its 3:2 spin-orbit resonance with the sun superposed on global contraction. Stresses from tides and rotation alone (Figure 5.2) have magnitudes of only a few kPa and are both tensile and compressive. Neither the compressive nor the tensile stresses are large enough to reach the compressive and tensile strengths of Mercury's lithosphere. This finding shows that solar tides and rotational bulging are insufficient to actively drive thrust faulting on Mercury.

However, we demonstrate that stresses from solar tides and rotation influence the orientations of faults if faulting is driven by other sources of stresses. For Mercury, global contraction without a doubt has driven thrust faulting, as evinced by the globally distributed population of thrust faults. By superposing enough compressive stress to predict thrust faulting onto the stress field of solar tides and rotation, we predict optimal orientations of thrust faults that show reasonably good agreement with the observed global fault pattern. The horizontal principal stresses produced by tides and rotation only differ by a few kPa, and when compression on the order of ~ 10 MPa is added to the point of rock failure, these stresses become near isotropic (Figure 5.3). A near isotropic range of σ_H and σ_h principal stresses allow for a wide range of plausible fault orientations. Therefore, the small

differences of horizontal stresses caused by tides and rotation allow for predicting just optimal thrust fault orientations provided the calculated stress regime. Such orientations are thus expected to be only subtly preserved in Mercury's geologic record.-We interpret these results as indication that Mercury's 3:2 spin-orbit resonance does in fact influence the orientations of Mercury's thrust faults caused by global contraction.

Due to its current orbit and that we find that solar tides and rotation play a role in Mercury's thrust fault patterns, Mercury's current orbit may influence the planet's seismicity. Moonquakes have been suggested to be linked to tides, but even so the largest moonquakes are relatively weak with amplitudes of ~3 (e.g., Lammlein et al., 1974). On Mars, tides induced from Phobos have been linked to seismic events (e.g., Manga et al., 2019; Pou et al., 2021). Therefore, tides on Mercury may cause seismicity, especially since the deformation from the Sun onto Mercury is estimated to be among the largest in the Solar System (Hoolst and Jacobs, 2003).

5.5 Figures Output Mean Radial Displacement [m] -60 Longitude [*]

Figure 5.1: Map of the time-averaged radial displacement produced by solar tides and Mercury's rotation due to Mercury's 3:2 spin—orbit resonance with the Sun. Map shown in equirectangular projection.

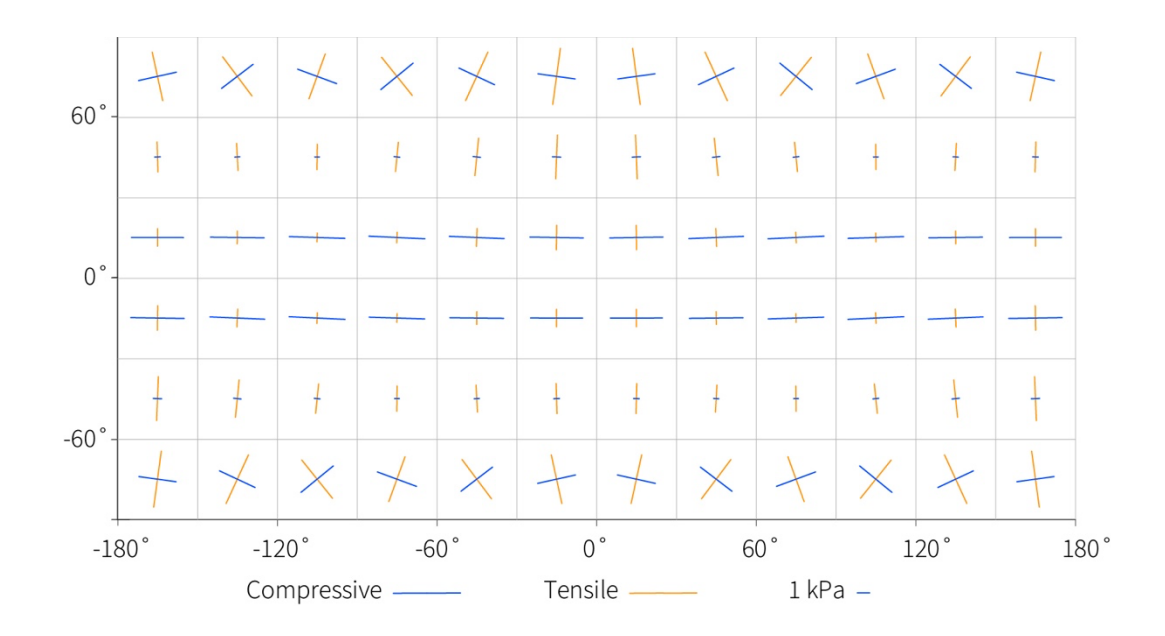


Figure 5.2: The orientations and magnitudes of the principal stresses produced by Mercury's orbit and rotation alone. Tensile and compressive stresses are represented as orange and blue line segments, respectively.

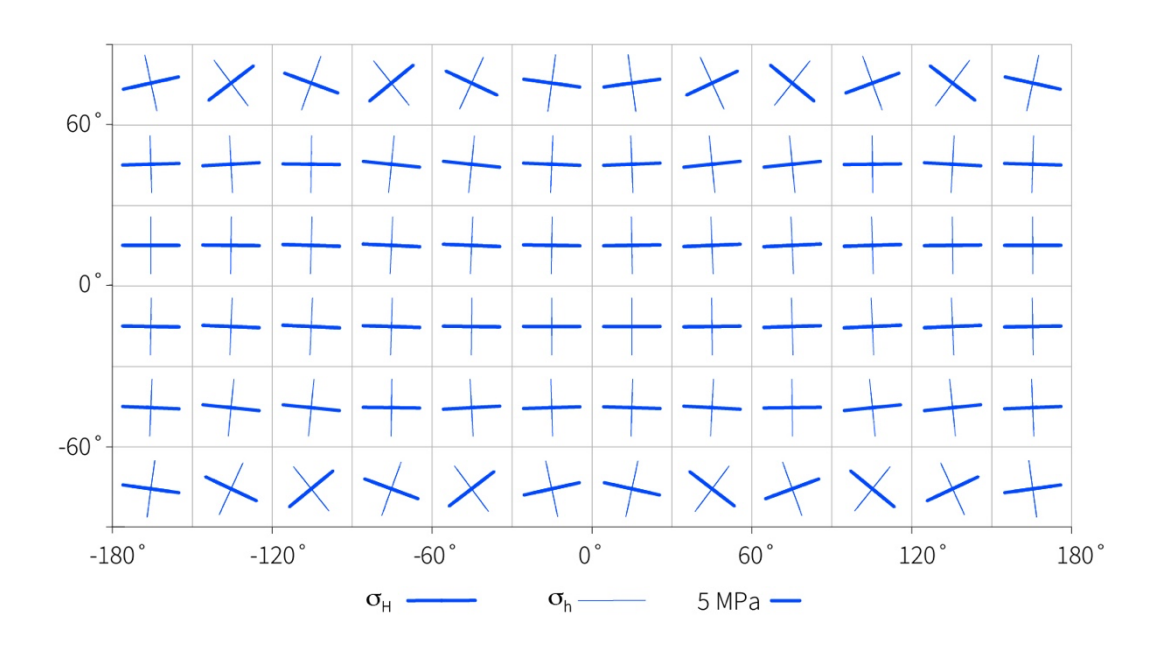


Figure 5.3: The horizontal principal stresses from Mercury's orbit and rotation shown as overlapping with stresses from global contraction.

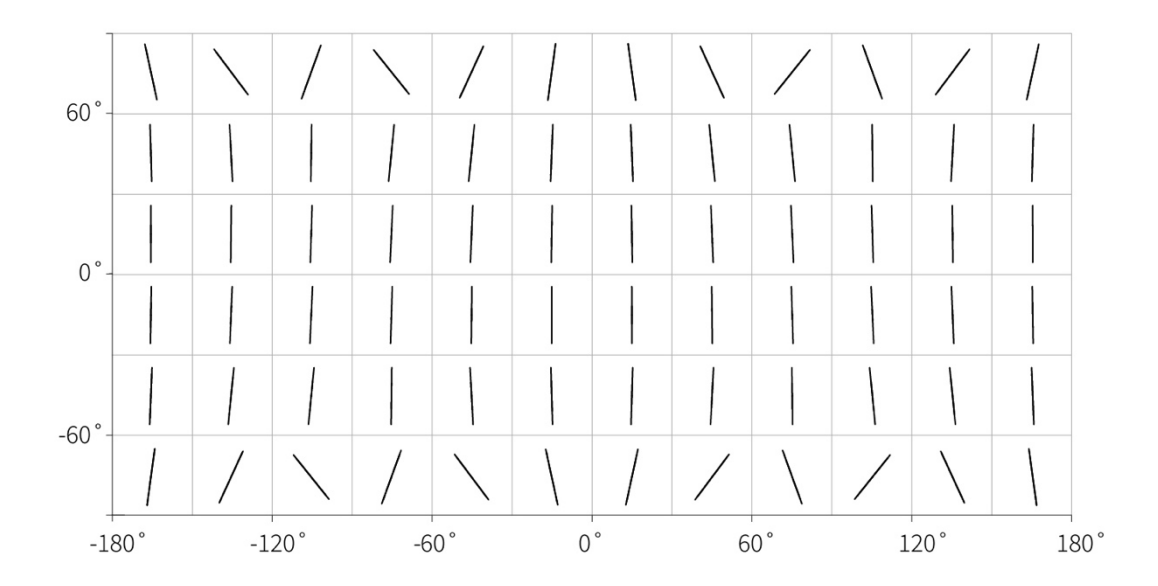


Figure 5.4: The optimal thrust fault orientations predicted for the stress field represented in Figure 5.3.

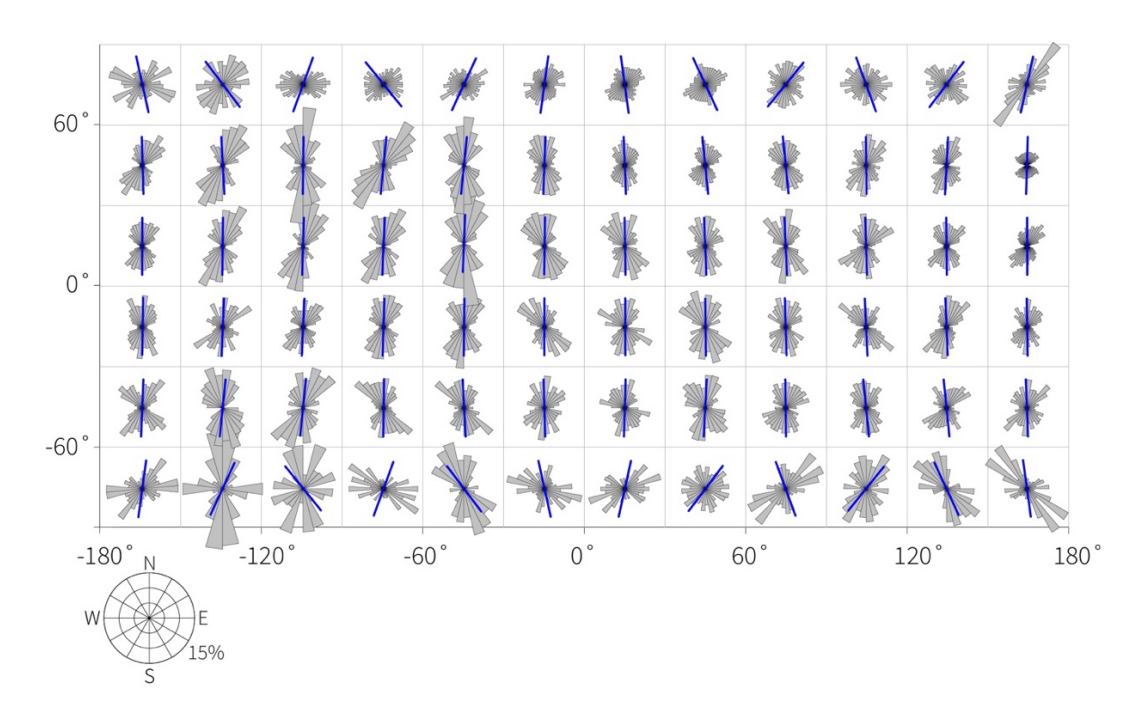


Figure 5.5: Predicted thrust fault patterns from Mercury's current eccentric 3:2 spin-orbit resonance with the sun superposed by global contraction shown as blue line segments overlain on rose diagrams representing a $30^{\circ} \times 30^{\circ}$ binning of latitudinal and longitudinal variations of structure orientations modified from Klimczak et al. (2025).

5.6 Tables

Table 5.1: Parameters used in the calculations of this work and the sources of their values.

Symbol	Definition	Value		
R	Radius of Mercury	2,440 km ^a		
h_2^T	Love number assuming fluid behavior	0.92 ^b		
n	Mean motion	$8.3 \times 10^7 \text{ rad/s}^{\circ}$		
G	Gravitational Constant	$6.67 \times 10^{-11} \text{ m}^3 \text{ kg}^{-1} \text{ s}^{-2 \text{ d}}$		
М	Mass of Mercury	$3.3 \times 10^{23} \text{ kg}^{\text{c}}$		
p	The spin/orbit ratio	3/2°		
e	Mercury's eccentricity	0.2056°		
$ heta_{ m rot}, \phi_{ m rot}$	Time averaged rotational pole coordinates	(2°, 0°)		
۵ ۵		(00° 0°)¢		
$ heta_{ ext{tidal}}, \phi_{ ext{tidal}}$	Time averaged subsolar point coordinates	(90,0)		

```
Mercury's 0.25<sup>e</sup>
                                ratio
                 Poisson's
                                           of
ν
                 lithosphere
                 The rigidity of Mercury's lithosphere
                                                                1.16 \times 10^{10} \text{ Pa}
μ
Е
                 Young's
                             Modulus of Mercury's 29 GPaf
                 lithosphere
<sup>a</sup>Perry et al. (2011)
<sup>b</sup>Xiao et al. (2024)
<sup>c</sup>Williams (2020)
<sup>d</sup>Newton (1686)
<sup>e</sup>Matsuyama and Nimmo (2009)
f(Klimczak and McCarthy, 2025)
```

Table 5.2 Thrust fault orientations for 30° by 30° latitudinal and longitudinal regions across Mercury as indicated by their center coordinates. Predicted thrust fault orientations of tides and rotation superposing global contraction are listed as optimal strikes. The weighted mean and standard deviation (Std. Dev.) of the observed fault strike data on Mercury are listed in comparison to the statistical modes. Data from Klimczak et al. (2025). All fault strike values are given in azimuth notation from 0° to 180°. Values in bold indicate match between predictions and orientations.

Lon	Lat	Optimal	Weighted Mean	Mode	Mode	Mode	Mode
(°)	(°)	Strike (°)	and Std Dev. (°)	1 (°)	2 (°)	3 (°)	4 (°)
-165	-75	8	176 ± 55	40	87	_	
-165	-45	2	9 ± 37	34	136	_	_
-165	-15	1	1 ± 38	12	154	_	_
-165	15	0	$\bm{2} \pm 40$	24	164	_	_
-165	45	178	3 ± 42	36	165	_	_
-165	75	168	6 ± 58	30	61	107	160
-135	-75	25	8 ± 50	12	90	169	_
-135	-45	6	9 ± 34	15	159	_	_
-135	-15	2	3 ± 35	51	157	_	_
-135	15	1	$\textbf{179} \pm \textbf{45}$	24	160	_	_
-135	45	177	$\textbf{175} \pm 36$	19	155	_	_
-135	75	143	10 ± 47	36	141	_	_
-105	-75	141	14 ± 59	28	96	166	_
-105	-45	6	16 ± 35	25	166	_	_

-105	-15	3	$\textbf{178} \pm 32$	33	153	_	_
-105	15	2	20 ± 41	15	171	_	_
-105	45	1	173 ± 39	10	154	_	_
-105	75	20	176 ± 48	88	_	_	_
-75	-75	20	4 ± 56	11	37	92	118
-75	-45	1	$\textbf{10} \pm 40$	27	136	_	_
-75	-15	2	176 ± 35	30	162	_	_
-75	15	3	5 ± 38	28	164	_	_
-75	45	6	$\textbf{176} \pm 40$	41	164	_	_
-75	75	141	177 ± 57	43	65	88	120
-45	-75	143	2 ± 55	13	153	_	_
-45	-45	177	10 ± 33	27	138	_	_
-45	-15	1	12 ± 31	14	155	_	_
-45	15	2	8 ± 36	13	172	_	_
-45	45	6	3 ± 41	8	169	_	_
-45	75	25	169 ± 38	25	62	133	_
-15	-75	168	173 ± 51	15	115	_	_
-15	-45	178	$\textbf{4} \pm 40$	16	56	159	_
-15	-15	0	175 ± 35	28	137	_	_
-15	15	1	14 ± 42	14	154	_	_
-15	45	2	$\textbf{4} \pm 46$	14	162	_	_
-15	75	8	8 ± 56	22	57	89	154
15	-75	12	1 ± 50	41	76	120	157

15	-45	2	4 ± 44	13	108	147	_
15	-15	0	$\textbf{7} \pm 40$	13	123	161	_
15	15	179	1 ± 41	13	160	_	_
15	45	178	4 ± 44	16	35	168	_
15	75	172	166 ± 59	41	62	155	_
45	-75	37	169 ± 50	53	81	157	_
45	-45	3	174 ± 42	17	131	_	_
45	-15	179	3 ± 42	21	159	_	_
45	15	178	169 ± 38	16	161	_	_
45	45	174	11 ± 42	12	46	171	_
45	75	155	6 ± 53	63	115	166	_
75	-75	160	179 ± 49	63	168	_	_
75	-45	179	164 ± 42	36	156	_	_
75	-15	178	6 ± 37	18	160	_	_
75	15	177	172 ± 41	11	148	_	_
75	45	174	171 ± 43	19	158	_	_
75	75	39	4 ± 48	34	126	165	_
105	-75	39	167 ± 54	31	96	171	_
105	-45	174	$\textbf{169} \pm 44$	35	158	_	_
105	-15	177	11 ± 39	29	131	_	_
105	15	178	177 ± 42	18	60	172	_
105	45	179	5 ± 42	9	43	102	146
105	75	160	3 ± 44	40	96	129	_

135	-75	155	5 ± 52	8	90	145	_
135	-45	174	$\textbf{176} \pm 39$	36	151	_	_
135	-15	178	$\textbf{179} \pm 39$	22	166	_	_
135	15	179	159 ± 38	42	153	_	_
135	45	3	168 ± 43	20	162	_	_
135	75	37	169 ± 43	20	53	134	_
165	-75	172	9 ± 48	74	128	147	_
165	-45	178	3 ± 42	44	160	_	_
165	-15	179	18 ± 40	22	45	152	_
165	15	0	3 ± 42	34	155	_	_
165	45	2	156 ± 46	15	35	52	126
165	75	12	169 ± 51	36	101	160	_

CHAPTER 6

CONCLUSIONS

This dissertation explores a wide range of topics concerning lithospheric shortening on Mercury. First, in *Chapter 2*, the legitimacy of the traditional categories "lobate scarps", "wrinkle ridges", and "high-relief ridges" is quantitatively tested using two multivariate statistical analyses. These analyses show that most landforms previously classified in one category are not distinctly different from landforms previously categorized into another. Second, in *Chapter 3* the subsurface of the wrinkle ridge and lobate scarp archetypes found from the distribution of the LDA in Chapter 2 is modeled using the MOVE geologic modeling software revealing that Mercury was host to a large variety of complex thrust systems. The data acquired from *Chapters 2* and 3 then informed the strain analysis in Chapter 4, which uses multiple fault data sets on Mercury to estimate multiple kilometers of radial contraction over a wide range of plausible physical configurations. Finally, in Chapter 5, the time-averaged horizontal stresses within Mercury's lithosphere caused by solar tides and Mercury's rotation are superposed onto the stresses caused by global contraction to predict fracture patterns. This dissertation thus covers four important topics regarding Mercury's contractional tectonic character. In the proceeding text, this chapter will summarize the contributions each chapter makes to the current understanding within the scientific community. Following this, open-ended questions and future work will be discussed.

Mercury's morphological spectrum of shortening landforms

Previously, most contractional tectonic landforms on non-Earth terrestrial bodies were classified as either lobate scarps, wrinkle ridges, or high-relief ridges (e.g., Melosh and McKinnon, 1988; Strom, 1979; Watters et al., 2004, 2001; Watters and Robinson, 1999). These landform designations are loosely defined by the general morphology of a few exemplary shortening landforms. Consequently, many shortening landforms on Mercury are difficult to designate to one of the traditional categories, and some works have since refrained from using these terminologies to describe Mercury's tectonics (e.g., Byrne et al., 2014; Crane and Klimczak 2019a). The principal component analysis and linear discriminant analyses presented in Chapter 2 demonstrates that the morphological variation across 100 randomly selected shortening landforms does not support the grouping of such landforms into the traditional categories. Instead, most shortening landforms fall on a spectrum between lobate scarps and wrinkle ridges, with few archetype landforms of each category. Additionally, the geologic unit a shortening landform forms in does not govern the morphology of that shortening landform. The variance of the morphologies of these shortening landforms formed in the smooth plains units and the intercrater plains shows substantial overlap. These findings suggest that the continued use of the traditional categories may prevent the enablement of new insights regarding the architecture of Mercury's contractional tectonics.

Geometric forward models of thrust systems on Mercury

The modeling results presented in *Chapter 3* inform the current understanding of Mercury's tectonic character. The 55 shortening landforms that make up the endmembers of the traditional category LDA conducted in *Chapter 2* are designated as lobate scarp and

wrinkle ridge archetypes and are selected for subsurface modeling. This modeling effort shows that Mercury is host to a wide range of complex thrust geometries including single-listric thrusts, imbricate stacks, and pop-up structures. Faults modeled in this work located in the smooth plains geologic units fault deeper than the depth estimates of the volcanically emplaced lavas that make up the smooth plains (Du et al., 2020; Head et al., 2011; Ostrach et al., 2015). This suggests that the formation mechanisms of the contractional tectonics both inside and outside the smooth plains units are the same. Alternatively, the load-induced subsidence suggested to form wrinkle ridges in the smooth plains units can be ruled out, and instead global contraction is likely the primary source of compressional horizontal stresses to create shortening landforms in both the intercrater plains and smooth plains units.

Resolving Mercury's global contraction discrepancy

The amount that Mercury has radially contracted due to long-sustained cooling is widely debated (e.g., Byrne et al., 2014; Watters, 2021). In *Chapter 4*, the methodology introduced by Twiss and Marrett (2010a, b) is successfully implemented to calculate Mercury's radial contraction using multiple fault data sets. The work in *Chapter 4* also calls into question the reasoning that a population of more-shallowly dipping thrust faults causes greater amounts of global contraction. This correlation is an artifact of the methodologies previously used to calculate Mercury's contraction. The method introduced by Twiss and Marrett (2010a, b) circumnavigates the strong dependence of the number of shortening landforms considered onto the amount of estimated radial contraction. The results of *Chapter 4* show that multiple data sets spanning almost three orders of magnitude of sample sizes produced relatively similar amounts of strain. *Chapter 4* both indicates that

this method can be applied to calculate the strain of non-Earth, faulted planetary surfaces, as well as advocates that Mercury has experienced multiple kilometers of radial contraction *after* the brittle strength of the lithosphere has been exceeded.

Mercury's Eccentric 3:2 Spin-Orbit Resonance and the Planet's Fracture Patterns

The effects of Mercury's current 3:2 spin-orbit resonance on the systematic fracture orientations throughout Mercury's surface have been proposed by previous works (Byrne et al., 2018; Klimczak et al., 2025) but have not yet been explored in detail as is done in *Chapter 5*. Here, the horizontal principal stresses caused by solar tides and Mercury's rotational bulge are calculated across Mercury's lithosphere and are found to only differ by a few KPa. Once global contraction forces all the stresses into compression past the unconfined compressive strength of the lithosphere (~10s of MPa; Schultz, 1993) the principal stresses become near isotropic. However, this small deviation from a near isotropic stress state causes the predicted thrust faulting to have preferred, optimal orientations. The work shown in *Chapter 5* reveals that these optimal fracture orientations align well with observed fracture trends presented in Klimczak et al. (2025, 2015). This work suggests that Mercury's current orbital configuration has likely affected the propagation of fractures on Mercury once compressional stresses from global contraction superseded the brittle strength of Mercury's lithosphere.

Open questions and future work

The research presented in this dissertation highlights the complex tectonic history of a planet that has undergone considerable global contraction. Further work using the same suite of analyses and modeling onto other terrestrial bodies that host a similar set of contractional tectonics would reveal much about their tectonic character and history.

Statistical analyses of contractional morphology, forward modeling of non-Earth fault architectures, application of alternative strain assessments, and new insight into tidal and rotational influence of fracture propagation of planetary bodies are all aspects of this dissertation that can be applied to other objects throughout the solar system.

Chapter 2 presents work on the application of statistical analyses onto the morphology of Mercury's shortening landforms revealing the variability of Mercury's contractional tectonics. A similar analysis has been applied to Mars in McCullough et al. (2024), from which the LDA showed similar distributions. However, McCullough et al. (2024) had further defined, quantitatively, the distinctions between lobate scarps and wrinkle ridges, rather than assess the legitimacy of these categories. Additionally, the assessment of the different terrain types and their potential to influence Martian shortening landform variability has yet to be explored. This analysis can also be applied to the Moon, which hosts an abundant number of shortening landforms that have been classified as lobate scarps and wrinkle ridges (e.g., Watters, 1988). Interestingly, topographic and image data available for Lunar lobate scarps and wrinkle ridges is of much higher resolution than data available for Mercury, with resolutions of less than 1m to up to a few m (e.g., Barker et al., 2016; Henriksen et al., 2017). Therefore, the morphology of Lunar shortening landforms of scales much smaller than those on Mercury have been studied (e.g., Frueh et al., 2025; Watters et al., 2010). Lunar shortening landforms may produce different morphological trends if similar statistical analyses are performed on these structures.

The modeling work done in *Chapter 3* could also be applied to a wide range of tectonic features found throughout the solar system. Similar modeling was conducted for shortening landforms on Mars (McCullough et al. 2024), however this work did not utilize

the new model control points presented in *Chapter 3*. Conducting a new analysis on a set of randomly selected shortening landforms on Mars would reveal important aspects of the Martian tectonic character. Furthermore, a similar modeling analysis on the moon would reveal whether wrinkle ridges in the Lunar Mare host faults that penetrate beneath the volcanic lava emplacements that make up the Mare geologic units, as such tectonics have also been ascribed to lithospheric subsidence (e.g., Watters, 1988).

Chapter 4 had proven that an alternative way to calculate the strain of a faulted volume was viable in determining the strain due to global contraction accommodated by Mercury's population of faults. Prior to this dissertation, the methodology introduced by Twiss and Marrett (2010a, b) had yet to be applied to any non-Earth faulted volume of rock. Future work using this methodology could be applied to terrestrial objects like the Moon, or Mars, which may have experienced global contraction (e.g., Frueh et al., 2023; Klimczak, 2015; Nahm and Schultz, 2011). Alternatively, a strain analysis of Venus' Tesserae could be used to compare with the strains associated with orogenic settings on Earth, which may provide clues if such regions were created via a plate tectonic-like mechanism. It is important to note that Chapters 2 and 3 informed the results of Chapter 4, and a similar suite of research projects should be conducted in order to best inform the results of other planetary objects when testing this method.

Chapter 5 had shown that stresses within Mercury's lithosphere caused by rotation and solar tides likely subtly influence tectonic patterns when they are overlain by stresses from global contraction. However, these stresses are time-dependently-cyclically loaded onto Mercury's surface throughout Mercury's 3:2 spin-orbit cycle. The application of the mechanical fatiguing of the lithosphere due to tides and rotation repeating over millions of

cycles of Mercury's orbit has yet to be fully explored. *Chapter 5* indicates that time-averaged stresses caused by solar tides and rotation alone are insufficient to produce stresses that would induce any fracturing, but the cyclicity of such stresses over geologically long time periods would weaken Mercury's lithosphere. The fatiguing in parts of Mercury's lithosphere that are geographically dependent on Mercury's 3:2 spin-orbit resonance has the potential to influence fault orientations and their area densities.

Future work will thus have to incorporate the fatiguing effects onto Mercury's lithosphere caused by the cyclical loading of tidal and rotational deformation. The weakening effects of Mercury's orbit has been previously proposed by Klimczak et al. (2015). Mechanical fatiguing related to tides is a process that has been proposed for planetary bodies throughout the solar system including the moon (Frohlich and Nakamura, 2009; Patzek and Rüsch, 2022) and the icy satellites (e.g., Hammond et al., 2018, 2015). For the moon, tidally induced mechanical fatiguing has been used to explain lunar seismic activity (Frohlich and Nakamura, 2009) and thermal fatiguing due to the moon's orbit has shown to be sufficient to breakdown rocks (Patzek and Rüsch, 2022). Cycloid fractures on Europa appear to form below the failure threshold expected for the moon's lithosphere (Hoppa et al., 1999), and so fatiguing has been proposed as the primary mode for these systematic fracture patterns (Rhoden et al., 2021). However, these objects orbit planets in a 1:1 spin-orbit resonance or have varying obliquities or precessions that could influence the stresses they experience. It is yet to be explored how the cyclical stresses of Mercury's current orbit overlain by substantial global contraction would be affected by tidally and rotation-driven fatiguing. Future work will then include the weakening effects of tidal and rotation fatiguing to assess the geographic variations of the brittle strength of Mercury's lithosphere, perhaps while incorporating empirical fatiguing data from rock testing of basalt.

Concluding remarks

The work presented in this dissertation highlights a wide range of questions that pertain to the tectonic character of lithospheric shortening throughout the solar system, all stemming from research regarding the shortening landforms of Mercury. Answering these questions will provide necessary insight into the structural elements, the tectonic histories, and the influence the thermal and orbital evolutions of terrestrial bodies throughout the solar system have on the deformation of their lithospheres.

REFERENCES

- Attewell, P.B., Farmer, I.W., 1973. Fatigue behaviour of rock. Int. J. Rock Mech. Min. Sci. Géoméch. Abstr. 10, 1–9. https://doi.org/10.1016/0148-9062(73)90055-7
- Bally, A. W., Gordy, P.L., and Steward, GA., 1966. Structure, seismic data and orogenic evolution of the southern Canadian Rocky Mountains. Bull. Can. Petrol. Geol. 14, 337–381.
- Banks, M.E., Xiao, Z., Watters, T.R., Strom, R.G., Braden, S.E., Chapman, C.R., Solomon, S.C., Klimczak, C., Byrne, P.K., 2015. Duration of activity on lobate-scarp thrust faults on Mercury. J Geophys Res Planets 120, 1751–1762. https://doi.org/10.1002/2015je004828
- Barker, M.K., Mazarico, E., Neumann, G.A., Zuber, M.T., Haruyama, J., Smith, D.E., 2016. A new lunar digital elevation model from the Lunar Orbiter Laser Altimeter and SELENE Terrain Camera. Icarus 273, 346–355. https://doi.org/10.1016/j.icarus.2015.07.039
- Becker, K. J., Robinson, M. S., Becker, T. L., Weller, L. A., Edmundson, K. L., Neumann, G. A., Perry, M. E., Solomon, S. C., 2016. First global digital elevation model of Mercury. Lunar Planet. Sci. XLVII. Abstract 2959.
- Benkhoff, J., Murakami, G., Baumjohann, W., Besse, S., Bunce, E., Casale, M., Cremosese, G., Glassmeier, K.-H., Hayakawa, H., Heyner, D., Hiesinger, H., Huovelin, J., Hussmann, H., Iafolla, V., Iess, L., Kasaba, Y., Kobayashi, M.,

- Milillo, A., Mitrofanov, I.G., Montagnon, E., Novara, M., Orsini, S., Quemerais, E., Reininghaus, U., Saito, Y., Santoli, F., Stramaccioni, D., Sutherland, O., Thomas, N., Yoshikawa, I., Zender, J., 2021. BepiColombo Mission Overview and Science Goals. Space Sci. Rev. 217, 90. https://doi.org/10.1007/s11214-021-00861-4
- Benz, W., Slattery, W.L. and Cameron, A.G.W. 1988. Collisional stripping of Mercury's mantle. Icarus, 74, 516–528.
- Bertone, S., Mazarico, E., Barker, M.K., Siegler, M.A., Martinez-Camacho, J.M., Hamill, C.D., Glantzberg, A.K., Chabot, N.L., 2023. Highly Resolved Topography and Illumination at Mercury's South Pole from MESSENGER MDIS NAC. Planet. Sci. J. 4, 21. https://doi.org/10.3847/psj/acaddb
- Beuthe, M., 2010. East—west faults due to planetary contraction. Icarus 209, 795–817. https://doi.org/10.1016/j.icarus.2010.04.019
- Bilotti, F., Suppe, J., 1999. The Global Distribution of Wrinkle Ridges on Venus. Icarus 139, 137–157. https://doi.org/10.1006/icar.1999.6092
- Boyer, S. E., Elliot, D. 1982. Thrust Systems. AAPG Bull. 66. https://doi.org/10.1306/03b5a77d-16d1-11d7-8645000102c1865d
- Brandes, C., Tanner, D.C., 2014. Fault-related folding: A review of kinematic models and their application. Earth-Sci. Rev. 138, 352–370.

 https://doi.org/10.1016/j.earscirev.2014.06.008

- Breuer, D., Hauck, S.A., Buske, M., Pauer, M., Spohn, T., 2007. Interior Evolution of Mercury. Space Sci. Rev. 132, 229–260. https://doi.org/10.1007/s11214-007-9228-9
- Buoninfante, S., Galluzzi, V., Ferranti, L., Rothery, D.A., Hiesinger, H., Guzzetta, L., Prüße, F., Man, B., Lennox, A.R., Blance, A., Milano, M., Palumbo, P., 2025.

 Geology of the Michelangelo quadrangle (H12), Mercury. J. Maps 21, 2451791.

 https://doi.org/10.1080/17445647.2025.2451791
- Burns, J. A., 1975. The angular momenta of solar system bodies: Implications for asteroid strengths. Icarus, 25, 545–554.
- Butler, R.W.H., 1987. Thrust sequences. J Geol Soc London 144, 619–634. https://doi.org/10.1144/gsjgs.144.4.0619
- Byrne, P. K., Klimczak, C., LaFond, J. K., 2016. The East Kaibab monocline: A Terran lobate scarp? Lunar Planet. Sci. XLVII. Abstract 1022.
- Byrne, P.K., Klimczak, C., McGovern, P.J., Mazarico, E., James, P.B., Neumann, G.A., Zuber, M.T., Solomon, S.C., 2015. Deep-seated thrust faults bound the Mare Crisium lunar mascon. Earth Planet. Sci. Lett. 427, 183–190.

 https://doi.org/10.1016/j.epsl.2015.06.022
- Byrne, P.K., Klimczak, C., Şengör, A.M.C., 2018. The tectonic character of Mercury. In: Solomon, S.C. (Ed.), Mercury. The View after MESSENGER. pp. 249–286.

- Byrne, P.K., Klimczak, C., Şengör, A.M.C., Solomon, S.C., Watters, T.R., II, S.A.H., 2014. Mercury's global contraction much greater than earlier estimates. Nat Geosci 7, 301–307. https://doi.org/10.1038/ngeo2097
- Cerfontaine, B., Collin, F., 2018. Cyclic and Fatigue Behaviour of Rock Materials:

 Review, Interpretation and Research Perspectives. Rock Mech. Rock Eng. 51,

 391–414. https://doi.org/10.1007/s00603-017-1337-5
- Chapple, W.M., 1978. Mechanics of thin-skinned fold-and-thrust belts. GSA Bulletin 89, 1189–1198. https://doi.org/10.1130/0016-7606(1978)89<1189:motfb>2.0.co;2
- Cladouhos, T.T., Marrett, R., 1996. Are fault growth and linkage models consistent with power-law distributions of fault lengths? J. Struct. Geol. 18, 281–293. https://doi.org/10.1016/s0191-8141(96)80050-2
- Clark, R.M., Cox, S.J.D., 1996. A modern regression approach to determining fault displacement-length scaling relationships. J Struct Geol 18, 147–152. https://doi.org/10.1016/s0191-8141(96)80040-x
- Clark, J. D., van der Bogert, C. H., Hiesinger H., Bernardt, H., 2017. Wrinkle ridgelobate scarp transition of West Serenitatis: Indications for recent tectonic activity. Lunar Planet. Sci. XLVIII. Abstract 1001.

- Collins, G.C., Patterson, G.W., Detelich, C.E., Prockter, L.M., Kattenhorn, S.A., Cooper,
 C.M., Rhoden, A.R., Cutler, B.B., Oldrid, S.R., Perkins, R.P., Rezza, C.A., 2022.
 Episodic Plate Tectonics on Europa: Evidence for Widespread Patches of Mobile-Lid Behavior in the Antijovian Hemisphere. J. Geophys. Res.: Planets 127,
 e2022JE007492. https://doi.org/10.1029/2022je007492
- Collins, M.S., Byrne, P.K., Klimczak, C., Mazarico, E., 2023. Thrust Faults Bound an Elevated Mantle Plug Beneath Several Lunar Basins. J. Geophys. Res.: Planets 128. https://doi.org/10.1029/2022je007682
- Connors, C.D., Hughes, A.N., Ball, S.M., 2021. Forward kinematic modeling of fault-bend folding. J. Struct. Geol. 143, 104252.

 https://doi.org/10.1016/j.jsg.2020.104252
- Cowie, P.A., Scholz, C.H., 1992. Displacement-length scaling relationship for faults: data synthesis and discussion. J Struct Geol 14, 1149–1156.

 https://doi.org/10.1016/0191-8141(92)90066-6
- Cowie, P.A., Scholz, C.H., Edwards, M., Malinverno, A., 1993. Fault strain and seismic coupling on mid-ocean ridges. J. Geophys. Res.: Solid Earth 98, 17911–17920. https://doi.org/10.1029/93jb01567
- Crane, K., 2020a. Structural interpretation of thrust fault-related landforms on Mercury using Earth analogue fault models. Geomorphology 369, 107366.

 https://doi.org/10.1016/j.geomorph.2020.107366

- Crane, K., 2020b. Approach and application of industry software to structural investigations in the subsurface of Mercury's thrust fault-related landforms. J Struct Geol 141, 104218. https://doi.org/10.1016/j.jsg.2020.104218
- Crane, K.T., Klimczak, C., 2017. Timing and rate of global contraction on Mercury.

 Geophys. Res. Lett. 44, 3082–3089. https://doi.org/10.1002/2017gl072711
- Crane, K.T., Klimczak, C., 2019a. Tectonic patterns of shortening landforms in Mercury's northern smooth plains. Icarus 317, 66–80.

 https://doi.org/10.1016/j.icarus.2018.05.034
- Crane, K.T., Klimczak, C., 2019b. A 3-D structural model of the Saddle Mountains,

 Yakima Fold Province, Washington, USA: Implications for Late Tertiary tectonic
 evolution of the Columbia River Flood Basalt Province. Tectonophysics 766, 1–
 13. https://doi.org/10.1016/j.tecto.2019.05.015
- Dahlstrom, C.D.A., 1969. Balanced cross sections. Can. J. Earth Sci. 6, 743–757. https://doi.org/10.1139/e69-069
- Davis, J. C., 2002. Statistics and Data Analysis in Geology, Third Edition. ISBN: 978-0-471-17275-8

- Denevi, B.W., Chabot, N.L., Murchie, S.L., Becker, K.J., Blewett, D.T., Domingue, D.L., Ernst, C.M., Hash, C.D., Hawkins, S.E., Keller, M.R., Laslo, N.R., Nair, H., Robinson, M.S., Seelos, F.P., Stephens, G.K., Turner, F.S., Solomon, S.C., 2017. Calibration, Projection, and Final Image Products of MESSENGER's Mercury Dual Imaging System. Space Sci. Rev. 214, 2. https://doi.org/10.1007/s11214-017-0440-y
- Denevi, B.W., Ernst, C.M., Meyer, H.M., Robinson, M.S., Murchie, S.L., Whitten, J.L.,
 Head, J.W., Watters, T.R., Solomon, S.C., Ostrach, L.R., Chapman, C.R., Byrne,
 P.K., Klimczak, C., Peplowski, P.N., 2013. The distribution and origin of smooth
 plains on Mercury. J Geophys Res Planets 118, 891–907.
 https://doi.org/10.1002/jgre.20075
- Denevi, B.W., Robinson, M.S., Solomon, S.C., Murchie, S.L., Blewett, D.T., Domingue, D.L., McCoy, T.J., Ernst, C.M., Head, J.W., Watters, T.R., Chabot, N.L., 2009.

 The Evolution of Mercury's Crust: A Global Perspective from MESSENGER.

 Science 324, 613–618. https://doi.org/10.1126/science.1172226
- Di Achille, G.D., Popa, C., Massironi, M., Epifani, E.M., Zusi, M., Cremonese, G., Palumbo, P., 2012. Mercury's radius change estimates revisited using MESSENGER data. Icarus 221, 456–460. https://doi.org/10.1016/j.icarus.2012.07.005

- Du, J., Wieczorek, M.A., Fa, W., 2020. Thickness of Lava Flows Within the Northern Smooth Plains on Mercury as Estimated by Partially Buried Craters. Geophys. Res. Lett. 47. https://doi.org/10.1029/2020g1090578
- Dzurisin, D., 1978. The tectonic and volcanic history of Mercury as inferred from studies of scarps, ridges, troughs, and other lineaments. J Geophys Res Solid Earth 83, 4883–4906. https://doi.org/10.1029/jb083ib10p04883
- Egan, S.S., Buddin, T.S., Kane, S., Williams, G.D., 1997. Three-dimensional modelling and visualisation in Structural Geology: New Techniques for the restoration and balancing of volumes. Elect. Geol. 1, 67–82.
- Egea-Gonzalez, I., Jiménez-Díaz, A., Parro, L.M., López, V., Williams, J.-P., Ruiz, J., 2017. Thrust fault modeling and Late-Noachian lithospheric structure of the circum-Hellas region, Mars. Icarus 288, 53–68.

 https://doi.org/10.1016/j.icarus.2017.01.028
- Egea-González, I., Ruiz, J., Fernández, C., Williams, J.-P., Márquez, Á., Lara, L.M., 2012. Depth of faulting and ancient heat flows in the Kuiper region of Mercury from lobate scarp topography. Planet Space Sci 60, 193–198.

 https://doi.org/10.1016/j.pss.2011.08.003
- Erarslan, N., Williams, D.J., 2012. The damage mechanism of rock fatigue and its relationship to the fracture toughness of rocks. Int. J. Rock Mech. Min. Sci. 56, 15–26. https://doi.org/10.1016/j.ijrmms.2012.07.015

- Ferrari, S., Massironi, M., Marchi, S., Byrne, P.K., Klimczak, C., Martellato, E., Cremonese, G., 2015. Age relationships of the Rembrandt basin and Enterprise Rupes, Mercury. Geol. Soc., Lond., Spéc. Publ. 401, 159–172. https://doi.org/10.1144/sp401.20
- Freed, A.M., Blair, D.M., Watters, T.R., Klimczak, C., Byrne, P.K., Solomon, S.C., Zuber, M.T., Melosh, H.J., 2012. On the origin of graben and ridges within and near volcanically buried craters and basins in Mercury's northern plains. J. Geophys. Res.: Planets 117. https://doi.org/10.1029/2012je004119
- Frohlich, C., Nakamura, Y., 2009. The physical mechanisms of deep moonquakes and intermediate-depth earthquakes: How similar and how different? Phys. Earth Planet. Inter. 173, 365–374. https://doi.org/10.1016/j.pepi.2009.02.004
- Frueh, T., Hetzel, R., Watters, T.R., Bogert, C.H. van der, Clark, J.D., Nypaver, C., Hiesinger, H., 2025. Extensional structures at lunar lobate scarps. Icarus 432, 116493. https://doi.org/10.1016/j.icarus.2025.116493
- Frueh, T., Hiesinger, H., Bogert, C.H. van der, Clark, J.D., Watters, T.R., Schmedemann,
 N., 2023. Timing and Origin of Compressional Tectonism in Mare Tranquillitatis.
 J. Geophys. Res.: Planets 128. https://doi.org/10.1029/2022je007533
- Galluzzi, V., Di Achille, G.D., Ferranti, L., Popa, C., Palumbo, P., 2015. Faulted craters as indicators for thrust motions on Mercury. Geol. Soc., Lond., Spéc. Publ. 401, 313–325. https://doi.org/10.1144/sp401.17

- Galluzzi, V., Ferranti, L., Massironi, M., Giacomini, L., Guzzetta, L., Palumbo, P., 2019.
 Structural Analysis of the Victoria Quadrangle Fault Systems on Mercury:
 Timing, Geometries, Kinematics, and Relationship with the High-Mg Region. J.
 Geophys. Res.: Planets 124, 2543–2562. https://doi.org/10.1029/2019je005953
- Galluzzi, V., Guzzetta, L., Ferranti, L., Di Achille, G.D., Rothery, D.A., Palumbo, P., 2016. Geology of the Victoria quadrangle (H02), Mercury. J. Maps 12, 227–238. https://doi.org/10.1080/17445647.2016.1193777
- Galluzzi, V., Guzzetta, L., Mancinelli, P., Giacomini, L., Lewang, A.M., Malliband, C., Masca, A., Pegg, D., Wright, J., Ferranti, L., Hiesinger, H., Massironi, M., Pauselli, C., Rothery, D.A., Palumbo, P., 2018. The making of the 1:3M geological map series of Mercury: status and updates. Mercury: Current and Future Science. Abstract 6075.
- Giacomini, L., Galluzzi, V., Massironi, M., Ferranti, L., Palumbo, P., 2022. Geology of the Kuiper quadrangle (H06), Mercury. J. Maps 18, 246–257.

 https://doi.org/10.1080/17445647.2022.2035268
- Giacomini, L., Guzzetta, L., Galluzzi, V., Ferranti, L., Palumbo, P., 2024. Geology of Tolstoj quadrangle (H08), Mercury. J. Maps 20, 2421600.

 https://doi.org/10.1080/17445647.2024.2421600
- Goldreich, P., Peale, S., 1966. Spin-orbit coupling in the solar system. Astron. J. 71, 425. https://doi.org/10.1086/109947

- Golombek, M. P., Plescia, J. B., Franklin, B. J., 1991. Faulting and folding in the formation of planetary wrinkle ridges. Proceed. of Lunar Planet. Sci., 21, 679–693. https://ui.adsabs.harvard.edu/abs/1991LPSC...21..679G
- Golombek, M.P., Anderson, F.S., Zuber, M.T., 2001. Martian wrinkle ridge topography:

 Evidence for subsurface faults from MOLA. J. Geophys. Res.: Planets 106,

 23811–23821. https://doi.org/10.1029/2000je001308
- Greenberg, R., Geissler, P., Hoppa, G., Tufts, B.R., Durda, D.D., Pappalardo, R., Head, J.W., Greeley, R., Sullivan, R., Carr, M.H., 1998. Tectonic Processes on Europa: Tidal Stresses, Mechanical Response, and Visible Features. Icarus 135, 64–78. https://doi.org/10.1006/icar.1998.5986
- Guzzetta, L., Galluzzi, V., Ferranti, L., Palumbo, P., 2017. Geology of the Shakespeare quadrangle (H03), Mercury. J. Maps 13, 227–238. https://doi.org/10.1080/17445647.2017.1290556
- Hammond, N.P., Barr, A.C., Cooper, R.F., Caswell, T.E., Hirth, G., 2018. Experimental Constraints on the Fatigue of Icy Satellite Lithospheres by Tidal Forces. J Geophys Res Planets 123, 390–404. https://doi.org/10.1002/2017je005464
- Hammond, N.P., Barr, A.C., Hirth, G., Parmentier, E.M., 2015. The fatigue of icy satellite lithospheres by diurnal tidal forces. Lunar Planet. Sci. XLVI. Abstract 1511.

- Hauck, S.A., Dombard, A.J., Phillips, R.J., Solomon, S.C., 2004. Internal and tectonic evolution of Mercury. Earth Planet. Sci. Lett. 222, 713–728. https://doi.org/10.1016/j.epsl.2004.03.037
- Head, J.W., Chapman, C.R., Strom, R.G., Fassett, C.I., Denevi, B.W., Blewett, D.T.,
 Ernst, C.M., Watters, T.R., Solomon, S.C., Murchie, S.L., Prockter, L.M., Chabot,
 N.L., Gillis-Davis, J.J., Whitten, J.L., Goudge, T.A., Baker, D.M.H., Hurwitz,
 D.M., Ostrach, L.R., Xiao, Z., Merline, W.J., Kerber, L., Dickson, J.L., Oberst, J.,
 Byrne, P.K., Klimczak, C., Nittler, L.R., 2011. Flood volcanism in the northern
 high latitudes of Mercury revealed by MESSENGER. Science 333, 1853–6.
 https://doi.org/10.1126/science.1211997
- Hedman, M.M., Gosmeyer, C.M., Nicholson, P.D., Sotin, C., Brown, R.H., Clark, R.N., Baines, K.H., Buratti, B.J., Showalter, M.R., 2013. An observed correlation between plume activity and tidal stresses on Enceladus. Nature 500, 182–184. https://doi.org/10.1038/nature12371
- Henriksen, M.R., Manheim, M.R., Burns, K.N., Seymour, P., Speyerer, E.J., Deran, A., Boyd, A.K., Howington-Kraus, E., Rosiek, M.R., Archinal, B.A., Robinson, M.S., 2017. Extracting accurate and precise topography from LROC narrow angle camera stereo observations. Icarus 283, 122–137. https://doi.org/10.1016/j.icarus.2016.05.012

- Herrero-Gil, A., Ruiz, J., Romeo, I., 2019. 3D modeling of planetary lobate scarps: The case of Ogygis Rupes, Mars. Earth Planet Sc Lett 532, 116004. https://doi.org/10.1016/j.epsl.2019.116004
- Herrero-Gil, A., Ruiz, J., Romeo, I., 2020. Lithospheric Contraction on Mars: A 3D Model of the Amenthes Thrust Fault System. J. Geophys. Res.: Planets 125. https://doi.org/10.1029/2019je006201
- Hoolst, T.V., Jacobs, C., 2003. Mercury's tides and interior structure. J. Geophys. Res.: Planets 108. https://doi.org/10.1029/2003je002126
- Hopgood, A.M., 1987. Imbricate structure. In: Structural Geology and Tectonics.

 Encyclopedia of Earth Science. pp 334–336. https://doi.org/10.1007/3-540-31080-0_50
- Hoppa, G.V., Tufts, B.R., Greenberg, R., Geissler, P.E., 1999. Formation of Cycloidal Features on Europa. Science 285, 1899–1902.

 https://doi.org/10.1126/science.285.5435.1899
- Hughes, A.N., Benesh, N.P., Shaw, J.H., 2014. Factors that control the development of fault-bend versus fault-propagation folds: Insights from mechanical models based on the discrete element method (DEM). J. Struct. Geol. 68, 121–141. https://doi.org/10.1016/j.jsg.2014.09.009

- Hurford, T.A., Asphaug, E., Spitale, J.N., Hemingway, D., Rhoden, A.R., Henning,
 W.G., Bills, B.G., Kattenhorn, S.A., Walker, M., 2016. Tidal disruption of Phobos as the cause of surface fractures. J. Geophys. Res.: Planets 121, 1054–1065.
 https://doi.org/10.1002/2015je004943
- Hurford, T.A., Henning, W.G., Maguire, R., Lekic, V., Schmerr, N., Panning, M., Bray, V.J., Manga, M., Kattenhorn, S.A., Quick, L.C., Rhoden, A.R., 2020. Seismicity on tidally active solid-surface worlds. Icarus 338, 113466.
 https://doi.org/10.1016/j.icarus.2019.113466
- Jackson, J., McKenzie, D., 1983. The geometrical evolution of normal fault systems. J. Struct. Geol. 5, 471–482. https://doi.org/10.1016/0191-8141(83)90053-6
- Kaula, W. M., 1968 (Ed.). An Introduction to Planetary Physics: The Terrestrial Planets.
- Klimczak, C., 2015. Limits on the brittle strength of planetary lithospheres undergoing global contraction. J. Geophys. Res.: Planets 120, 2135–2151.

 https://doi.org/10.1002/2015je004851
- Klimczak, C., Byrne, P.K., Solomon, S.C., 2015. A rock-mechanical assessment of Mercury's global tectonic fabric. Earth Planet Sc Lett 416, 82–90. https://doi.org/10.1016/j.epsl.2015.02.003
- Klimczak, C., Crane, K.T., Byrne, P.K., 2025. Mercury has multiple, superposed global tectonic patterns. Earth Planet. Sci. Lett. 658, 119331.

 https://doi.org/10.1016/j.epsl.2025.119331

- Klimczak, C., Ernst, C.M., Byrne, P.K., Solomon, S.C., Watters, T.R., Murchie, S.L., Preusker, F., Balcerski, J.A., 2013. Insights into the subsurface structure of the Caloris basin, Mercury, from assessments of mechanical layering and changes in long-wavelength topography. J. Geophys. Res.: Planets 118, 2030–2044. https://doi.org/10.1002/jgre.20157
- Klimczak, C., Kling, C.L., Byrne, P.K., 2018. Topographic Expressions of Large Thrust Faults on Mars. J Geophys Res Planets 123, 1973–1995.

 https://doi.org/10.1029/2017je005448
- Klimczak, C., McCarthy, C., 2025 Planetary Geomechanics. In: Klimczak, C., Collins, G., Byrne, P. K. (Eds.): Comparative Tectonism across the Solar System.

 (Chapter 3), Book chapter Accepted Book Chapter
- Klimczak, C., Watters, T.R., Ernst, C.M., Freed, A.M., Byrne, P.K., Solomon, S.C., Blair, D.M., Head, J.W., 2012. Deformation associated with ghost craters and basins in volcanic smooth plains on Mercury: Strain analysis and implications for plains evolution. J. Geophys. Res.: Planets 117.

 https://doi.org/10.1029/2012je004100
- Lammlein, D.R., Lathan, G.B., Dorman, J., Nakamura, Y., Ewing, M., 1974. Lunar seismicity, structure, and tectonics. Rev. Geophys. 12, 1–21. https://doi.org/10.1029/rg012i001p00001

- Last, G.V., Winsor, K., Unwin, S.D., 2012. A Summary of Information on the Behavior of the Yakima Fold Belt as a Structural Entity -- Topical Report. https://doi.org/10.2172/1053763
- Latham, G., Ewing, M., Dorman, J., Lammlein, D., Press, F., Toksoz, N., Sutton, G.,

 Duennebier, F., Nakamura, Y., 1971. Moonquakes. Sci. (N. York, NY) 174, 687–
 92. https://doi.org/10.1126/science.174.4010.687
- Loveless, S., Klimczak, C., McCullough, L., Crane, K., Holland, S., Byrne, P., 2024a.

 Code and Data for 'A statistical evaluation of the morphological variability of shortening landforms on Mercury.', Revised, Mendeley Data, V2, doi:10.17632/8968vkgpds.2
- Loveless, S., Klimczak, C., Crane, K., Byrne, P., 2024b. Models, topographic profiles, and data for 'Geometric forward modeling of thrust systems underlying shortening landforms on Mercury.', Mendeley Data, V1, https://doi.org/10.17632/k4yrmr5j6k.1.
- Maindonald, J., Braun, W.J., 2003. Data Analysis and Graphics Using R an Example-Based Approach, Third Edition. ISBN-13 978-0-511-71286-9
- Malliband, C.C., Rothery, D.A., Balme, M.R., Conway, S.J., Pegg, D.L., Wright, J., 2023. Geology of the Derain quadrangle (H10), Mercury. J. Maps 19, 2112774. https://doi.org/10.1080/17445647.2022.2112774

- Man, B., Rothery, D.A., Balme, M.R., Conway, S.J., Wright, J., 2023a. Widespread small grabens consistent with recent tectonism on Mercury. Nat. Geosci. 16, 856–862. https://doi.org/10.1038/s41561-023-01281-5
- Man, B., Rothery, D.A., Balme, M.R., Conway, S.J., Wright, J., Pegg, D.L., Lennox,
 A.R., Buoninfante, S., 2023b. Geology of the Neruda quadrangle (H13), Mercury.
 J. Maps 19, 2256353. https://doi.org/10.1080/17445647.2023.2256353
- Mancinelli, P., Minelli, F., Pauselli, C., Federico, C., 2016. Geology of the Raditladi quadrangle, Mercury (H04). J. Maps 12, 190–202. https://doi.org/10.1080/17445647.2016.1191384
- Manga, M., Zhai, G., Wang, C., 2019. Squeezing Marsquakes Out of Groundwater. Geophys. Res. Lett. 46, 6333–6340. https://doi.org/10.1029/2019gl082892
- Marshall, S.T., Kattenhorn, S.A., 2005. A revised model for cycloid growth mechanics on Europa: Evidence from surface morphologies and geometries. Icarus 177, 341–366. https://doi.org/10.1016/j.icarus.2005.02.022
- Martinez-Torres, L.M., Ramon-Lluch, R., Eguiluz, L., 1994. Tectonic wedges: geometry and kinematic interpretation. J. Struct. Geol. 16, 1491–1494.

 https://doi.org/10.1016/0191-8141(94)90011-6
- Matsuyama, I., Keane, J.T., Trinh, A., Beuthe, M., Watters, T.R., 2021. Global tectonic patterns of the Moon. Icarus 358, 114202. https://doi.org/10.1016/j.icarus.2020.114202

- Matsuyama, I., Nimmo, F., 2008. Tectonic patterns on reoriented and despun planetary bodies. Icarus 195, 459–473. https://doi.org/10.1016/j.icarus.2007.12.003
- Matsuyama, I., Nimmo, F., 2009. Gravity and tectonic patterns of Mercury: Effect of tidal deformation, spin-orbit resonance, nonzero eccentricity, despinning, and reorientation. J Geophys Res Planets 114. https://doi.org/10.1029/2008je003252
- Matthews, V., Work, D.F., 1978. Laramide Folding Associated with Basement Block Faulting in the Western United States. Geol. Soc. Am. Mem. 101–124. https://doi.org/10.1130/mem151-p101
- McClay, K.R., 1978. Thrust and nappe tectonics. Tectonophysics 50, 79. https://doi.org/10.1016/0040-1951(78)90200-7
- McClay, K. R., Price, N. J., 1981. (Eds.), Thrust and Nappe Tectonics, Spec. Publ. 9, 539 pp., Geological Society of London, Oxford.
- McCullough, L., 2023. Morphological and structural characterization of shortening landforms on Mars. Mississippi State University Theses and Dissertations. 6025. https://scholarsjunction.msstate.edu/td/6025
- McCullough, L.R., Crane, K.T., Loveless, S.R., Klimczak, C., 2024. Morphological and Structural Characterization of Shortening Landforms on Mars. J. Geophys. Res.: Planets 129. https://doi.org/10.1029/2023je008196
- Melosh, H. J., McKinnon, W. B. 1988. The tectonics of Mercury. In: Vilas, F., Chapman, C. R., Matthews, M. S. (Eds.), Mercury, pp. 374–400.

- Melosh, H.J., 1977. Global tectonics of a despun planet. Icarus 31, 221–243. https://doi.org/10.1016/0019-1035(77)90035-5
- Michel, N.C., Hauck, S.A., Solomon, S.C., Phillips, R.J., Roberts, J.H., Zuber, M.T., 2013. Thermal evolution of Mercury as constrained by MESSENGER observations. J. Geophys. Res.: Planets 118, 1033–1044. https://doi.org/10.1002/jgre.20049
- Morley, C.K., 1988. Out-of-Sequence Thrusts. Tectonics 7, 539–561. https://doi.org/10.1029/tc007i003p00539
- Mueller, K., Golombek, M., 2004. Compressional Structures on Mars. Earth Planet. Sci. 32, 435–464. https://doi.org/10.1146/annurev.earth.32.101802.120553
- Mueller, K., Vidal, A., Robbins, S., Golombek, M., West, C., 2014. Fault and fold growth of the Amenthes uplift: Implications for Late Noachian crustal rheology and heat flow on Mars. Earth Planet Sc Lett 408, 100–109. https://doi.org/10.1016/j.epsl.2014.09.047
- Nahm, A.L., Schultz, R.A., 2011. Magnitude of global contraction on Mars from analysis of surface faults: Implications for martian thermal history. Icarus 211, 389–400. https://doi.org/10.1016/j.icarus.2010.11.003
- Nahm, A.L., Watters, T.R., Johnson, C.L., Banks, M.E., Bogert, C.H. van der, Weber, R.C., Andrews-Hanna, J.C., 2023. Tectonics of the Moon. Rev. Miner. Geochem. 89, 691–727. https://doi.org/10.2138/rmg.2023.89.16

- Newton, I., 1686. Philosophiae naturalis principia mathematica. London. https://doi.org/10.5479/sil.52126.39088015628399
- Nimmo, F., Porco, C., Mitchell, C., 2014. Tidally modulated eruptions on Enceladus:

 Cassini ISS observations and models. Astron. J. 148, 46.

 https://doi.org/10.1088/0004-6256/148/3/46
- Nimmo, F., Watters, T.R., 2004. Depth of faulting on Mercury: Implications for heat flux and crustal and effective elastic thickness. Geophys. Res. Lett. 31. https://doi.org/10.1029/2003gl018847
- Okubo, C.H., Schultz, R.A., 2004. Mechanical stratigraphy in the western equatorial region of Mars based on thrust fault–related fold topography and implications for near-surface volatile reservoirs. GSA Bull. 116, 594–605. https://doi.org/10.1130/b25361.1
- Olsen, K.G., Hurford, T.A., Schmerr, N.C., Huang, M., Brunt, K.M., Zipparo, S., Cole, H.M., Aster, R.C., 2021. Projected Seismic Activity at the Tiger Stripe Fractures on Enceladus, Saturn, From an Analog Study of Tidally Modulated Icequakes Within the Ross Ice Shelf, Antarctica. J. Geophys. Res.: Planets 126. https://doi.org/10.1029/2021je006862
- Ostrach, L.R., Robinson, M.S., Whitten, J.L., Fassett, C.I., Strom, R.G., Head, J.W., Solomon, S.C., 2015. Extent, age, and resurfacing history of the northern smooth plains on Mercury from MESSENGER observations. Icarus 250, 602–622. https://doi.org/10.1016/j.icarus.2014.11.010

- Padovan, S., Wieczorek, M.A., Margot, J., Tosi, N., Solomon, S.C., 2015. Thickness of the crust of Mercury from geoid-to-topography ratios. Geophys. Res. Lett. 42, 1029–1038. https://doi.org/10.1002/2014gl062487
- Patzek, M., Rüsch, O., 2022. Experimentally Induced Thermal Fatigue on Lunar and Eucrite Meteorites—Influence of the Mineralogy on Rock Breakdown. J. Geophys. Res.: Planets 127. https://doi.org/10.1029/2022je007306
- Pearson, K., 1901. LIII. On lines and planes of closest fit to systems of points in space.

 Philos. Mag. Ser. 6 2, 559–572. https://doi.org/10.1080/14786440109462720
- Pechmann, J.B., Melosh, H.J., 1979. Global fracture patterns of a despun planet:

 Application to Mercury. Icarus 38, 243–250. https://doi.org/10.1016/0019-1035(79)90181-7
- Pegg, D.L., Rothery, D.A., Balme, M.R., Conway, S.J., Malliband, C.C., Man, B., 2021.

 Geology of the Debussy quadrangle (H14), Mercury. J. Maps 17, 718–729.

 https://doi.org/10.1080/17445647.2021.1996478
- Perry, M.E., Kahan, D.S., Barnouin, O.S., Ernst, C.M., Solomon, S.C., Zuber, M.T., Smith, D.E., Phillips, R.J., Srinivasan, D.K., Oberst, J., Asmar, S.W., 2011.

 Measurement of the radius of Mercury by radio occultation during the MESSENGER flybys. Planet. Space Sci. 59, 1925–1931.

 https://doi.org/10.1016/j.pss.2011.07.022

- Peterson, G.A., Johnson, C.L., Byrne, P.K., Phillips, R.J., 2019. Distribution of Areal Strain on Mercury: Insights Into the Interaction of Volcanism and Global Contraction. Geophys. Res. Lett. 46, 608–615. https://doi.org/10.1029/2018gl080749
- Peterson, G.A., Johnson, C.L., Byrne, P.K., Phillips, R.J., 2020. Fault Structure and Origin of Compressional Tectonic Features Within the Smooth Plains on Mercury. J Geophys Res Planets 125. https://doi.org/10.1029/2019je006183
- Petterson, M.G., Neal, C.R., Mahoney, J.J., Kroenke, L.W., Saunders, A.D., Babbs, T.L., Duncan, R.A., Tolia, D., McGrail, B., 1997. Structure and deformation of north and central Malaita, Solomon Islands: tectonic implications for the Ontong Java Plateau-Solomon arc collision, and for the fate of oceanic plateaus.

 Tectonophysics 283, 1–33. https://doi.org/10.1016/s0040-1951(97)00206-0
- Pfiffner, O.A., 2017. Thick-Skinned and Thin-Skinned Tectonics: A Global Perspective.

 Geosciences 7, 71. https://doi.org/10.3390/geosciences7030071
- Pierdominici, S., Mariucci, M.T., Montone, P., 2011. A study to constrain the geometry of an active fault in southern Italy through borehole breakouts and downhole logs.

 J. Geodyn. 52, 279–289. https://doi.org/10.1016/j.jog.2011.02.006
- Plescia, J.B., Golombek, M.P., 1986. Origin of planetary wrinkle ridges based on the study of terrestrial analogs. GSA Bull. 97, 1289–1299. https://doi.org/10.1130/0016-7606(1986)97<1289:oopwrb>2.0.co;2

- Pou, L., Nimmo, f., Lognonné, P., Mimoun, D., Garcia, R.F., Pinot, B., Rivoldini, A., Banfield, D., Banerdt, W.B., 2021. Forward modeling of the Phobos tides and applications to the first Martian year of the InSight mission. Earth Space Sci. 8. https://doi.org/10.1029/2021ea001669
- Preusker, F., Oberst, J., Head, J.W., Watters, T.R., Robinson, M.S., Zuber, M.T., Solomon, S.C., 2011. Stereo topographic models of Mercury after three MESSENGER flybys. Planet. Space Sci. 59, 1910–1917.

 https://doi.org/10.1016/j.pss.2011.07.005
- Rhoden, A.R., Militzer, B., Huff, E.M., Hurford, T.A., Manga, M., Richards, M.A., 2010.

 Constraints on Europa's rotational dynamics from modeling of tidally-driven fractures. Icarus 210, 770–784. https://doi.org/10.1016/j.icarus.2010.07.018
- Rhoden, A.R., Mohr, K.J., Hurford, T.A., Henning, W., Sajous, S., Patthoff, D.A.,
 Dubois, D., 2021. Obliquity, Precession, and Fracture Mechanics: Implications of
 Europa's Global Cycloid Population. J. Geophys. Res.: Planets 126.
 https://doi.org/10.1029/2020je006710
- Riley, S. J., DeGloria, S. D., Elliot, R., 1999. A terrain ruggedness index that quantifies topographic heterogeneity. Int. J. Therm. Sci. 5 (1–4), 23–27.
- Ritzer, J.A., Hauck, S.A., Barnouin, O.S., Solomon, S. C., Watters, T.R., 2010.

 Mechanical structure of Mercury's lithosphere from MESSENGER observations of lobate scarps. Lunar Planet. Sci. XLI. Abstract 2122.

- Rothery, D.A., Massironi, M., 2010. Beagle Rupes Evidence for a basal decollement of regional extent in Mercury's lithosphere. Icarus 209, 256–261. https://doi.org/10.1016/j.icarus.2009.12.009
- Schleicher, L.S., Watters, T.R., Martin, A.J., Banks, M.E., 2019. Wrinkle ridges on Mercury and the Moon within and outside of mascons. Icarus 331, 226–237. https://doi.org/10.1016/j.icarus.2019.04.013
- Scholz, C.H., Cowie, P.A., 1990. Determination of total strain from faulting using slip measurements. Nature 346, 837–839. https://doi.org/10.1038/346837a0
- Schultz, R.A., 1993. Brittle strength of basaltic rock masses with applications to Venus. J. Geophys. Res.: Planets 98, 10883–10895. https://doi.org/10.1029/93je00691
- Schultz, R.A., 2000. Localization of bedding plane slip and backthrust faults above blind thrust faults: Keys to wrinkle ridge structure. J Geophys Res Planets 105, 12035–12052. https://doi.org/10.1029/1999je001212
- Schultz, R.A., Watters, T.R., 2001. Forward mechanical modeling of the Amenthes Rupes Thrust Fault on Mars. Geophys. Res. Lett. 28, 4659–4662. https://doi.org/10.1029/2001gl013468
- Shaw, J.H., Connors, C., Suppe, J. (Eds.), 2005. Seismic Interpretation of Contractional Fault-Related Folds, Studies in Geology. American Association of Petroleum Geologists. https://doi.org/10.1306/st531003

- Simangunsong, G.M., Safitri, Y., 2022. The Effect of Cyclic Impact Loads on Rock

 Properties. J. Eng. Technol. Sci. 54, 220611.

 https://doi.org/10.5614/j.eng.technol.sci.2022.54.6.11
- Smythe, DK., Dobinson, A., McQuillan, R., Brewer, J.A., Matthews, D.H., Blundell, D.J., Kelk, B., 1982. Deep Structure of the Scottish Calendonides revealed by the MOIST reflection profile. Nature, Lond. 199, 338–340.
- Sokal, R.R., Rohlf, F.J., 1995 (Ed.) Biometry The Principles and Practice of Statistics in Biological Research. Third Edition.
- Solomon, S.C., 1977. The relationship between crustal tectonics and internal evolution in the moon and Mercury. Phys Earth Planet In 15, 135–145.

 https://doi.org/10.1016/0031-9201(77)90026-7
- Solomon, S.C., 1978. On volcanism and thermal tectonics on one-plate planets. Geophys. Res. Lett. 5, 461–464. https://doi.org/10.1029/g1005i006p00461
- Solomon, S.C., Jr., R.L.M., Watters, T.R., Lawrence, D.J., Feldman, W.C., Head, J.W.,
 Krimigis, S.M., Murchie, S.L., Phillips, R.J., Slavin, J.A., Zuber, M.T., 2008.
 Return to Mercury: A Global Perspective on MESSENGER's First Mercury
 Flyby. Science 321, 59–62. https://doi.org/10.1126/science.1159706
- Solomon, S.C., Smrekar, S.E., Bindschadler, D.L., Grimm, R.E., Kaula, W.M., McGill, G.E., Phillips, R.J., Saunders, R.S., Schubert, G., Squyres, S.W., Stofan, E.R.,

- 1992. Venus tectonics: An overview of Magellan observations. J Geophys Res Planets 97, 13199–13255. https://doi.org/10.1029/92je01418
- Squyres, S.W., Jankowski, D.G., Simons, M., Solomon, S.C., Hager, B.H., McGill, G.E., 1992. Plains tectonism on Venus: The deformation belts of Lavinia Planitia. J. Geophys. Res.: Planets 97, 13579–13599. https://doi.org/10.1029/92je00481
- Strom, R.G., 1979. Mercury: A post-Mariner 10 assessment. Space Sci. Rev. 24, 3–70. https://doi.org/10.1007/bf00221842
- Strom, R.G., Trask, N.J., Guest, J.E., 1975. Tectonism and volcanism on Mercury. J. Geophys. Res. 80, 2478–2507. https://doi.org/10.1029/jb080i017p02478
- Suppe, J., 1983. Geometry and kinematics of fault-bend folding. Am. J. Sci. 283, 684–721. https://doi.org/10.2475/ajs.283.7.684
- Suppe, J., Namson, J., 1979. Fault-bend origin of front folds of the western Taiwan fold-and-thrust belt. Petrol. Geol. of Taiwan 16, 1–18.
- Thor, R.N., Kallenbach, R., Christensen, U.R., Stark, A., Steinbrügge, G., Ruscio, A.D., Cappuccio, P., Iess, L., Hussmann, H., Oberst, J., 2020. Prospects for measuring Mercury's tidal Love number h2 with the BepiColombo Laser Altimeter. Astron. Astrophys. 633, A85. https://doi.org/10.1051/0004-6361/201936517
- Toda, S., Stein, R.S., Richards-Dinger, K., Bozkurt, S.B., 2005. Forecasting the evolution of seismicity in southern California: Animations built on earthquake stress transfer. J. Geophys. Res.: Solid Earth 110. https://doi.org/10.1029/2004jb003415

- Toksöz, M.N., Goins, N.R., Cheng, C.H., 1977. Moonquakes: mechanisms and relation to tidal stresses. Science. 196, 979–81. https://doi.org/10.1126/science.196.4293.979
- Tosi, N., Grott, M., Plesa, A. -C., Breuer, D., 2013. Thermochemical evolution of Mercury's interior. J. Geophys. Res.: Planets 118, 2474–2487. https://doi.org/10.1002/jgre.20168
- Trask, N.J., Guest, J.E., 1975. Preliminary geologic terrain map of Mercury. J. Geophys. Res. 80, 2461–2477. https://doi.org/10.1029/jb080i017p02461
- Turcotte, D., Schubert, G. (2014). Stresses and Strains in Solids. In: Turcotte D., Schubert, G. (Ed.), Geodynamics (3rd ed.). Cambridge: Cambridge University Press. pp. 92-129.
- Turner, A.R., Hawthorne, J.C., Gaddes, M., 2022. Stresses in the Lunar Interior: Insights

 From Slip Directions in the A01 Deep Moonquake Nest. J. Geophys. Res.: Planets

 127. https://doi.org/10.1029/2022je007364
- Twiss, R. J., Marrett, R., 2010a. Determining brittle extension and shear strain using fault-length and displacement systematics: Part I: Theory. J Struct Geol 32, 1960–1977. https://doi.org/10.1016/j.jsg.2010.04.007
- Twiss, R. J., Marrett, R., 2010b. Determining brittle extension and shear strain using fault length and displacement systematics: Part II: Data evaluation and test of the theory. J Struct Geol 32, 1978–1995. https://doi.org/10.1016/j.jsg.2010.04.006

- Watters, T. R., Nimmo, F., 2010. The tectonics of Mercury. In: Watters, T. R., Schultz, R. A. (Eds) Planetary Tectonics. pp. 15–80. https://doi.org/10.1017/cbo9780511691645.002
- Watters, T.R., 1988. Wrinkle ridge assemblages on the terrestrial planets. J Geophys Res Solid Earth 93, 10236–10254. https://doi.org/10.1029/jb093ib09p10236
- Watters, T.R., 1993. Compressional tectonism on Mars. J Geophys Res 98, 17049. https://doi.org/10.1029/93je01138
- Watters, T.R., 2003. Lithospheric flexure and the origin of the dichotomy boundary on Mars. Geology 31, 271–274. <a href="https://doi.org/10.1130/0091-7613(2003)031<0271:lfatoo>2.0.co;2">https://doi.org/10.1130/0091-7613(2003)031<0271:lfatoo>2.0.co;2
- Watters, T.R., 2021. A case for limited global contraction of Mercury. Commun. Earth Environ. 2, 9. https://doi.org/10.1038/s43247-020-00076-5
- Watters, T.R., Cook, A.C., Robinson, M.S., 2001. Large-scale lobate scarps in the southern hemisphere of Mercury. Planet. Space Sci. 49, 1523–1530. https://doi.org/10.1016/s0032-0633(01)00090-3
- Watters, T.R., James, P.B., Selvans, M.M., 2021. Mercury's Crustal Thickness and Contractional Strain. Geophys. Res. Lett. 48, e2021GL093528.

 https://doi.org/10.1029/2021gl093528

- Watters, T.R., Montési, L.G.J., Oberst, J., Preusker, F., 2016. Fault-bound valley associated with the Rembrandt basin on Mercury. Geophys. Res. Lett. 43, 11,536-11,544. https://doi.org/10.1002/2016gl070205
- Watters, T.R., Nimmo, F., Robinson, M.S., 2005. Extensional troughs in the Caloris Basin of Mercury: Evidence of lateral crustal flow. Geology, 33, 669–672.
- Watters, T.R., Robinson, M.S., 1999. Lobate scarps and the Martian crustal dichotomy. J. Geophys. Res.: Planets 104, 18981–18990. https://doi.org/10.1029/1998je001007
- Watters, T.R., Robinson, M.S., Beyer, R.A., Banks, M.E., III, J.F.B., Pritchard, M.E.,
 Hiesinger, H., Bogert, C.H. van der, Thomas, P.C., Turtle, E.P., Williams, N.R.,
 2010. Evidence of Recent Thrust Faulting on the Moon Revealed by the Lunar
 Reconnaissance Orbiter Camera. Science 329, 936–940.
 https://doi.org/10.1126/science.1189590
- Watters, T.R., Robinson, M.S., Bina, C.R., Spudis, P.D., 2004. Thrust faults and the global contraction of Mercury. Geophys Res Lett 31.

 https://doi.org/10.1029/2003gl019171
- Watters, T.R., Robinson, M.S., Cook, A.C., 1998. Topography of lobate scarps on Mercury: New constraints on the planet's contraction. Geology 26, 991–994. https://doi.org/10.1130/0091-7613(1998)026<0991:tolsom>2.3.co;2
- Watters, T.R., Schultz, R.A., 2002. The fault geometry of planetary lobate scarps: Listric versus planar. Lunar Planet. Sci. XXXIII. Abstract 1668.

- Watters, T.R., Selvans, M.M., Banks, M.E., Hauck, S.A., Becker, K.J., Robinson, M.S., 2015a. Distribution of large-scale contractional tectonic landforms on Mercury: Implications for the origin of global stresses. Geophys Res Lett 42, 3755–3763. https://doi.org/10.1002/2015gl063570
- Watters, T.R., Robinson, M.S., Collins, G.C., Banks, M.E., Daud, K., Williams, N.R., Selvans, M.M., 2015b. Global thrust faulting on the Moon and the influence of tidal stresses. Geology 43, 851–854. https://doi.org/10.1130/g37120.1
- Watters, T.R., Solomon, S.C., Klimczak, C., Freed, A.M., Head, J.W., Ernst, C.M., Blair, D.M., Goudge, T.A., Byrne, P.K., 2012. Extension and contraction within volcanically buried impact craters and basins on Mercury. Geology 40, 1123–1126. https://doi.org/10.1130/g33725.1
- Watters, T.R., Solomon, S.C., Robinson, M.S., Head, J.W., André, S.L., Hauck, S.A., Murchie, S.L., 2009. The tectonics of Mercury: The view after MESSENGER's first flyby. Earth Planet. Sci. Lett. 285, 283–296. https://doi.org/10.1016/j.epsl.2009.01.025
- Watters, T.R., Weber, R.C., Collins, G.C., Howley, I.J., Schmerr, N.C., Johnson, C.L., 2019. Shallow seismic activity and young thrust faults on the Moon. Nat. Geosci. 12, 411–417. https://doi.org/10.1038/s41561-019-0362-2
- Watterson, J., Walsh, J.J., Gillespie, P.A., Easton, S., 1996. Scaling systematics of fault sizes on a large-scale range fault map. J. Struct. Geol. 18, 199–214. https://doi.org/10.1016/s0191-8141(96)80045-9

- Wickham, J., 1995. Fault displacement-gradient folds and the structure at Lost Hills,

 California (U.S.A.). J. Struct. Geol. 17, 1293–1302. https://doi.org/10.1016/0191-8141(95)00029-d
- Williams, D.R., 2020. Mercury Fact Sheet [WWW Document]. NASA. URL https://nssdc.gsfc.nasa.gov/planetary/factsheet/mercuryfact.html
- Williams, J., Ruiz, J., Rosenburg, M.A., Aharonson, O., Phillips, R.J., 2011. Insolation driven variations of Mercury's lithospheric strength. J. Geophys. Res.: Planets 116. https://doi.org/10.1029/2010je003655
- Williams, N.R., Watters, T.R., Pritchard, M.E., Banks, M.E., Bell, J.F., 2013. Fault dislocation modeled structure of lobate scarps from Lunar Reconnaissance Orbiter Camera digital terrain models. J. Geophys. Res.: Planets 118, 224–233. https://doi.org/10.1002/jgre.20051
- Wright, J., Rothery, D.A., Balme, M.R., Conway, S.J., 2019. Geology of the Hokusai quadrangle (H05), Mercury. J. Maps 15, 509–520. https://doi.org/10.1080/17445647.2019.1625821
- Xiao, H., Stark, A., Steinbrügge, G.B., Briaud, A., Lara, L.M., Gutiérrez, P.J., 2024.

 Mercury's tidal Love number h2 from co-registration of MLA profiles. ESS Open

 Archive. https://doi.org/10.22541/essoar.172552289.92187534/v1
- Zanazzi, J.J., Triaud, A.H.M.J., 2019. The ability of significant tidal stress to initiate plate tectonics. Icarus 325, 55–66. https://doi.org/10.1016/j.icarus.2019.01.029

Zuber, M.T., Smith, D.E., Phillips, R.J., Solomon, S.C., Neumann, G.A., II, S.A.H.,
Peale, S.J., Barnouin, O.S., Head, J.W., Johnson, C.L., Lemoine, F.G., Mazarico,
E., Sun, X., Torrence, M.H., Freed, A.M., Klimczak, C., Margot, J.-L., Oberst, J.,
Perry, M.E., Jr., R.L.M., Balcerski, J.A., Michel, N., Talpe, M.J., Yang, D., 2012.
Topography of the Northern Hemisphere of Mercury from MESSENGER Laser
Altimetry. Science 336, 217–220. https://doi.org/10.1126/science.1218805

APPENDIX A: CHAPTER 2

Table A2.1: Transformations used to normalize all of the measurements in this study. After these transformations, the data was scaled using the measurement's z-scores (where $z = (x - \mu)/\sigma$).

Parameter	Normalized Transformation
Relief	ln(x)
Breadth	ln(x)
Total Cross-Sectional Length	ln(x)
Shortening Strain	ln(x)
Forelimb Slope	ln(x)
Backlimb Slope	ln (-x)
Symmetry	ln (x)
Forelimb Length	ln(x)
Backlimb Length	ln(x)
% Backlimb Downslope	ln(x)
Mapped Length	ln(x)
TRI	ln(x)

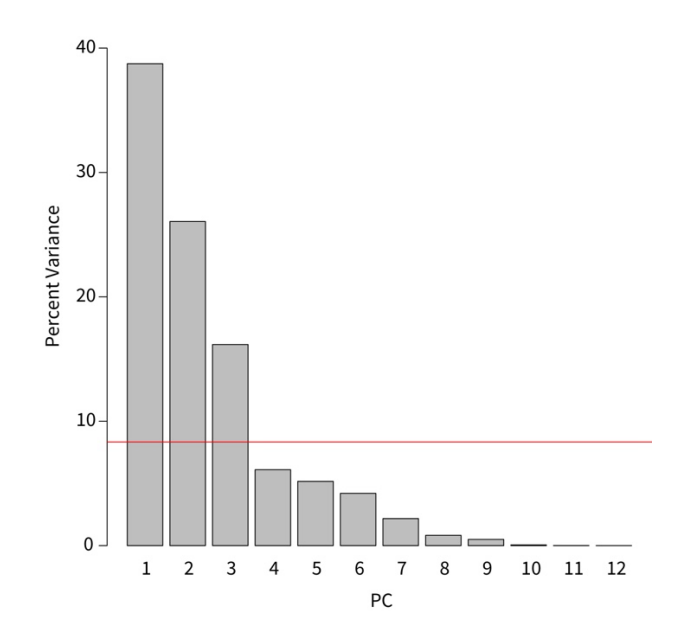


Figure A2.1: Scree plot depicting the percent variance described by each of the 12 principal components. The red horizontal line depicts the percent variance each PC would have if they each equally contributed to the total variance observed across the data (i.e., 100% variance/12 parameters).

 Table A2.2: Extracted morphology values for 100 shortening landforms

	D !: (5 3	D 111.7.7	0 0	
<u>ID #</u>	Relief [m]	Breadth [m]	CrossSection[m]	Strain
1	1414.7531	42526.7063	42630.774	0.00244114
2	823.3459	28531.7712	28633.9304	0.00356776
3	1415.5202	37238.2114	37573.4665	0.00892266
4	1203.0848	29636.3524	29817.9583	0.00609049
5	802.9927	42437.7454	42598.5608	0.00377514
6	1781.1514	42599.7651	42806.0202	0.00481837
7	647.5123	47766.8962	47782.9792	0.00033658
8	1550.7377	24819.1458	25244.2102	0.0168381
9	2842.878	36748.6307	37114.5679	0.00985967
10	1229.6014	38903.8359	39051.8106	0.00378919
11	1091.315	78337.1439	78534.7767	0.0025165
12	950.2112	20378.7798	20523.8215	0.00706699
13	1612.3143	100045.575	100123.617	0.00077945
14	221.2723	4333.60635	4353.17784	0.00449591
15	1736.4284	60375.2936	60916.0961	0.00887783
16	229.2747	21917.1499	21925.162	0.00036543
17	2166.0015	29558.6143	29802.3743	0.00817921
18	572.0013	27335.3806	27384.9034	0.0018084
19	3261.757	261819.743	262520.975	0.00267115
20	1432.3385	31157.6789	31462.7864	0.00969741
21	756.7711	10583.4863	10687.5329	0.00973533
22	528.3406	38240.5145	38434.6025	0.00504983
23	1146.6646	20890.4225	21078.7039	0.0089323
24	3631.6634	44893.5447	46544.6826	0.03547425
25	1675.2407	57000.6292	57180.0884	0.00313849
26	486.4815	31560.4968	31612.5302	0.00164597
27	1413.4661	57248.4787	57403.6841	0.00270375
28	423.6231	37660.8846	37678.3001	0.00046222
29	405.6563	19923.0495	19957.8296	0.00174268
30	442.216	28902.3786	29198.6378	0.01014634
31	1166.88	34298.3851	34441.522	0.00415594
32	791.9257	43597.8141	43676.3045	0.00179709
33	300.2517	48405.9177	48425.6295	0.00040705
34	1575.7803	40823.0403	41028.9797	0.00501936
35	1494.8211	58188.1933	58460.7637	0.00466245
36	2315.9009	71780.1216	72125.52	0.00478885
37	871.629	16659.2543	16746.1424	0.00518855

38	2220 2006	52100 4754	52765.131	0.01250640
39	3338.2986 2876.7431	52100.4754 68384.4369	68871.6772	0.01259649 0.00707461
40	2648.8584	39703.1234	40208.4858	0.00707461
40	721.8928	16107.5105	16253.5991	0.01230833
42	1011.5381	45838.5339	45937.4948	0.00036606
43	191.8138	27039.1022	27043.1876	0.00215425
43 44	315.6608	19842.1864	19855.8012	0.00013107
44 45	637.6115	35654.7232	35717.4473	0.00066569
45 46	1339.1792	31860.1452	31978.0891	0.00173012
40 47	534.5221	24505.2428	24546.6923	0.00368827
48	1546.2202	107962.668	108268.807	0.0016666
40 49	1253.4104	52800.8995	52888.5406	0.00282739
50	1891.0696	47429.4332	47814.7893	0.00165709
50 51	1890.8744	68477.7235	68629.5921	0.00803933
52	1561.2718	71660.3615	71936.0761	0.00221287
	180.7307	29923.3794	29934.1921	
53 54			16995.6659	0.00036122
54 55	413.1501	16978.5985		0.00100422
55 50	1538.9979	114825.265	114938.198	0.00098256
56	304.1298	26756.0438	26815.9895	0.00223545
57	2310.064	48727.3531	49060.9416	0.00679947
58	460.8051	27106.0022	27150.0391	0.00162198
59	1151.851	50431.8737	50511.4042	0.00157451
60	661.7843	47328.3053	47374.1255	0.0009672
61	723.9938	67633.8733	67697.364	0.00093786
62	2441.737	108679.397	108922.243	0.00222954
63	643.1144	57545.8891	57697.5568	0.00262867
64	787.6495	46419.8163	46483.0248	0.00135982
65	1542.0267	21226.7505	21557.7177	0.01535261
66	1611.9516	51171.034	51855.0343	0.01319062
67	478.3598	27166.4589	27209.3595	0.00157669
68	553.7783	17504.4993	17562.8132	0.0033203
69	1105.5798	74129.8799	74329.6723	0.00268792
70	964.6781	30538.1027	30951.2725	0.01334904
71	997.1419	25672.7245	25896.2253	0.00863063
72	839.5641	38299.3496	38357.485	0.00151562
73	834.2471	38317.6591	38362.6317	0.0011723
74 	2894.3435	47422.4755	48296.4109	0.01809525
75	1090.5031	54253.7608	54349.8462	0.00176791
76	3189.4176	76816.9086	77411.3091	0.00767847
77	667.7308	29883.3246	29910.3179	0.00090247

78	1335.6184	28906.3636	29077.5134	0.00588598
79	1455.6099	49797.4674	50240.7561	0.00882329
80	968.2256	20228.6765	20375.4518	0.00720354
81	617.6321	15444.5436	15511.5306	0.00431853
82	780.9744	35969.3971	36009.9357	0.00112576
83	267.427	35633.2622	35651.1806	0.0005026
84	332.8557	35134.6654	35156.4129	0.00061859
85	762.2883	44785.0123	44822.0975	0.00082739
86	344.0871	13473.4272	13489.294	0.00117625
87	423.5033	40085.8368	40115.7661	0.00074607
88	1738.6533	54950.7019	55142.9328	0.00348605
89	1699.4111	46916.0186	47118.0924	0.00428867
90	1233.548	51665.0028	51776.1223	0.00214615
91	2260.825	54083.1276	54400.9202	0.00584168
92	1726.3409	51638.9512	51748.4537	0.00211605
93	1213.8447	55061.1697	55207.9054	0.00265788
94	283.8638	29590.7322	29603.3527	0.00042632
95	1051.7507	31840.2654	32112.1001	0.00846518
96	741.6715	24526.6213	24612.2341	0.00347846
97	2507.0921	70138.1022	70488.7924	0.00497512
98	494.2391	41441.0797	41475.2635	0.0008242
99	885.7175	43427.0448	43472.2099	0.00103894
100	962.0807	28133.0479	28328.6195	0.00690368

ID#	FLSlope[deg]	BLSlope[deg]	Symm [deg]	FLLength[m]	BLLength[m]
1	4.33437615	-1.7221491	2.61222706	18871.0904	23759.6836
2	4.28815714	-1.9512687	2.33688839	11079.176	17554.7544
3	7.08615801	-4.0679367	3.01822132	11595.9321	25977.5344
4	6.84118787	-3.3631054	3.47808245	10316.9645	19500.9938
5	10.7091503	-1.2389679	9.47018237	4590.45992	38008.1009
6	8.19034495	-3.1115268	5.07881817	12766.2247	30039.7955
7	1.19022801	-1.3818176	-0.1915896	31191.247	16591.7322
8	19.5412803	-3.0712122	16.4700682	5244.57243	19999.6378
9	10.7835876	-4.2108801	6.57270758	15604.2942	21510.2738
10	5.82833844	-2.894981	2.93335748	12330.6952	26721.1153
11	2.46211918	-0.5438498	1.91826943	25654.5011	52880.2756
12	8.60299906	-3.7279153	4.8750838	6521.03796	14002.7835
13	2.02521036	-1.2769238	0.74828654	45775.6172	54347.9998
14	5.30508684	-3.041099	2.2639878	2423.55148	1929.62637
15	11.1349	-1.6816272	9.45327277	9487.25361	51428.8425
16	1.69685519	-0.6842528	1.01260243	7753.99363	14171.1684
17	7.13795842	-1.3856369	5.75232151	17982.693	11819.6812
18	5.04742212	-1.1299734	3.91744869	6649.91594	20734.9874
19	5.55530827	-0.5454401	5.0098682	34636.93	227884.045
20	7.71263668	-4.2910074	3.42162924	11121.1708	20341.6157
21	8.2825555	-3.1428291	5.13972639	5355.92217	5331.61076
22	1.88200588	-2.001642	-0.1196361	16869.1984	21565.4041
23	6.67832263	-3.9942308	2.68409178	10062.7573	11015.9466
24	22.5675883	-1.2670319	21.3005564	11850.596	34694.0865
25	8.77638967	-1.4943078	7.28208188	11234.3158	45945.7726
26	4.52841191	-0.7227509	3.80566102	6204.13894	25408.3912
27	6.12187344	-1.2806706	4.84120285	13391.7016	44011.9825
28	2.47487738	-0.7766711	1.69820633	9824.5252	27853.7749
29	3.1945116	-3.2220462	-0.0275346	7328.13018	12629.6994
30	4.60206005	-1.4829924	3.11906766	5565.05753	23633.5803
31	8.04235204	-2.2201431	5.82220899	8500.0347	25941.4873
32	4.69318863	-0.9095408	3.78364786	9789.60977	33886.6947
33	2.50616623	-0.2211198	2.28504641	6878.4167	41547.2128
34	10.7297507	-1.9392173	8.79053341	8723.53496	32305.4448
35	10.0961839	-1.4177259	8.67845799	8785.80427	49674.9594
36	12.0392373	-1.9870173	10.0522201	11585.3783	60540.1417
37	5.21244231	-4.2999692	0.91247315	9705.42767	7040.71468
38	14.8396327	-3.5836382	11.2559945	13786.8926	38978.2383
39	9.45730269	-2.6854072	6.77189552	18308.0783	50563.5989

40	13.1669947	-4.1885875	8.97840719	12299.8954	27908.5903
41	9.16255712	-1.4924726	7.67008452	4722.57831	11531.0208
42	5.85192378	-2.0410572	3.81086661	10029.537	35907.9578
43	1.04184322	-0.7641516	0.27769165	10554.0612	16489.1264
44	2.7074319	-1.2510107	1.45642121	6697.57397	13158.2272
45	4.15858003	-2.2887612	1.86981879	8824.22653	26893.2207
46	5.48778264	-1.9480223	3.53976038	14165.7502	17812.3389
47	3.13158868	-2.8537392	0.27784945	9823.69026	14723.002
48	8.64953772	-1.983849	6.66568867	10716.9439	97551.8631
49	5.5726165	-1.3104196	4.26219693	13024.6796	39863.861
50	11.7153143	-3.8205656	15.5358799	12500.0888	35314.7005
51	5.59622047	-0.9876966	4.60852383	19553.0506	49076.5415
52	9.80954268	-2.1123154	7.69722731	9466.11247	62469.9636
53	3.61009936	-0.5597266	3.05037273	2883.92798	27050.2641
54	2.86933322	-1.2605264	1.60880685	8277.30286	8718.36301
55	3.50709202	-0.3663037	3.1407883	25290.4571	89647.7406
56	5.59643767	-1.5194053	4.07703234	3149.64594	23666.3436
57	10.9737834	-2.6145666	8.35921683	12802.0485	36258.893
58	4.70818216	-2.0893543	2.6188279	5642.24216	21507.7969
59	3.87796939	-1.0636195	2.8143499	17189.7625	33321.6417
60	3.85375476	-1.0187958	2.83495891	9892.99542	37481.1301
61	1.95928734	-1.3595472	0.59974009	21244.7664	46452.5976
62	4.75031376	-0.7636002	3.98671356	30024.7996	78897.4437
63	5.56964578	-1.3107604	4.25888535	6703.69611	50993.8607
64	1.84812212	-2.0518746	-0.2037525	24560.0204	21923.0044
65	9.09156692	-9.8404842	-0.7489172	9997.14662	11560.571
66	18.3455751	-2.0137784	16.3317966	6018.51433	45836.5199
67	5.42620769	-1.5421615	3.88404621	5109.00117	22100.3583
68	5.74922954	-3.3172895	2.43194004	5568.15886	11994.6543
69	6.56574378	-0.9479773	5.61776653	9826.25085	64503.4215
70	16.2649877	-2.4957175	13.7692702	4200.1425	26751.13
71	4.76839349	-2.5638817	2.20451183	12599.6595	13296.5658
72	3.05598145	-1.8407863	1.2151951	15837.7038	22519.7813
73	2.5895742	-1.5239533	1.06562093	18530.1916	19832.44
74	18.8763479	-5.2032381	13.6731098	10253.1232	38043.2877
75	3.14634156	-1.7547005	1.39164107	19983.8048	34366.0414
76	10.7699828	-1.172075	9.59790781	18436.6534	58974.6557
77	2.13591043	-2.0012117	0.13469873	17947.3536	11962.9643
78	6.73505466	-1.2846205	5.45043412	12545.7006	16531.8127
79	3.56841871	-2.8218137	0.74660504	24181.1135	26059.6426

80	4.75314649	-4.2177919	0.5353546	11943.5635	8431.88831
81	7.76443129	-1.4604338	6.30399752	4692.49213	10819.0385
82	2.9539605	-2.0585928	0.89536771	15188.8545	20821.0812
83	2.80802469	-0.7022452	2.10577945	5476.67457	30174.506
84	3.52274734	-0.753642	2.76910535	5445.03238	29711.3805
85	2.51147986	-1.3212894	1.19019049	17440.1893	27381.9082
86	3.88954773	-1.0928557	2.79669203	5093.43099	8395.86296
87	3.76646369	-0.8367953	2.92966838	6475.96679	33639.7993
88	8.03219948	-1.5634731	6.46872639	12743.5229	42399.41
89	7.15687389	-2.548597	4.60827693	13846.7169	33271.3756
90	5.9619167	-1.7055367	4.25637998	12000.5789	39775.5434
91	9.532602	-2.9300773	6.6025247	14098.9102	40302.01
92	3.33033829	-1.9068747	1.42346358	29876.2233	21872.2304
93	5.07282174	-2.3028254	2.7699963	13887.6851	41320.2203
94	2.62935594	-0.5634701	2.06588579	6203.39943	23399.9532
95	7.09791248	-4.1352187	2.96269374	8920.09864	23192.0015
96	6.23973855	-2.1103115	4.12942702	6917.55894	17694.6751
97	8.50028562	-1.8374819	6.66280377	17618.5531	52870.2393
98	3.98665269	-0.8486063	3.13804635	7145.04131	34330.2222
99	4.23954861	-0.6999844	3.53956423	12030.7039	31441.506
100	7.3953577	-2.8896203	4.50573743	7610.99011	20717.6294

<u>ID#</u>	Back % DS	Length [m]	<u>Type</u>	Map_Pattern	Terrain_Type
1	76	584067.883	LS	CC	SP
2	83.3333333	95265.0575	LS	CV	SP
3	92.0353982	148745.564	WR	ST	SP
4	82.7160494	231721.946	LS	CC	ICP
5	70.1388889	157429.145	LS	CV	SP
6	100	173135.621	LS	ST	ICP
7	100	89247.503	LS	CV	SP
8	68.2926829	205172.914	WR	CV	SP
9	96	713501.292	LS	CV	ICP
10	95.9349594	172035.282	WR	SV	SP
11	60.989011	331039.824	LS	CV	ICP
12	90.625	33247.1877	LS	ST	ICP
13	93.9759036	245318.552	LS	ST	ICP
14	88.888889	57982.3502	WR	ST	SP
15	81.3397129	114674.78	LS	ST	SP
16	86.1538462	46169.8734	LS	CV	SP
17	90.4761905	383446.351	LS	ST	ICP
18	75.7894737	30153.1339	LS	ST	ICP
19	54.4843049	1016397.49	LS	CV	ICP
20	86.0465116	165327.838	LS	CC	ICP
21	69.5652174	91811.6231	WR	ST	SP
22	67.0454546	171838.009	WR	ST	SP
23	80.4347826	277181.536	WR	SV	ICP
24	87.8504673	264458.757	LS	CC	ICP
25	92.5	232790.158	WR	CV	SP
26	64.6551724	72910.4218	LS	ST	ICP
27	68.7861272	476406.251	LS	SV	ICP
28	80.4878049	104573.459	WR	CV	SP
29	100	105642.66	LS	ST	ICP
30	69.3877551	50153.3501	WR	ST	SP
31	84.4660194	412107.7	LS	CV	ICP
32	66.8831169	248928.947	LS	ST	ICP
33	60	136685.223	WR	CV	SP
34	100	175995.589	LS	ST	ICP
35	61.3333333	322692.829	LS	ST	ICP
36	90.2173913	339451.504	LS	ST	ICP
37	92	183083.727	LS	CV	ICP
38	80.9248555	175405.712	LS	ST	ICP
39	88.3116883	86228.1949	LS	ST	ICP

40	90.6976744	413258.918	LS	CV	ICP
41	70.8333333	44263.5481	LS	ST	SP
42	88.3435583	264170.482	LS	SV	ICP
43	100	137426.246	WR	SV	SP
44	92.8571429	113012.418	WR	CC	SP
45	89.1666667	153399.225	LS	CV	ICP
46	76.7123288	289548.092	LS	CV	ICP
47	100	82027.9011	WR	SV	ICP
48	86.4864865	614188.341	LS	CV	ICP
49	97.5	135361.176	LS	ST	ICP
50	86.8965517	147509.187	LS	CV	ICP
51	63.2911392	353511.532	WR	SV	SP
52	85.2631579	202239.698	LS	ST	ICP
53	79.6052632	114744.885	LS	CV	SP
54	85	61276.042	WR	SV	SP
55	55.1470588	633835.691	LS	CV	ICP
56	73.8095238	87069.9018	LS	ST	ICP
57	98.2142857	372346.859	LS	ST	ICP
58	87.6404494	59963.8842	LS	ST	ICP
59	84.939759	308717.292	LS	CV	ICP
60	71.7948718	266855.486	LS	ST	ICP
61	95.7746479	209827.824	LS	CV	ICP
62	67.5	215074.875	LS	ST	ICP
63	68.75	96992.921	LS	CV	ICP
64	97.1428571	725541.644	WR	SV	SP
65	97.826087	124140.85	LS	ST	ICP
66	65.6410256	91147.0014	LS	CC	ICP
67	90.0990099	139813.232	WR	CV	ICP
68	98.1818182	59247.1728	LS	ST	ICP
69	66.023166	187098.695	LS	ST	ICP
70	67.5925926	98854.0378	LS	CV	SP
71	85.4545455	173777.298	WR	ST	SP
72	95.4545455	66893.8259	LS	CV	ICP
73	100	166335.453	WR	SN	SP
74	100	116861.67	LS	CC	ICP
75	73.7179487	217442.645	LS	CV	ICP
76	74.444444	179329.277	LS	ST	ICP
77	92.3076923	91832.9148	LS	CC	ICP
78	89.6551724	154465.653	LS	CV	ICP
79	73.5849057	113118.536	LS	CV	SP

80	82.8571429	214755.411	WR	CV	SP
81	86.0465116	75954.821	WR	CC	SP
82	96.2962963	102527.432	LS	ST	ICP
83	69.2771084	128315.987	WR	CV	SP
84	75.1677852	179964.326	WR	SV	SP
85	86.5168539	156455.715	LS	ST	ICP
86	94.8717949	53307.0123	LS	ST	ICP
87	69.1358025	127370.954	WR	ST	SP
88	98.4615385	268334.099	LS	ST	ICP
89	78.807947	174329.608	LS	CV	ICP
90	87.5	192266.094	LS	ST	ICP
91	98.3870968	212040.625	LS	ST	ICP
92	73.9130435	179539.942	LS	CV	ICP
93	100	172425.118	LS	CV	ICP
94	71.9626168	113141.477	LS	CV	ICP
95	82.1782178	81230.2971	LS	ST	ICP
96	78.0821918	177710.561	LS	ST	ICP
97	90.5172414	445421.91	LS	CV	ICP
98	83.2061069	193656.585	LS	ST	ICP
99	66.666667	69374.6942	LS	ST	ICP
100	69.1489362	92590.6711	LS	CV	ICP

<u>ID #</u>	TRI	Longitude[deg]	Latitude[deg]
1	69.3438249	77.922263	5.037331
2	20.9162111	-143.58591	57.549008
3	31.4289475	1.525039	57.904785
4	27.0443175	-13.268803	-72.933222
5	23.3289423	78.206399	64.859683
6	59.2978222	101.502874	-28.557211
7	17.2207048	76.575795	4.921491
8	46.5004916	-34.769593	73.89957
9	62.059886	-96.794286	-49.914551
10	15.7823154	100.26	49.39
11	18.7716757	15.514446	-40.738363
12	26.6177783	-13.934785	-1.558415
13	26.1924712	9.440699	-36.009377
14	24.110678	-47.437094	75.172131
15	24.4165178	-165.12844	52.794662
16	5.98795385	-133.85836	20.346179
17	76.6400751	-145.04759	-35.113607
18	13.3020716	-122.88483	5.650176
19	15.1340842	81.672632	-32.377029
20	33.6327886	160.012391	56.027688
21	33.9625764	19.04462	67.28654
22	25.1632703	-67.422804	78.442622
23	33.6246935	-26.673686	62.882416
24	64.8427652	-52.628714	58.245027
25	46.4334553	117.706938	-42.449749
26	12.6915444	-101.30613	-7.165898
27	18.0104381	65.633289	-50.312925
28	6.94785783	-126.22177	46.546291
29	14.9137983	-105.96778	35.033733
30	35.0569478	-102.46533	68.962233
31	23.3239235	66.607711	-28.385816
32	12.9072726	-21.050565	6.953675
33	2.80801734	38.831812	62.152694
34	66.5484069	-178.09639	-7.043594
35	19.6284344	-64.885453	-20.764056
36	65.7853947	-70.778464	-41.903033
37	29.9477228	37.696557	22.368543
38	35.2642779	-34.108979	51.459815
39	80.0030898	56.501872	-4.768983

40	106.677432	43.564966	19.523098
41	33.2189572	129.467892	73.006214
42	14.4106723	-112.57768	12.854376
43	30.4782681	170.699396	65.913308
44	8.86227542	6.04407	37.013483
45	13.4030755	168.843045	53.515638
46	21.3027244	28.06513	-30.165926
47	57.0581058	147.823402	-0.508532
48	39.355251	-171.92419	-58.562305
49	57.5054245	12.042639	1.880505
50	31.3129792	-174.96293	-74.161057
51	41.8893084	-164.29777	23.264114
52	58.5022334	151.285125	8.287738
53	4.82693665	62.201109	57.05819
54	27.3220065	42.097741	44.468632
55	29.4689243	102.705785	1.259371
56	19.1203283	-133.29573	23.011225
57	77.7215205	67.197281	-7.42877
58	13.9331363	-103.2915	31.331447
59	10.6346347	-31.350246	38.354478
60	43.4282339	141.559736	20.994221
61	28.7667363	9.127369	16.35234
62	44.6002016	53.228844	16.676984
63	18.7132556	-92.022571	31.593786
64	33.7065078	-39.641455	-65.308742
65	44.8837914	47.264397	-34.192529
66	39.1308739	173.982222	61.565743
67	12.4327147	-97.718928	-7.025252
68	18.1141249	-42.843891	17.173965
69	15.7398617	53.615377	-58.022215
70	42.230102	12.424462	80.610875
71	32.9912996	-8.590569	73.447571
72	14.285837	40.722586	32.417555
73	32.0344958	171.940191	-11.569986
74	85.7999797	124.690101	-57.880756
75	10.8516274	-65.053295	-4.346401
76	83.9803992	22.108039	-16.937989
77	42.3826758	106.340245	-6.795465
78	64.8099183	148.292773	-29.601304
79	33.1644211	-95.764571	77.900197

80	29.8820557	115.527757	78.934831
81	24.4731544	118.33	75.46127
82	37.9726669	104.039669	40.416535
83	5.66487582	44.755001	55.1378
84	7.07479903	27.411263	62.611347
85	12.6689081	-98.322293	46.704889
86	10.7311632	-103.83707	46.70867
87	7.98315617	24.605854	55.243704
88	55.6703096	-68.137551	-64.873283
89	19.841403	-100.32781	-15.720014
90	65.2837881	126.317936	2.69957
91	71.964816	103.655316	-17.734348
92	64.8035798	132.897981	10.000297
93	40.3212755	-138.4018	-41.964729
94	6.46072261	-109.95028	46.154289
95	30.5976984	-67.253211	58.22483
96	20.5436433	71.236676	-26.426689
97	46.1645592	-40.55403	-57.472881
98	10.73221	-166.19316	32.795531
99	42.1553644	102.421014	30.271132
100	26.243627	-134.63239	-5.609274

CODE IN R USED FOR STATISTICAL ANALYSIS OF CHAPTER 2

```
setwd('') # Set directory
thrustFaults <- read.table(file='Loveless et al
Supplementary Table.csv', header=TRUE, row.names=1,
sep=',')
# Units, if applicable, are the last value in each
measurement name. For example, Relief, with units of meters
is labeled as 'Relief m'
# Defining Categories from the data table
# Traditional Categories
lobateScarps <- thrustFaults$Type == 'LS'</pre>
wrinkleRidges <- thrustFaults$Type == 'WR'</pre>
# Map Patterns
concave <- thrustFaults$Map Pattern == 'CC'</pre>
convex <- thrustFaults$Map Pattern == 'CV'</pre>
straight <- thrustFaults$Map Pattern == 'ST'</pre>
switchingVergence <- thrustFaults$Map Pattern == 'SV'</pre>
sinuous <- thrustFaults$Map Pattern == 'SN'</pre>
```

```
# Terrain Type
interCraterPlains <- thrustFaults$Terrain Type == 'ICP'</pre>
smoothPlains <- thrustFaults$Terrain Type == 'SP'</pre>
# Data Transformations
attach(thrustFaults)
up fault <- cbind(log(Relief m), log(Breadth m),</pre>
log(Tot CrossSectional Length m), log(Strain),
log(Fore Slope deg), log(-Back Slope deg),
log(abs(Symmetry deg)), log(Fore Length m),
log(Back Length m), log(Back Perc DS),
log(Mapped Length m), log(TRI), thrustFaults[12],
thrustFaults[13], thrustFaults[14])
colnames(up fault) <- c('Relief', 'Breadth', 'TopoLength',</pre>
'Strain', 'Fslope', 'Bslope', 'symmetry', 'FL', 'BL',
```

'BPD', 'SL', 'TRI', 'Type', 'Map', 'Terrain')

```
detach(thrustFaults)
PCA data <- up fault[ , 1:12]</pre>
pca <- prcomp(PCA data, scale.=TRUE)</pre>
# Define statistics Derived from the PCA
variance <- (pca$sdev)^2</pre>
loadings <- pca$rotation</pre>
scores <- pca$x</pre>
varPercent <- variance/sum(variance) * 100</pre>
# Observe how much variance is accounted for in each PC
varPercent
# View Scree Plot
barplot(varPercent, xlab='PC', ylab='Percent Variance',
names.arg=1:length(varPercent), las=1, col='gray')
```

```
dev.new()
# Display PCA loadings
round(loadings, 2)[, 1:3]
# Traditional Categories Panel
plot(scores[, 1], scores[, 2], xlab='PC 1', ylab='PC 2',
type='n', asp=1, las=1, cex.lab=1., cex.axis=1.)
points(scores[lobateScarps, 1], scores[lobateScarps, 2],
pch=16, cex=1., col='green')
points(scores[wrinkleRidges, 1], scores[wrinkleRidges, 2],
pch=16, cex=1., col='black')
legend(-6.5, 5, bty='n', legend=c('Lobate Scarps', 'Wrinkle
Ridges'), col=c('green', 'black'), pch=c(16, 16), cex=1.)
text(-5, -5, 'a)', cex=1)
# Map Patterns Panel
dev.new()
plot(scores[, 1], scores[, 2], xlab='PC 1', ylab='PC 2',
type='n', asp=1, las=1, cex.lab=1, cex.axis=1)
```

```
points(scores[concave, 1], scores[concave, 2], pch= 17,
cex=1, col='blue')
points(scores[switchingVergence, 1],
scores[switchingVergence, 2], pch= 17, cex=1, col='red')
points(scores[convex, 1], scores[convex, 2], pch=17, cex=1,
col='black')
points(scores[straight, 1], scores[straight, 2], pch= 17,
cex=1, col='gray')
points(scores[sinuous, 1], scores[sinuous, 2], pch= 17,
cex=1, col='green')
legend(-6.5, 5, bty='n', legend=c('Concave', 'Switching
Vergence', 'Convex', 'Straight', 'Sinuous'), col=c('blue',
'red', 'black', 'gray', 'green'), pch=c(17, 17, 17, 17,
17), cex=1)
text(-5, -5, 'b)', cex=1)
# Terrain Type Panel
dev.new()
plot(scores[, 1], scores[, 2], xlab='PC 1', ylab='PC 2',
type='n', asp=1, las=1, cex.lab=1, cex.axis=1)
points(scores[interCraterPlains, 1],
scores[interCraterPlains, 2], pch=1, cex=1, col='black')
```

```
points(scores[smoothPlains, 1], scores[smoothPlains, 2],
pch=16, cex=1, col='red')
legend(-6.5, 5, bty='n', legend=c('Cratered Plains',
'Smooth Plains'), col=c('black', 'red'), pch=c(1, 16),
cex=1)
text(-5, -5, 'c)', cex=1)
# =============== DFA =================
# scale data, using z transformation
zScale \leftarrow function(x) \{ (x - mean(x)) / sd(x) \}
detach(thrustFaults)
head(up fault)
scaled_Faults <- up_fault[ , 1:12]</pre>
scaled Faults <- apply(scaled Faults, 2, FUN=zScale)</pre>
up fault[ , 1:12] <- scaled Faults[ , 1:12]</pre>
head(up fault)
#attach(up fault)
```

```
library(MASS)
# Traditional Category (cat) DFA =====
LDA cat <- lda(Type ~ Relief + Breadth + TopoLength +
Strain + Fslope + Bslope + symmetry + FL + BL + BPD + SL +
TRI, data=up fault)
LDA cat # cat stands for category as in traditional
category
# Observe loadings
round(LDA cat$scaling, 2)
predictions cat <- predict(LDA cat)</pre>
#Observe accuracy with original data
acc cat <- table(up fault$Type, predictions cat$class)</pre>
acc cat
sum(acc cat[row(acc cat) == col(acc cat)]) / sum(acc cat)
```

```
classifications of traditional categories
jackknife cat <- lda(Type ~ Relief + Breadth + TopoLength +</pre>
Strain + Fslope + Bslope + symmetry + FL + BL + BPD + SL +
TRI, data=up fault, CV=TRUE)
accJack cat <- table(up fault$Type, jackknife cat$class)</pre>
accJack cat
# True accuracy of traditional category DFA
sum(accJack cat[row(accJack cat) == col(accJack cat)]) /
sum(accJack cat)
# Terrain type (terr) DFA =====
LDA terr <- lda(Terrain ~ Relief + Breadth + TopoLength +
Strain + Fslope + Bslope + symmetry + FL + BL + BPD + SL +
TRI, data=up fault)
LDA terr # cat stands for category as in traditional
category
# Observe loadings
round(LDA terr$scaling, 2)
```

Perform jackknife resampling to accurately predict

```
predictions terr <- predict(LDA terr)</pre>
#Observe accuracy with original data
acc terr <- table(thrustFaults$Terrain Type,</pre>
predictions terr$class)
acc terr
sum(acc terr[row(acc terr) == col(acc terr)]) /
sum(acc terr)
# Perform jackknife resampling to accurately predict
classifications of terrain type
jackknife terr <- lda(Terrain ~ Relief + Breadth +</pre>
TopoLength + Strain + Fslope + Bslope + symmetry + FL + BL
+ BPD + SL + TRI, data=up fault, CV=TRUE)
accJack terr <- table(thrustFaults$Terrain Type,</pre>
jackknife terr$class)
accJack terr
True accuracy of Terrain Type DFA
sum(accJack terr[row(accJack terr) == col(accJack terr)]) /
sum(accJack terr)
```

```
# Observe predictions on LD axis
# Traditional Categories
dev.new()
stripchart(predictions cat$x ~ thrustFaults$Type, pch =
c(16, 16), col=c('green', 'black'), xlim=c(-3.5, 3.5),
method='jitter', xlab='Lobate Scarps
LD
                                  Wrinkle Ridges')
# Terrain Type
dev.new()
stripchart (predictions terr$x ~ thrustFaults$Terrain Type,
pch = c(1, 16), col=c('black', 'red'), xlim=c(-3.5, 3.5),
method='jitter', xlab='Cratered Plains
                                         Smooth Plains')
LD
# ======= DFA No Breadth
& Cross-Sectional Length (NBC) ===========
# Traditional Categories
LDA cat NBC <- lda(Type ~ Relief + Strain + Fslope + Bslope
+ symmetry + FL + BL + BPD + SL + TRI, data=up fault)
```

```
LDA cat NBC # cat stands for category as in traditional
category
# Observe Loadings
round(LDA cat NBC$scaling, 2)
predictions cat NBC <- predict(LDA cat NBC)</pre>
#Observe Accuracy of original data
acc cat NBC <- table(up fault$Type,</pre>
predictions cat NBC$class)
acc cat NBC
sum(acc cat NBC[row(acc cat NBC) == col(acc cat NBC)]) /
sum(acc cat NBC)
# Perform jackknife resampling
jackknife cat NBC <- lda(Type ~ Relief + Strain + Fslope +</pre>
Bslope + symmetry + FL + BL + BPD + SL + TRI,
data=up fault, CV=TRUE)
accJack cat NBC <- table(up fault$Type,</pre>
jackknife cat NBC$class)
accJack cat NBC
```

```
#True accuracy traditional categories
sum(accJack cat NBC[row(accJack cat NBC) ==
col(accJack cat NBC)]) / sum(accJack cat NBC)
# Terrain type
LDA terr NBC <- lda(Terrain ~ Relief + Strain + Fslope +
Bslope + symmetry + FL + BL + BPD + SL + TRI,
data=up fault)
LDA terr NBC
predictions_terr_NBC <- predict(LDA_terr_NBC)</pre>
# Observe Loadings
round(LDA terr NBC$scaling, 2)
#Check Accuracy with original data
acc terr NBC <- table(thrustFaults$Terrain Type,</pre>
predictions terr NBC$class)
acc terr NBC
```

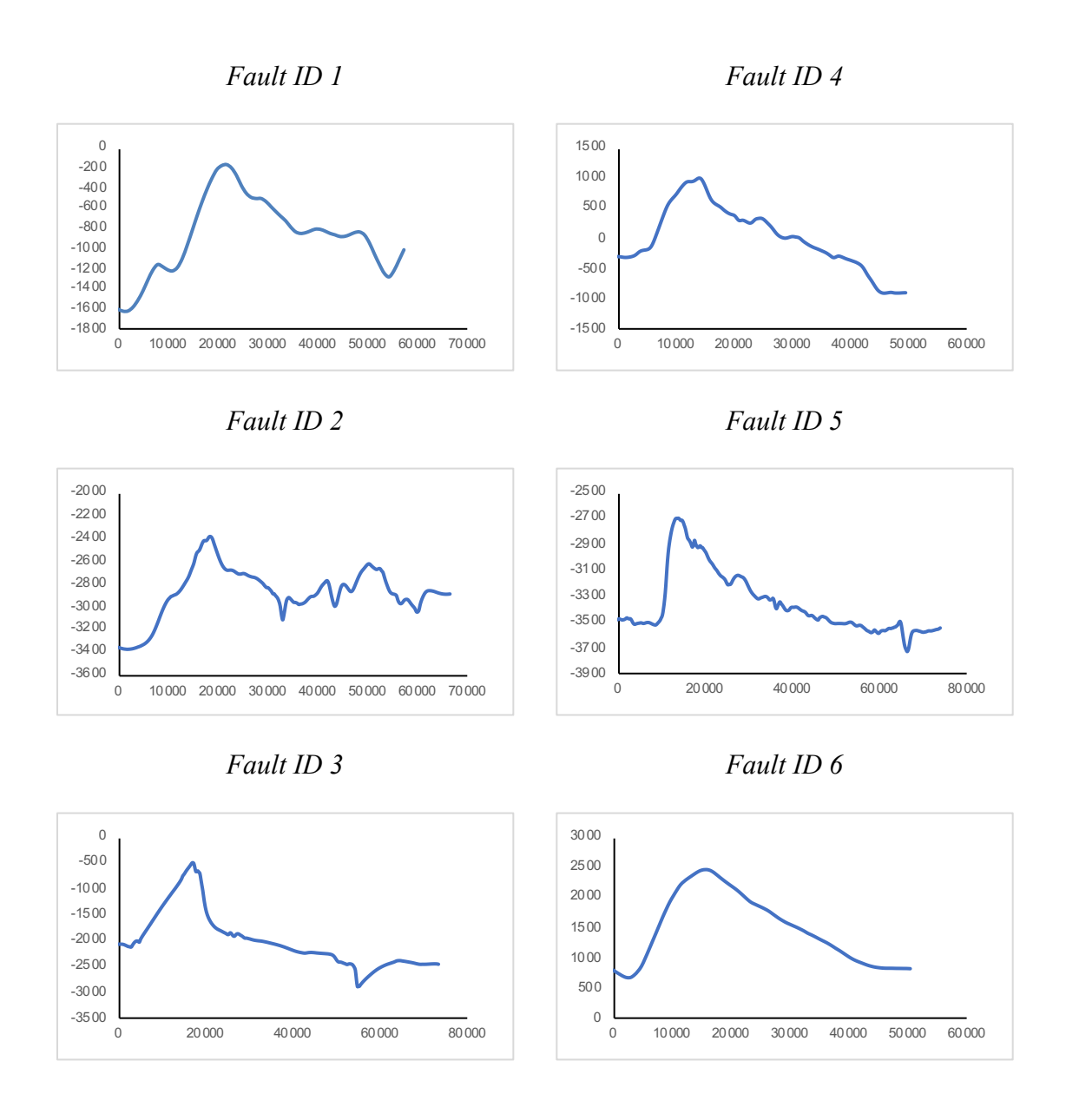
```
sum(acc_terr_NBC[row(acc_terr_NBC) == col(acc_terr_NBC)]) /
sum(acc_terr_NBC)

# jackknife technique
jackknife_terr_NBC <- lda(Terrain ~ Relief + Strain +
Fslope + Bslope + symmetry + FL + BL + BPD + SL + TRI,
data=up_fault, CV=TRUE)
accJack_terr_NBC <- table(thrustFaults$Terrain_Type,
jackknife_terr_NBC$class)
accJack_terr_NBC

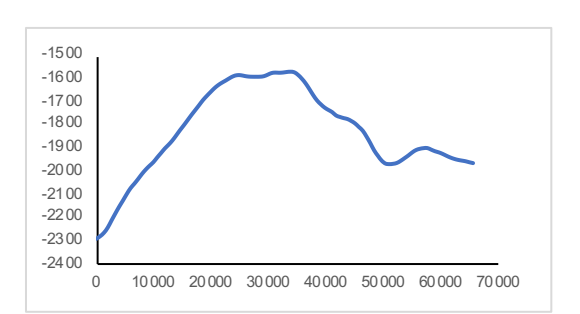
#True accuracy Terrain type
sum(accJack_terr_NBC[row(accJack_terr_NBC) ==
col(accJack_terr_NBC)]) / sum(accJack_terr_NBC)</pre>
```

Figure A2.2: 100 shortening landforms analyzed in Chapter 2

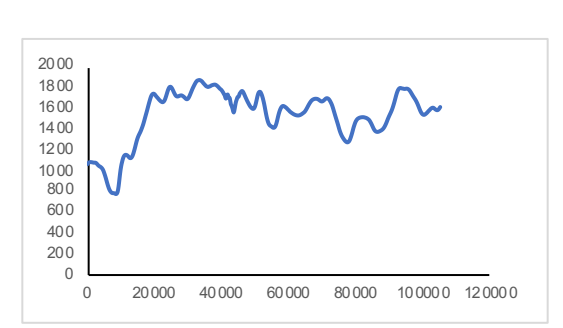
All axes are in meters. Y-axis is elevation and X-axis is horizontal distance.



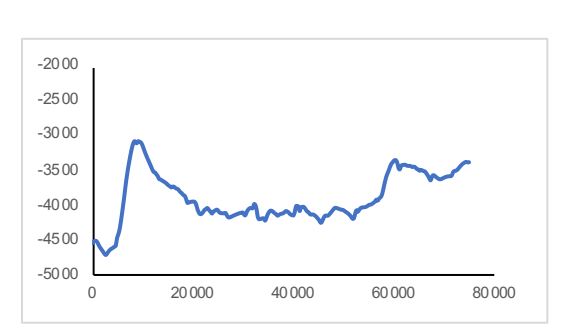
Fault ID 7



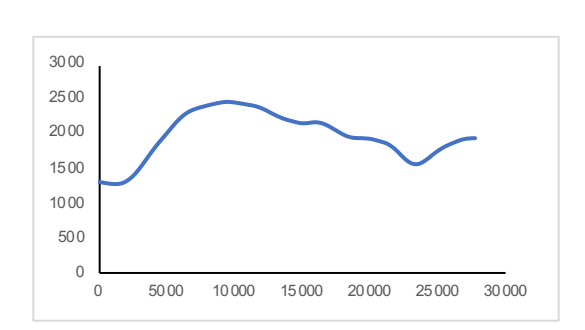
Fault ID 11



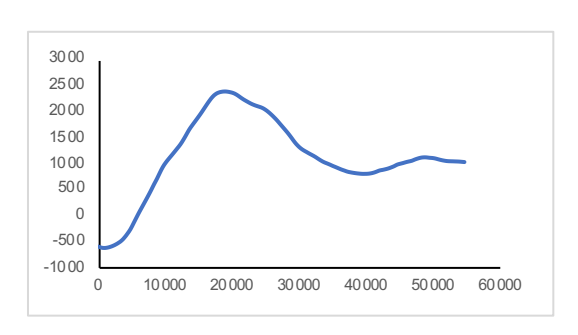
Fault ID 8



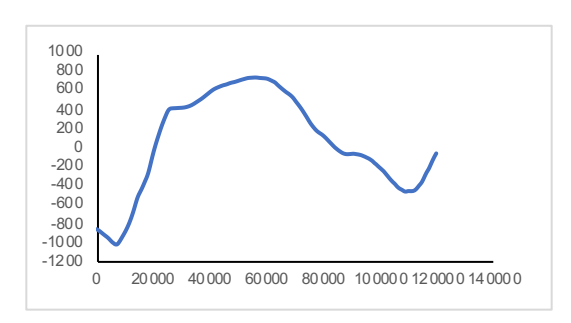
Fault ID 12



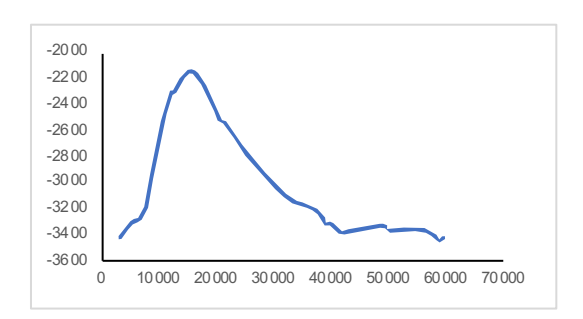
Fault ID 9



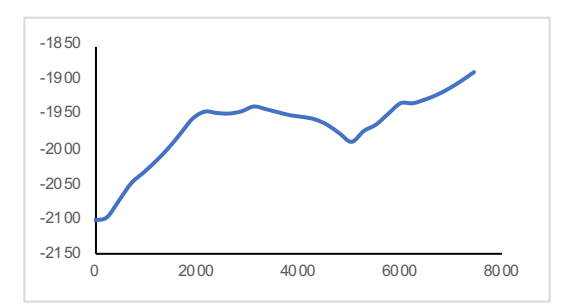
Fault ID 13



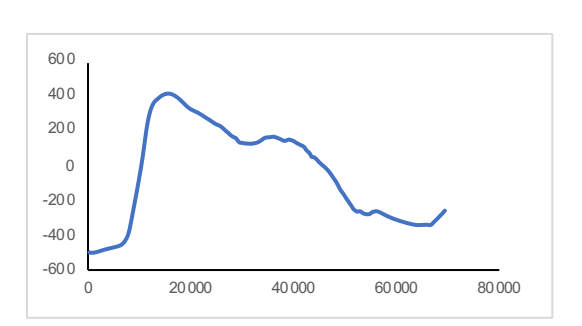
Fault ID 10



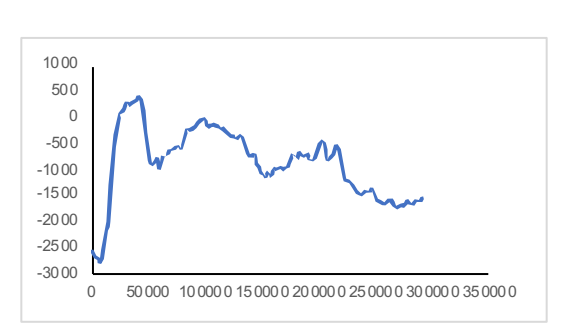
Fault ID 14



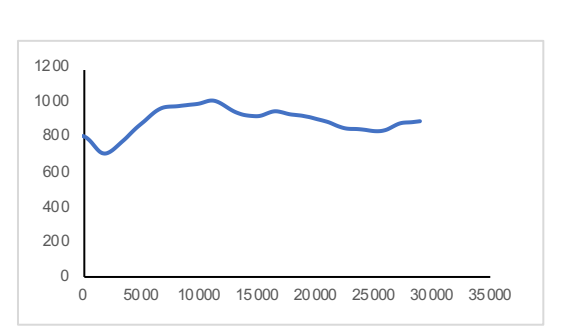
Fault ID 15



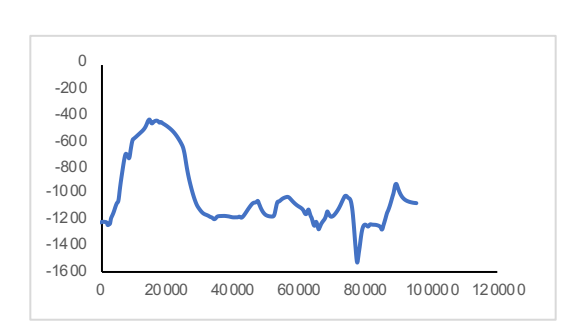
Fault ID 19



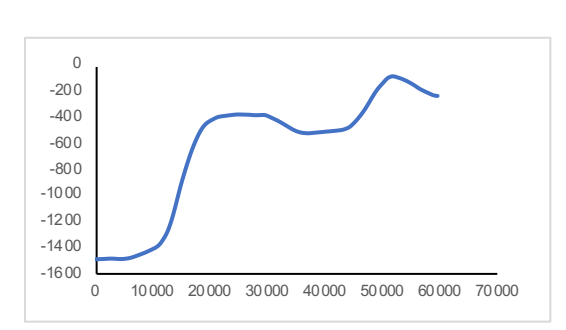
Fault ID 16



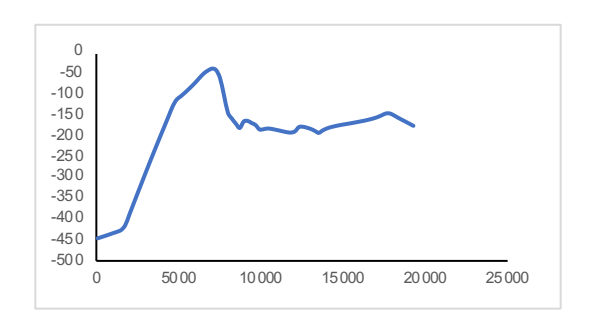
Fault ID 20



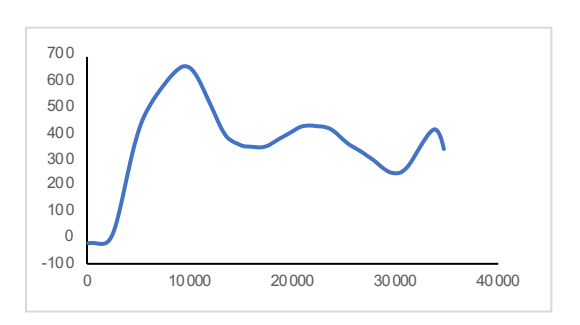
Fault ID 17



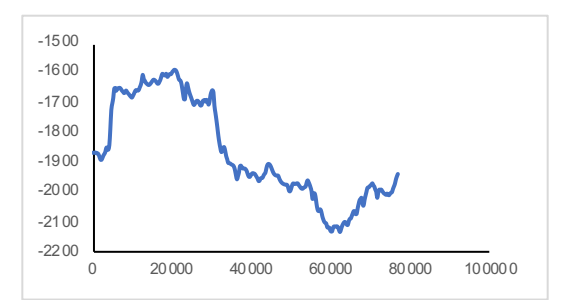
Fault ID 21



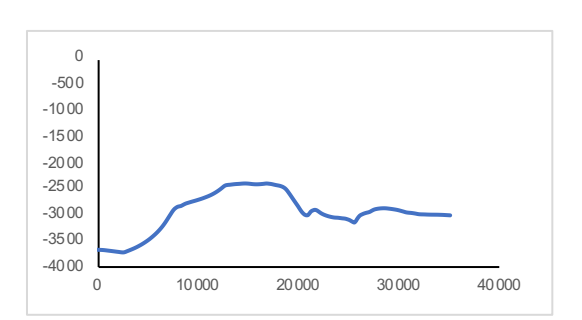
Fault ID 18



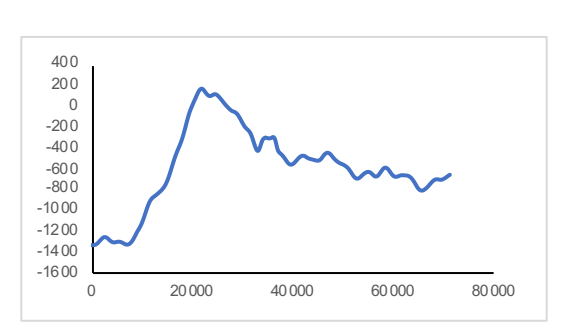
Fault ID 22



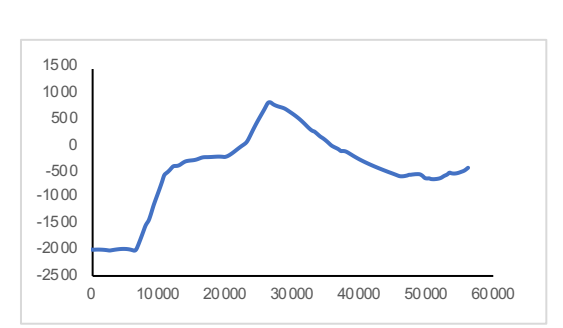
Fault ID 23



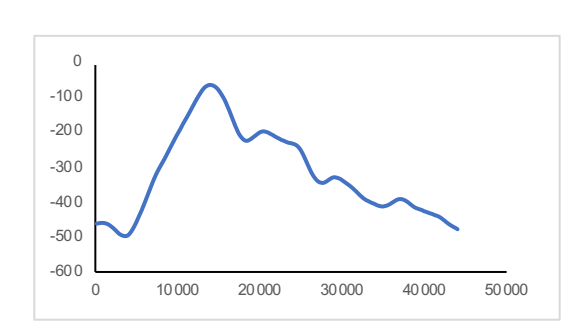
Fault ID 27



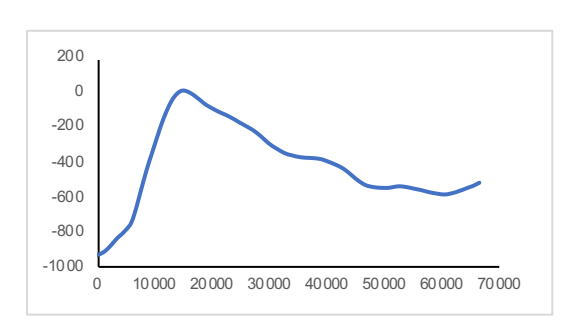
Fault ID 24



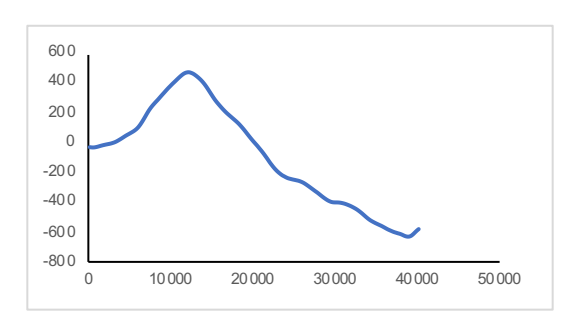
Fault ID 28



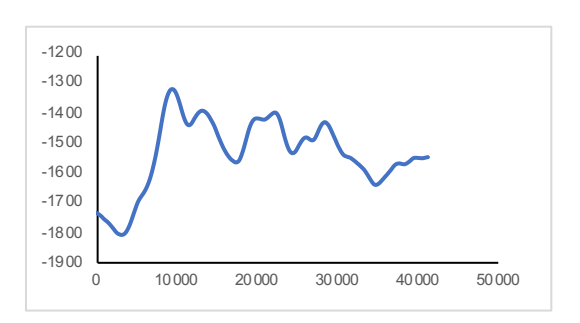
Fault ID 25



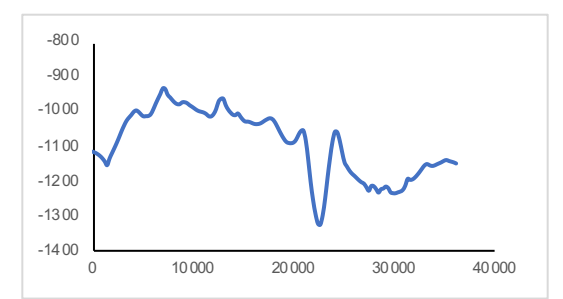
Fault ID 29



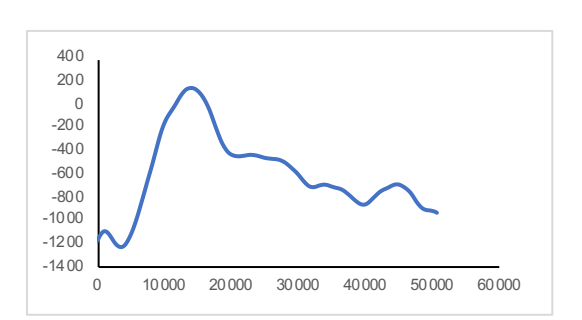
Fault ID 26



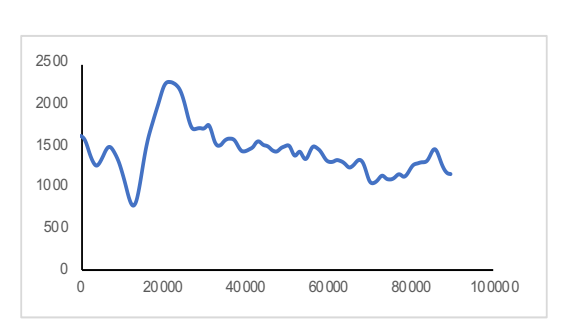
Fault ID 30



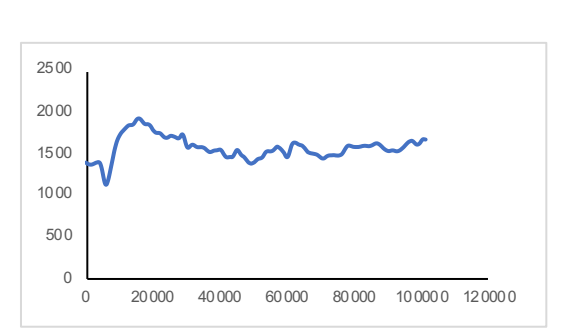
Fault ID 31



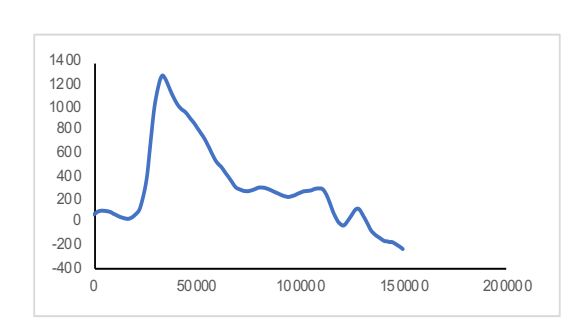
Fault ID 35



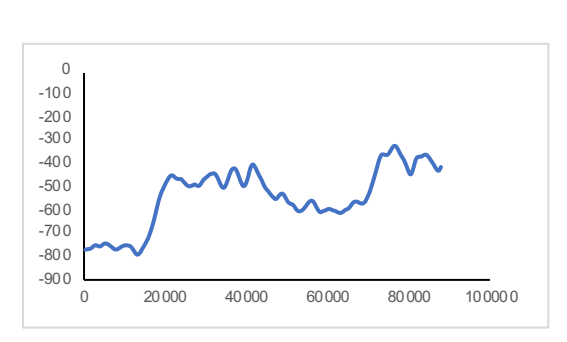
Fault ID 32



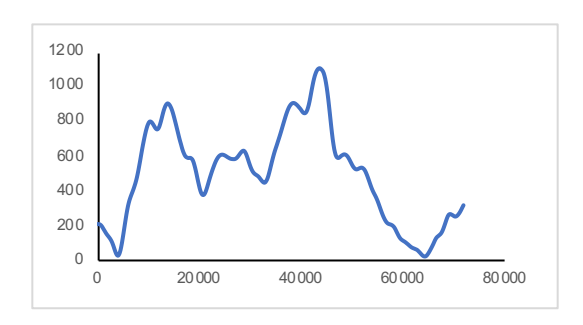
Fault ID 36



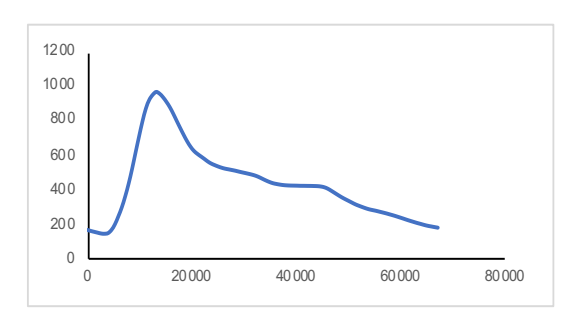
Fault ID 33



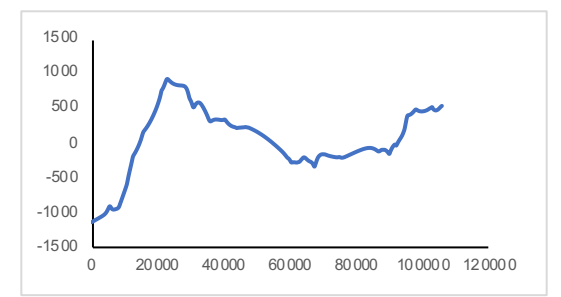
Fault ID 37



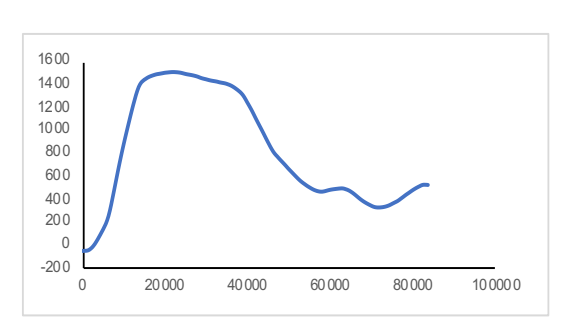
Fault ID 34



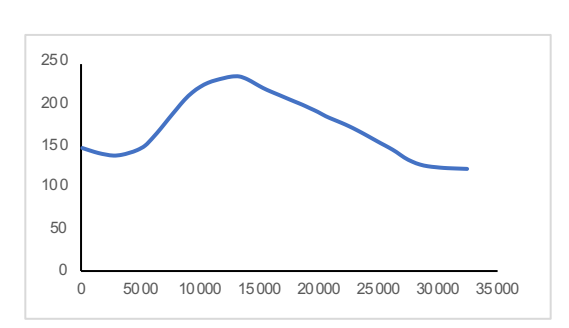
Fault ID 38



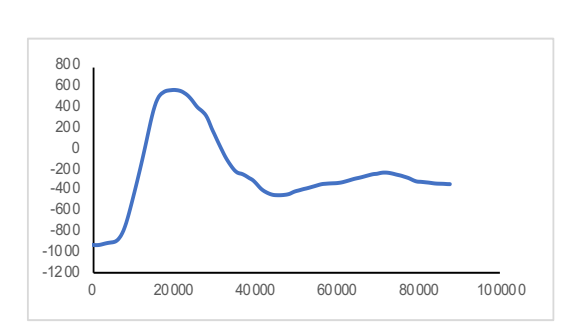
Fault ID 39



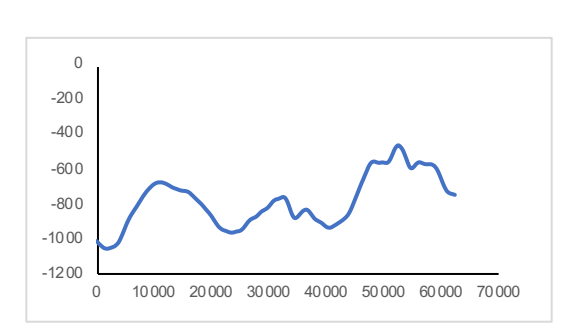
Fault ID 43



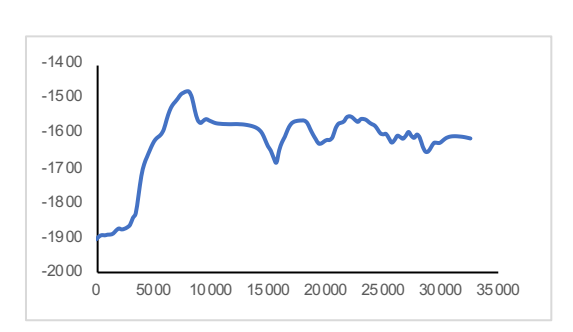
Fault ID 40



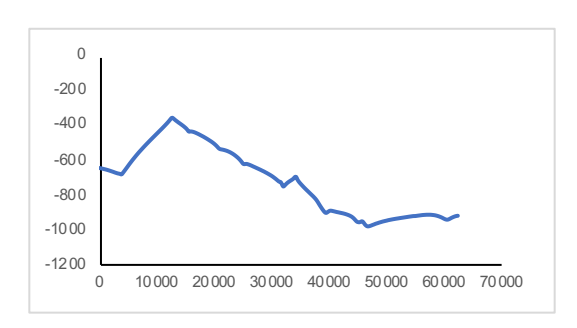
Fault ID 44



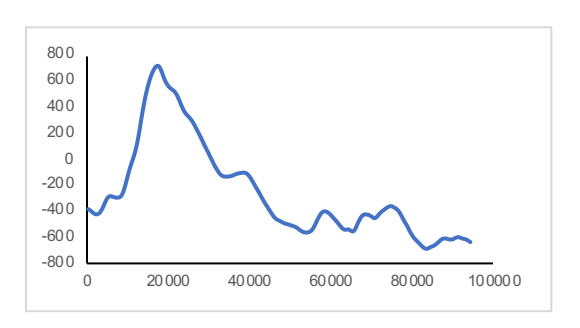
Fault ID 41



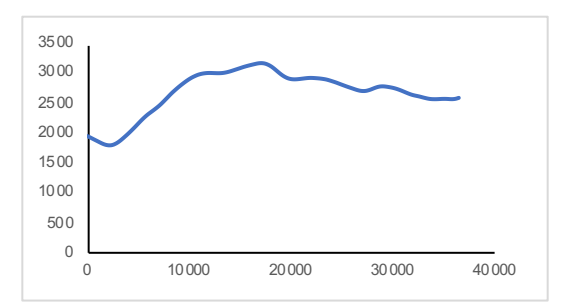
Fault ID 45



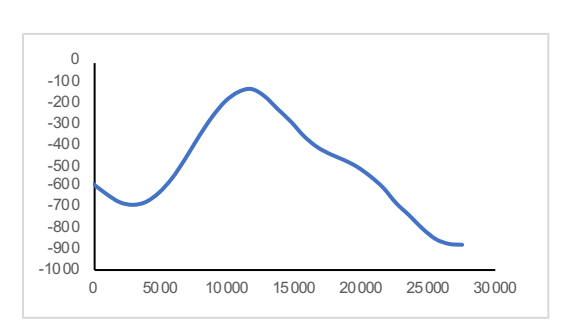
Fault ID 42



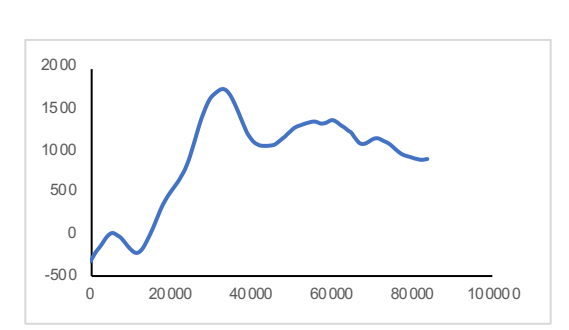
Fault ID 46



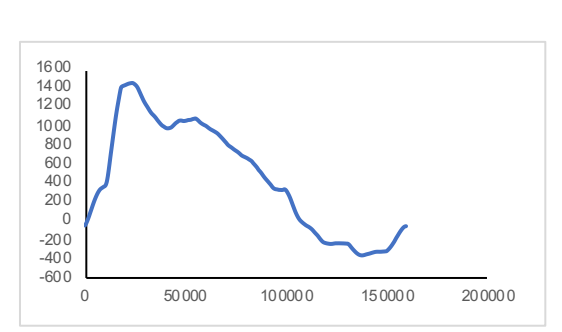
Fault ID 47



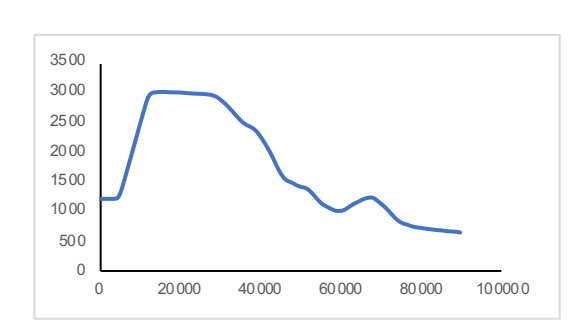
Fault ID 51



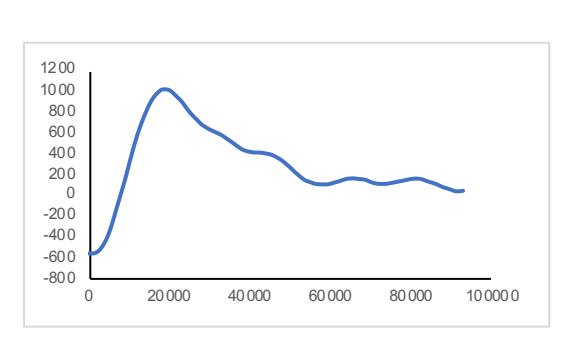
Fault ID 48



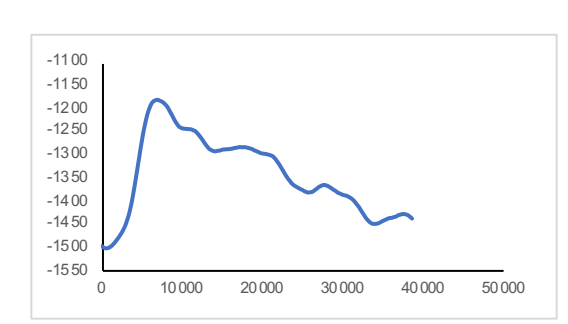
Fault ID 52



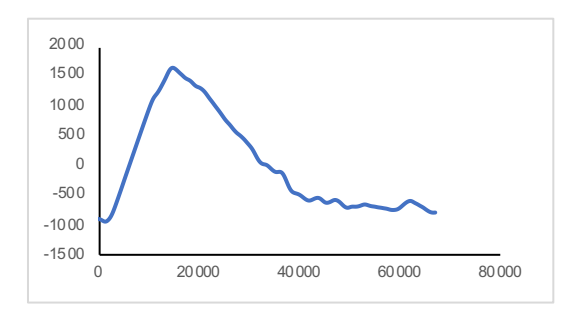
Fault ID 49



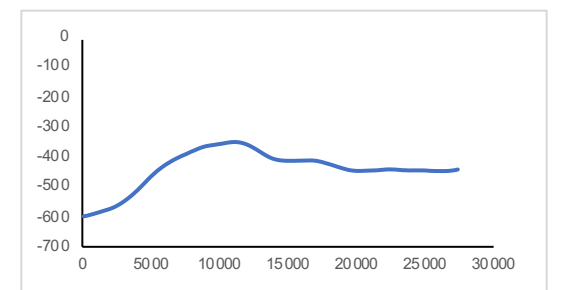
Fault ID 53



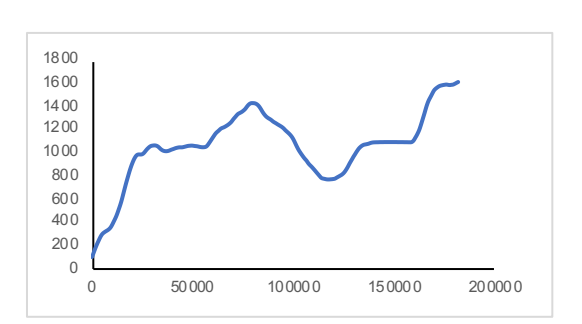
Fault ID 50



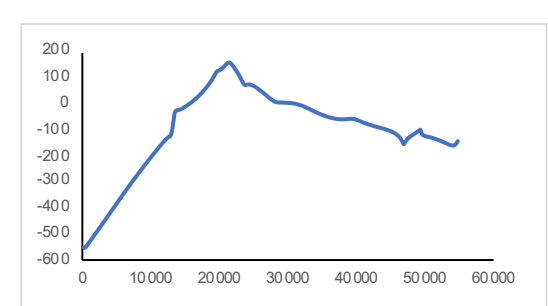
Fault ID 54



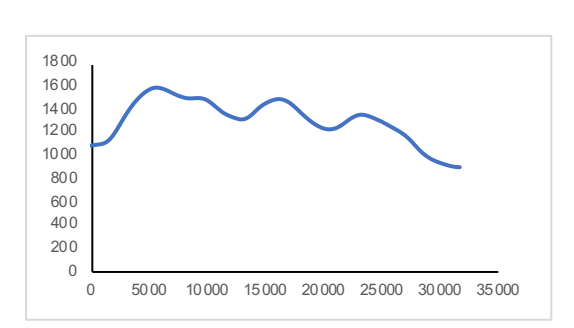
Fault ID 55



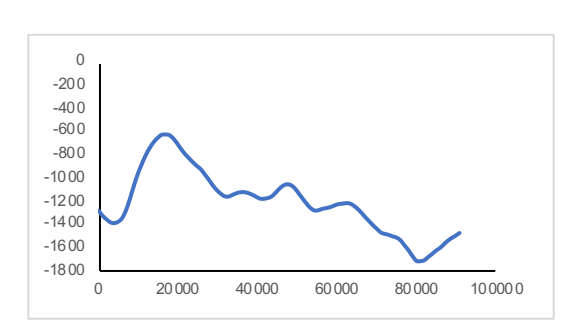
Fault ID 59



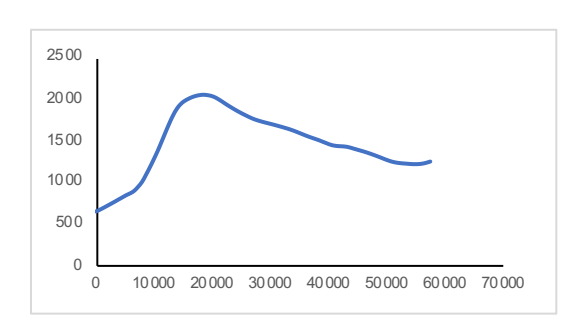
Fault ID 56



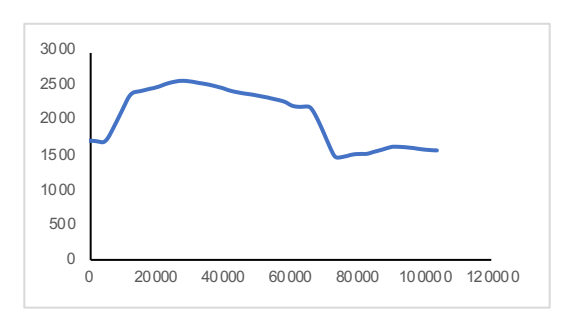
Fault ID 60



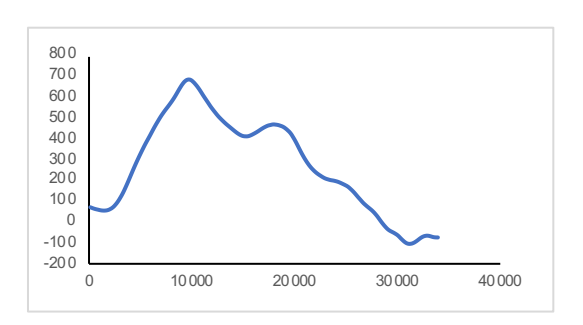
Fault ID 57



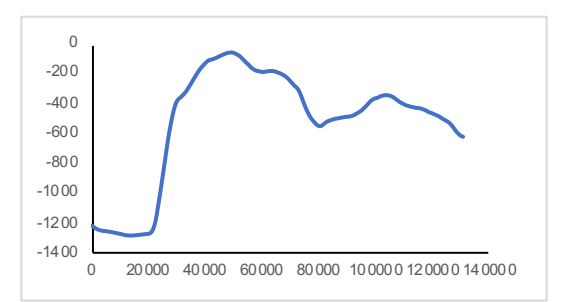
Fault ID 61



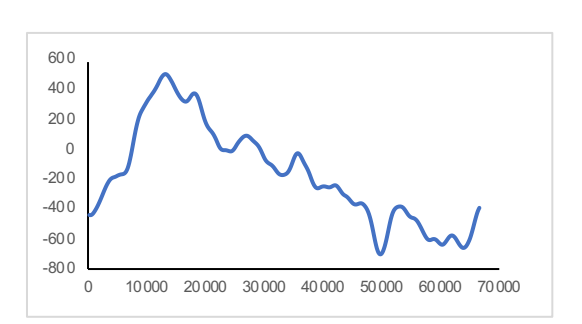
Fault ID 58



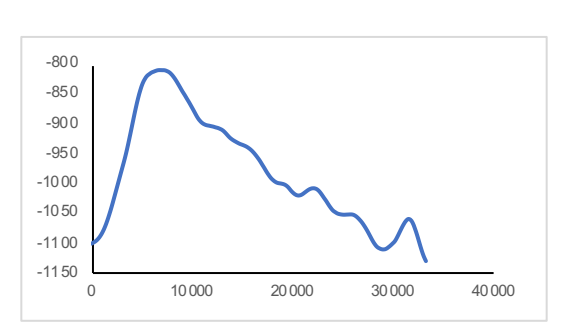
Fault ID 62



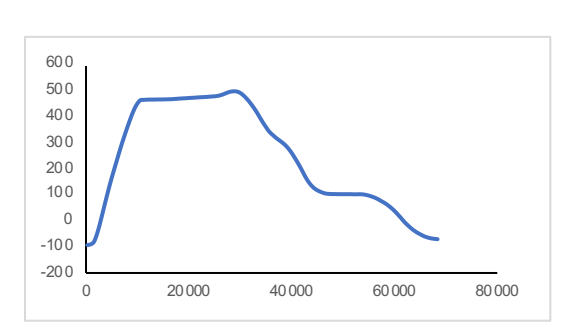
Fault ID 63



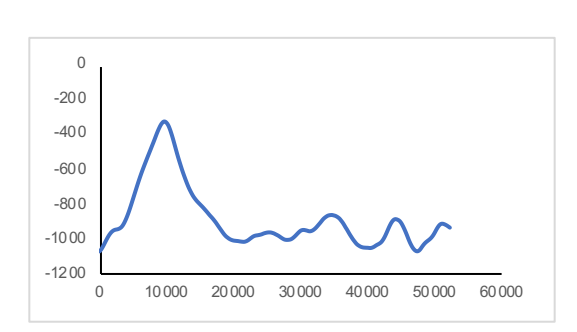
Fault ID 67



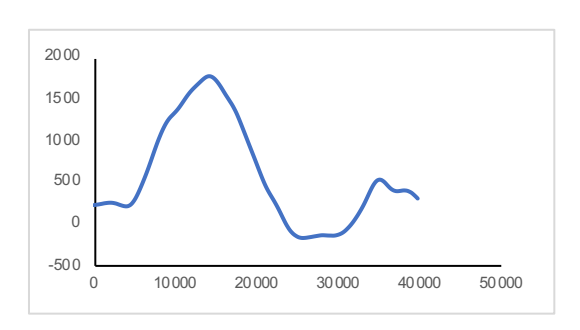
Fault ID 64



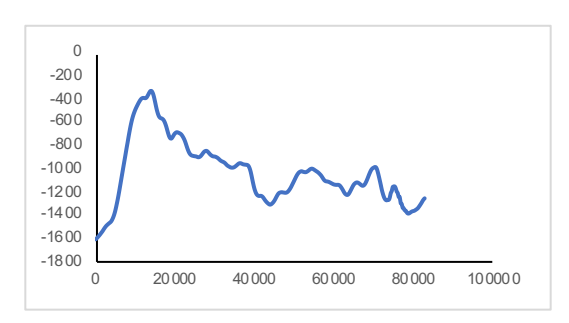
Fault ID 68



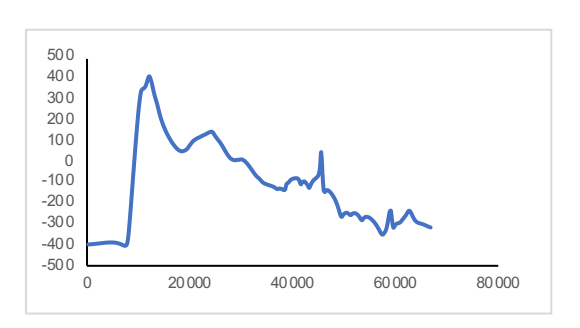
Fault ID 65



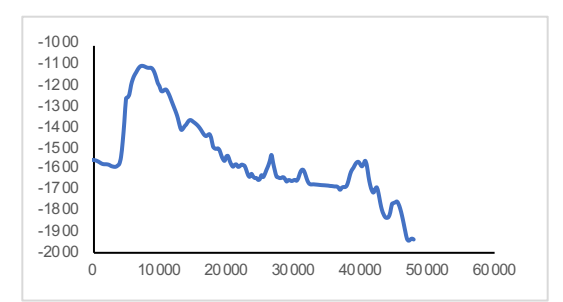
Fault ID 69



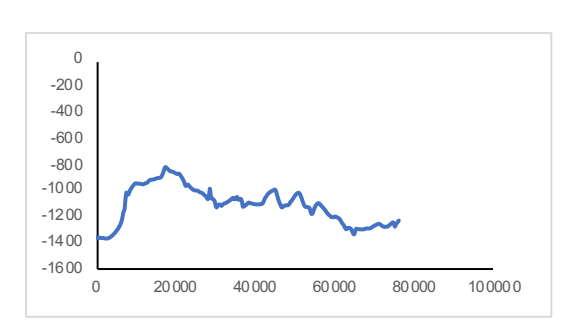
Fault ID 66



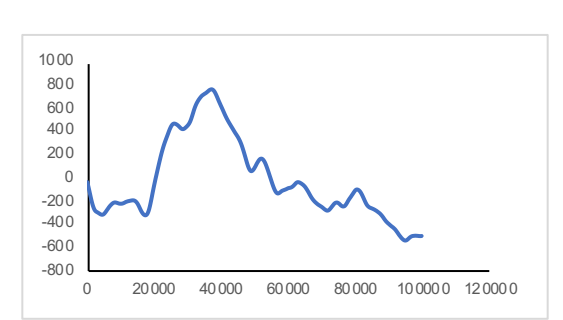
Fault ID 70



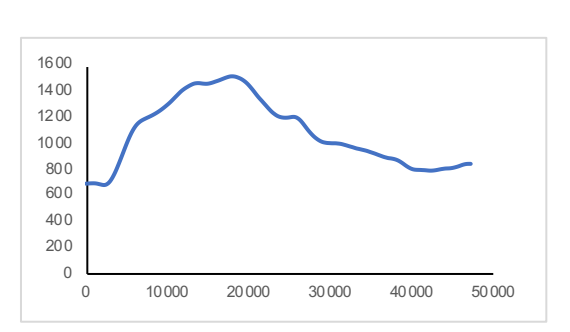
Fault ID 71



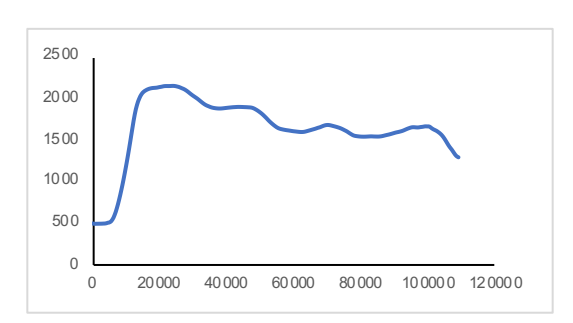
Fault ID 75



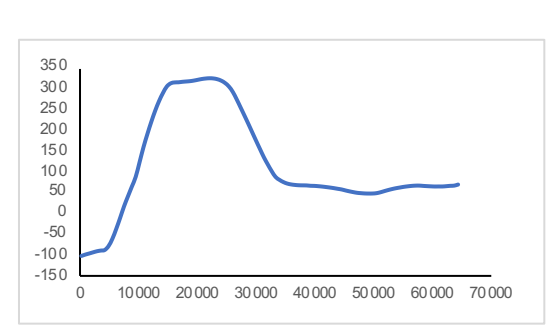
Fault ID 72



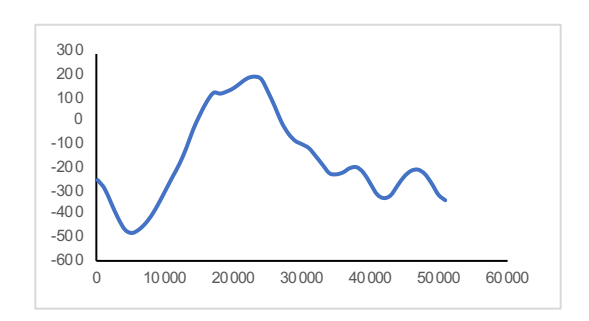
Fault ID 76



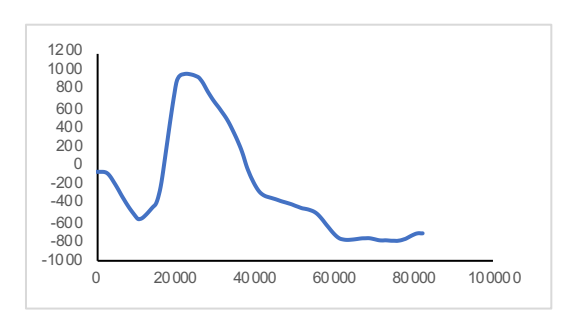
Fault ID 73



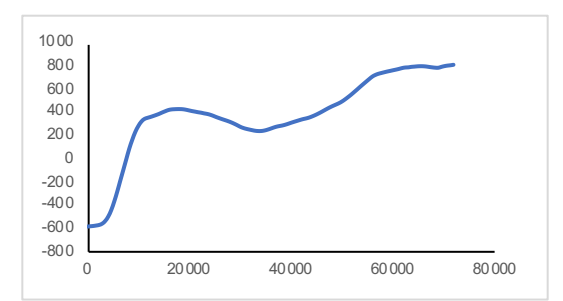
Fault ID 77



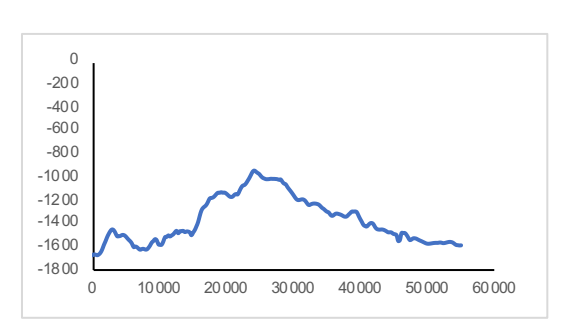
Fault ID 74



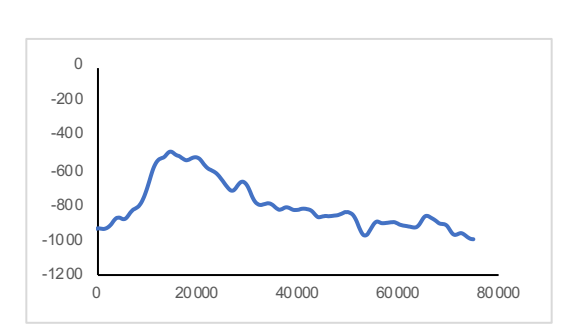
Fault ID 78



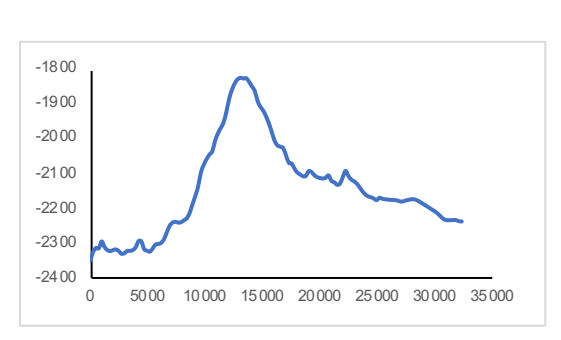
Fault ID 79



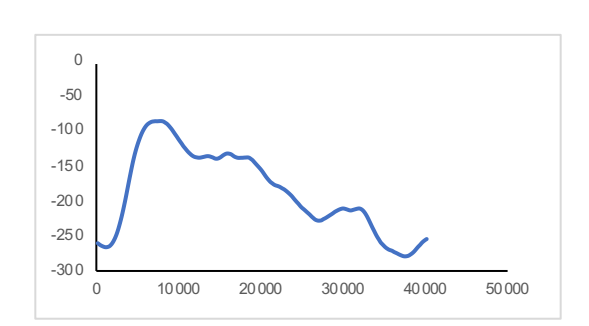
Fault ID 83



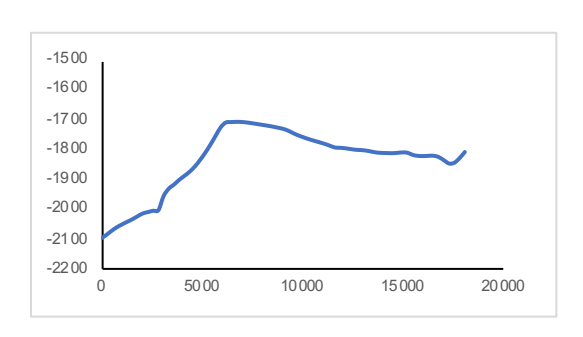
Fault ID 80



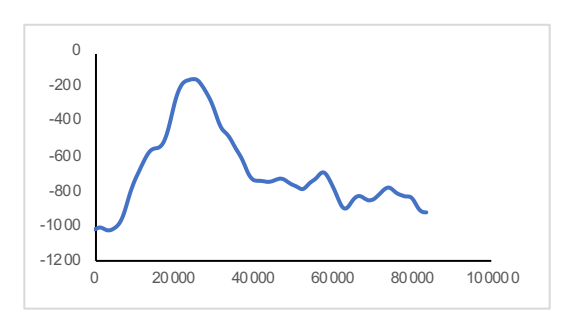
Fault ID 84



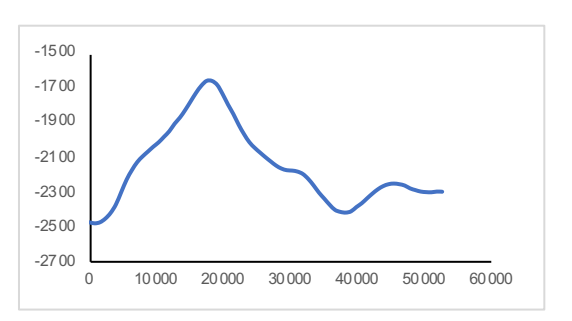
Fault ID 81



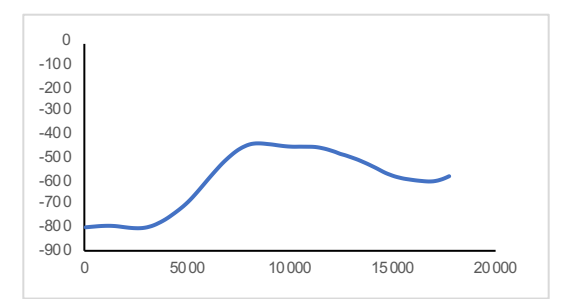
Fault ID 85



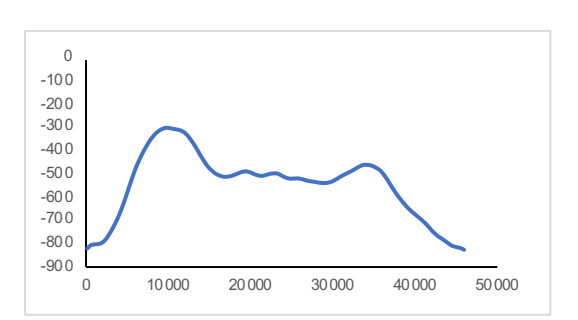
Fault ID 82



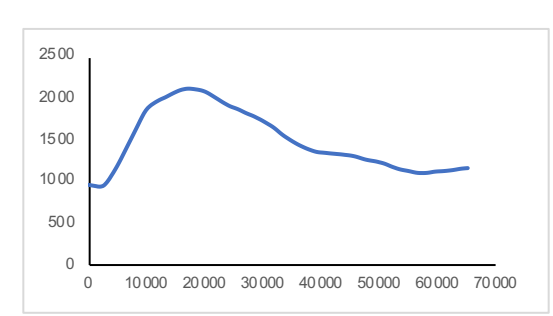
Fault ID 86



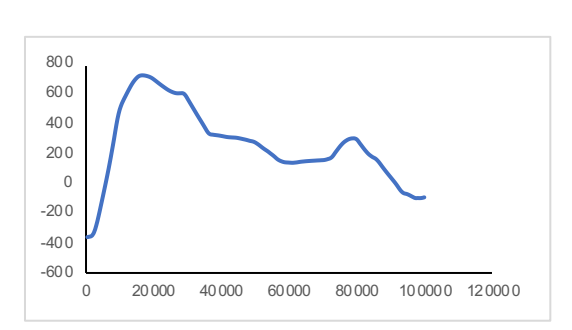
Fault ID 87



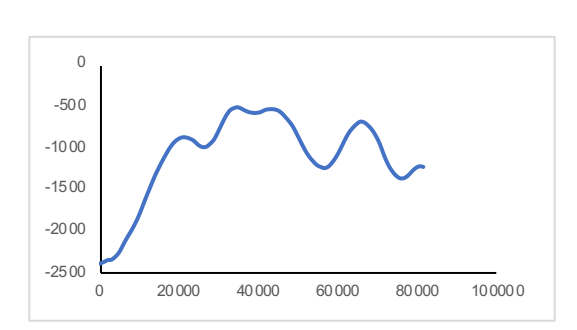
Fault ID 91



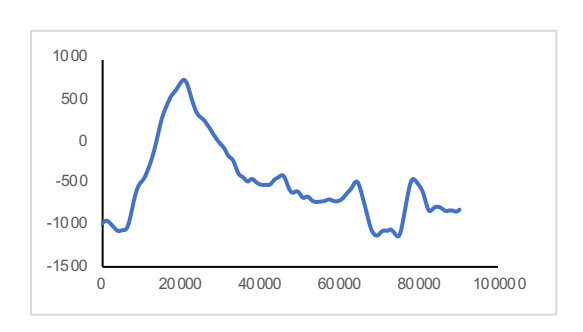
Fault ID 88



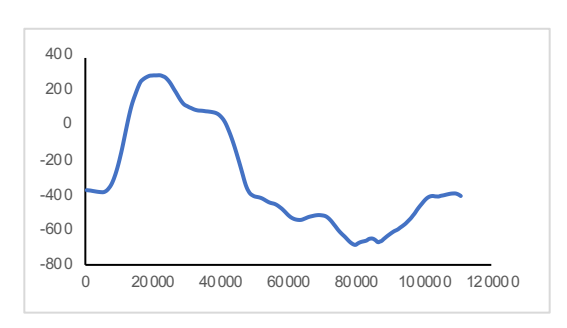
Fault ID 92



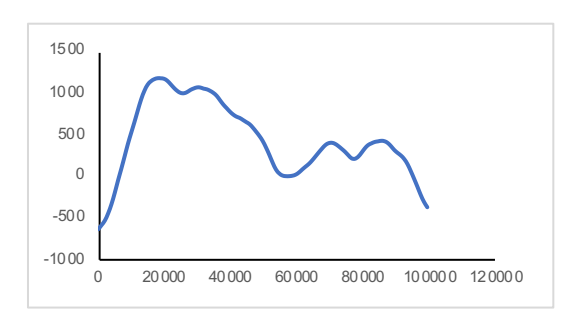
Fault ID 89



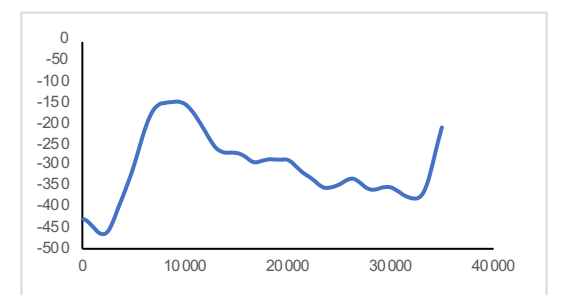
Fault ID 93



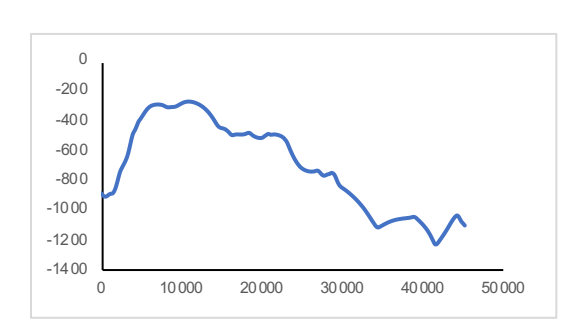
Fault ID 90



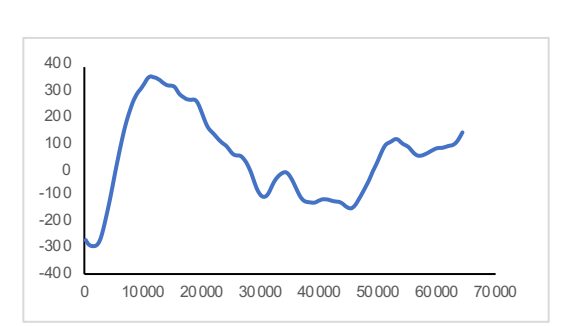
Fault ID 94



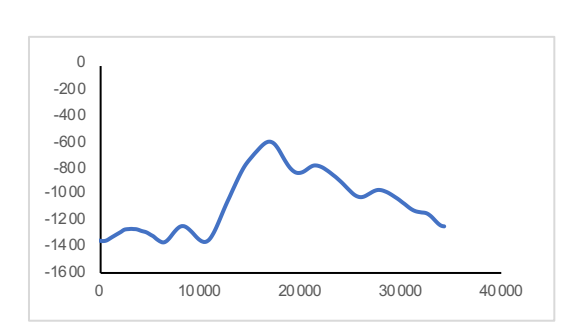
Fault ID 95



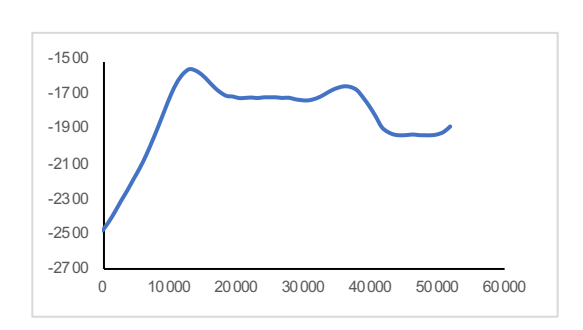
Fault ID 98



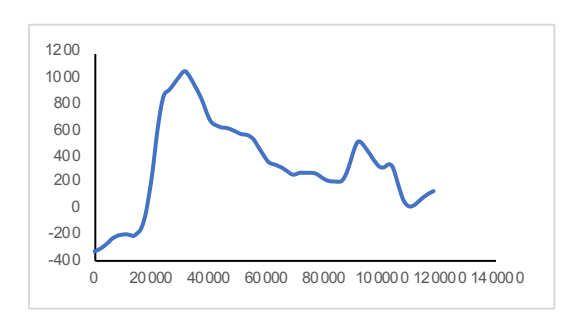
Fault ID 96



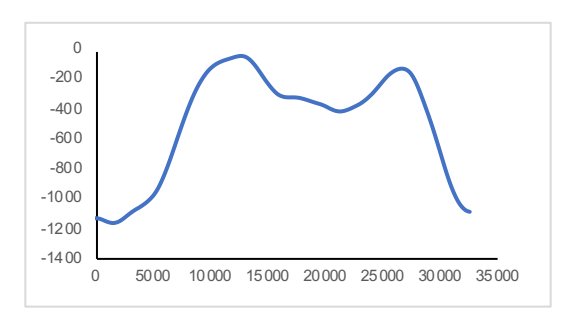
Fault ID 99



Fault ID 97



Fault ID 100



APPENDIX B: CHAPTER 3

 Table B3.1: Extracted modeled values for 55 shortening landforms

		4 ·D:	N D:	01 1 1 1	
<u>ID #</u>	NearSurfDip	<u>AvgDip</u>	<u>MaxDip</u>	ShorteningInput	MaxSlip
3	17.4523293	16.664975	30.6548524	1600	1093.8
6	31.4376616	28.6293578	50.4783039	750	1087.6
8	35.4218911	37.7403089	59.6563648	525	903.5
10	24.9187624	20.00801	41.6298063	750	932.2
13	19.7423434	22.8567914	38.5314512	1200	1476.4
14	27.0987698	28.2204263	40.6191981	100	124.6
15	33.0362945	35.5505958	57.7206132	700	1166.6
18	25.587665	28.5341646	46.5989515	600	821.8
19	9.26562479	9.78909079	21.2638761	11700	9302
21	21.4097102	33.1177196	56.6355393	500	457.9
22	15.1453844	16.5947491	37.0497505	700	533
23	10.1081836	11.4505312	24.4536685	2200	1296.6
25	24.0420398	29.9662603	50.0581356	700	997.8
28	12.8349691	15.1794956	29.5889576	800	898.7
30	17.2324122	13.107212	30.4027008	620	685.5
31	29.9317113	34.0069952	53.3221232	850	1307.3
33	14.3486836	17.4440833	31.8827002	800	647.6
35	32.6215617	28.4820299	43.2609184	1700	2184.1
36	24.6884556	21.2341145	37.7269578	1500	1815.2
38	29.0068782	29.7217589	44.1766589	1650	2167.8
39	18.8505749	16.5476046	35.8012632	2000	2359.1
42	14.5932629	17.2551672	28.7261919	1750	1946.2
43	12.6351179	14.1498884	32.1198152	150	173.6
44	12.1663845	19.7743227	34.1328216	550	642.3
47	13.6031011	21.6790501	42.1037836	625	802.7
48	12.782887	11.0039327	48.2239091	4200	4387.8
49	26.0466719	24.9789806	41.7156239	1650	2080.3
50	28.7531061	22.8485415	46.1610024	2400	3194.9
51	14.2265962	18.3236293	33.3679355	4700	5621.424
52	24.8980114	20.956467	40.2266276	2000	2473.3
54	12.9281711	16.2720796	36.9170103	550	461.7
62	15.8398562	15.6562063	29.256544	4800	4311.5

63	33.0647349	23.8693261	44.5565016	700	920
64	14.4396979	19.9474767	33.3436626	700	811.4
65	28.102828	31.276406	61.1520975	900	1537.6
66	45.2808138	39.4467879	65.7348623	400	786
67	20.2484234	16.6758432	35.562357	400	471.5
69	21.6381341	21.892657	39.4452366	1300	1623.8
71	22.5628835	17.734026	35.8290923	1150	1324.6
72	22.8747058	22.6464562	41.8984768	1000	1285.7
73	14.6159115	15.4567379	35.7799029	900	712.1
74	26.5285914	20.5088512	45.3879263	1400	1889.8
76	27.41693	25.5879833	44.6694318	1600	2139.7
80	16.7913944	23.6725809	38.2365638	700	600.4
81	6.26275276	7.93933851	15.7115534	900	826.1
83	16.6838411	13.7952238	22.8207701	700	749.7
84	21.3449306	17.5822944	36.7301331	250	297
87	8.6868375	9.38995944	24.9408628	2100	1134.6
88	18.8260813	17.253773	26.7478861	1600	1760.1
89	20.4018377	23.3940046	40.600054	2000	2470.9
90	28.9389655	32.2673101	47.2412694	1250	1722.2
91	28.2768339	33.6132966	51.1721855	975	1440.2
92	24.2615146	29.3721004	41.4762492	2400	2913.8
97	23.2505631	26.3792121	42.0492666	1400	1395.6
99	25.1964116	30.8249482	41.6722882	1000	1206.3

<u>ID#</u>	<u>AvgHeave</u>	<u>AvgSlip</u>	<u>AvgThrow</u>	<u>DepthofFaulting</u>	<u>FaultHeight</u>
3	868.8	908.1	241.1	8994.11894	41702.5
6	704.8	929.7	575.3	28913.151	63861.9
8	470.7	665.3	442	17639.9469	32186.8
10	710.8	805.1	339	18987.7705	64256
13	1158.8	1350.2	662.8	48310.3821	120490.5
14	95	112.6	58	2382.75764	5274.1
15	652	872.3	542.1	39740.0604	77917.3
18	568.2	699.5	391.2	18741.3496	39137.5801
19	8121.8	8239.7	1293.1	38408.2057	296045.4
21	316.4	377.4	202.6	15994.7189	31604.8
22	345.3	367.6	111.2	9403.87686	41425.2
23	1167.1	1233.4	383.8	18104.1053	66302.6
25	650.7	827.9	482.3	38079.1611	80567.2229
28	786.7	839.4	270.9	11739.1364	55190.4017
30	464.5	491	140.6	11981.9572	69370.5
31	792.4	1048.1	654.6	24826.8868	48810
33	474.9	505	166.3	17680.3297	56827.8267
35	1610.7	1862.5	908.2	35385.9004	80038.6464
36	1450.9	1666.7	747.9	22795.4191	89247
38	1563.3	1934.8	1101.4	36085.9283	76883.3
39	1925.3	2245	1090.5	31258.8428	82857
42	1718.3	1859.6	681.6	8412.30111	27350.5
43	147.2	162.5	64.6	7887.01002	28218.2402
44	532.3	590.9	245.8	7407.93819	25712.2489
47	593.5	714.7	379.3	8500	24158.1909
48	2689.2	2774.5	610.1	18643.2582	129472.689
49	1568.2	1790.5	817.8	23032.3099	59226.1
50	2244	2814.1	1615.7	24200.0758	71732.3
51	3186.7	3445.4	1261.7	31285.3253	94139.2
52	1904.2	2289.5	1190.8	33211.2817	86556.4287
54	322.1	352.8	136.1	13668.7966	44901.9
62	3845.3	4147.4	1457.1	27024.7543	126170.8
63	672.4	781.9	364.8	14932.3452	43455.7731
64	684.4	739.9	262.8	18353.2286	62857.9298
65	795.5	1257.6	912.8	17619.4321	34798.2
66	350.8	649	523.6	47872.8996	73281.6706
67	386.4	434.8	187.9	7901.28728	30308.8694
69	1268.5	1418.6	591.3	26202.3527	85860.7186
71	986.4	1075.4	393.8	13930.0497	68843

72	963.4	1144.2	577.9	19557.6595	52894.6073
73	525.8	579.7	217.3	17301.4368	61986.6
74	1338	1675.1	926.5	20474.03	64460.6
76	1538.9	1870.2	999.6	38717.5446	103905.852
80	424.7	475.3	193.1	10614.3408	35911.7
81	577	587.5	98	1931.18996	17758
83	693.8	725.8	197.3	6190.69691	35139.1466
84	240.3	271.4	118.1	10840.3134	40588.71
87	1062	1078.2	166.1	6258.05065	47126.3843
88	1574.3	1693.9	594.6	20930.7475	75839.4113
89	1916.5	2191.7	985.4	18603.7625	52564.5
90	1169.9	1549.6	985.6	37227.0583	67487.0396
91	913.6	1207.5	757.9	37481.1503	71325.1909
92	2182.7	2651	1478	48000	92594.5293
97	1342	1578	787	35957.1192	87650.2
99	900.1	1121.6	659.9	29180.1556	53728.28

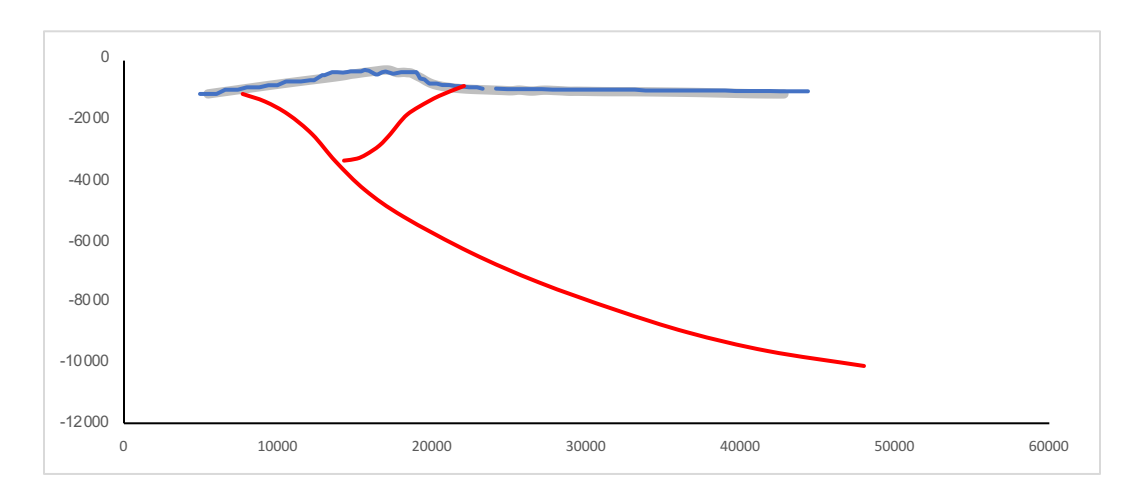
<u>ID #</u>	<u>AspectRatio</u>	<u>NumofFaults</u>	<u>ModeledStrain</u>	<u>observedstrain</u>	<u>Type</u>
3	0.2803613	2	-0.0032972	-0.0023068	WR
6	0.36885477	1	-0.0030006	-0.0012162	LS
8	0.15687646	1	-0.0059493	-0.0044036	WR
10	0.37350478	2	-0.0014138	-0.0009559	WR
13	0.49115935	1	-0.0007959	-0.0007795	LS
14	0.09096044	1	-0.0028581	-0.0011323	WR
15	0.67946326	1	-0.0043936	-0.0052743	LS
18	1.29796061	1	-0.0023394	-0.0018084	LS
19	0.29126932	2	-0.0012714	-0.0026711	LS
21	0.34423528	2	-0.0031977	-0.002477	WR
22	0.24107123	2	-0.0007956	-0.0012881	WR
23	0.2392028	2	-0.0008782	-0.0005995	WR
25	0.34609377	1	-0.0024414	-0.000792	WR
28	0.52776682	1	-0.0008594	-0.0004622	WR
30	1.38316782	3	-0.0004912	-0.0026176	WR
31	0.11843991	1	-0.0047637	-0.0041559	LS
33	0.41575691	2	-0.0006448	-0.0004071	WR
35	0.24803355	1	-0.0040296	-0.0046624	LS
36	0.26291532	1	-0.0026624	-0.0012175	LS
38	0.43831697	1	-0.0041409	-0.003233	LS
39	0.9609038	1	-0.0027812	-0.0018029	LS
42	0.10353352	1	-0.0041236	-0.0021543	LS
43	0.2053337	1	-0.0002677	-3.78E-05	WR
44	0.22751702	1	-0.0013113	-0.0006857	WR
47	0.29451187	1	-0.0026672	-0.0016886	WR
48	0.21080291	2	-0.000857	-0.0007157	LS
49	0.43754127	1	-0.0035827	-0.0016571	LS
50	0.48629039	1	-0.0080121	-0.0080594	LS
51	0.2662974	3	-0.0032507	-0.0022129	WR
52	0.42798931	1	-0.0043434	-0.0038328	LS
54	0.73278069	2	-0.0015795	-0.0002515	WR
62	0.58663663	2	-0.0021918	-0.0005628	LS
63	0.44803036	1	-0.0041019	-0.0026287	LS
64	0.08663587	1	-0.0006676	-0.0003411	WR
65	0.28031224	1	-0.0161714	-0.0153526	LS
66	0.80399431	1	-0.004594	-0.0035105	LS
67	0.21678112	1	-0.001457	-0.0003956	WR
69	0.45890603	1	-0.00194	-0.0026879	LS
71	0.39615646	3	-0.0014694	-0.0022405	WR

72	0.7907248	1	-0.0026241	-0.0015156	LS
73	0.37266018	2	-0.0012037	-0.0002937	WR
74	0.55159746	1	-0.0050177	-0.0047544	LS
76	0.57941377	1	-0.0033263	-0.0019861	LS
80	0.1672214	2	-0.000636	-0.0018251	WR
81	0.23379688	2	-0.0008705	-0.0010947	WR
83	0.27384855	1	-0.0008196	-0.0005026	WR
84	0.22553753	1	-0.0008573	-0.0001549	WR
87	0.36999318	2	-0.0010992	-0.0007461	WR
88	0.28263054	1	-0.0010693	-0.0008807	LS
89	0.30152365	1	-0.0046653	-0.0042887	LS
90	0.35100853	1	-0.0035168	-0.0021462	LS
91	0.33637512	1	-0.0024771	-0.0014811	LS
92	0.5157322	1	-0.003803	-0.0021161	LS
97	0.19678017	1	-0.0022704	-0.0012664	LS
99	0.77446511	1	-0.0029164	-0.0010389	LS

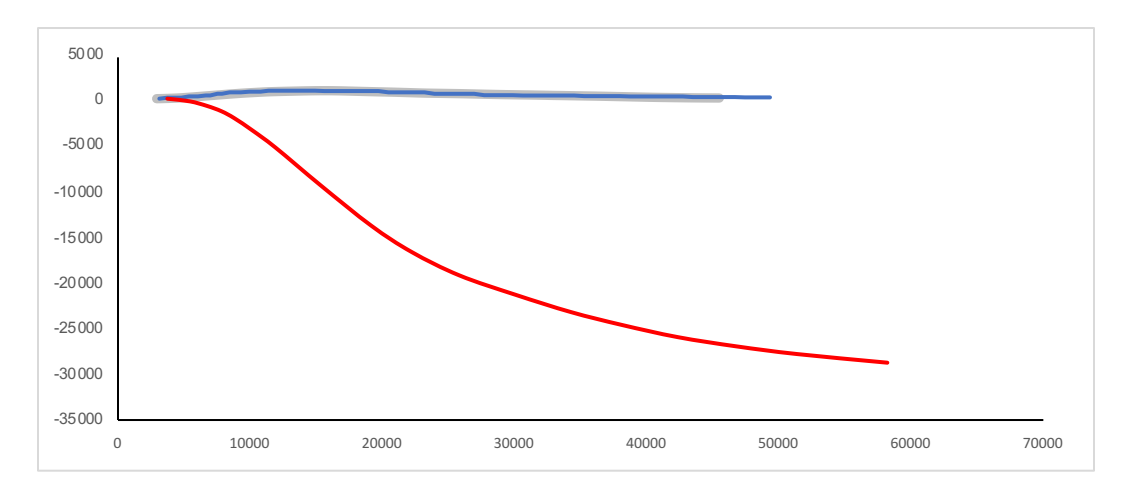
Figure B3.1: Subsurface models of 55 shortening landforms in Chapter 3

All axes are in meters. Y-axis is elevation and X-axis is horizontal distance. Blue lines are the modeled surface. Red lines are the modeled faults. Gray, thick lines in the background are the matched, observed topography.

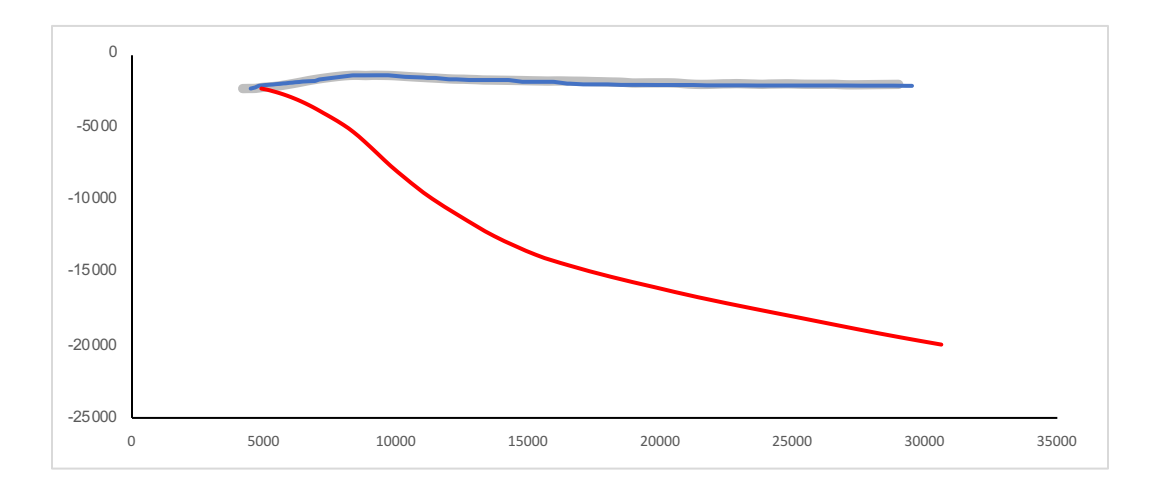
Fault ID 3



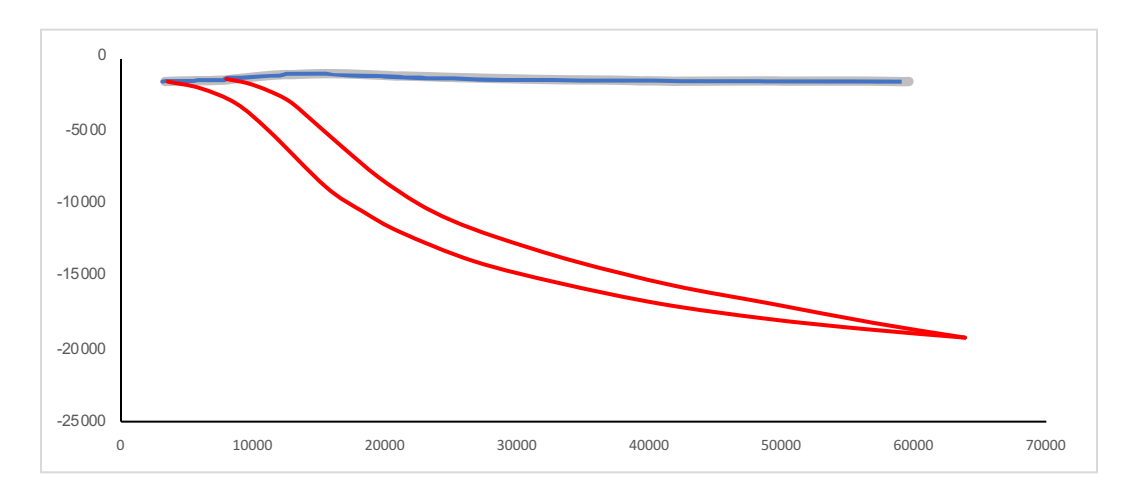
Fault ID 6



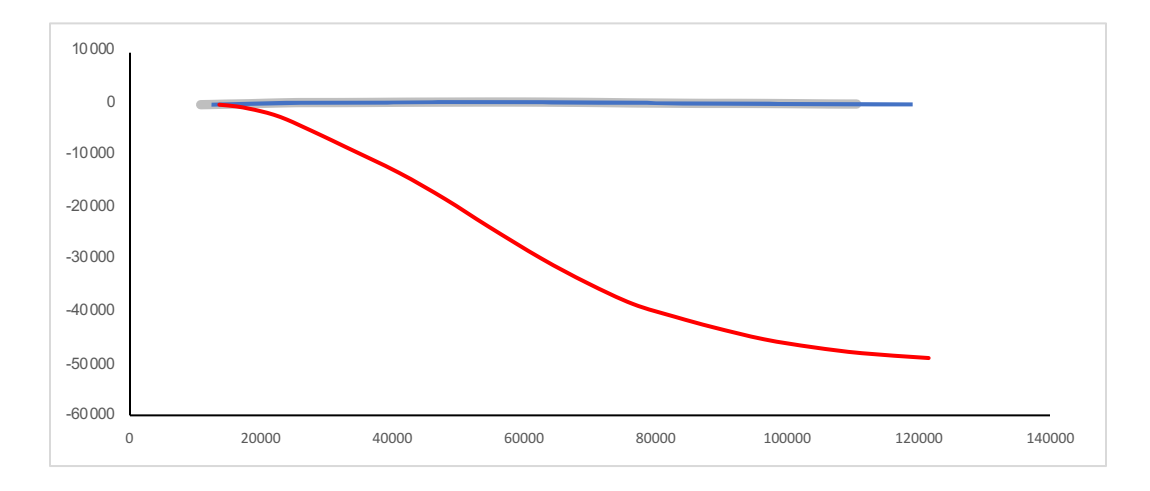
Fault ID 8



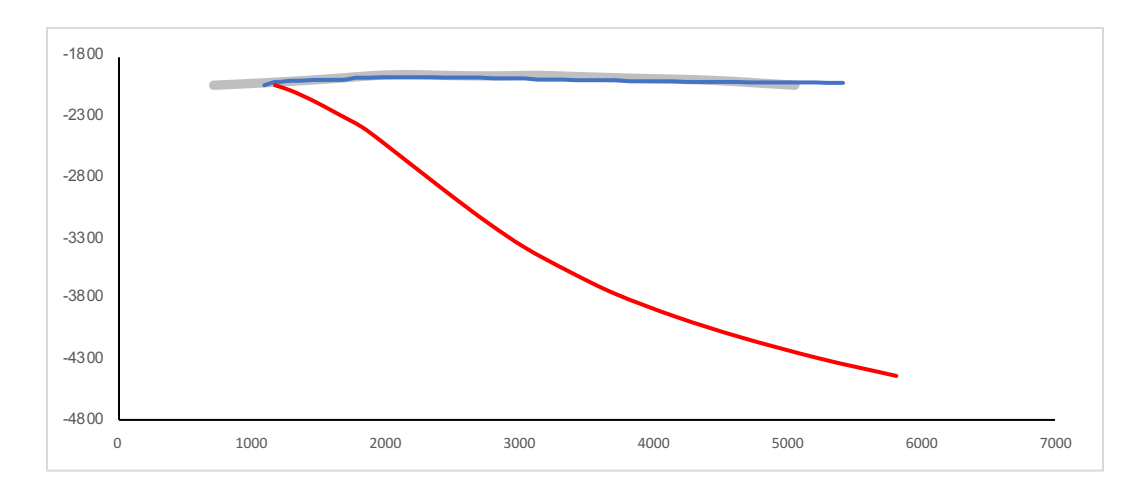
Fault ID 10



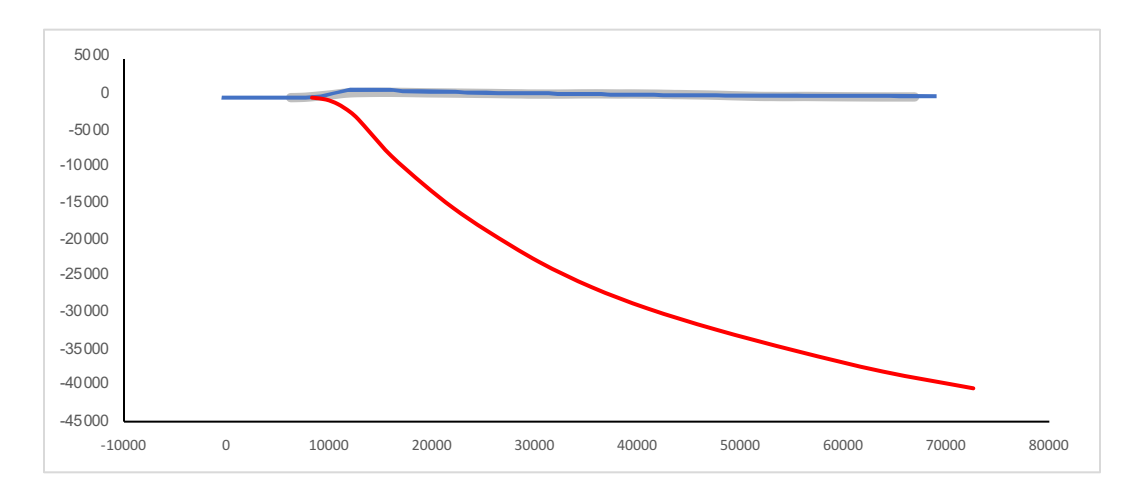
Fault ID 13



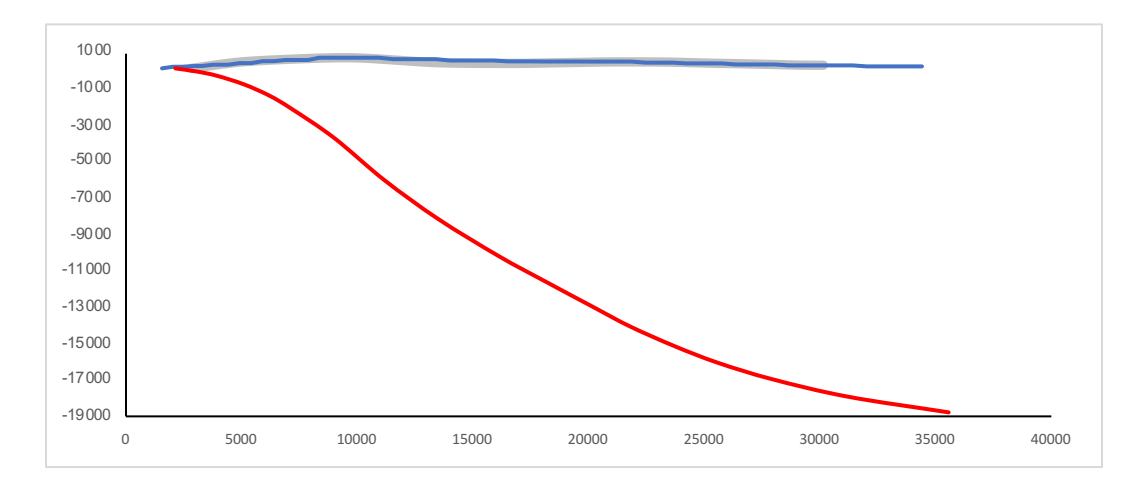
Fault ID 14



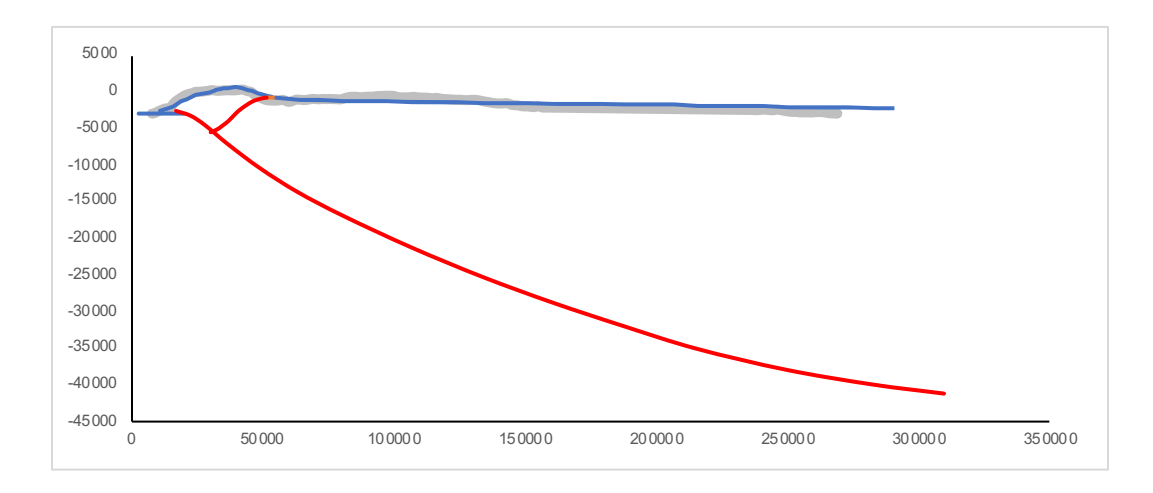
Fault ID 15



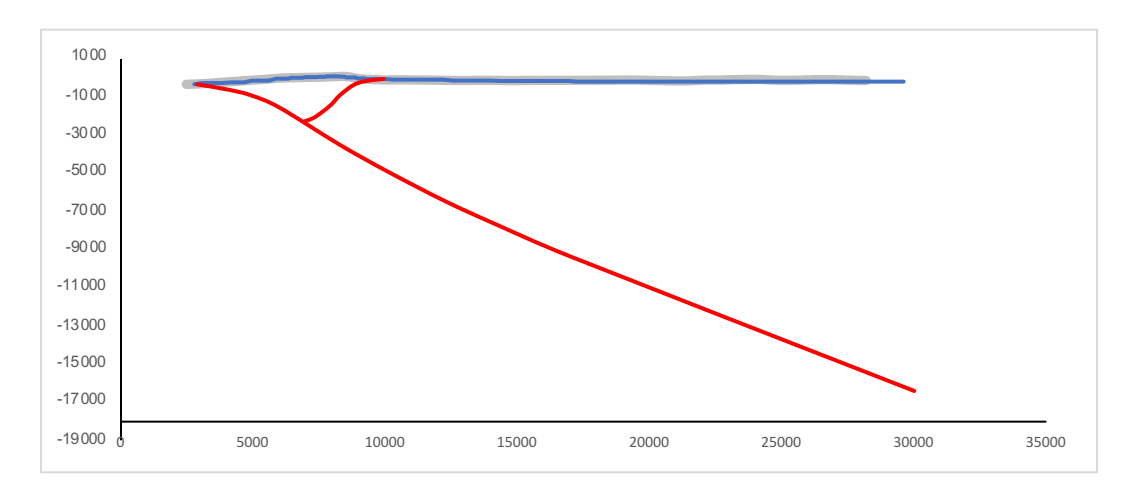
Fault ID 18



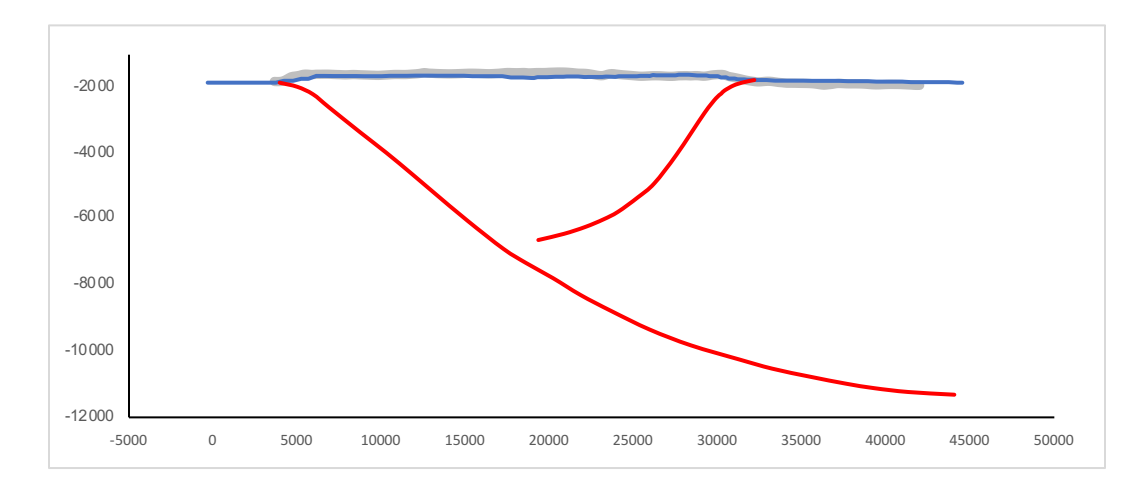
Fault ID 19



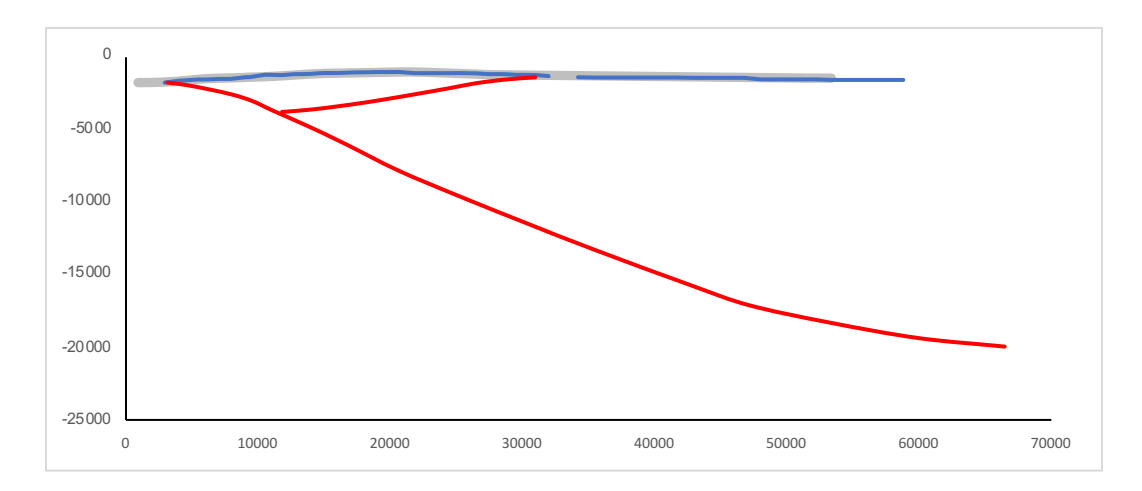
Fault ID 21



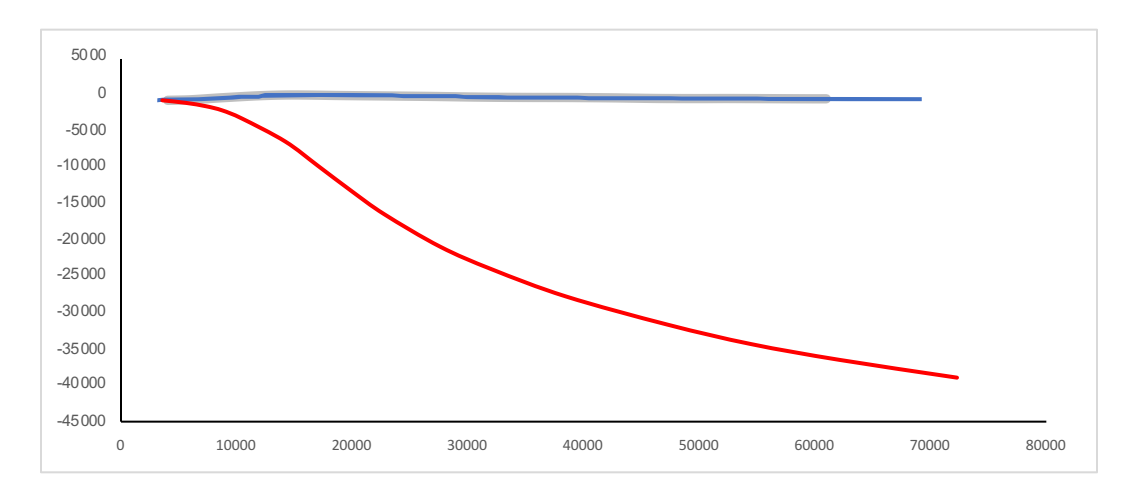
Fault ID 22



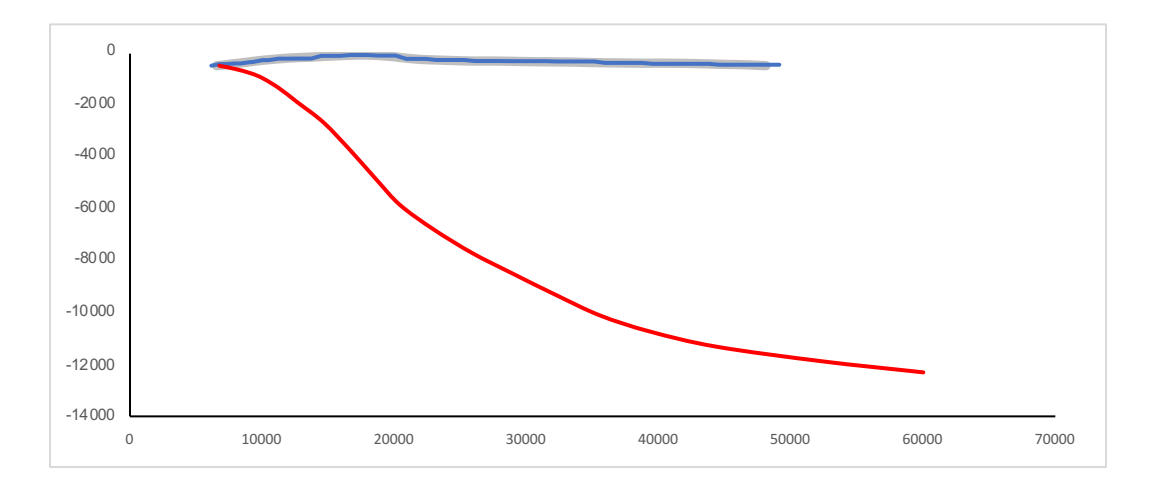
Fault ID 23



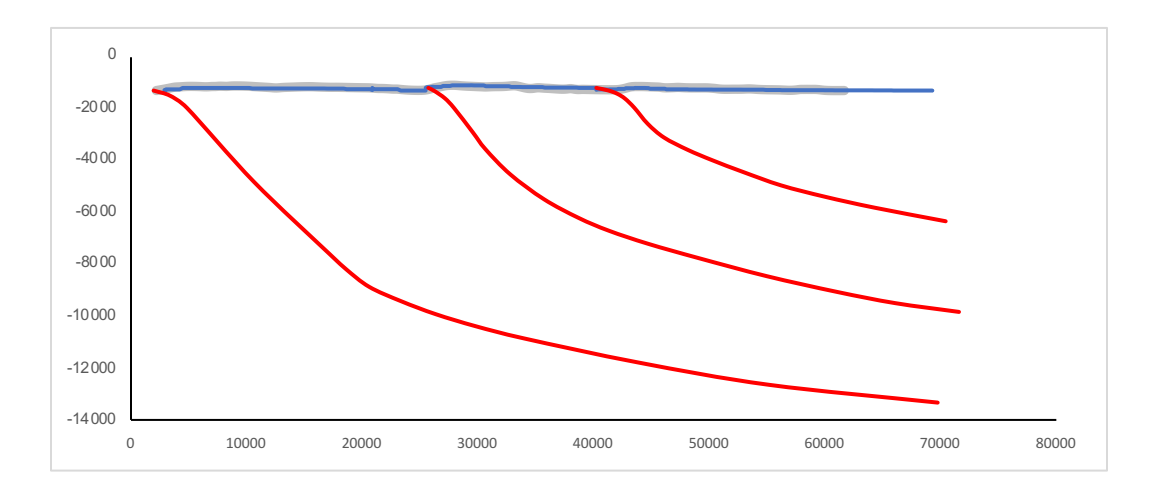
Fault ID 25



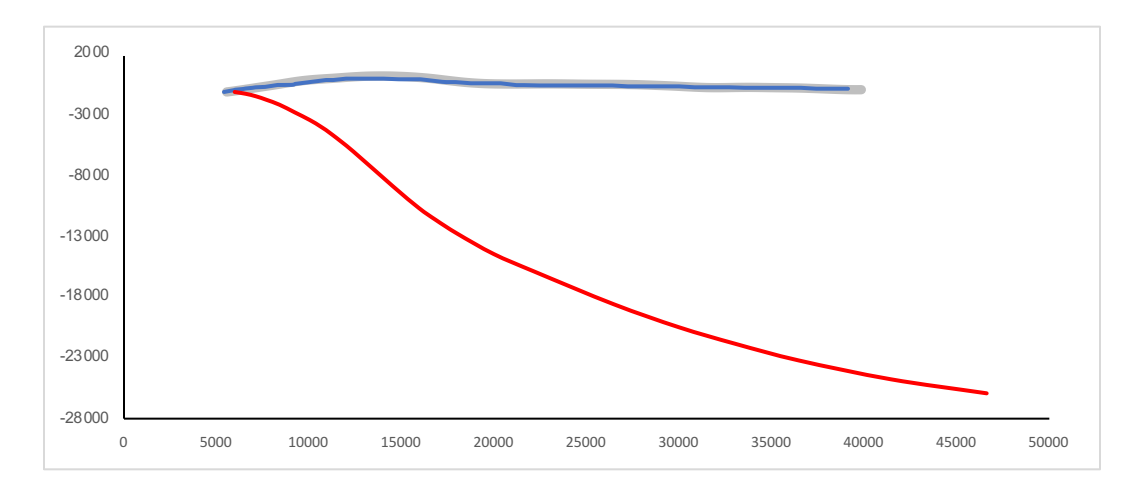
Fault ID 28



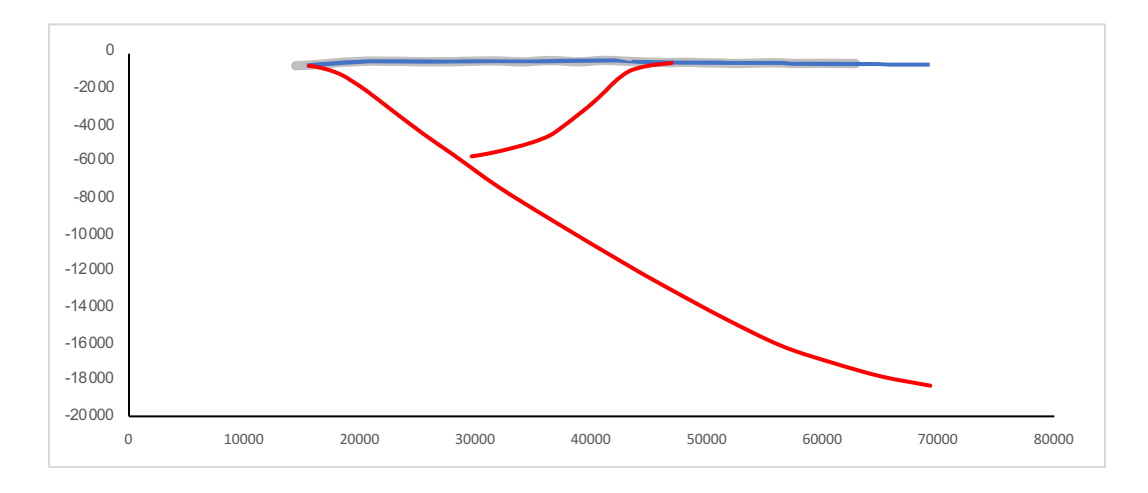
Fault ID 30



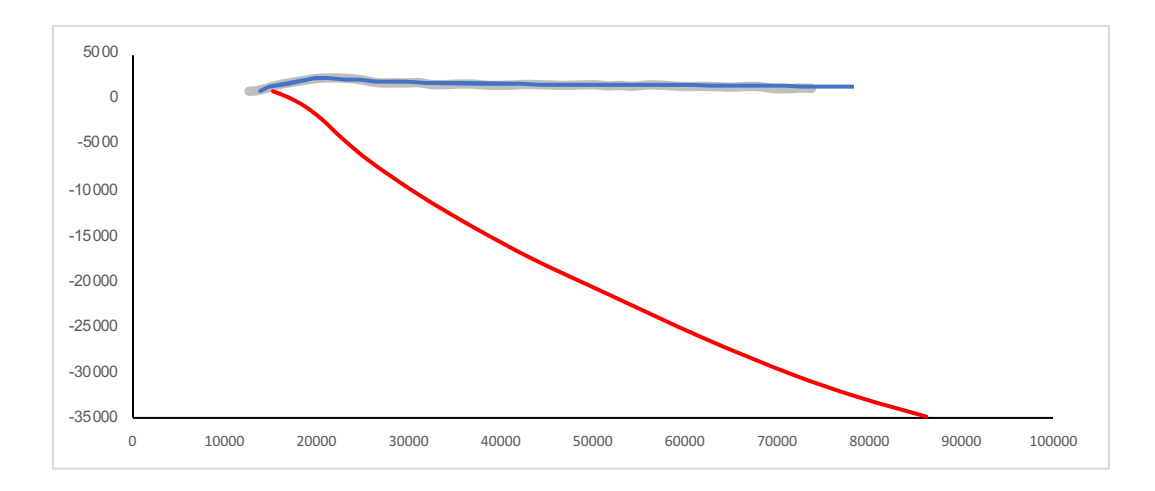
Fault ID 31



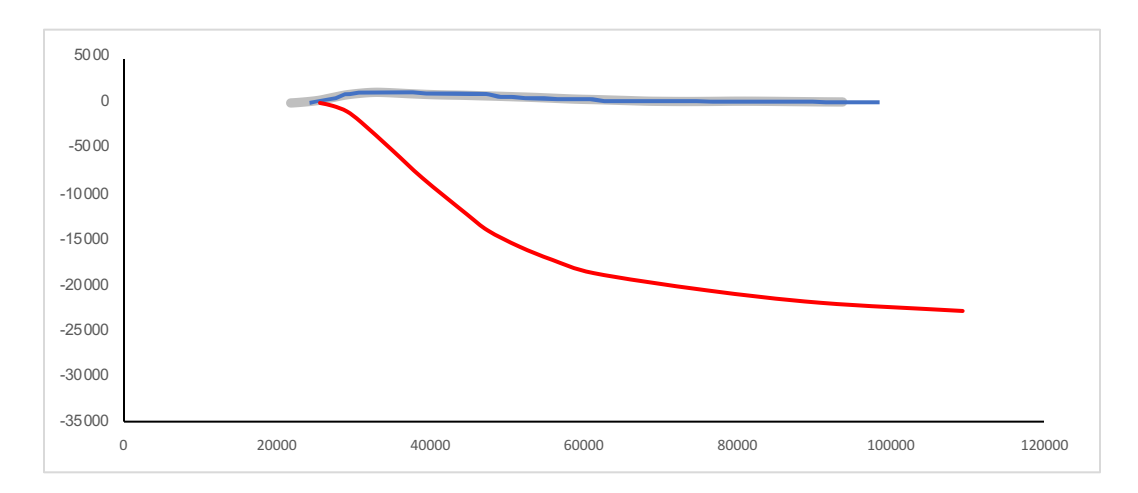
Fault ID 33



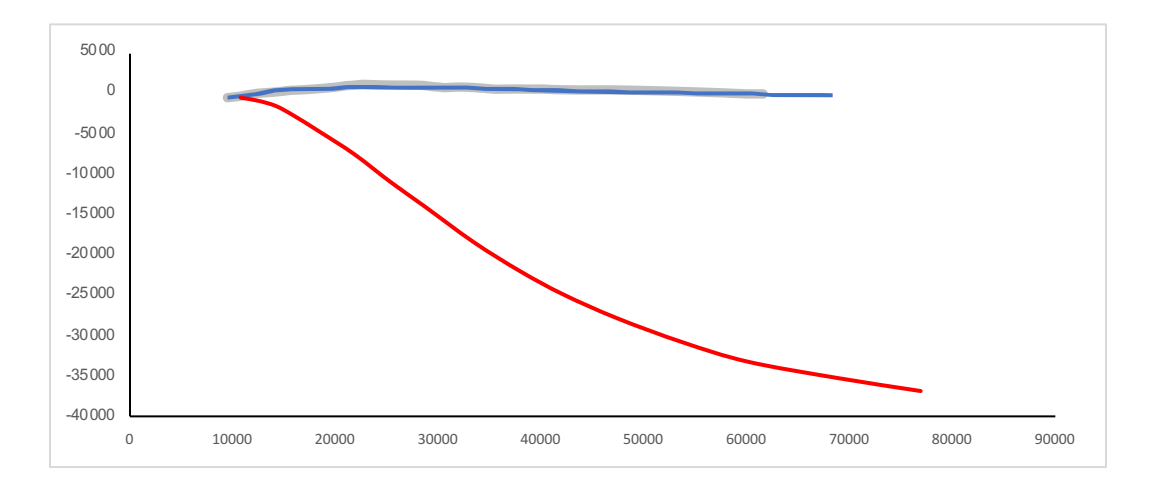
Fault ID 35



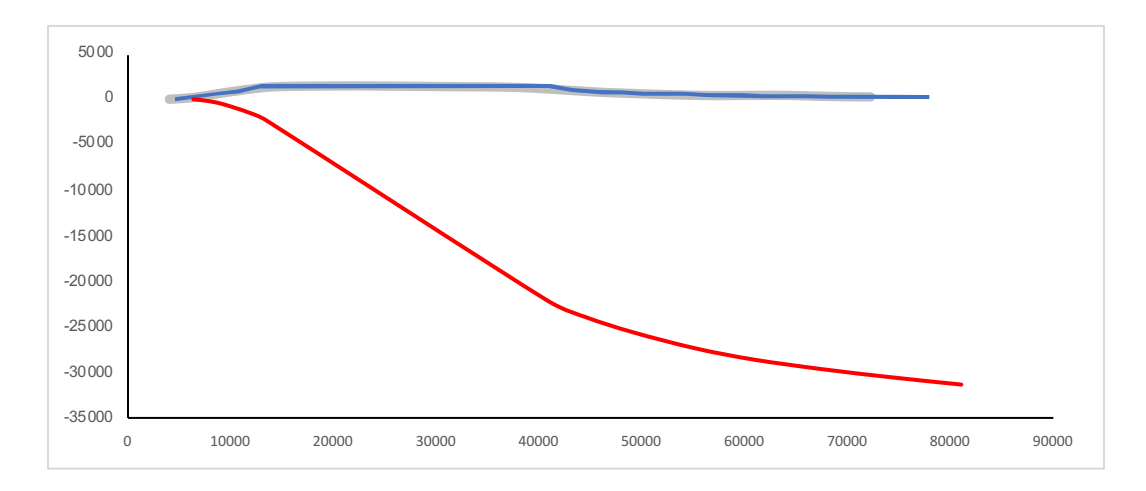
Fault ID 36



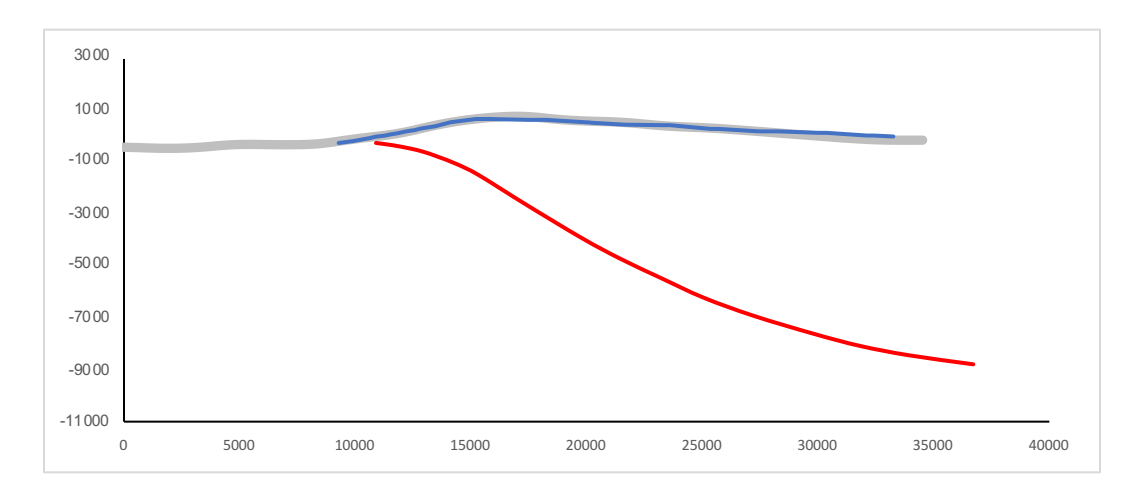
Fault ID 38



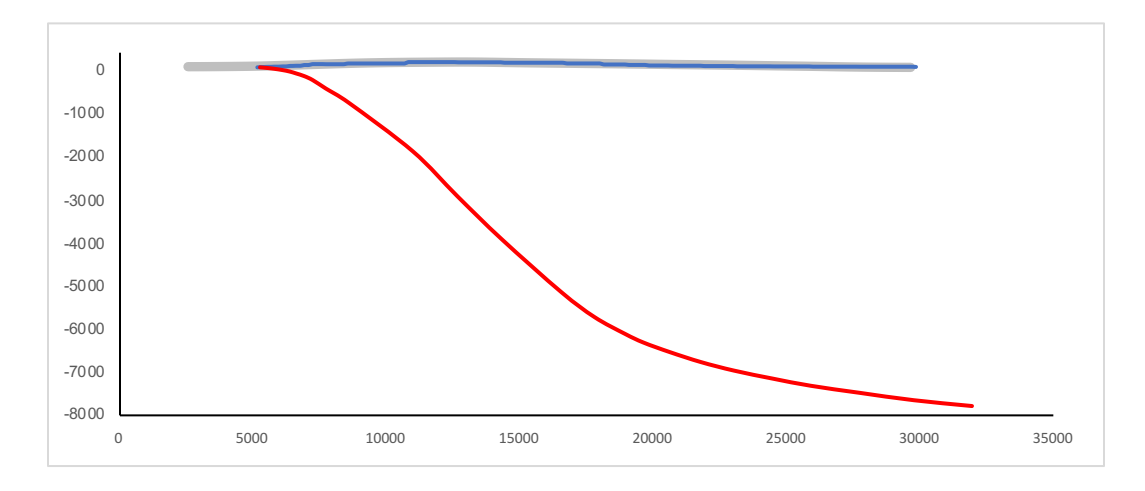
Fault ID 39



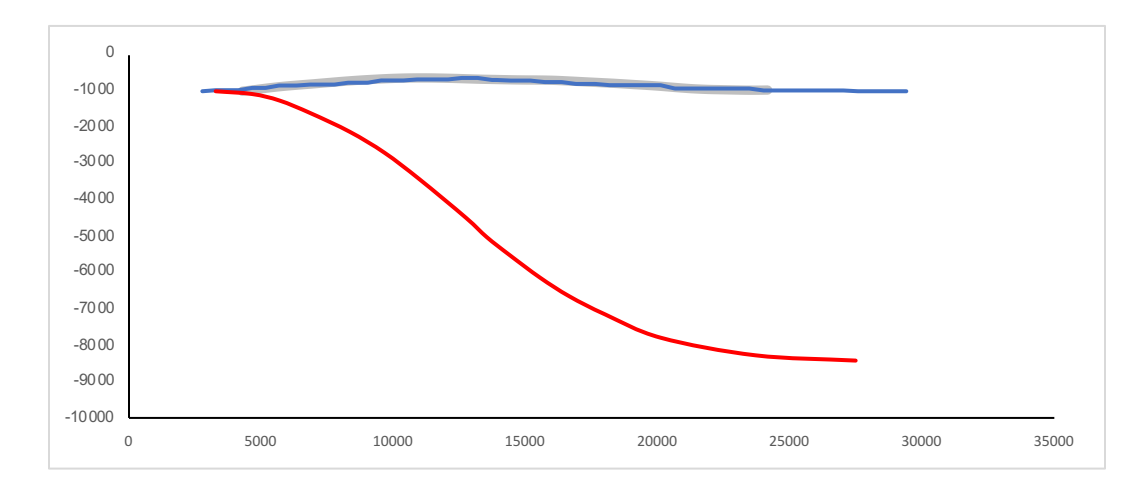
Fault ID 42



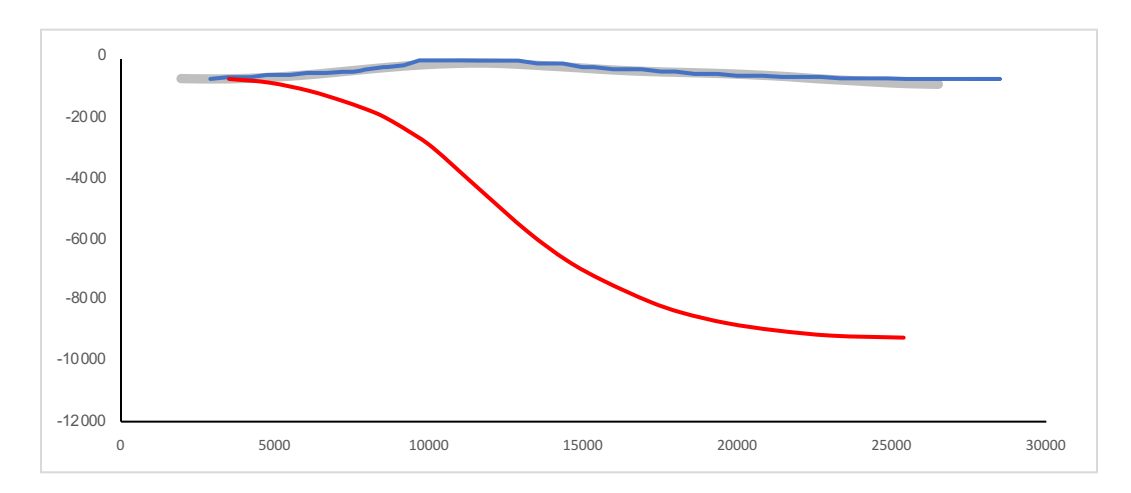
Fault ID 43



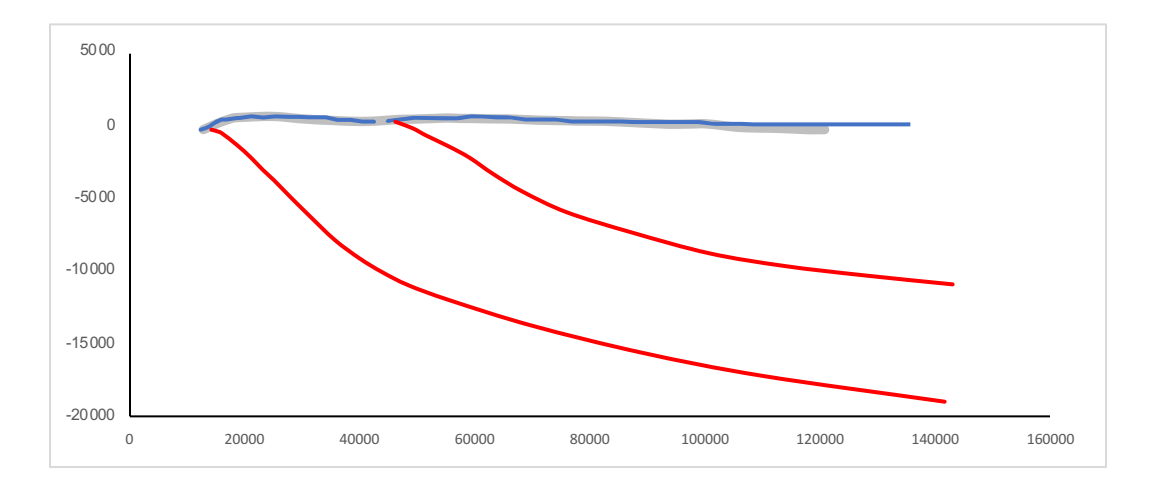
Fault ID 44



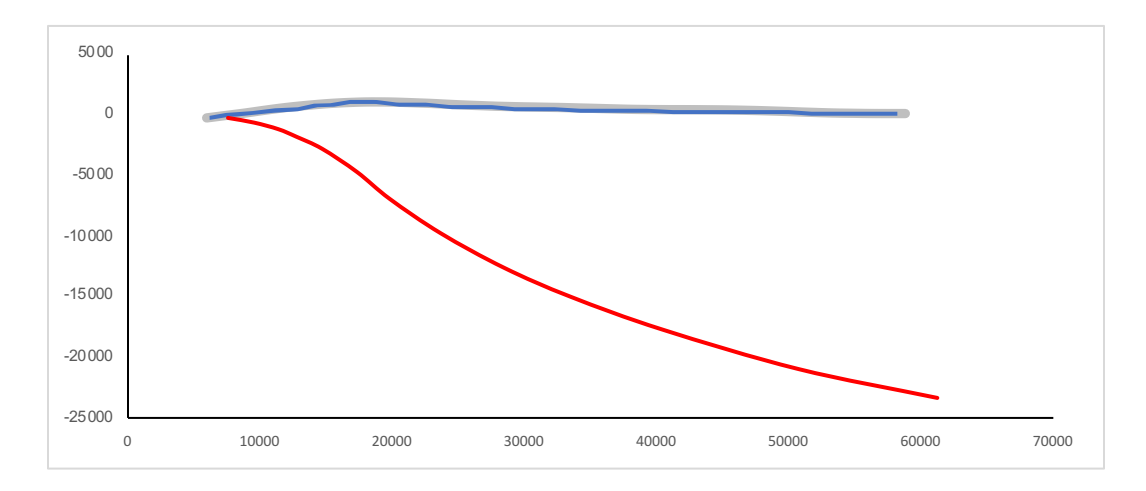
Fault ID 47



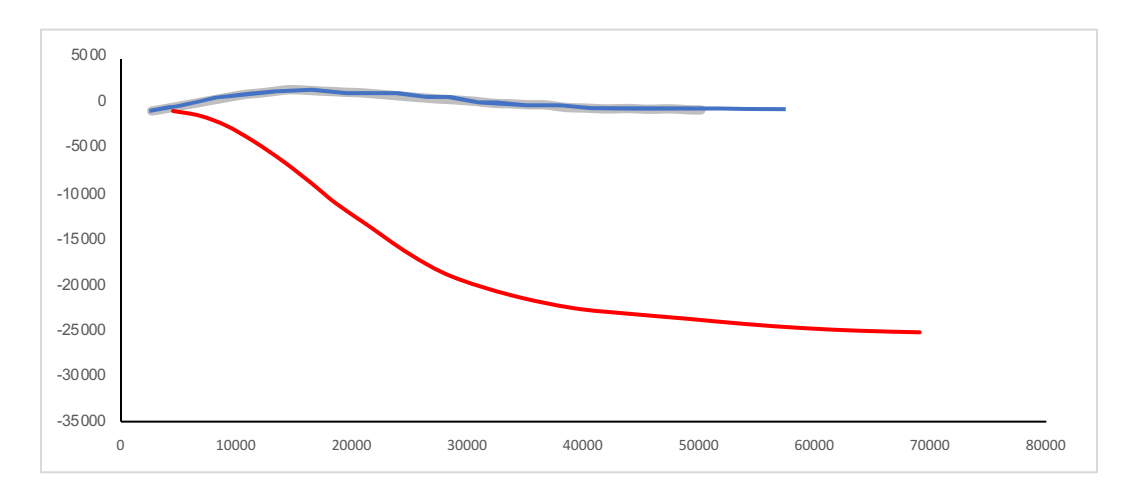
Fault ID 48



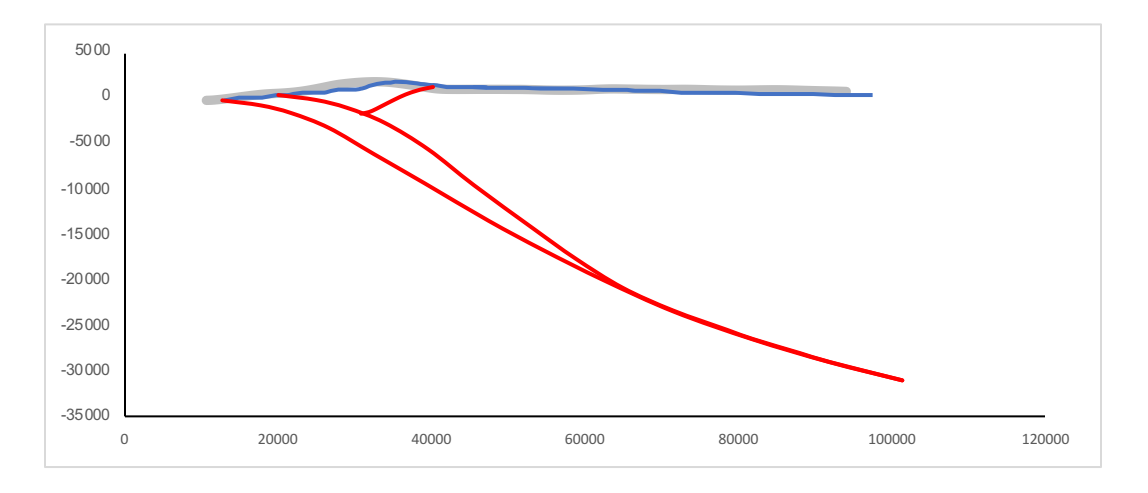
Fault ID 49



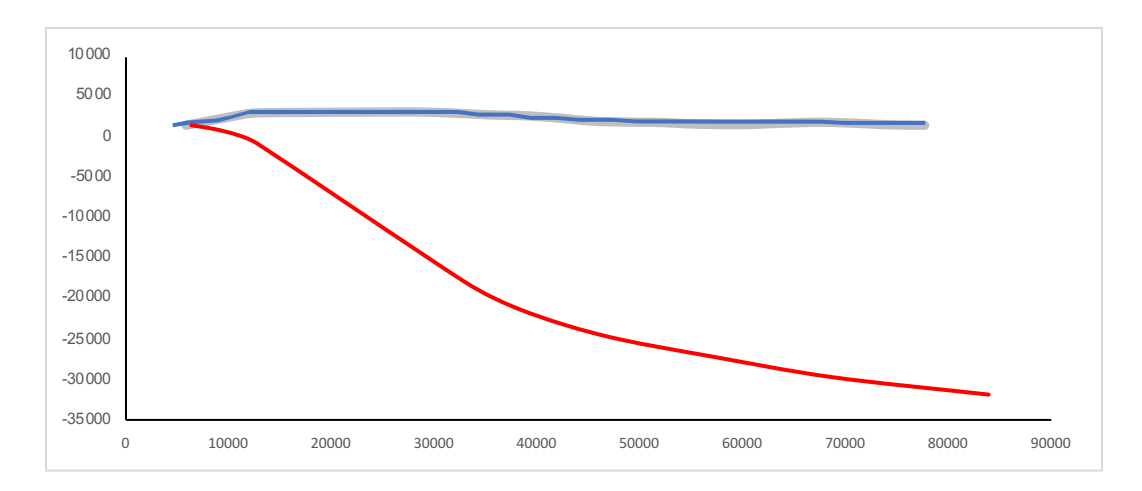
Fault ID 50



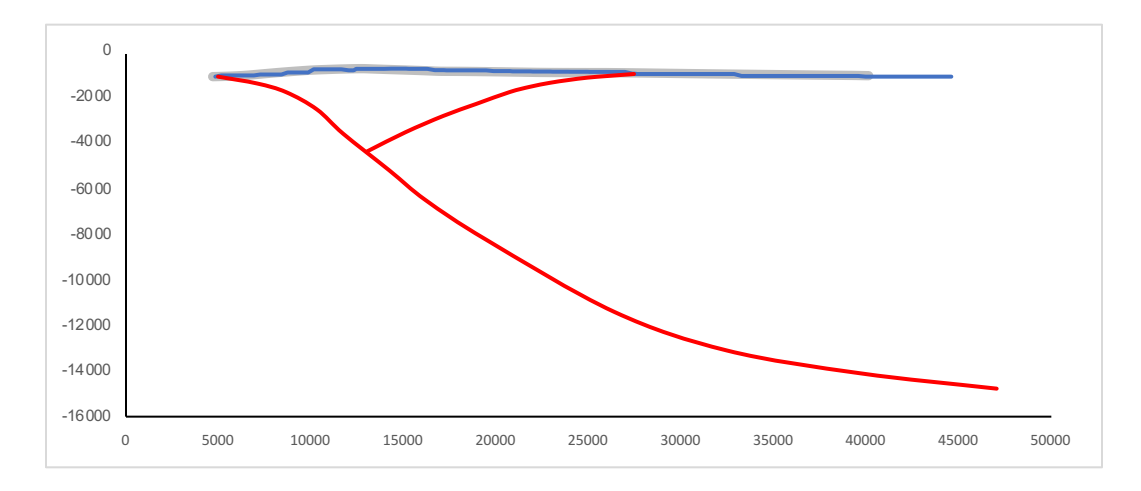
Fault ID 51



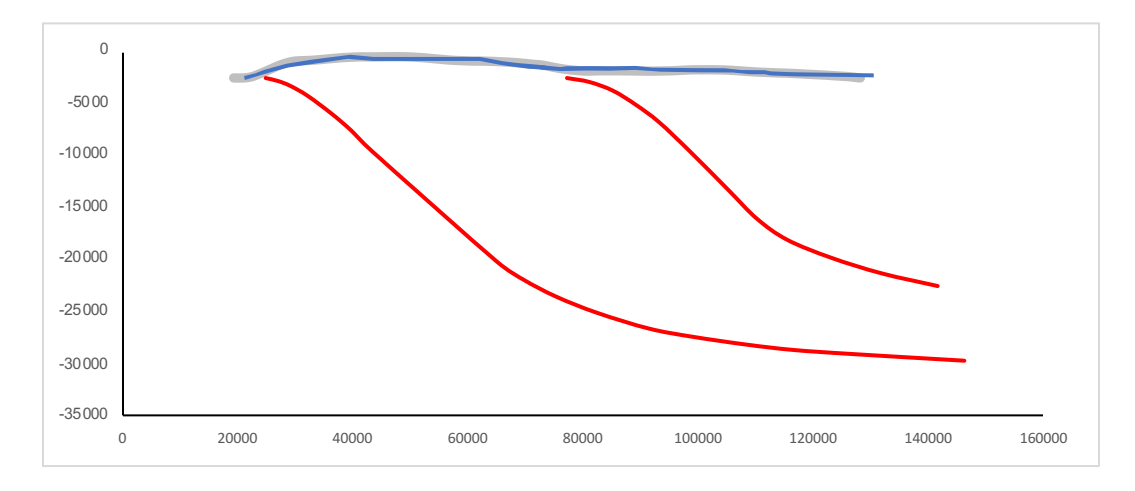
Fault ID 52



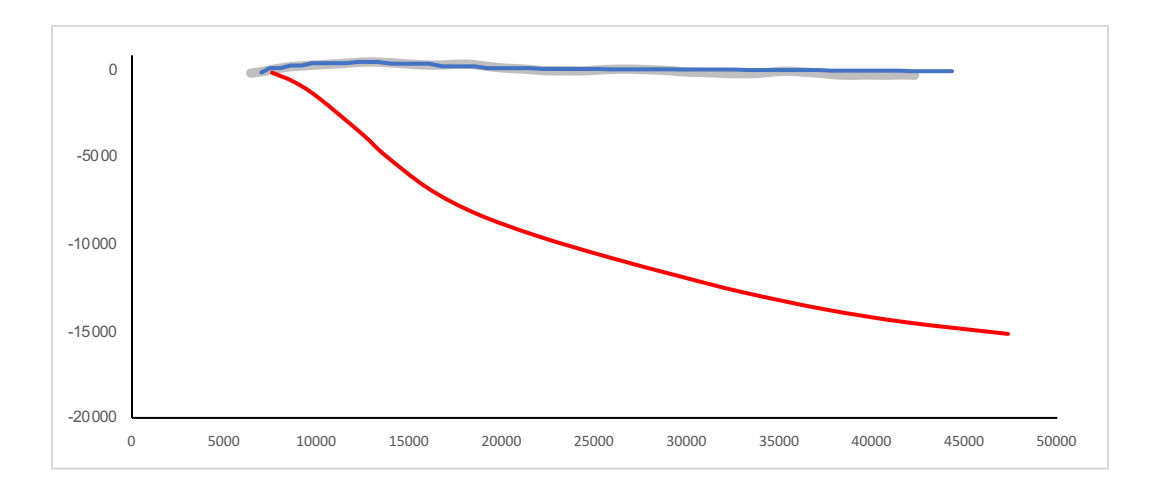
Fault ID 54



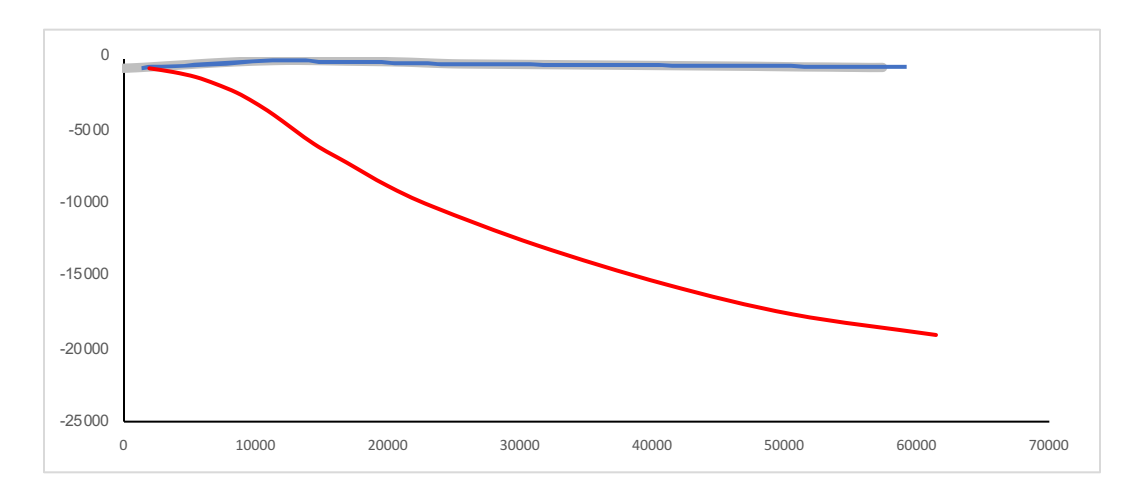
Fault ID 62



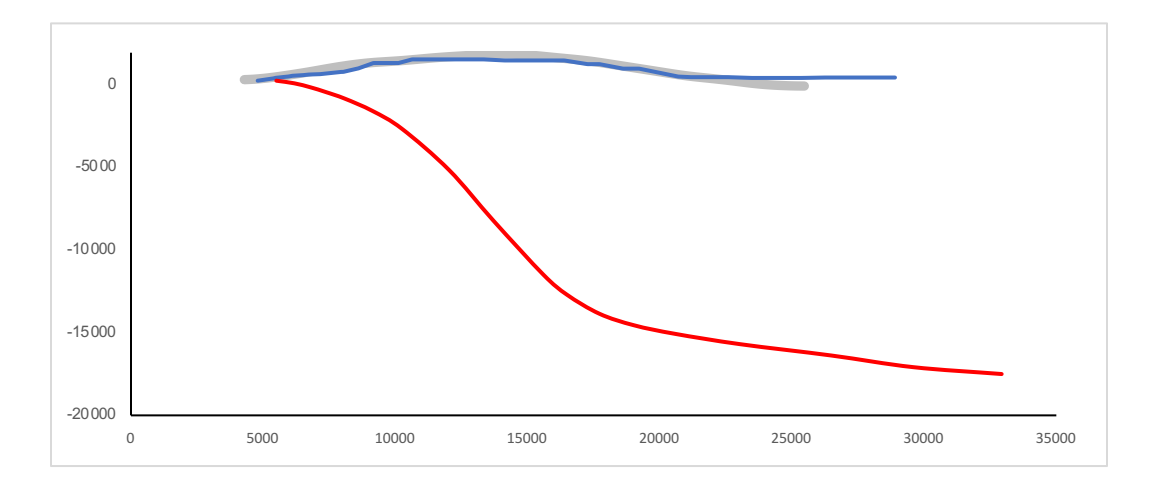
Fault ID 63



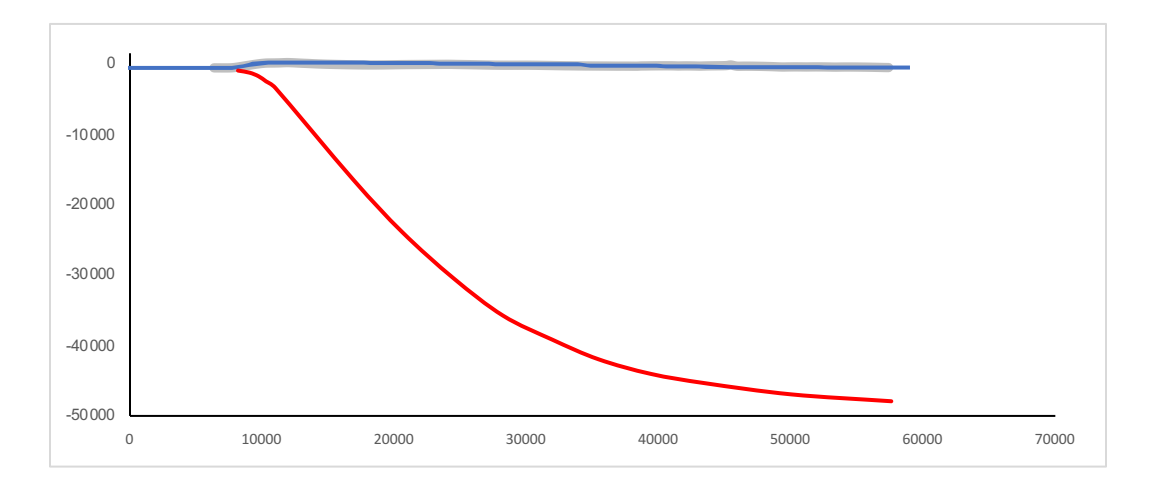
Fault ID 64



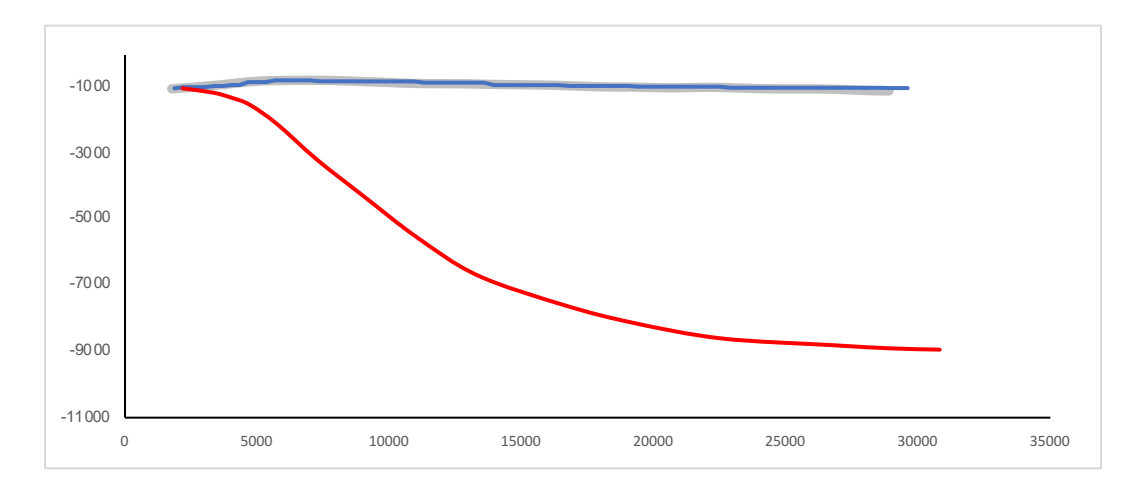
Fault ID 65



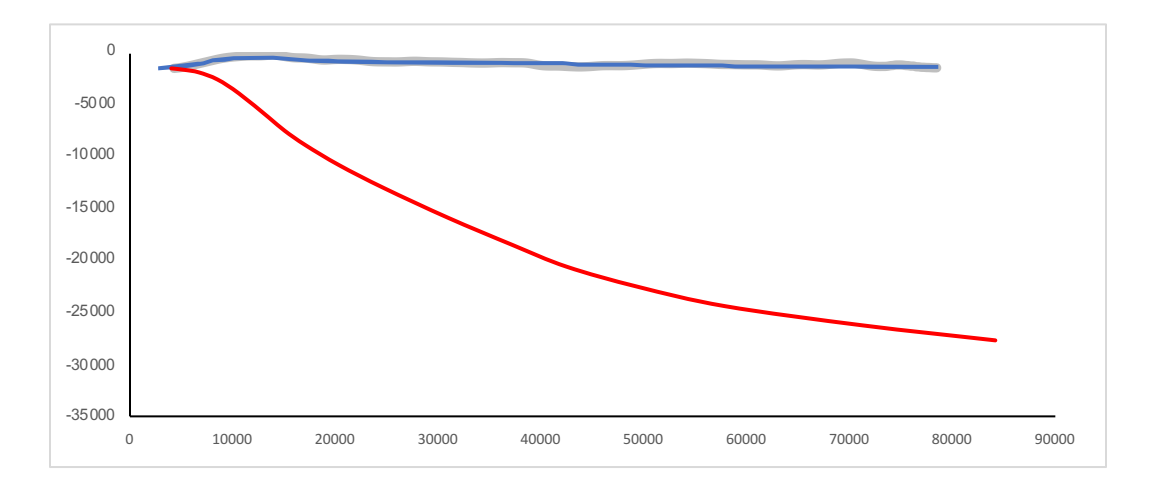
Fault ID 66



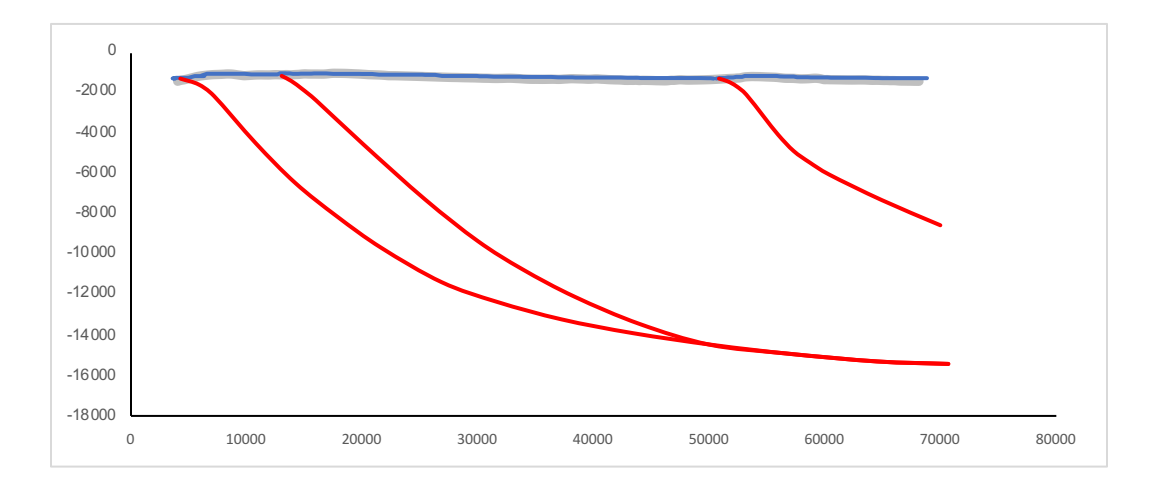
Fault ID 67



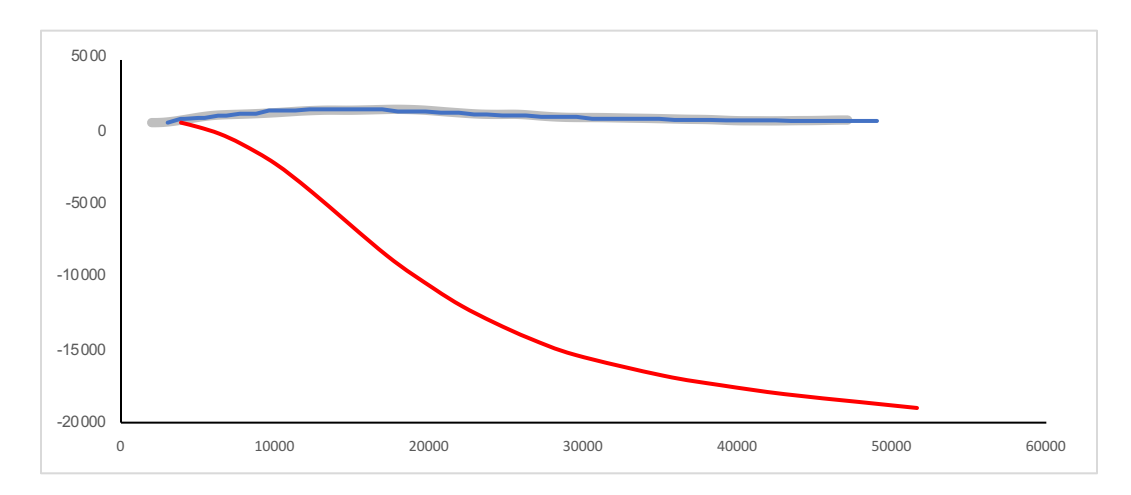
Fault ID 69



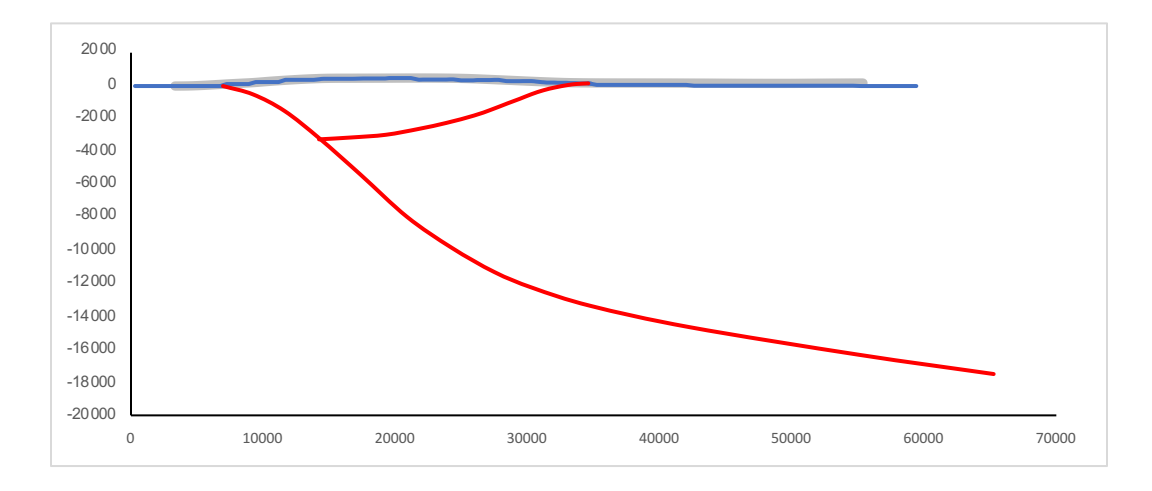
Fault ID 71



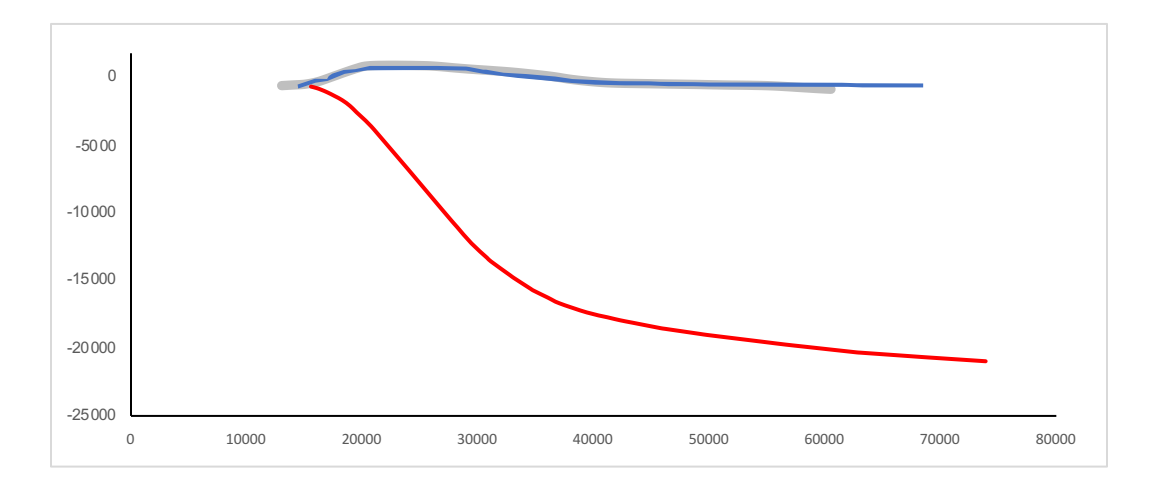
Fault ID 72



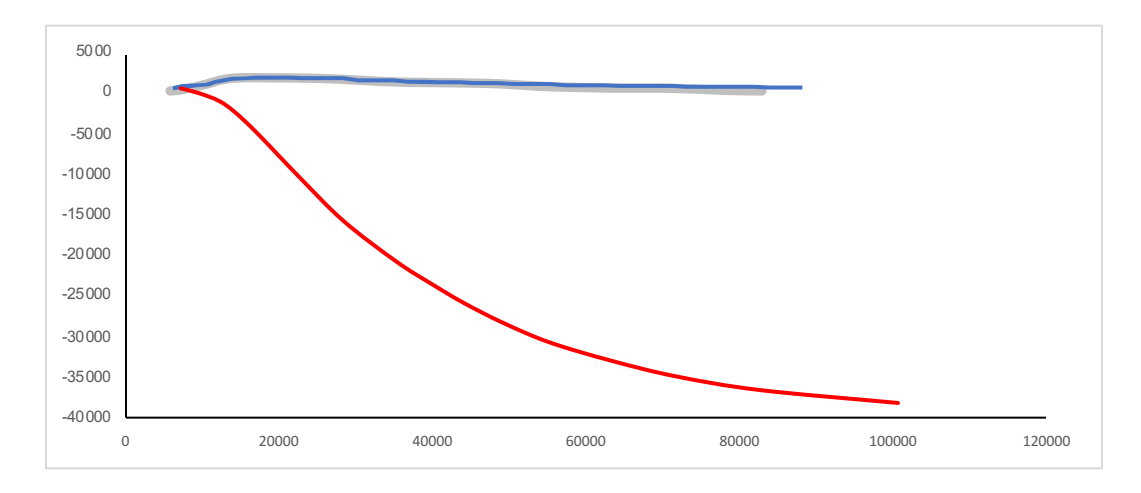
Fault ID 73



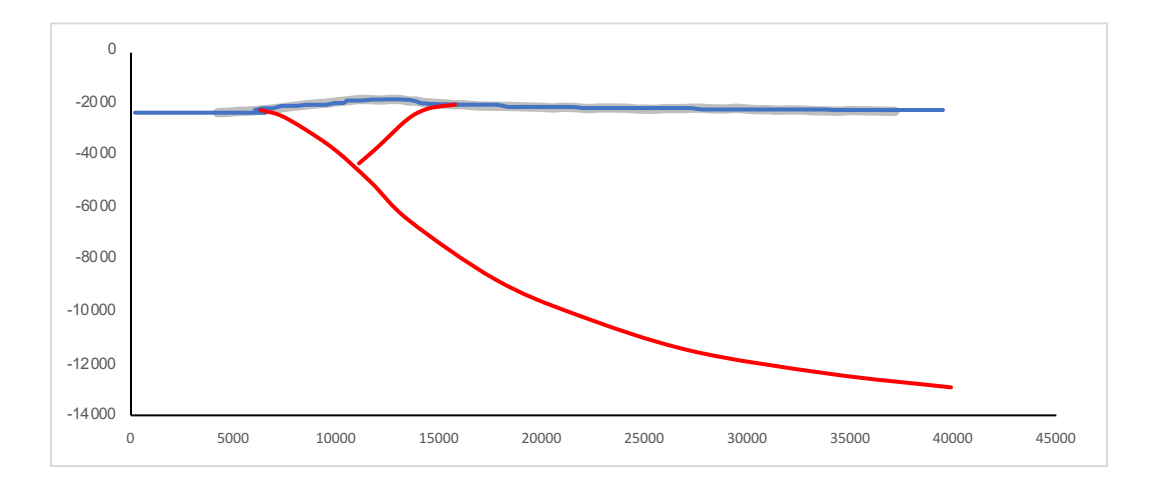
Fault ID 74



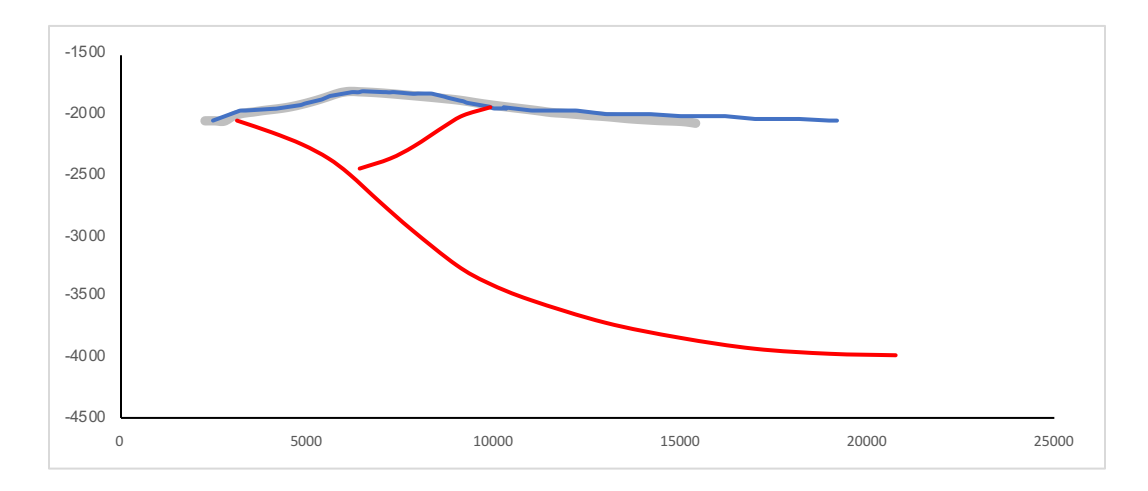
Fault ID 76



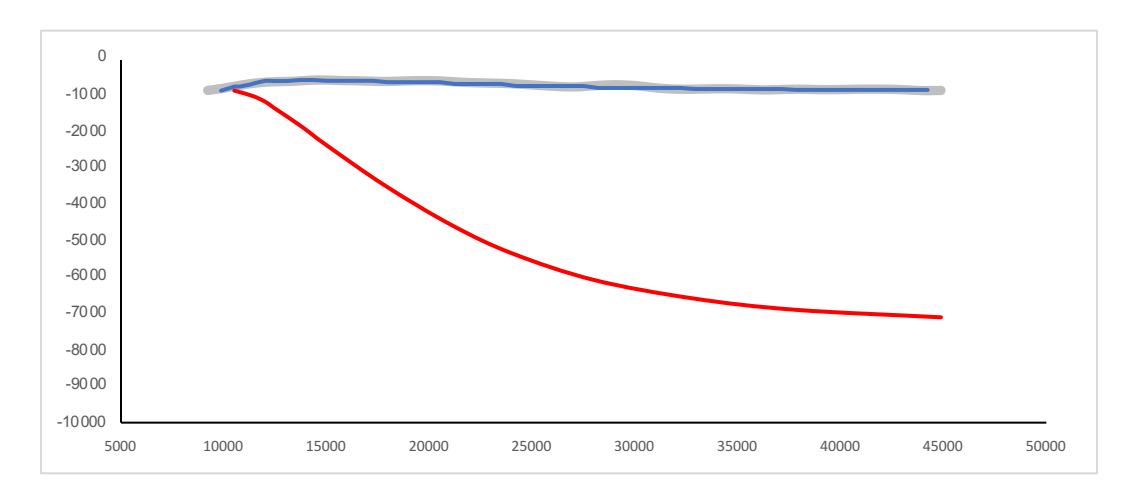
Fault ID 80



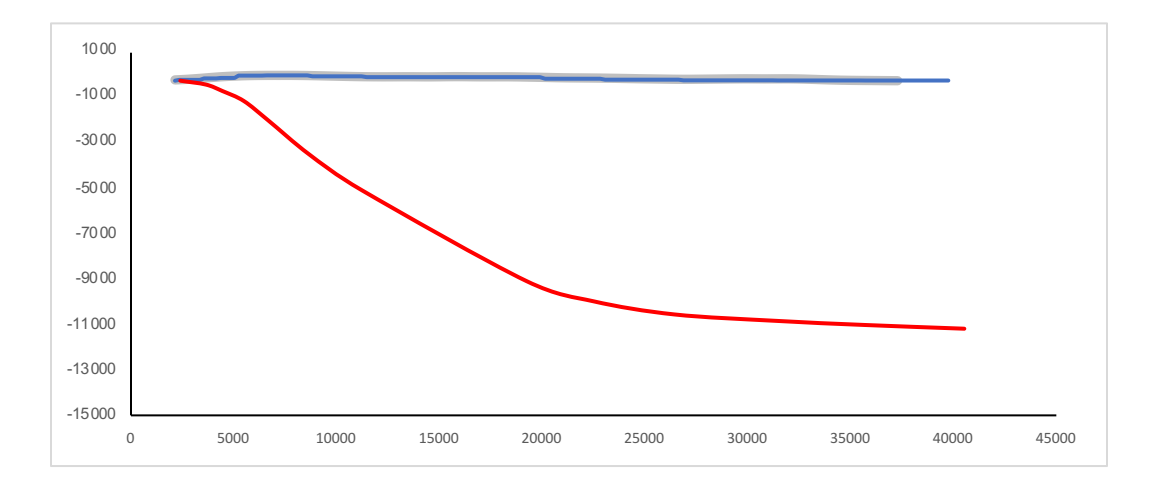
Fault ID 81



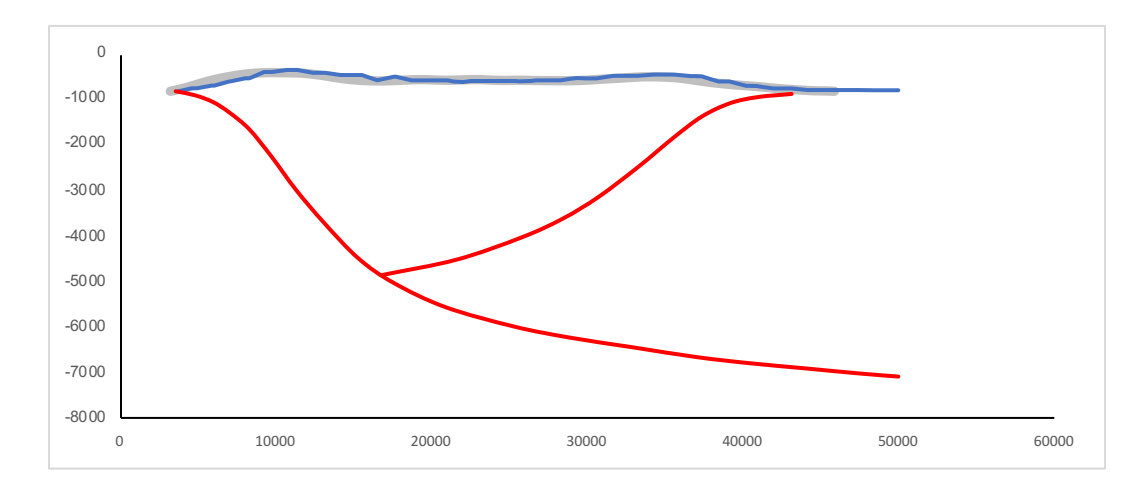
Fault ID 83



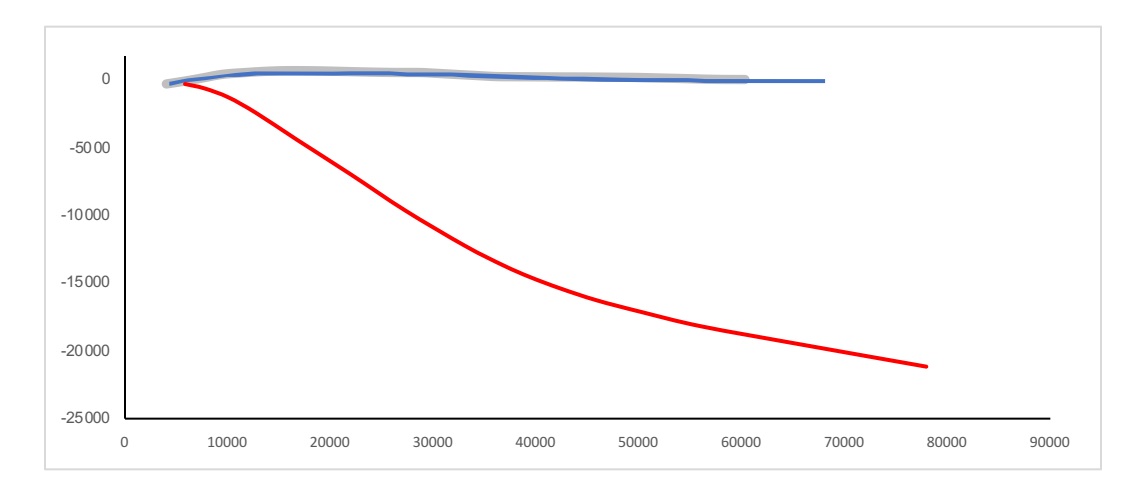
Fault ID 84



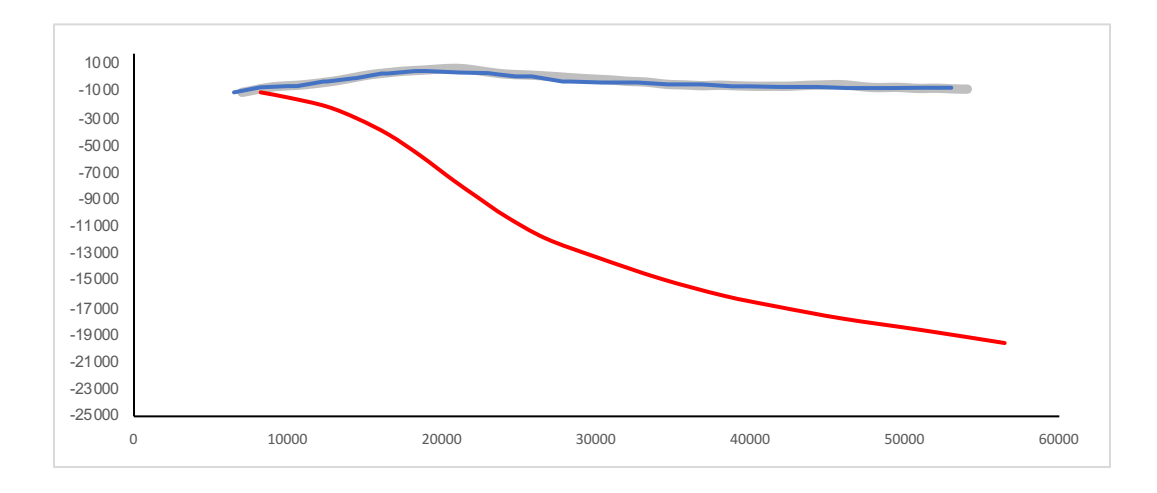
Fault ID 87



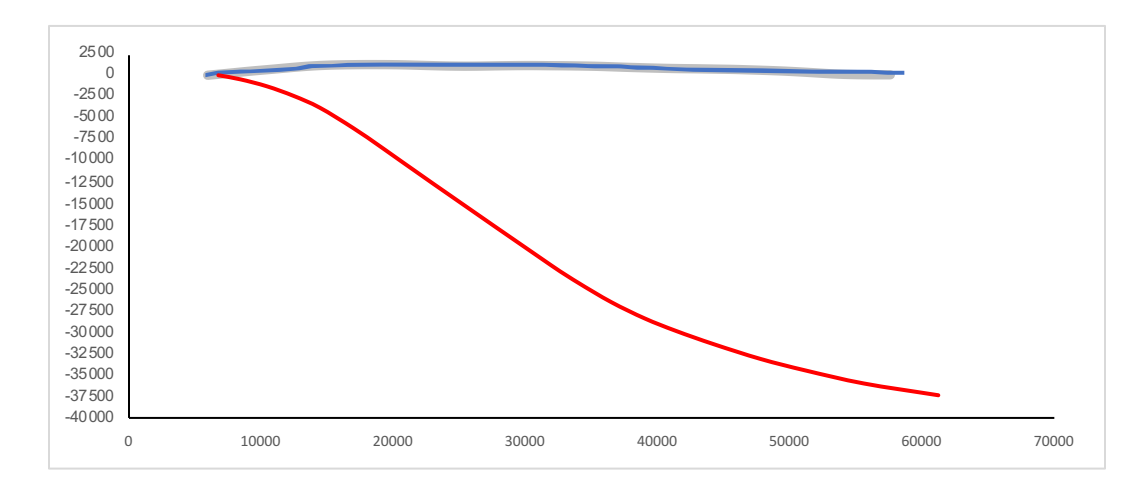
Fault ID 88



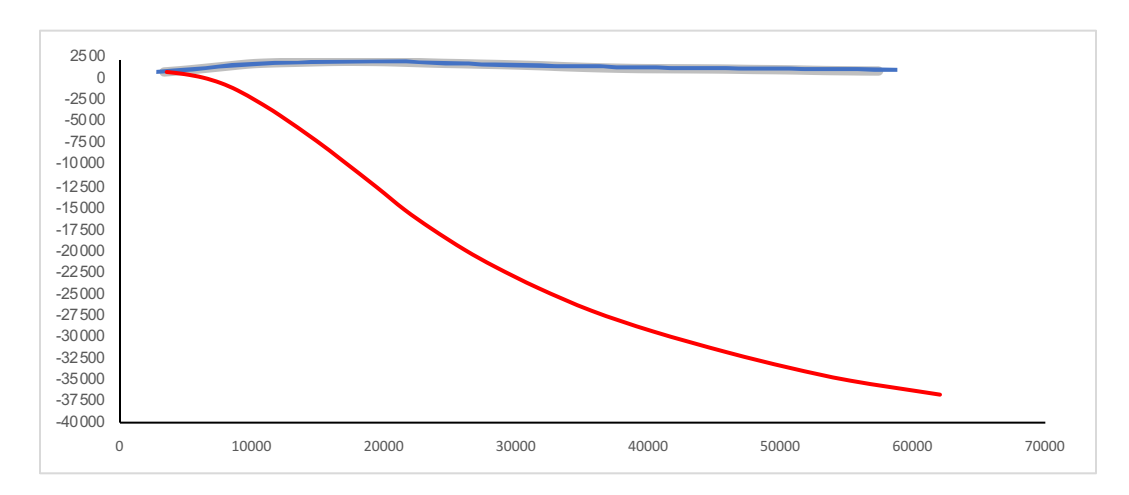
Fault ID 89



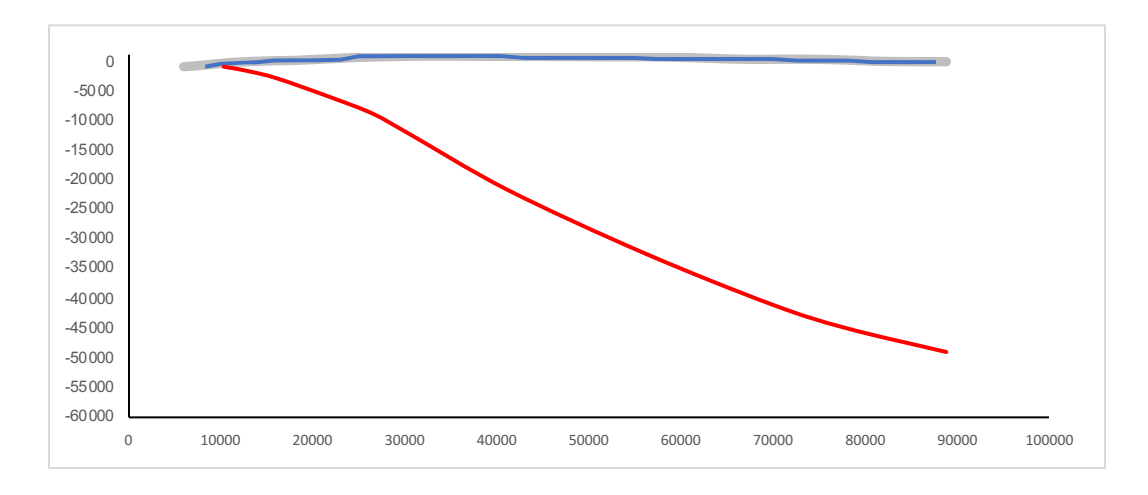
Fault ID 90



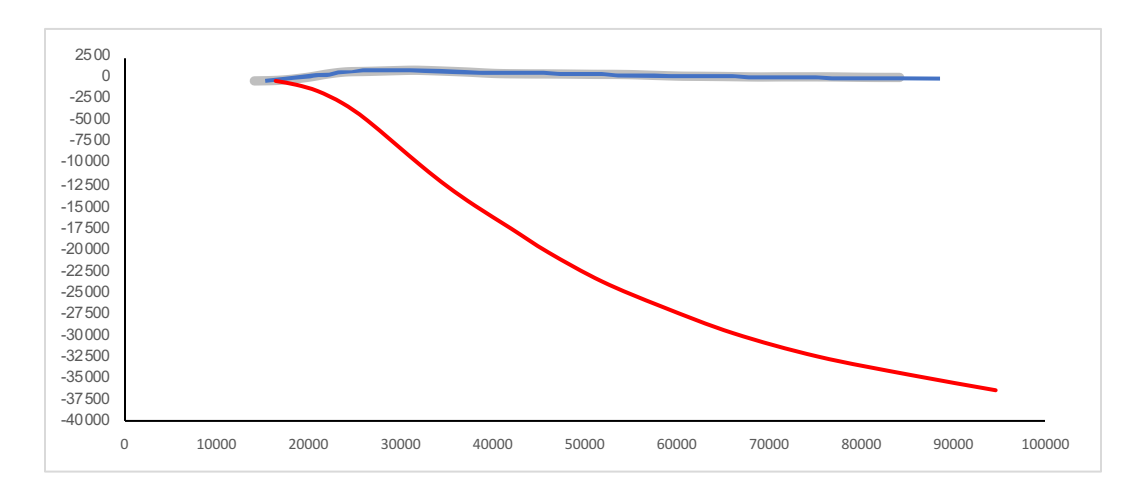
Fault ID 91



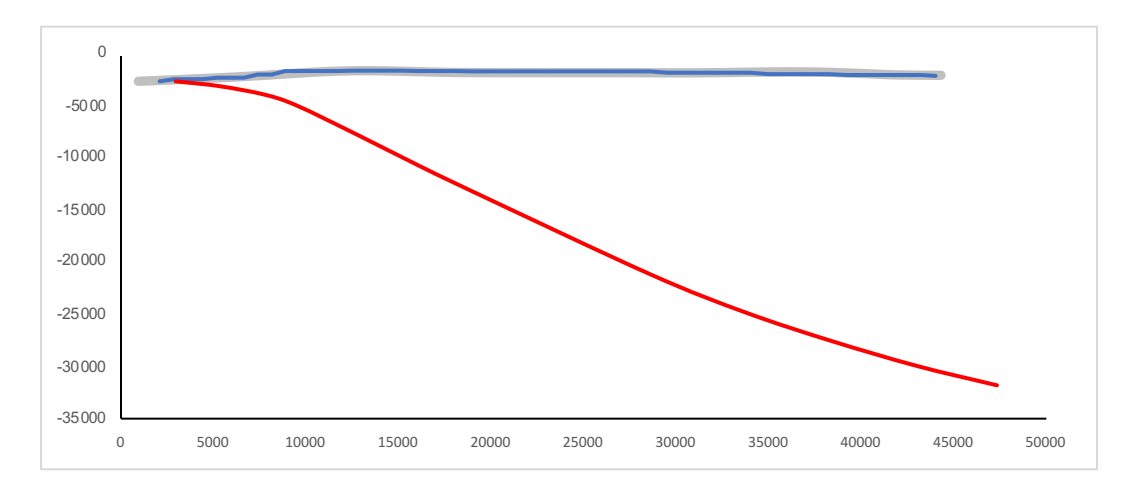
Fault ID 92



Fault ID 97



Fault ID 99



APPENDIX C: CHAPTER 4

Table C4.1: Complete ΔR and strain results table

	Depth of Faulted Volume									
Data Set	ΔR	Values []	km]	Strain Values						
Loveless	30 km	40 km	<u>50 km</u>	<u>30 km</u>	40 km	<u>50 km</u>				
$22^{\circ} \operatorname{dip} \& \lambda = \frac{\pi}{4} \frac{l}{L}$	2.5	1.9	1.5	-2.0×10 ⁻³	-1.5×10 ⁻³	-1.2×10 ⁻³				
$22^{\circ} \operatorname{dip} \& \lambda = \frac{l}{L}$	3.1	2.4	1.9	-2.6×10 ⁻³	-1.9×10 ⁻³	-1.6×10 ⁻³				
$30^{\circ} \operatorname{dip} \& \lambda = \frac{\pi}{4} \frac{l}{L}$	3.1	2.3	1.9	-2.5×10 ⁻³	-1.9×10 ⁻³	-1.5×10 ⁻³				
$30^{\circ} \operatorname{dip} \& \lambda = \frac{l}{L}$	3.9	2.9	2.4	-3.2×10 ⁻³	-2.4×10 ⁻³	-1.9×10 ⁻³				
$40^{\circ} \operatorname{dip} \& \lambda = \frac{\pi}{4} \frac{l}{L}$	3.5	2.6	2.1	-2.9×10 ⁻³	-2.1×10 ⁻³	-1.7×10 ⁻³				
$40^{\circ} \operatorname{dip} \& \lambda = \frac{\iota}{L}$	4.4	3.3	2.7	-3.6×10 ⁻³	-2.7×10 ⁻³	-2.2×10 ⁻³				
Byrne	30 km	40 km	<u>50 km</u>	<u>30 km</u>	40 km	<u>50 km</u>				
$22^{\circ} \operatorname{dip} \& \lambda = \frac{\pi}{4} \frac{l}{L}$	1.7	1.3	1.1	-1.4×10 ⁻³	-1.1×10 ⁻³	-8.7×10 ⁻⁴				
$22^{\circ} \operatorname{dip} \& \lambda = \frac{l}{L}$	2.2	1.7	1.3	-1.8×10 ⁻³	-1.4×10 ⁻³	-1.1×10 ⁻³				
$30^{\circ} \operatorname{dip} \& \lambda = \frac{\pi}{4} \frac{l}{L}$	3.7	2.8	2.2	-3.0×10 ⁻³	-2.3×10 ⁻³	-1.8×10 ⁻³				
$30^{\circ} \operatorname{dip} \& \lambda = \frac{l}{L}$	4.7	3.5	2.8	-3.8×10 ⁻³	-2.9×10 ⁻³	-2.3×10 ⁻³				
$40^{\circ} \operatorname{dip} \& \lambda = \frac{\pi}{4} \frac{l}{L}$	6.6	4.9	4.0	-5.4×10 ⁻³	-4.0×10 ⁻³	-3.2×10 ⁻³				
$40^{\circ} \operatorname{dip} \& \lambda = \frac{l}{L}$	8.4	6.3	5.0	-6.8×10 ⁻²	-5.1×10 ⁻³	-4.1×10 ⁻³				

Watters	<u>30 km</u>	<u>40 km</u>	<u>50 km</u>	<u>30 km</u>	<u>40 km</u>	<u>50 km</u>
$22^{\circ} \operatorname{dip} \& \lambda = \frac{\pi}{4} \frac{l}{L}$	1.4	1.1	0.9	-1.2×10 ⁻³	-8.8×10 ⁻⁴	-7.1×10 ⁻⁴
$22^{\circ} \operatorname{dip} \& \lambda = \frac{l}{L}$	1.8	1.4	1.1	-1.5×10 ⁻³	-1.1×10 ⁻³	-9.0×10 ⁻⁴
$30^{\circ} \operatorname{dip} \& \lambda = \frac{\pi}{4} \frac{l}{L}$	3.2	2.4	1.9	-2.6×10 ⁻³	-2.0×10 ⁻³	-1.6×10 ⁻³
$30^{\circ} \operatorname{dip} \& \lambda = \frac{l}{L}$	4.0	3.0	2.4	-3.3×10 ⁻³	-2.5×10 ⁻³	-2.0×10 ⁻³
$40^{\circ} \operatorname{dip} \& \lambda = \frac{\pi}{4} \frac{l}{L}$						
$40^{\circ} \operatorname{dip} \& \lambda = \frac{l}{L}$	7.6	5.7	4.6	-6.2×10 ⁻³	-4.7×10 ⁻³	-3.8×10 ⁻³

CODE IN R USED FOR STRAIN CALCULATIONS OF CHAPTER 4

setwd(' ') # SET DIRECTORY FOR FAULT DATA SETS

Reading in files and assigning data to appropriate vector names. All data is log transformed for regressions.

Displacement length data should be in a two-column data table and in meters. Assessment of the cumulative number length distribution should be done prior and the truncated data table containing only the linear portion of the data should be read in.

```
# == Loveless et al ==

Loveless_dispLength <- read.table('modeled_DL.csv', sep=','
, header=TRUE)

Loveless_length <- log10(Loveless_dispLength$SL)

Loveless_disp <- log10(Loveless_dispLength$AvgSlip)</pre>
```

```
Loveless_Number_Data <-
read.table('Loveless_NUM_L_Linear.csv', sep=',' ,
header=TRUE)
Loveless linear Num <- log10(Loveless Number Data$NUM)</pre>
```

```
Loveless linear length <-
log10(Loveless Number Data$length m)
# == Byrne et al ==
Byrne dispLength <- read.table('Byrne DL.csv', sep=',',
header=TRUE)
Byrne length <- log10(Byrne dispLength$Length m)</pre>
Byrne disp22 <- log10(Byrne dispLength$Displacement 22)</pre>
Byrne disp25 <- log10(Byrne dispLength$Displacement 25)</pre>
Byrne disp30 <- log10(Byrne dispLength$Displacement 30)</pre>
Byrne disp35 <- log10(Byrne dispLength$Displacement 35)</pre>
Byrne disp40 <- log10(Byrne dispLength$Displacement 40)</pre>
Byrne_Number_Data <- read.table('Byrne NUM L Linear.csv',</pre>
sep=',' , header=TRUE)
Byrne linear Num <- log10(Byrne Number Data$NUM)</pre>
Byrne linear length <- log10(Byrne Number Data$Length m)</pre>
# == Watters ==
Watters dispLength <- read.table('Watters DL.csv', sep=','
, header=TRUE)
```

```
Watters length <- log10(Watters dispLength$Length m)</pre>
Watters disp22 <- log10(Watters dispLength$Displacement 22)</pre>
Watters disp25 <- log10(Watters dispLength$Displacement 25)</pre>
Watters disp30 <- log10(Watters dispLength$Displacement 30)</pre>
Watters disp35 <- log10(Watters dispLength$Displacement 35)</pre>
Watters disp40 <- log10(Watters dispLength$Displacement 40)</pre>
Watters Number Data <-
read.table('Watters NUM L Linear.csv', sep=',' ,
header=TRUE)
Watters linear Num <- log10(Watters Number Data$NUM)</pre>
Watters linear length <- log10(Watters Number Data$Sph Len)</pre>
# Model 2 regression functions - package was troublesome
smaSlope <- function(x, y) { # Slope</pre>
     cor <- cor(x, y)
   sign < -ifelse(cor >= 0, 1, -1)
   b1 < - sign * sd(y)/sd(x)
   b1
}
smaIntercept <- function(x, y) { # Intercept</pre>
```

```
b1 <- smaSlope(x, y)
   b0 <- mean(y) - mean(x)*b1
   b0
}
seSlope <- function(x, y) { # Standard Error of Slope</pre>
     b1 <- smaSlope(x, y)
     se <- abs(b1) *sqrt((1-(cor(x,y))^2)/length(x))
     se
}
seIntercept <- function(x, y) { # Standard Error of</pre>
Intercept
     A < - sd(y)
     B \leftarrow sqrt((1-(cor(x,y))^2)/length(x))
     C \leftarrow sqrt(1+((mean(x))^2)/(sd(x))^2)
     se <- A*B*C
     se
}
# Running Functions to derive statistics P, B, M, and G
Loveless P <- smaSlope (Loveless length, Loveless disp)
Loveless B <- 10^(-1*smaIntercept(Loveless length,
Loveless disp))
```

```
Loveless_M <- -1 * smaSlope(Loveless linear length,
Loveless linear Num)
Loveless G <- smaIntercept (Loveless linear length,
Loveless linear Num)
Loveless P se <- seSlope(Loveless length, Loveless disp)
Loveless B se <- 10^(-1*seIntercept(Loveless length,
Loveless disp))
Loveless M se <- seSlope(Loveless linear length,
Loveless linear Num)
Byrne P22 <- smaSlope(Byrne length, Byrne disp22)</pre>
Byrne B22 <- 10^(-1*smaIntercept(Byrne length,
Byrne disp22))
Byrne P25 <- smaSlope(Byrne length, Byrne disp25)</pre>
Byrne B25 <- 10^(-1*smaIntercept(Byrne length,
Byrne disp25))
Byrne P30 <- smaSlope(Byrne length, Byrne disp30)</pre>
Byrne B30 <- 10^(-1*smaIntercept(Byrne length,
Byrne disp30))
```

```
Byrne_M <- -1 * smaSlope(Byrne linear length,</pre>
Byrne linear Num)
Byrne G <- smaIntercept(Byrne linear length,</pre>
Byrne linear Num)
Byrne P35 <- smaSlope(Byrne length, Byrne disp35)</pre>
Byrne B35 <- 10^(-1*smaIntercept(Byrne length,
Byrne disp35))
Byrne P40 <- smaSlope(Byrne length, Byrne disp40)</pre>
Byrne B40 <- 10^(-1*smaIntercept(Byrne length,
Byrne disp40))
Watters P22 <- smaSlope(Watters length, Watters disp22)
Watters B22 <- 10^(-1*smaIntercept(Watters length,
Watters disp22))
Watters P25 <- smaSlope(Watters length, Watters disp25)</pre>
Watters B25 <- 10^(-1*smaIntercept(Watters length,
Watters disp25))
Watters P30 <- smaSlope(Watters length, Watters disp30)</pre>
```

```
Watters B30 <- 10^(-1*smaIntercept(Watters length,
Watters disp30))
Watters P35 <- smaSlope(Watters length, Watters disp35)</pre>
Watters B35 <- 10^(-1*smaIntercept(Watters length,
Watters disp35))
Watters_M <- -1 * smaSlope(Watters linear length,
Watters linear Num)
Watters G <- smaIntercept(Watters linear length,
Watters linear Num)
Watters P40 <- smaSlope(Watters length, Watters disp40)
Watters B40 <- 10^(-1*smaIntercept(Watters length,
Watters disp40))
# Standard deviations for regression Statistics for P B and
Μ
Loveless P se <- seSlope(Loveless length, Loveless disp)
Loveless B se <- 10^(-1*seIntercept(Loveless length,
Loveless disp))
Loveless M se <- seSlope (Loveless linear length,
Loveless linear Num)
```

```
Byrne_M_se <- seSlope(Byrne linear length,</pre>
Byrne linear Num)
Byrne P25 se <- seSlope(Byrne length, Byrne disp25)
Byrne B25 se <- 10^(-1*seIntercept(Byrne length,
Byrne disp25))
Byrne P30 se <- seSlope(Byrne length, Byrne disp30)</pre>
Byrne B30 se <- 10^(-1*seIntercept(Byrne length,
Byrne disp30))
Byrne P35 se <- seSlope(Byrne length, Byrne disp35)
Byrne B35 se <- 10^(-1*seIntercept(Byrne length,
Byrne disp35))
Watters M se <- seSlope(Watters linear length,
Watters linear Num)
Watters_P25_se <- seSlope(Watters length, Watters disp25)</pre>
Watters B25 se <- 10^(-1*seIntercept(Watters length,
Watters disp25))
Watters P30 se <- seSlope(Watters length, Watters disp30)</pre>
```

```
Watters B30 se <- 10^(-1*seIntercept(Watters length,
Watters disp30))
Watters_P35_se <- seSlope(Watters_length, Watters_disp35)</pre>
Watters B35 se <- 10^(-1*seIntercept(Watters length,
Watters disp35))
# Stating Derived Statistics
Loveless_G
Watters_G
Byrne G
Loveless_P
Byrne P22
Watters P22
Byrne P30
Watters P30
Loveless P
Byrne P40
```

Watters P40

Loveless B

Byrne B30

Watters B30

 ${\tt Loveless_M}$

Byrne M

 ${\tt Watters}\ {\tt M}$

Loveless_P_se

Byrne_B30_se

Watters P30 se

Loveless_B_se

Byrne_B30_se

Watters B30 se

Strain & Radius Change Function. The annotation
strain_real_lower is the calculation ran for an elliptical
fault shape (lower values). Strain_real_upper is the
calculation for rectangular fault shapes (higher values)

```
strain real lower <- function(p, B, m, dipangle, lithrad){</pre>
          p norm <- p
          B norm <- B
          m norm <- m
          nu <- pi/4. # Geometric Shape factor for
elliptical faults
          phi <- ((180-dipangle)*pi/180)</pre>
          rho <- phi
          theta <- (90-dipangle) *pi/180
          R Mercury <- 2.44 * 10^6 # Meters
          R Lith <- (2.44 * 10^6) - (lithrad * 1000.) #
Meters. lithrad is the depth of the brittle lithosphere of
Mercury
          Vol Mercury <- (4/3) * pi * (R Mercury^3)</pre>
          Vol Lith <- Vol Mercury - ((4/3) * pi *
(R Lith) ^3)
          s <- m norm/p norm
          Enterprise Relief <- 3261.8 #meters</pre>
          disp1 <- 9300 # modeled Enterprise Relief</pre>
          A <- nu * 0.41 * (B norm^(2./p norm)) #geometric
factor and average from models
          Bird <- 1./Vol Lith
          C <- (disp1)^{(1 + (2./p norm))}
          D <- -1*\cos(theta) * \cos(phi)
```

```
E <- (1+(2./p norm))/(1-(s-(2/p norm)))
           strainTOT <- -1*A*Bird*C*D*E
           Vol initial <- Vol Lith/(strainTOT + 1)</pre>
           R Initial = ((R Mercury^2)/(strainTOT+1))^0.5
           radiusDif <- R Initial - R Mercury</pre>
           c(strainTOT, radiusDif)
}
strain real upper <- function(p, B, m, dipangle, lithrad){</pre>
          p norm <- p #rnorm(1, mean=p, sd=psd) #creating</pre>
random values for each statistic
           B norm <- B #rnorm(1, mean=B, sd=bsd) # and using
their estimates and standard errors
          m norm <- m # rnorm(1, mean=m, sd=msd) # found</pre>
from the regression to generate random values
          n_{11} < -1.
          phi <- ((180-dipangle)*pi/180)</pre>
          rho <- phi
          theta <- (90-dipangle) *pi/180
          R Mercury <- 2.44 * 10^6 # Meters</pre>
          R Lith <- (2.44 * 10^6) - (lithrad * 1000.) #
Meters. lithrad is the depth of the brittle lithosphere of
Mercury
          Vol Mercury <- (4/3) * pi * (R Mercury^3)</pre>
```

```
Vol Lith <- Vol Mercury - ((4/3) * pi *
(R Lith) ^3)
           s <- m norm/p norm
          Enterprise Relief <- 3261.8 #meters</pre>
          disp1 <- 9300 # Enterprise Relief/sin(phi)</pre>
          A <- nu * 0.41 * (B norm^(2./p norm)) #geometric
factor and average from models
          Bird <- 1./Vol Lith</pre>
          C \leftarrow (disp1)^(1 + (2./p norm))
          D <- -1*cos(theta) * cos(phi)
          E \leftarrow (1+(2./p norm))/(1-(s-(2/p norm)))
           strainTOT <- -1*A*Bird*C*D*E</pre>
          Vol initial <- Vol Lith/(strainTOT + 1)</pre>
          R Initial = ((R Mercury^2)/(strainTOT+1))^0.5
           radiusDif <- R Initial - R Mercury</pre>
          c(strainTOT, radiusDif)
}
# ====== Calcultating Strain and Radius change for
Elliptical Fault Shape for all data sets ======
# Fault dip of 22 deg
```

```
strain real lower (Loveless P, Loveless B, Loveless M, 22,
30)
strain real lower (Byrne P22, Byrne B22, Byrne M, 22, 30)
strain real lower (Watters P22, Watters B22, Watters M, 22,
30)
strain real lower (Loveless P, Loveless B, Loveless M, 22,
40)
strain real lower (Byrne P22, Byrne B22, Byrne M, 22, 40)
strain real lower (Watters P22, Watters B22, Watters M, 22,
40)
strain real lower (Loveless P, Loveless B, Loveless M, 22,
50)
strain real lower (Byrne P22, Byrne B22, Byrne M, 22, 50)
strain real lower (Watters P22, Watters B22, Watters M, 22,
50)
# ====== Elliptical Fault Shape ====== optimal 30 degrees
# Fault dip of 30 deg
strain real lower (Loveless P, Loveless B, Loveless M, 30,
30)
```

```
strain real lower (Byrne P30, Byrne B30, Byrne M, 30, 30)
strain real lower (Watters P30, Watters B30, Watters M, 30,
30)
strain real lower (Loveless P, Loveless B, Loveless M, 30,
40)
strain real lower (Byrne P30, Byrne B30, Byrne M, 30, 40)
strain real lower (Watters P30, Watters B30, Watters M, 30,
40)
strain real lower (Loveless P, Loveless B, Loveless M, 30,
50)
strain real lower (Byrne P30, Byrne B30, Byrne M, 30, 50)
strain real lower (Watters P30, Watters B30, Watters M, 30,
50)
# Fault dip of 40 deg
strain real lower (Loveless P, Loveless B, Loveless M, 40,
30)
strain real lower (Byrne P40, Byrne B40, Byrne M, 40, 30)
strain real lower (Watters P40, Watters B40, Watters M, 40,
30)
```

```
strain real lower (Loveless P, Loveless B, Loveless M, 40,
40)
strain real lower (Byrne P40, Byrne B40, Byrne M, 40, 40)
strain real lower (Watters P40, Watters B40, Watters M, 40,
40)
strain real lower (Loveless P, Loveless B, Loveless M, 40,
50)
strain real lower (Byrne P40, Byrne B40, Byrne M, 40, 50)
strain real lower (Watters P40, Watters B40, Watters M, 40,
50)
# ====== Calcultating Strain and Radius change for
Rectangular Fault Shape for all data sets ======
# Fault dip of 22 deg
strain real upper (Loveless P, Loveless B, Loveless M, 22,
30)
strain real upper (Byrne P22, Byrne B22, Byrne M, 22, 30)
strain real upper (Watters P22, Watters B22, Watters M, 22,
30)
```

```
strain real upper (Loveless P, Loveless B, Loveless M, 22,
40)
strain real upper (Byrne P22, Byrne B22, Byrne M, 22, 40)
strain real upper (Watters P22, Watters B22, Watters M, 22,
40)
strain real upper (Loveless P, Loveless B, Loveless M, 22,
50)
strain real upper (Byrne P22, Byrne B22, Byrne M, 22, 50)
strain real upper (Watters P22, Watters B22, Watters M, 22,
50)
# ====== Rectangular Fault Shape ======
# Fault dip of 30 deg
strain real upper (Loveless P, Loveless B, Loveless M, 30,
30)
strain real upper (Byrne P30, Byrne B30, Byrne M, 30, 30)
strain real upper (Watters P30, Watters B30, Watters M, 30,
30)
strain real upper (Loveless P, Loveless B, Loveless M, 30,
40)
```

```
strain real upper (Byrne P30, Byrne B30, Byrne M, 30, 40)
strain real upper (Watters P30, Watters B30, Watters M, 30,
40)
strain real upper (Loveless P, Loveless B, Loveless M, 30,
50)
strain real upper (Byrne P30, Byrne B30, Byrne M, 30, 50)
strain real upper (Watters P30, Watters B30, Watters M, 30,
50)
# Fault dip of 40 deg
strain real upper (Loveless P, Loveless B, Loveless M, 40,
30)
strain real upper (Byrne P40, Byrne B40, Byrne M, 40, 30)
strain real upper (Watters P40, Watters B40, Watters M, 40,
30)
strain real upper (Loveless P, Loveless B, Loveless M, 40,
40)
strain real upper (Byrne P40, Byrne B40, Byrne M, 40, 40)
strain real upper (Watters P40, Watters B40, Watters M, 40,
40)
```

```
strain_real_upper(Loveless_P, Loveless_B, Loveless_M, 40,
50)
strain_real_upper(Byrne_P40, Byrne_B40, Byrne_M, 40, 50)
strain_real_upper(Watters_P40, Watters_B40, Watters_M, 40,
50)
```